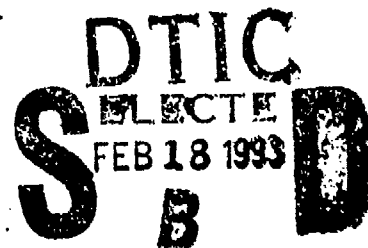


AD-A260 530



UNITED
TECHNOLOGIES
RESEARCH
CENTER

UTRC Report R92-958325-6



An Oscillating Three-Dimensional Wing Experiment: Compressibility, Sweep, Rate, Waveform, and Geometry Effects on Unsteady Separation and Dynamic Stall

Final Report

by

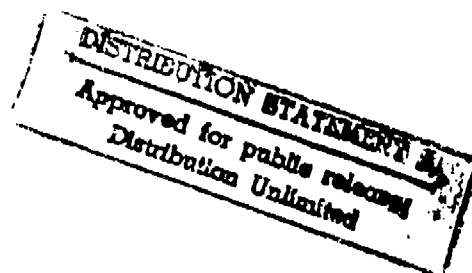
Peter F. Lorber, Franklin O. Carta and Alfred F. Covino, Jr

United Technologies Research Center
East Hartford, CT 06108

93-03117

Prepared For

U.S. Army Research Office
Contract DAAL03-89-C-0013



November 30, 1992

Distribution Unlimited

The views, opinions, and/or findings contained in this report are those of the authors and should not be construed as an official department of the Army position, policy, or decision, unless so designated by other documentation.

REPORT DOCUMENTATION PAGE			Form Approved OMB No. 0704-0188	
<small>Public reporting burden for this collection of information is estimated to average 1 hour per response, including the time for reviewing instructions, searching existing data sources, gathering and maintaining the data needed, and completing and reviewing the collection of information. Send comments regarding this burden estimate or any other aspect of this collection of information, including suggestions for reducing this burden, to Washington Headquarters Services, Directorate for Information Operations and Reports, 1215 Jefferson Davis Highway, Suite 1204, Arlington, VA 22202-4302, and to the Office of Management and Budget, Paperwork Reduction Project (0704-0188), Washington, DC 20503.</small>				
1. AGENCY USE ONLY (Leave blank)		2. REPORT DATE November 1992		3. REPORT TYPE AND DATES COVERED Final Report Apr 1989 - Nov 1992
4. TITLE AND SUBTITLE An Oscillating Three-Dimensional Wing Experiment: Compressibility, Sweep, Rate, Waveform, and Geometry Effects on Unsteady Separation and Dynamic Stall			5. FUNDING NUMBERS DAAL03-89-C-0013	
6. AUTHOR(S) Peter F. Lorber, Franklin O. Carta, and Alfred F. Covino, Jr.				
7. PERFORMING ORGANIZATION NAME(S) AND ADDRESS(ES) United Technologies Research Center 400 Main Street - MS 129-18 East Hartford, Connecticut 06108			8. PERFORMING ORGANIZATION REPORT NUMBER R92-958325-6	
9. SPONSORING/MONITORING AGENCY NAME(S) AND ADDRESS(ES) U. S. Army Research Office P. O. Box 12211 Research Triangle Park, NC 27709-2211			10. SPONSORING/MONITORING AGENCY REPORT NUMBER ARO 26631.8-EG	
11. SUPPLEMENTARY NOTES The view, opinions and/or findings contained in this report are those of the author(s) and should not be construed as an official Department of the Army position, policy, or decision, unless so designated by other documentation.				
12a. DISTRIBUTION/AVAILABILITY STATEMENT Approved for public release; distribution unlimited.			12b. DISTRIBUTION CODE	
13. ABSTRACT (Maximum 200 words) Experimental measurements of the unsteady separation and dynamic stall process on an oscillating three-dimensional wing are reported. The experiment was conducted at Mach numbers of 0.2-0.6, Reynolds numbers of 2-6 million, and sweep angles of 0, 15, and 30°. At low Mach number, as angle of attack is increased the location of transition to turbulence moves forward, the turbulent boundary layer separates near the leading edge, and a strong stall vortex is formed. At higher Mach number, compressibility causes formation of a shock, an earlier, more gradual separation, and reduced unsteady loads. Unsteady tip loads at 0 sweep are increased by the growth of a strong tip vortex. This effect is lessened by sweep-back and compressibility, and enhanced by replacing the round tip cap with a flat tip. Away from the tip, sweep effects on loads are well represented by the swept infinite wing normalization until stall. After stall, vortex propagation patterns are highly dependent on sweep and spanwise position. Sinusoidal and constant pitch rate ramp motions show similar behavior. There is significant hysteresis in both the transition/re-laminarization and the separation/reattachment processes. For small amplitude motions simulating stall flutter, substantial regions of negative aerodynamic damping were found at all studied Mach numbers, sweep angles, and reduced frequencies. The near-simultaneous stall along the span of the swept wing strengthens the resulting instability. An empirical representation of the damping characteristics was developed.				
14. SUBJECT TERMS Unsteady Flow Separated Flow Transition Helicopter Aero- Dynamic Stall Stall Flutter Supermaneuverability Dynamics Unsteady Aerodynamics			15. NUMBER OF PAGES 187	
17. SECURITY CLASSIFICATION OF REPORT UNCLASSIFIED			18. SECURITY CLASSIFICATION OF THIS PAGE UNCLASSIFIED	
19. SECURITY CLASSIFICATION OF ABSTRACT UNCLASSIFIED			20. LIMITATION OF ABSTRACT UL	

FOREWORD

This experiment was conducted under contract DAAL03-89-C-0013 with the U.S. Army Research Office. Dr. Thomas Doligalski was the technical monitor. Support for the contract was also provided by the U.S. Air Force Office of Scientific Research. Captain Hank Helin and Major Daniel Fant were the AFOSR representatives. The low amplitude (stall flutter simulation) portion of the contract was supported by NASA Lewis Research Center. The contract paid for fabricating the instrumented tip portion of the model, conducting the wind tunnel test, and reducing, analyzing, and documenting the results.

The model support structure, hydraulic drive system, and the uninstrumented portion of the model were developed previously with funding provided by the Sikorsky Aircraft Division of United Technologies Corporation. The signal conditioning and data acquisition system was developed under United Technologies Research Center's Corporate-Sponsored Research program. The main instrumented airfoil panel was fabricated as part of an earlier two-dimensional experiment supported by the AFOSR (Contract F49620-84-C-0082).

The Principal Investigator for this experiment was Peter Lorber, the Program Manager was Franklin Carta, and the Lead Technician was Alfred Covino. This program is part of continuing activity at UTRC's Aeromechanics Research Section (managed by Anton J. Landgrebe) to advance unsteady aerodynamics technology related to helicopter rotors, propellers, and fixed wings. The authors thank John Ayer and the staff of the UTRC Large Subsonic Wind Tunnel for their assistance during the two month test program.

DTIC QUALITY INSPECTED 3

Accession For	
NTIS GRA&I	<input checked="checked" type="checkbox"/>
DTIC TAB	<input type="checkbox"/>
Unannounced	<input type="checkbox"/>
Justification	
By	
Distribution/	
Availability Codes	
Dist	Avail and/or Special
A-1	

TABLE OF CONTENTS

	Page
LIST OF TABLES.....	v
LIST OF ILLUSTRATIONS.....	vi
NOMENCLATURE.....	vii
INTRODUCTION.....	1
DESCRIPTION OF EXPERIMENT.....	4
SUMMARY OF RESULTS.....	11
LIST OF PUBLICATIONS, PERSONNEL, AND INVENTIONS.....	15
REFERENCES.....	17
TABLES.....	20
ILLUSTRATIONS.....	24
APPENDIX I TEST MATRICES.....	32
APPENDIX II RUN LIST.....	40
APPENDIX III DOCUMENTATION OF THE EXPERIMENTAL DATA BASE.....	67
APPENDIX IV "INCIPIENT TORSIONAL STALL FLUTTER AERODYNAMIC EXPERIMENTS ON A SWEPT THREE-DIMENSIONAL WING".....	74
APPENDIX V "DYNAMIC STALL EXPERIMENTS ON A SWEPT THREE-DIMENSIONAL WING IN COMPRESSIBLE FLOW".....	84
APPENDIX VI "UNSTEADY TRANSITION MEASUREMENTS ON A PITCHING THREE-DIMENSIONAL WING".....	100
APPENDIX VII "COMPRESSIBILITY EFFECTS ON THE DYNAMIC STALL OF A THREE-DIMENSIONAL WING".....	114
APPENDIX VIII "DYNAMIC STALL OF A SINUSOIDALLY OSCILLATING THREE-DIMENSIONAL SWEPT WING IN COMPRESSIBLE FLOW.....	131
APPENDIX IX "TIP VORTEX, STALL VORTEX, AND SEPARATION RESULTS FOR PITCHING THREE-DIMENSIONAL WINGS".....	147
APPENDIX X AN EMPIRICAL MODEL FOR AERODYNAMIC DAMPING.....	164

LIST OF TABLES

	Page
1. Surface coordinates for Sikorsky SSC-A09 Airfoil.....	20
2. Surface derivitives for Sikorsky SSC-A09 Airfoil.....	21
3. Pressure transducer locations.....	22
4. Hot film gage locations	23
5. Additional instrumentation.....	23

LIST OF ILLUSTRATIONS

	Page
1. Planform and instrumentation locations at $\Lambda = 0$	24
2. Sikorsky SSC-A09 airfoil section.....	24
3. Planforms at $\Lambda = 0, 15^\circ$, and 30°	25
4. Side view of the model at $\Lambda = 0$	26
5. Top view of the model at $\Lambda = 30^\circ$	26
6. Top view of the model and the support and drive system.....	27
7. Time histories of α during ramp motions.....	28
8. Time histories of α during large amplitude sinusoids.....	28
9. Time histories of α during small amplitude sinusoids.....	29
10. Inside view of the model and instrumentation.....	30
11. Close-up view of the model, showing multiplexers and pressure transducers.....	30
12. Wind tunnel control room, showing unsteady data acquisition system.....	31

NOMENCLATURE

A	nondimensional pitch rate, $\dot{\alpha}c/2U_c$
c	airfoil chord, (17.3 in. , 43.9 cm)
k	reduced frequency, $\omega c/2U_c$
M_c	chordwise Mach number, $M_\infty \cos \Lambda$
T	data acquisition period, sec
U_c	chordwise velocity, $U_\infty \cos \Lambda$
x	distance along chord, perpendicular to leading edge
z	distance along span from wing tip
α	geometric angle of attack, deg
α_0	mean angle for sinusoidal motions
α_1	angular amplitude for sinusoidal motions
$\dot{\alpha}$	pitch rate, rad/sec
Λ	wing sweep back, deg
τ	nondimensional time, t/T
E	aerodynamic pitch damping coefficient, see Appendix IV or X

INTRODUCTION

The process of unsteady separation and dynamic stall, because of its importance to applications such as helicopter rotor, maneuvering aircraft, highly loaded propellers, and turbomachinery, as well as its inherent interest as a fluid dynamic problem, has been extensively studied by numerous researchers using a wide variety of experimental, analytical, and computational techniques.¹⁻¹⁹ Various methods, such as force balances,¹⁴ flow visualization,^{6,7-9,12} interferometers,¹⁰ laser velocimeters, and surface pressure transducers^{1-6,11,13} have been used to measure flow field characteristics and loads on the aerodynamic surfaces. Model geometries and test conditions have been quite diverse. Models have included two-dimensional (2D) airfoils,^{1-3,6,8-11,13} three-dimensional (3D) wings,^{4-5,12} and complex multi-element configurations.⁷ The conditions of each experiment may be defined by the parameters that quantify the relative motion between the surface and the fluid: Mach number, Reynolds number, type of unsteadiness (plunging, pitching, or translation), waveform (sinusoid, constant-rate ramp, or arbitrary), amplitude, and frequency (or pitch rate). Each study usually concentrates on a relatively small region of this multi-parameter field. The listed references provide a selection of recent work, and illustrate the considerable information that has been uncovered. A unified picture of the inception and progression of unsteady separation and stall that encompasses conditions of both practical and academic interest has, however, still not been developed.

The present experiment is concerned with a sizable, but still limited, subset of this field. The geometry was a rectangular semi-span wing pitching about its quarter chord. The approach was to make extensive surface measurements (using pressure and hot film sensors) at Mach and Reynolds numbers representative of full scale applications such as helicopter rotors or maneuvering aircraft. The pressure measurements were then integrated to obtain the aerodynamic force and moment at five spanwise stations, all within 1.6 chord lengths of the tip. The objectives were straightforward: to obtain a clear picture of the unsteady separation and stall process on this model, and to examine in a single experiment the effects of Mach number, frequency, waveform, pitching amplitude, and wing sweep.

4

A considerable portion of the experiment dealt with large amplitude motions, such as constant pitch rate ramps from $\alpha = 0$ to 30° or sinusoidal oscillations with amplitudes of ± 6 or 10° . Test Mach numbers ranged from $M_c = 0.2$ to 0.6 , sweep angles from $\Lambda = 0$ to 30° , and nondimensional pitch rates from $A = 0.001$ to 0.025 . The model chord of 17.3 in (44 cm) was typical of a full-scale helicopter main rotor, and resulted in Reynolds numbers of 2 to 6 million. The appropriateness of these conditions to helicopter dynamic stall was confirmed during a recent wind tunnel test of a pressure-instrumented model rotor.²⁰ For moderate speed forward flight, dynamic stall occurred on the inboard region of the rotor blade at local pitch rates between $A = 0.01$ and 0.015 and Mach numbers between 0.2 and 0.4 . Qualitative features of stall observed on the model rotor were quite similar to results for oscillating airfoils,²¹⁻²² and to measurements on the inboard portion of the current 3D wing.

In addition to investigating large amplitude dynamic stall, this experiment also examined the aerodynamics of small amplitude pitching oscillations near static stall. The motivation for this research is the self-induced torsional stall flutter problem experienced by propeller blades. The instability may be encountered during high thrust static testing or at the start of the takeoff roll, when the blades are operating at high angles of attack. The characteristic behavior includes a small amplitude initiation, a rapid growth to a large amplitude, and a reduction in growth rate to establish a constant amplitude, limit-cycle oscillation. Early phenomenological studies²³⁻²⁵ used strain gages to record the decay or growth of the airfoil torsional response, but were unable to determine the actual aerodynamic damping or characterize the underlying physical mechanism. The related problem of stall flutter of helicopter rotor blades was studied, starting in the 1960's, by measuring aerodynamic loads during forced motions of relatively large amplitude ($\pm 5-8^\circ$).²⁶⁻²⁸ A preliminary experiment²⁹ made pressure measurements on a two-dimensional airfoil model oscillating in pitch at amplitudes of 0.5 , 2.0 , and 4.0° . The strongest negative (unstable) damping coefficients were found near the static stall angle for amplitudes of 0.5 and 2.0° . The measured damping coefficients were then applied in a simple model problem to compute the behavior of a single degree-of-freedom torsional oscillation. The predicted rapid growth to a limit cycle oscillation was similar to the early stall flutter results.

This previous incipient stall flutter experiment²⁹ used a two-dimensional model, and was limited to relatively low Reynolds number, Mach number, and frequency ($Re = 650,000$, $M_\infty = 0.18$, and $k \leq 0.16$). The small wind tunnel had less than ideal flow quality (relatively high turbulence level and unknown angularity), resulting in an early static stall (at 9.5°). The current experiment is more sophisticated, and was conducted with a larger model and wind tunnel, with significantly improved instrumentation, and over a much wider range of conditions. The effects of six independent parameters (Mach number, mean angle of attack, oscillation amplitude, reduced frequency, sweep angle, and spanwise position) were studied. The resulting conceptual model of incipient stall flutter may aid the design of lightweight propellers that avoid potential instabilities but do not require excessive stiffness.

This work described in this report is part of a continuing research program. Unswept tunnel-spanning wing (2D) results for this model have been presented in Refs. 21-22. Computational simulations of the 2D experiment were described in Refs. 15-16. An earlier version of the UTRC oscillating wing was tested in a swept 2D configuration.¹⁻²

The body of this report consists of this discussion of the motivation for the experiment, a description of the experiment and procedures, and a summary of the primary observations and conclusions. Additional material is provided in the attached Appendices. The first two Appendices contain test matrices and run lists for all conditions studied. Appendix III provides documentation for the experimental data base that has been generated. At the request of the ARO, a set of digital tapes containing this data base has been provided to Dr. Lawrence Carr at NASA Ames Research Center. Copies of the data tapes should be available from NASA Ames as well as from the authors. The primary technical results of this experiment have been presented in the series of papers that are provided as Appendices IV-IX. The final Appendix (X) describes an empirical model for aerodynamic damping, and the tabulated data upon which it is based.

DESCRIPTION OF EXPERIMENT

MODEL AND WIND TUNNEL

The model was a straight, rectangular, untwisted, semi-span wing of 17.3 in. (44 cm) chord and 48 in. (122 cm) semi-span. The planform is shown in Fig. 1. The aspect ratio of a full wing would be 5.6. The wing consisted of a steel spar and fiberglass airfoil panels, and had a Sikorsky SSC-A09 9% thickness cambered airfoil section (Fig. 2). Airfoil coordinates and surface derivatives are provided in Tables 1 and 2, respectively. The wing was mounted at sweep angles of 0, 15, and 30° from the side wall of the 8 ft (2.4 m) octagonal test section of the UTRC Large Subsonic Wind Tunnel. As shown by the planforms in Fig. 3, additional airfoil panels were added to the spar at higher sweep angles in order to keep the wing tip quarter-chord at the tunnel centerline. At $\Lambda = 30^\circ$ the semi-span was thus increased to 55 in. (140 cm).

Figure 4 shows the model in the unswept configuration in the wind tunnel. The fiberglass airfoil panels and wooden tip cap are apparent. The dark circles on the model are filled bolt holes. The majority of the data were acquired with the tip cap shown here, an approximate half body of revolution. Limited data were also acquired using a square tip cap at $z = 0$. Figure 5 shows a top view of the model in the $\Lambda = 30^\circ$ configuration. The upper section of the wind tunnel has been removed for this picture. The metal tape was added to the joints of the inboard (uninstrumented) sections at high speed ($M_c \geq 0.5$) to prevent air leakage. The tape was not required at lower speeds, and was never used on the instrumented sections. Note the part span support at $z/c = 1.75$. The strut is required to maintain spar loads within the required safety factors, and to reduce bending deflections. At the maximum speed, maximum lift conditions, the wing load of approximately 4000 lbs (18,000 N) produced a bending moment at the strut of 13,000 in-lbs (1480 Nm). The strut is mounted to the spar using a bearing at the quarter-chord, and its lower portion is rotated to keep it parallel to the flow. All instrumentation is outboard of this strut.

The model had a first natural frequency in flatwise bending of approximately 20 Hz, as determined by rap testing and by examination of peaks in the bending strain gage response (instrumentation details are provided below). The bending stiffness was calculated to be approximately 9×10^6 lb in² (2.6×10^4

Nm^2). This was verified by applying concentrated loads at the spar tip and measuring the resulting deflection. At the maximum lift condition (4000 lb), the tip deflection is calculated to be approximately 0.6 in. (1.5 cm, 40% of the wing thickness). Tip deflections scale approximately as $\Delta y(\text{in}) = \text{Lift}(\text{lb}) \times 1.5 \times 10^{-4}$. The bending response of the model primarily consisted of a quasi-steady response to the applied lift and a damped oscillation near the natural frequency upon impulsive starts (as during ramp motions). These oscillations were usually extremely small, resulting in tip deflections of less than 0.1 in. (2 mm).

The first torsional natural frequency was calculated to be 216 Hz, while the measured initial peak in the torsional strain gage response was near 180 Hz, probably reflecting deficiencies in the simple model used in the calculation. The torsional stiffness was calculated to be $1.3 \times 10^7 \text{ lb in}^2$ ($3.7 \times 10^4 \text{ Nm}^2$). The stiffness was also verified (approximately) by measuring deflections in response to a concentrated torque applied to the spar tip. The maximum torsional deflections at the wing tip caused by aerodynamic loads are estimated to be approximately 0.2° . Since the frequencies used in the experiment are much less than the natural torsional frequency, aeroelastic twist nonlinearities should be quite small (on the order of 1% at 20 Hz). The torsional strain gages did detect damped oscillation at frequencies between 50-90 Hz in response to impulsive starts. These oscillations were usually of small amplitude, generating deflections of less than 0.2 - 0.3° which appeared to have little effect on the aerodynamic loads. A much more detailed study of the dynamics of the hydraulic drive, shaft coupler, shaft, spar, wing system would be required for full understanding. This was not considered necessary.

Application of standard wind tunnel wall correction procedures³⁰ to this geometry produces a small flow angle correction of $\Delta\alpha = 0.54^\circ * C_L$ to approximate free flight. (This correction has not been applied in the published data or to the data base.) Corrections to the freestream velocity and to the measured force coefficients were negligible. A minimal gap of $0.005c$ was maintained between the wing root and the wind tunnel wall at $\Lambda = 0$. The maximum gaps in the swept configuration were larger (up to $0.02c$) and varied with α . Oil visualization in steady-state showed the primary effect of the wall on the surface flow vectors to be a corner vortex which covered a triangular region having an extent at the trailing edge of $0.2c$. Beyond this region, the oil pattern did not show obvious wall influence.

ROTARY DRIVE SYSTEM

A hydraulic rotary drive was used to oscillate the model in pitch about the line connecting the root and tip quarter-chord. The drive is shown mounted at the end of its turntable, outside the wind tunnel walls, in Fig. 6. The actuator provides up to 22,500 in-lb (2600 Nm) of torque, and is controlled by high-response servo valves operated by a closed-loop control system, which compares the the measured and desired pitching waveforms. The desired waveform was supplied by a digital synthesizer. The synthesizer read the waveform from a programmable memory chip. The frequency, amplitude, and mean value of the waveform were manually adjusted. In addition to supplying an analog waveform to the hydraulic control system, the synthesizer also supplied synchronizing clock pulses to the data acquisition system.

Two pitching waveforms were used, sinusoids and ramps. The ramps began at a steady-state condition (typically $\alpha = 0$), increased at constant rate to a maximum angle, maintained that maximum for a short time, and then returned to the initial condition. A time delay of 2-4 sec was imposed between ramps to regain steady-state. The sufficiency of the time delay was verified using an unsteady pitot-static probe located 2.8c above the tip quarter-chord to show that conditions returned to steady-state before motion resumed. The maximum angles for ramps were 30° at $M_c = 0.2$ and 0.3 , 20 or 25° at $M_c = 0.4$, 16 or 18° at $M_c = 0.5$, and 10 , 12 , or 13.5° at $M_c = 0.6$. These maxima were determined by the stall characteristics and structural loads at each Mach number and sweep angle. Stall penetration was achieved at each Mach number. The nondimensional pitch rates were selected between $A = \dot{\alpha}c/2U_c$ of 0.001 and 0.025 , bounded by a limiting dimensional pitch rate of $560^\circ/\text{sec}$. Typical ramp time histories, at $M_c = 0.2$ and $\Lambda = 30^\circ$, are shown in Fig. 7. Five pitch rates are shown from $A = 0.001$ to 0.025 , corresponding to dimensional rates of 18 to $450^\circ/\text{sec}$. The primary departure from an ideal constant-rate motion was rounding of the ramp corners at higher rates. At rates very close to the $560^\circ/\text{sec}$ limit, the impulsive start of the ramp caused the spar strain gages to detect bending and torsional oscillations. Below the limiting rate, the oscillations were not significant.

The large amplitude sinusoids were performed at frequencies from 1.25 to 12 Hz ($0.025 \leq k \leq 0.15$), at amplitudes primarily of 6 and 10° , and at numerous

mean angles. Figure 8 shows time histories of α for $10^\circ - 10^\circ \cos 2\pi t$ oscillations at $M_c \approx 0.2$, which are typical. The reduced frequency varies between $k = 0.025$ and 0.15 (1.26 and 7.6 Hz). For such moderate frequency, high amplitude motion the waveform is quite good, with minimal distortion. The distortion of the waveform is increased for the high frequency, low amplitude sinusoids used in the incipient stall flutter portion of the experiment. Figure 9 shows time histories at amplitudes of 1° (Fig. 9a) and 0.5° (Fig. 9b), for $M_c \approx 0.2$ and reduced frequencies between 0.1 and 0.6 (5 to 30 Hz). The distortion is significant for frequencies above 15 Hz, and particularly strong for very small amplitude oscillations at frequencies close to the spar natural bending frequency of approximately 20 Hz.

INSTRUMENTATION

Unsteady surface pressure measurements were made on the wing model using 112 miniature transducers (Kulite 15 psi (10^5 Pa) differential transducers contained in 0.093 in. (2.5 mm) diameter cylinders) distributed among five spanwise stations. The suction surface transducer locations are shown by the dots in Fig. 1. The transducer coordinates are provided in Table 3. The chordwise arrays on the upper surface had 10 , 14 , or 18 transducers each. The lower surface arrays were less dense, containing 6 or 18 transducers each. The frequency response of the installed transducers has been measured by comparing their response to white noise with that of a reference microphone.³¹ The initial resonance is typically between 4 and 12 kHz, considerably higher than the frequency range required for the current experiment, which has fundamental frequencies between 1 and 30 Hz. Steady state calibration was performed over the full range of pressures ($+2.5$ to -12.5 psi) and temperatures (50 to 110 F) expected. This procedure results in a steady-state calibration accuracy of better than 0.5% of the full scale pressure range.^{22,31}

Figure 10 shows the instrumentation mounted inside the model. The lower surface fiberglass panels have been removed to show the interior details. The 5.5 in. wide spar is identified at the top of the picture. The ten dark squares are the circuit boards containing the $8:1$ multiplexers, also shown in a close-up view in Fig. 11. The multiplexers operate as electronic switches. Data are acquired for complete cycles for each of the 14 pressure channels (the 10 shown

in Fig. 10 plus 5 on the lower surface panels), and then all of the multiplexers are switched to the next position, and the motion is repeated. Also visible in Fig. 12 are several pressure transducers (gray cylinders) and the manifolds that distribute the tunnel total pressure to the reference side of each transducer. The transducers are connected to surface by 0.1 in. (typical) long 0.018 in. ID pipettes that pass through the fiberglass panels.

Sixteen surface hot film gages were used to determine transition and separation locations. The gages were located in chordwise arrays at three spanwise stations, $z/c = 0.08, 0.27, \text{ and } 0.70$. The locations are shown by the X marks in Fig. 1, and are listed in Table 4. The $x/c = 0.026$ and 0.103 gages at $z/c = 0.70$ were offset by 1 in. (to $z/c = 0.65$) to reduce the chance for thermal interference. TSI model 1268 gages were installed in holes drilled through the fiberglass airfoil skins. Each gage consists of a heated element deposited on the end of a 0.15 in. (0.38 cm) diameter quartz rod. The hot films were operated in the constant-temperature mode, at a nominal operating temperature of 225 C, corresponding to an overheat ratio (hot to cold gage resistance) of 1.35. The anemometer circuits were mounted immediately outside of the wind tunnel wall to minimize lead lengths.

The hot film gages were intended to provide only qualitative information on transition and separation locations. When the flow over the hot film gage is laminar, the heat transfer is generally low, with little random unsteadiness. Movement of transition past the gage is indicated by a rapid rise in heat transfer, accompanied by an increase in the higher frequency, random portion of the signal. Separation is indicated by a low level of average heat transfer, but a high level of randomness. Interpretation of hot film signals is simplified in a periodic unsteady flow because the changes from one flow state to another can be more readily identified than the characteristics of a steady-state flow. (It is particularly difficult to determine if a single steady flow with moderately high randomness is turbulent, separated, or transitional.)

Additional instrumentation (listed in Table 5) included three spar strain gage bridges to verify that limit stresses were not exceeded, a spar angle of attack sensor, and an unsteady pitot-static probe mounted on the upper wind tunnel wall over the blade tip to identify far field disturbances. Standard

wind tunnel instruments were used to measure total and static pressures, total temperature, and dewpoint.

DATA ACQUISITION

Figure 12 shows the wind tunnel control room with the data acquisition system installed. The output of each pressure, hot film, or other sensor was buffered and filtered using unity gain amplifiers and 10 kHz low pass 4-pole Butterworth filters. On-line digitization of the unsteady signals was performed by a 32 channel Preston GMAD-1A analog to digital converter system having a maximum rate of one million 15 bit samples per second. The digitization rate was controlled by the waveform synthesizer (described above), at a rate of 1024 samples per cycle. A cycle is defined as one period for sinusoidal motion and as the sequence of steady state low α , pitch up, and steady state high α for ramp motion. For ramp motions, a second cycle of 1024 samples was acquired during the pitch down. Data were obtained from 20 pitching oscillations for ramps and large amplitude sinusoids, and from 40 pitching oscillations for small amplitude sinusoids. For constant- α conditions, the data were digitized at the rate of 1000 samples/second over a five second period.

The data acquisition was controlled by a Perkin Elmer (now Concurrent Computer) 3230 processor. The computer was configured with 10 MB of internal memory, 1200 MB of disk storage, a 6250 BPI nine-track tape drive, five terminals, two text printers, and a laser graphics printer. The data acquisition software consisted of ten individual programs running simultaneously and communicating by means of shared memory and inter-task messages. In addition to storing the digitized data on magnetic tape, the computer also ensemble averaged the signals, applied calibration factors, converted the time histories to coefficient form, integrated the pressures to determine sectional airloads, and stored the results on disc for on-line analysis and plotting. A separate set of steady-state acquisition hardware (also controlled by the 3230) was used to obtain time averaged values of the wind tunnel conditions and model operating conditions. This information was stored for each test point and was also available on-line for monitoring the operation of the model and wind tunnel. This 'trim and safety' information was displayed on a separate terminal and updated every two seconds.

The pressure transducer results were corrected for thermal effects based upon pre-test calibration (described above). Transducer drift was minimized by taking frequent zero points with no airflow. The calibration was checked periodically by applying a known pressure to the reference ports of all transducers. Since the ramp motions typically began at steady-state, $\alpha = 0$, most additional errors caused by problems with individual transducers could be identified and compensated for. The pressures were integrated along the chord at each of the five spanwise stations to determine the unsteady lift, pressure drag, and pitching moment coefficients. Integrations were performed using segmented Gaussian quadrature, a technique that minimizes integration error for relatively sparse point spacings.^{32,33} All parameters were available for on-line analysis and display shortly after each test point had been acquired.

TEST CONDITIONS

The wind tunnel test took place during June and July, 1990. The $\Lambda = 0$ data were acquired first, followed by the $\Lambda = 15^\circ$ and 30° configurations. Data were obtained for a total of 234 large amplitude sinusoids, 110 ramps, 263 small amplitude sinusoids, and 295 steady-state conditions. Appendix I provides a series of nine test matrices illustrating these conditions. Appendix II provides a list of all of the test conditions, allowing particular points in the data base to be identified.

SUMMARY OF RESULTS

A detailed presentation of the results of this experiment is provided in the series of papers reprinted as Appendices IV - IX. A compilation of the primary conclusions is provided here. Further information on each topic may be obtained in the Appendices listed at the end of each paragraph.

In steady flow, aerodynamic load characteristics are as expected for a simple subsonic wing. The effects of increasing Mach number include increasing the lift curve slope in attached flow, reducing the maximum load coefficients, and reducing the stall angle. For the unswept 3D wing, the tip vortex reduces the effective angle of attack, generating attached flow spanwise load distributions in approximate agreement with lifting line models. Prior to stall, the effects of sweep on the pressures and airloads on the inboard portion of the wing can be accounted for using the swept infinite wing normalization ($U_c = U_\infty \cos \Lambda$). Such simple correlations do not suffice close to the wing tip or after stall. (Appendices IV, V)

For large amplitude ramps at low Mach number ($M_c = 0.2$) and high Reynolds number (≈ 2 million), the following transition, separation, and stall mechanism was observed at all sweep angles. At the initial steady state condition ($\alpha = 0$) pressure gradients are low, and the upper surface boundary layer remains laminar for $x/c \leq 0.3$. As α increases, the adverse pressure gradients downstream of the suction peak cause the transition point to move very close to the leading edge ($x/c \leq 0.026$), leading to an essentially turbulent boundary layer by $\alpha = 10-12^\circ$. At higher angle of attack ($\alpha \geq 18^\circ$) this boundary layer separates, starting near $x/c = 0.1$, and the separation very quickly (within $\Delta\alpha \approx 0.2^\circ$) expands, leading to loss of leading edge suction and formation of an intense and concentrated stall vortex. The vortex propagates downstream, increasing the lift, drag, and pitching moment. The fundamentals of this process are quite similar to those identified on the 2D model, and in several earlier experiments at similar Reynolds numbers. (Appendix V)

At $M_c = 0.3$, a small region of slightly supersonic flow ($M \approx 1.1$) develops near the leading edge. The supersonic region is believed to be the source of a relatively high frequency oscillation that is first observed near $x/c = 0.1$. This oscillation grows, leading to separation at an angle of attack 2° lower than

at $M_c = 0.2$. At $M_c = 0.4, 0.5$, and 0.6 , the supersonic region forms earlier, becomes stronger (reaching $M \approx 1.5$), and extends further downstream (to $x/c = 0.2$ at $M_c = 0.6$). At low angles of attack ($\alpha \approx 7-10^\circ$) transition to turbulence is initiated near the shock, and does not move as far forward as at low Mach number. As α increases, high frequency pressure oscillations appear at the shock, beginning a gradual separation. By $M_c = 0.6$ it takes 16 times longer (in terms of $\Delta\alpha$) than at $M_c = 0.2$ for the separation to expand to cover the forward 30% of chord, and the stall vorticity appears to be much more diffuse. This observation agrees with the visualization results of Ref. 8. Unsteady effects on the aerodynamic loads are still present, including measurable stall delays and increases in the maximum lift, drag, and moment. (Appendices VI, VII)

The effects of other parameters (Λ , A , and tip cap geometry) on the airloads during ramps have also been examined. Sweep and tip geometry effects are most significant very close to the wing tip and after the beginning of stall. The rollup of the tip vortex over the upper surface of the unswept wing distorts the pressure distributions and interacts with the stall vortex to increase the unsteady increment to C_L^{\max} by up to a factor of 2. This effect, which was first described in Refs. 5 and 7, is magnified when the approximate body of revolution tip cap is replaced by a flat plate at $z = 0$. The flat plate appears to generate a stronger and more compact vortex. For the swept wing, the tip vortex effects are weaker, as also observed in Refs. 34 and 35. The tip stalls at nearly the same α as the inboard region, and the unsteady increments to the tip loads are reduced. After stall, there are large differences with sweep angle, including strong periodic oscillations at $\Lambda = 15^\circ$ and strong spanwise gradients at $\Lambda = 30^\circ$. (Appendix V)

Pressure distributions close to the wing tip have been used to estimate the direct contribution of the tip vortex to the unsteady force and moment. At low Mach number prior to stall, up to 25% of the tip normal force and virtually all of the pitching moment can be attributed to the tip vortex distorting the pressure distributions. This effect is reduced at higher Mach numbers, because stall occurs before the tip vortex becomes very strong. (Appendix IX)

Dynamic stall vortex propagation patterns can be estimated by tracking the minimum pressure locations on the wing surface. Inboard on the unswept wing, vortex propagation is similar to that observed in 2D (a speed of $0.25U_c$ at $A =$

0.01). Closer to the tip, the vortex appears later because of the delay in stall, and propagates more slowly. Quite different patterns occur on the swept wing. The inboard propagation speed is reduced, in agreement with earlier infinite swept wing results, but propagation speeds closer to the tip are higher than on the unswept wing, possibly because of reduced tip vortex influence. (Appendix IX)

For large amplitude sinusoidal motions, the basic characteristics of the transition, separation, and stall process are the same as for constant pitch rate motions. During pitch-up, there is a substantial stall delay, large unsteady increments to the airloads, and the formation of a strong leading edge vortex. During pitch-down, flow reattachment begins near the leading edge and moves aft. Near the tip of the unswept wing, the tip vortex alters these characteristics. The vortex not only lowers the effective angle of attack over a relatively large span, but also rolls up over the upper surface, increasing the trailing edge loading and generating a strong but smoothly increasing negative moment. Interaction between the tip and stall vortices increases the relative unsteady loads near the tip. During pitch down, the trailing edge load is reestablished later than the leading edge suction, causing considerable hysteresis. There is also substantial hysteresis in the forward and aft motion of the transition point, even in the absence of separation. (Appendices VI and VIII)

A series of moderate amplitude ($\alpha_1 = 6^\circ$) sinusoidal conditions at increasing mean angle show an abrupt shift between conditions without stall and conditions with dynamic stall. No conditions were found that generated significant stall delays and C_L^{\max} increments without creating a strong stall vortex and a large negative moment. (Appendix VIII)

For small amplitude oscillations ($\alpha_1 = 0.5-2^\circ$), the primary concern is stability, as determined by the sign of the aerodynamic pitch damping. If the instantaneous angle of attack never exceeds the static stall angle, α_{ss} , the damping was found to be positive, and in general agreement with unsteady thin airfoil theory. Motions about mean angles (α_0) near α_{ss} typically have negative damping. The basic mechanism is an unsteady delay in stall beyond α_{ss} during the pitch-up portion of the cycle, a loss of leading edge suction at stall (leading to a negative or nose-down moment), and finally a delay in reattachment

during pitch-down. The resulting hysteresis in C_M causes the negative damping. This mechanism was observed for the complete range of reduced frequencies ($0.1 \leq k \leq 0.6$), Mach numbers ($0.2 \leq M_c \leq 0.6$), and sweep angles ($\Lambda = 0, 15, \text{ and } 30^\circ$) tested. If α_0 is high enough so that the flow remains separated throughout the cycle, the damping was found to again become positive. Three-dimensionality and sweep alter the damping characteristics primarily through their effects on α_{ss} . As α_0 is increased with the unswept wing, the inboard region stalls first, followed by the tip. Since negative damping occurs only for $\alpha_0 \approx \alpha_{ss}$, the unswept wing therefore is never simultaneously unstable. At $\Lambda = 30^\circ$, stall occurs over the entire span within $\Delta\alpha \approx 1^\circ$, allowing a simultaneous instability. An empirical model for the aerodynamic damping that follows the observed trends and parameter dependencies has been developed. (Appendices IV, X)

Continued examination of the results of this experiment is anticipated, as is use of the data to validate computational methods. In addition, there are several areas where further investigation with this experiment may be desirable. To date, only unswept and aft swept configurations have been studied. Depending on flight speed, azimuth, spanwise position, and geometric tip sweep, dynamic stall near the tip of a helicopter blade may occur at local forward sweep angles of up to 30° . (Forward and aft sweep effects should differ only near the tip. Over the forward half of the disc, the flight velocity causes forward sweep, while the geometric sweep of many current rotor tips contributes $20\text{--}30^\circ$ of aft sweep.) Since the combination of sweep and tip vortex effects were found to have a strong influence on unsteady characteristics, an extension of the experiment to include forward sweep would provide important information. Second, the desire to cover many spanwise stations limited the spatial resolution at any one area. Rearranging the existing instrumentation could provide more closely spaced and simultaneous (rather than sequentially multiplexed) measurements of the transition and separation process over the forward 15% of chord at a single station. This might resolve questions regarding transitional separation bubbles at high Reynolds number and the relation between transition, the shock, and separation at higher Mach number. Finally, continued development of quantitative flow field imaging techniques may allow accurate velocity and vorticity information to be obtained in the critical (but, at these Reynolds numbers, extremely small) leading edge boundary layer region before and during separation.

LIST OF PUBLICATIONS, PERSONNEL, AND INVENTIONS

Conference Publications

1. Lorber, P.F., and Carta, F.O., "Incipient Torsional Stall Flutter Experiments on a Swept Three-Dimensional Wing," AIAA Paper 91-0935, 32nd Structures, Structural Dynamics, and Materials Conference, Baltimore MD, April 1991.
2. Lorber, P.F., Carta, F.O., and Covino, A.F. Jr., "Dynamic Stall Experiments on a Swept Three-Dimensional Wing In Compressible Flow," AIAA Paper 91-1795, 22nd Fluid Dynamics, Plasma Dynamics, and Lasers Conference, Honolulu HI, June 1991.
3. Lorber, P.F., and Carta, F.O., "Unsteady Transition Measurements on a Pitching Three-Dimensional Wing," Proceedings of the Fifth Symposium on Numerical and Physical Aspects of Aerodynamic Flows, Long Beach CA, January 1992.
4. Lorber, P.F., "Compressibility Effects on the Dynamic Stall of a Three-Dimensional Wing," AIAA Paper 92-0191, 30th Aerospace Sciences Meeting, Reno NV, Jan. 1992.
5. Lorber, P.F., "Dynamic Stall of a Sinusoidally Oscillating Three-Dimensional Swept Wing in Compressible Flow," Proceedings of the 48th Annual Forum of the American Helicopter Society, Washington DC, June 1992.
6. Lorber, P.F., "Tip Vortex, Stall Vortex, and Separation Results for Pitching Three-Dimensional Wings," Abstract submitted for AIAA 24th Fluid Dynamics Conference, Orlando FL, July 1993.

Other Presentations

1. Lorber, P.F., and Carta, F.O., "Unsteady Separation Experiments on 2-D Airfoils, 3-D Wings, and Model Helicopter Rotors," in "Physics of Unsteady Separation", a NASA/AFOSR/ARO Workshop at Ames Research Center, April 1990, reported in NASA CP 3144, L.W. Carr, ed.

2. Lorber, P.F., "Observations, Speculations, and Questions on Unsteady Separation at Large Scale," presented at "Supermaneuverability: Physics of Unsteady Flows Past Lifting Surfaces at High Angle of Attack," an AFOSR Workshop at Lehigh University, April 1992.

Personnel Supported

Franklin O. Carta, Supervisor, Experimental and Analytical Aeromechanics

Peter F. Lorber, Research Engineer, Aeromechanics Research

Alfred F. Covino, Jr. Group Leader, Electronic Technicians

John E. Ayer, Project Engineer, Test Facilities

No degrees were awarded.

No inventions were made.

REFERENCES

1. St. Hilaire, A.O., Carta, F.O., Fink, M.R., and Jepson, W.D., "The Influence of Sweep on the Aerodynamic Loading of an Oscillating NACA 0012 Airfoil," NASA CR-3092, 1979.
2. St. Hilaire, A.O. and Carta, F.O., "Analysis of Unswept and Swept Wing Chordwise Pressure Data from an Oscillating NACA 0012 Airfoil Experiment," NASA CR 3567, 1983.
3. Walker, J.M., Helin, H.E., and Chou, D.C., "Unsteady Surface Pressure Measurements on a Pitching Airfoil," AIAA Paper 85-0532, March 1985.
4. Robinson, M.C. and Wissler, J.B., "Unsteady Surface Pressure Measurements on a Pitching Rectangular Wing," AIAA Paper 88-0328, Jan. 1988.
5. Robinson, M.C. and Wissler, J.B., "Pitch Rate and Reynolds Number Effects on a Pitching Rectangular Wing," AIAA Paper 88-2577-CP, 1988.
6. Albertson, J.A., Troutt, T.R., and Kedzie, C.R., "Unsteady Aerodynamic Forces at Low Airfoil Pitching Rates," AIAA Paper 88-2579-CP, 1988.
7. Walker, J.M. and Robinson, M.C., "Dynamic Stall Development Dependence on Wing Planform," 4th Symposium on Numerical and Physical Aspects of Aerodynamic Flows, Long Beach, CA, Jan. 1989.
8. Chandrasekhara, M.S. and Carr, L.W., "Flow Visualization Studies of the Mach Number Effects on the Dynamic Stall of an Oscillating Airfoil," Journal of Aircraft, Vol. 27, June 1990, pp. 516-522.
9. Chandrasekhara, M.S., Ahmed, S., and Carr, L.W., "Schlieren Studies of Compressibility Effects on Dynamic Stall of Airfoils in Transient Pitching Motion," AIAA Paper 90-3038-CP, 8th AIAA Applied Aerodynamics Conference, Portland, OR, 1990.
10. Carr, L.W., Chandrasekhara, M.S., Ahmed, S., and Brock, N.J., "A Study of Dynamic Stall Using Real Time Interferometry," AIAA Paper 91-0007, 29th Aerospace Sciences Meeting, Reno, NV, Jan 1991.
11. Jumper, E.J., and Stephen, E.J., "Toward Unsteady Lift Augmentation: An Assessment of the Role of Competing Phenomena in Dynamic Stall," 2nd AFOSR Workshop on Unsteady Separated Flows, USAF Academy, CO, July 1987.
12. Freymuth, P., "Vortex Patterns of Dynamic Separation," Chapter 11 of the Encyclopedia of Fluid mechanics, N.P. Chermisinoff, Ed., Gulf Publishing Co., Vol 8., 1989.
13. Strickland, J.H., and Graham, G.M., "Dynamic Stall Inception Correlation for Airfoils Undergoing Constant Pitch Rate Motions," AIAA Journal, Vol. 24, April 1986, pp. 678-680.
14. Favier, D., Agnes, A., Barbi, C., and Maresca, C, "Combined Translation/Pitch Motion: A New Airfoil Dynamic Stall Simulation," Journal of Aircraft, Vol. 25, Sept. 1988, pp. 805-814.

15. Patterson, M.T., and Lorber, P.F., "Computational and Experimental Studies of Compressible Dynamic Stall," Journal of Fluids and Structures, Vol. 4, 1990, pp.259-285.
16. Ekaterinaris, J., "Compressible Studies of Dynamic Stall," AIAA Paper 89-0024, 27th Aerospace Sciences Meeting, Reno, NV, Jan. 1989.
17. Visbal, M.R., "Effect of Compressibility on Dynamic Stall of a Pitching Airfoil," AIAA Paper 88-0132, 26th Aerospace Sciences Meeting, Reno, NV, Jan. 1988.
18. Visbal, M.R., "On Some Physical Aspects of Airfoil Dynamic Stall," ASME Symposium on Non-Steady Fluid Dynamics," Toronto, Canada, June 1990.
19. Landgrebe, A.J. and Bellinger, E.D., "A Systematic Study of Helicopter Rotor Stall Using Model Rotors," 30th Annual Forum of the American Helicopter Society, May 1974
20. Lorber, P.F., "Aerodynamic Results of a Pressure-Instrumented Model Rotor Test at the DNW," Journal of the American Helicopter Society, Vol. 36 (4), Oct. 1991.
21. Lorber, P.F., and Carta, F.O., "Airfoil Dynamic Stall at Constant Pitch Rate and High Reynolds Number," Journal of Aircraft, Vol. 25, June 1988, pp. 548-556.
22. Lorber, P.F., and Carta, F.O., "Unsteady Stall Penetration Experiments at High Reynolds Number", AFOSR TR-87-1202, April 1987.
23. Baker, J.E., "The Effects of Various Parameters, Including Mach Number, on Propeller-Blade Flutter, with Emphasis on Stall Flutter," NACA RML50L12b, 1950; reissued as NACA TN3557, 1955.
24. Fanti, R., Carta, F.O., and Pitt, W.R., "Stall Flutter Characteristics of Several 16-Series Cantilevered Airfoil Models," United Aircraft Corporation Research Department Report R-2 24-2, East Hartford, CT, May 1954.
25. Lemnios, A.Z., "Aerodynamic Damping Tests of Propeller Blade Airfoil Sections," United Aircraft Corporation Research Department Report R-0997-1, East Hartford, CT, Oct. 1957.
26. Ham, N.D., "Stall Flutter of Helicopter Rotor Blades: A Special Case of the Dynamic Stall Phenomenon," Journal of the American Helicopter Society, Vol. 12, No. 4, Oct 1967.
27. Carta, F.O., and Niebanck, C.F., "Prediction of Rotor Instabilities at High Forward Flight Speeds. Volume III. Stall Flutter." USAAVLABS TR 68-18C, Ft. Eustis, VA, Feb. 1969.
28. McCroskey, W.J., and Pucci, S.L., "Viscous Inviscid Interaction on Oscillating Airfoils in Subsonic Flow," AIAA paper 81-0051, Jan. 1981.
29. Carta, F.O., and Lorber, P.F., "Experimental Study of the Aerodynamics of Incipient Torsional Stall Flutter," Journal of Propulsion and Power, Vol. 3, March-April 1987, pp. 164-170.

30. Rae, W.H., and Pope, A., Low-Speed Wind Tunnel Testing, 2nd Edition, John Wiley & Sons, NY, 1984.
31. Marcolini, M.A., Lorber, P.F., Miller, W.T., and Covino, A.F. Jr., "Frequency Response Calibration of Recess-Mounted Pressure Transducers," Instrumentation Society of America 37th Annual Instrumentation Symposium, San Diego, CA, May 1991, also NASA TM 104031, March 1991.
32. St. Hilaire, A.O., "The Segmented Gaussian Quadrature and its Application for Optimizing Airfoil Instrumentation Arrays," United Technologies Research Center Report 76-150, October 1976.
33. Stroud, A.H., and Secrest, D., "Gaussian Quadrature Formulas," Prentice-Hall, Englewood Cliffs, N.J., 1966.
34. Ashworth, J., Huyer, S., and Luttgies, M., "Comparisons of Unsteady Flow Fields about Straight and Swept Wings using Flow Visualization and Hotwire Anemometry," AIAA 87-1334, 19th Fluid Dynamics, Plasma Dynamics, and Lasers Conference, Honolulu HI, June 1987.
35. Ashworth J., Crisler, W., and Luttgies, M., "Vortex Flows Created by Sinusoidal Oscillation of Three-Dimensional Wings " AIAA 89-2227, 7th Applied Aerodynamics Conference, Seattle WA, July 1989.

TABLE 1. SURFACE COORDINATES FOR SIKORSKY SSC-A09

x/c	y/c Upper	y/c Lower	x/c	y/c Upper	y/c Lower
0.000000	0.000000	0.000000	0.376873	0.055494	-0.034506
0.000199	0.002000	-0.001454	0.416754	0.055039	-0.034637
0.000798	0.003946	-0.002869	0.436694	0.054663	-0.034558
0.001994	0.006482	-0.004573	0.456635	0.054182	-0.034376
0.002991	0.008029	-0.005446	0.476575	0.053595	-0.034087
0.004487	0.009868	-0.006445	0.496515	0.052899	-0.033683
0.006979	0.012392	-0.007703	0.516456	0.052093	-0.033165
0.009970	0.014921	-0.008877	0.536396	0.051176	-0.032532
0.015952	0.019076	-0.010704	0.556336	0.050149	-0.031790
0.021934	0.022500	-0.012175	0.576277	0.049009	-0.030949
0.027916	0.025445	-0.013447	0.596217	0.047755	-0.030018
0.033898	0.028039	-0.014588	0.616157	0.046381	-0.029002
0.039881	0.030369	-0.015631	0.636097	0.044875	-0.027904
0.045863	0.032494	-0.016594	0.656039	0.043220	-0.026720
0.051845	0.034449	-0.017487	0.675979	0.041391	-0.025448
0.057827	0.036249	-0.018314	0.695919	0.039368	-0.024088
0.067797	0.038903	-0.019568	0.715860	0.037140	-0.022642
0.077767	0.041143	-0.020691	0.735800	0.034719	-0.021121
0.087737	0.043016	-0.021706	0.755740	0.032138	-0.019540
0.097707	0.044583	-0.022638	0.775680	0.029445	-0.017918
0.112665	0.046504	-0.023910	0.795621	0.026681	-0.016272
0.127618	0.048054	-0.025064	0.815561	0.023871	-0.014617
0.142573	0.049345	-0.026124	0.835501	0.021012	-0.012957
0.157529	0.050444	-0.027104	0.855442	0.018089	-0.011289
0.172485	0.051385	-0.028013	0.875382	0.015093	-0.009598
0.187440	0.052184	-0.028853	0.895323	0.012051	-0.007863
0.202395	0.052860	-0.029628	0.915264	0.009046	-0.006081
0.217350	0.053427	-0.030339	0.935204	0.006229	-0.004290
0.232305	0.053911	-0.030988	0.955144	0.003849	-0.002610
0.247261	0.054322	-0.031579	0.975084	0.002288	-0.001325
0.277171	0.054958	-0.032594	0.985055	0.001987	-0.000992
0.307082	0.055369	-0.033402	0.995025	0.002135	-0.000863
0.336992	0.055564	-0.034007	1.000000	0.002408	-0.000803

TABLE 2. SURFACE DERIVATIVES FOR THE SIKORSKY SSC-A09

x/c	dw/dx upper	dw/dx lower	x/c	dw/dx upper	dw/dx lower
0.000000	0.000000	0.000000	0.356932	-0.001800	-0.012500
0.000100	10.051900	-7.304500	0.396813	-0.011400	-0.003300
0.000499	3.247399	-2.363099	0.426724	-0.018900	0.004000
0.001396	2.120399	-1.424199	0.446665	-0.024100	0.009200
0.002493	1.551600	-0.876400	0.466605	-0.029400	0.014500
0.003739	1.230300	-0.667400	0.486545	-0.034900	0.020200
0.005733	1.012199	-0.504700	0.506485	-0.040400	0.026000
0.008475	0.845500	-0.392800	0.526426	-0.046000	0.031700
0.012961	0.694600	-0.305400	0.546366	-0.051500	0.037200
0.018943	0.572400	-0.245800	0.566306	-0.057200	0.042200
0.024925	0.492400	-0.212600	0.586247	-0.062900	0.046700
0.030907	0.433700	-0.190700	0.606187	-0.068900	0.050900
0.036890	0.389400	-0.174400	0.626127	-0.075500	0.055100
0.042872	0.355200	-0.161000	0.646068	-0.083000	0.059400
0.048854	0.326800	-0.149300	0.666009	-0.091700	0.063800
0.054836	0.300900	-0.138400	0.685949	-0.101500	0.068200
0.062812	0.266200	-0.125800	0.705889	-0.111700	0.072500
0.072782	0.224700	-0.112600	0.725830	-0.121400	0.076300
0.082751	0.187900	-0.101800	0.745770	-0.129400	0.079300
0.092722	0.152000	-0.093500	0.765710	-0.135100	0.081400
0.105185	0.115000	-0.085100	0.785651	-0.138600	0.082600
0.120140	0.073600	-0.077100	0.805591	-0.140900	0.083000
0.135095	0.036300	-0.070900	0.825531	-0.143400	0.083200
0.150051	0.003400	-0.065500	0.845472	-0.146600	0.083700
0.165007	0.062900	-0.060800	0.865412	-0.150200	0.084800
0.179962	0.053500	-0.056100	0.885353	-0.152500	0.087000
0.194917	0.045100	-0.051900	0.905293	-0.150700	0.089400
0.209873	0.038000	-0.047500	0.925234	-0.141300	0.089900
0.224828	0.032300	-0.043400	0.945174	-0.119300	0.084200
0.239783	0.027500	-0.039500	0.965114	-0.078300	0.064400
0.262216	0.021300	-0.033900	0.980069	-0.030200	0.033400
0.292126	0.013700	-0.027000	0.990040	0.014800	0.013000
0.322037	0.006500	-0.020300	0.997512	0.054800	0.012100

TABLE 3. PRESSURE TRANSDUCER LOCATIONS.

#	Spanwise Position, z/c									
	0.08		0.30		0.59		1.06		1.52	
	Upper x/c	Lower x/c	Upper x/c	Lower x/c	Upper x/c	Lower x/c	Upper x/c	Lower x/c	Upper x/c	Lower x/c
1	.0050	.0200	.0050	.0200	.0050	.0050	.0100	.0200	.0100	.0200
2	.0256	.0746	.0256	.0746	.0256	.0256	.0492	.0746	.0492	.0746
3	.0597	.1575	.0597	.1575	.0597	.0597	.1066	.1575	.1066	.1575
4	.1028	.3934	.1028	.3934	.1028	.1028	.1640	.3934	.1640	.3934
5	.1490	.7012	.1490	.7012	.1490	.1490	.2031	.7012	.2031	.7012
6	.1921	.9371	.1921	.9371	.1921	.1921	.2501	.9371	.2501	.9371
7	.2468		.2468		.2262	.2262	.3947		.3947	
8	.3023		.3023		.2468	.2468	.6066		.6066	
9	.3718		.3718		.2616	.2616	.8184		.8184	
10	.4638		.4638		.3023	.3023	.9631		.9631	
11	.5702		.5702		.3718	.3718				
12	.6816		.6816		.4638	.4638				
13	.7880		.7880		.5702	.5702				
14	.9495		.9495		.6816	.6816				
15					.7880	.7880				
16					.8801	.8801				
17					.9495	.9495				
18					.9902	.9902				

(CPKT1Sxx)

(CPKT2Sxx)

(CPK04Sxx)

(CPK12Sxx)

(CPK20Sxx)

Swept Array

#	x/c	z/c
1	.0050	.800
2	.0597	.771
3	.1490	.720
4	.2262	.675

(CPK45Sxx)

TABLE 4. HOT FILM GAGE LOCATIONS.

#	x/c	z/c	x/c	z/c	x/c	z/c
1	.0256	.65	.0256	.27	.0256	.08
2	.0597	.70	.0597	.27	.0597	.08
3	.1028	.65	.1028	.27	.1028	.08
4	.1921	.70	.1921	.27	.1921	.08
5	.3023	.70				
6	.4638	.70				
7	.6816	.70				
8	.8801	.70				
	(SFG06Sx)		(SFGT25x)		(SFGT1Sx)	

TABLE 5. ADDITIONAL INSTRUMENTATION.

	z/c	x/c	ENAME
Flatwise Spar Bending Strain Gage	1.750	0.250	STR_BEND_1
Flatwise Spar Bending Strain Gage	3.400	0.250	STR_BEND_2
Torsional Spar Strain Gage	3.400	0.250	STR_TORS_1
Geometric Angle of Attack	At hydraulic drive		ALPHA_E_1
Wind Tunnel Total Pressure	Stilling section (Slow response)		TUNL_TOTAL
Wind Tunnel Static Pressure	Calibrated differential probe located in the test section (Slow)		TUNL_STATIC
Wind Tunnel Total Temperature	Stilling section		
Wind Tunnel Dewpoint			
Model Dynamic Pressure	Pitot probe above tip 1/4 chord, 6 in. below test section wall (Rapid response)		MODEL_Q_1

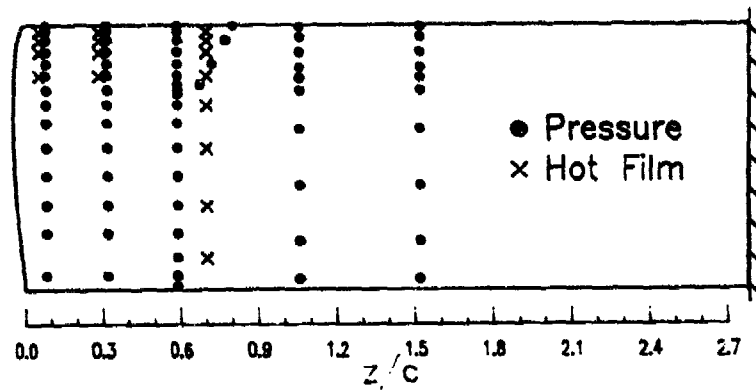


Fig. 1. Planform and instrumentation locations at $\Lambda = 0$.



Fig. 2. Sikorsky SSC-A09 airfoil section.

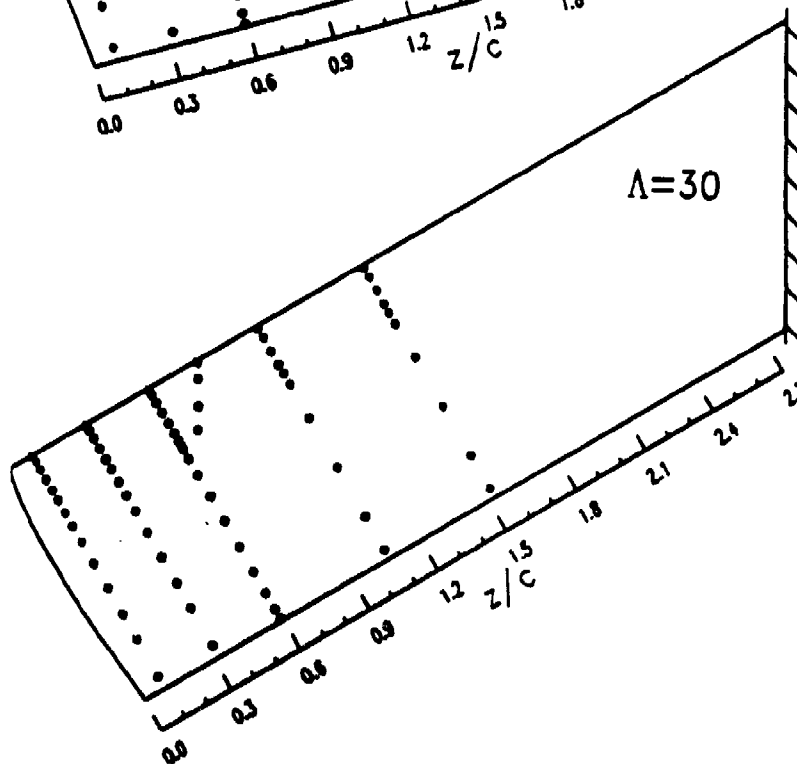
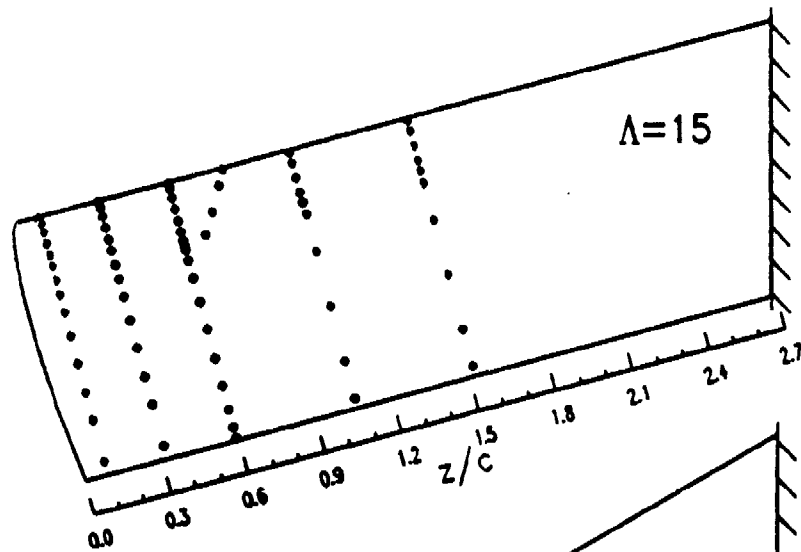
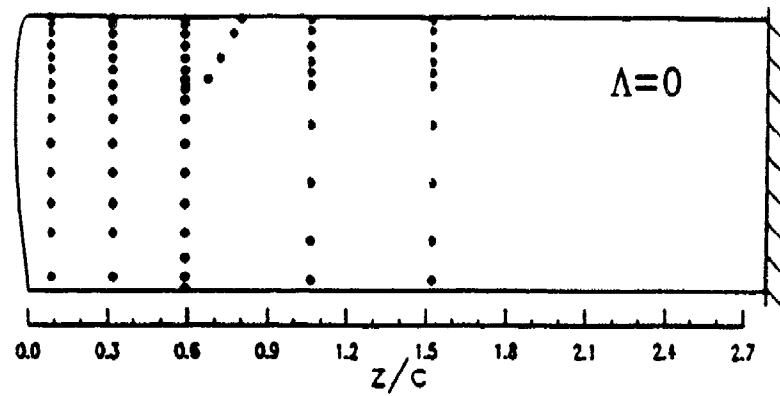


Fig. 3. Planforms and upper surface pressure transducer locations

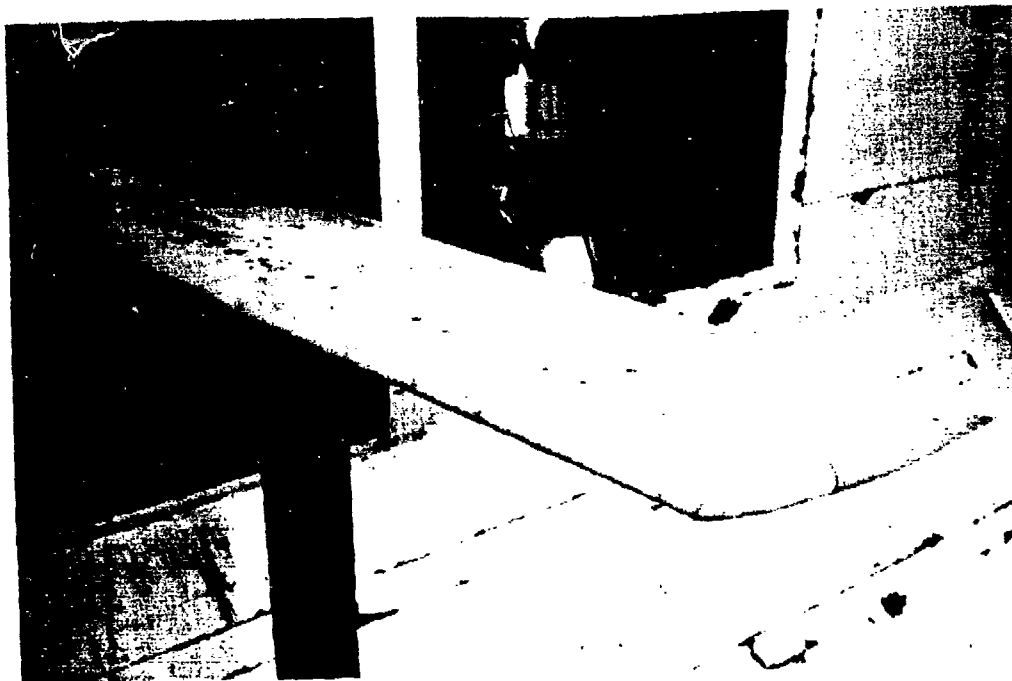


Fig. 4. Side View of Model at $\Lambda = 0^\circ$

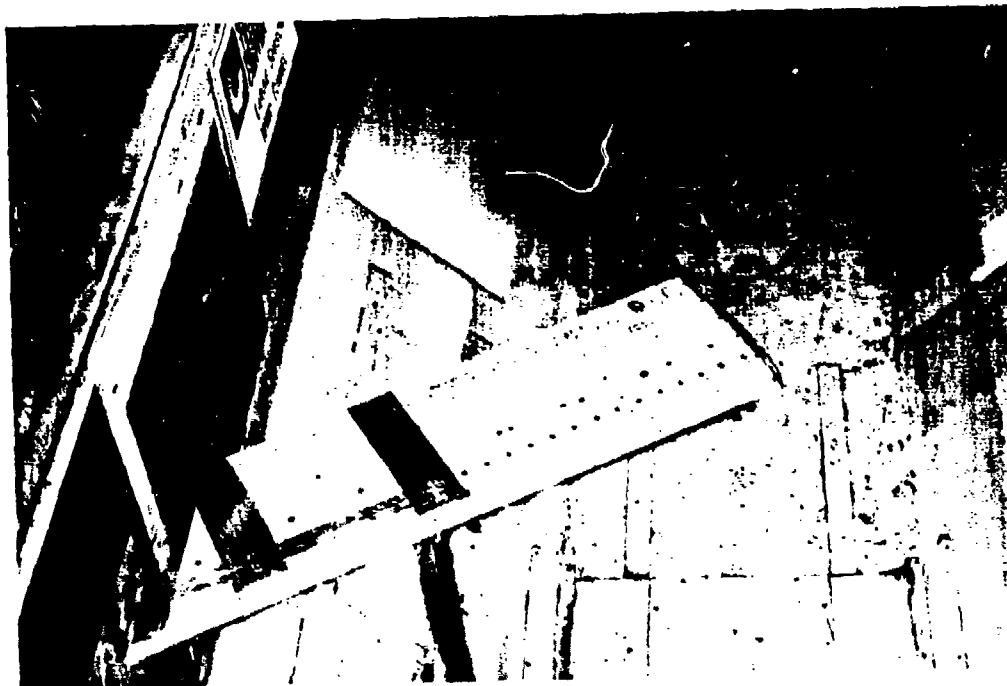


Fig. 5. Top View of Model at $\Lambda = 30^\circ$

C90-247 A-7
C90-302 D-3

92-11-7-1

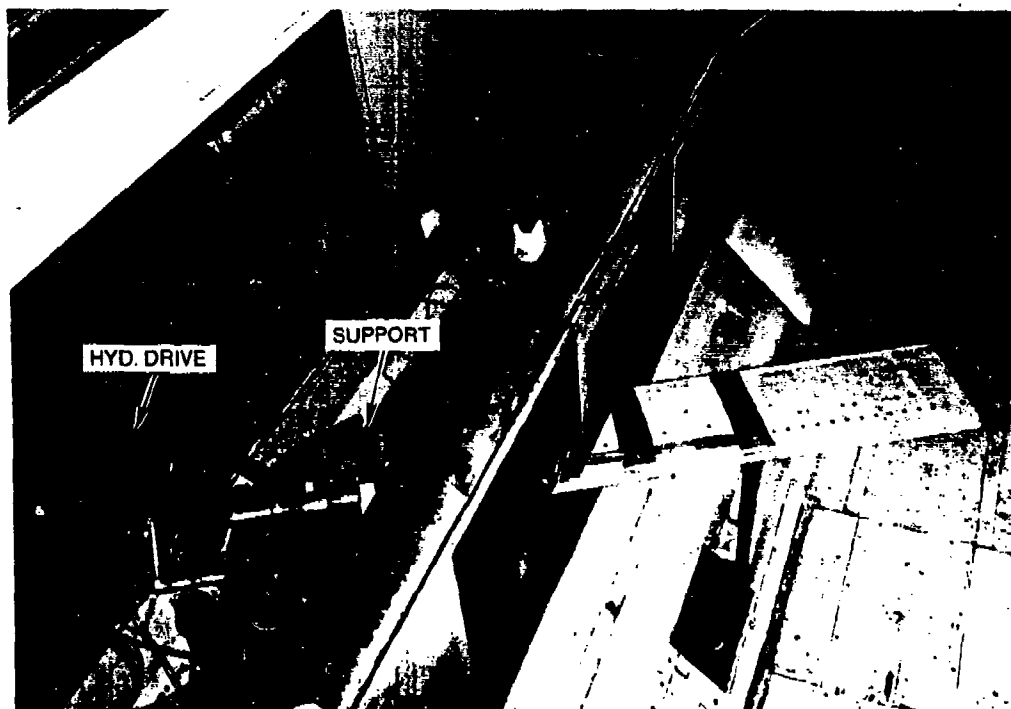


Fig. 6. Top View of the Model and the Support and Drive System

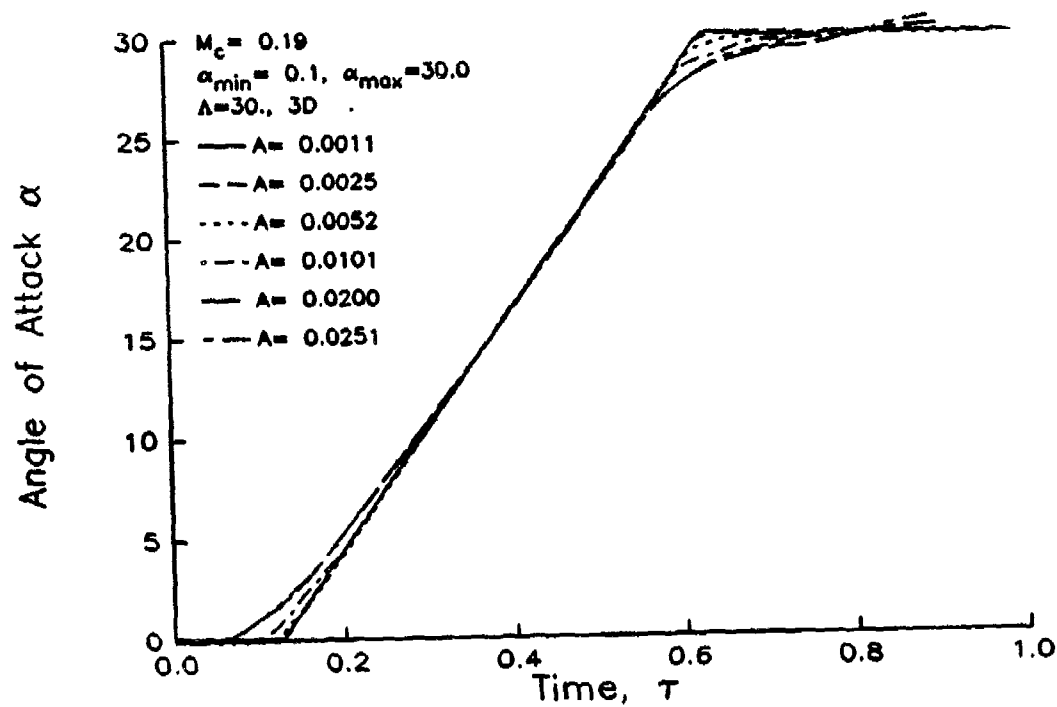


Fig. 7. Measured angle during ramp motion.

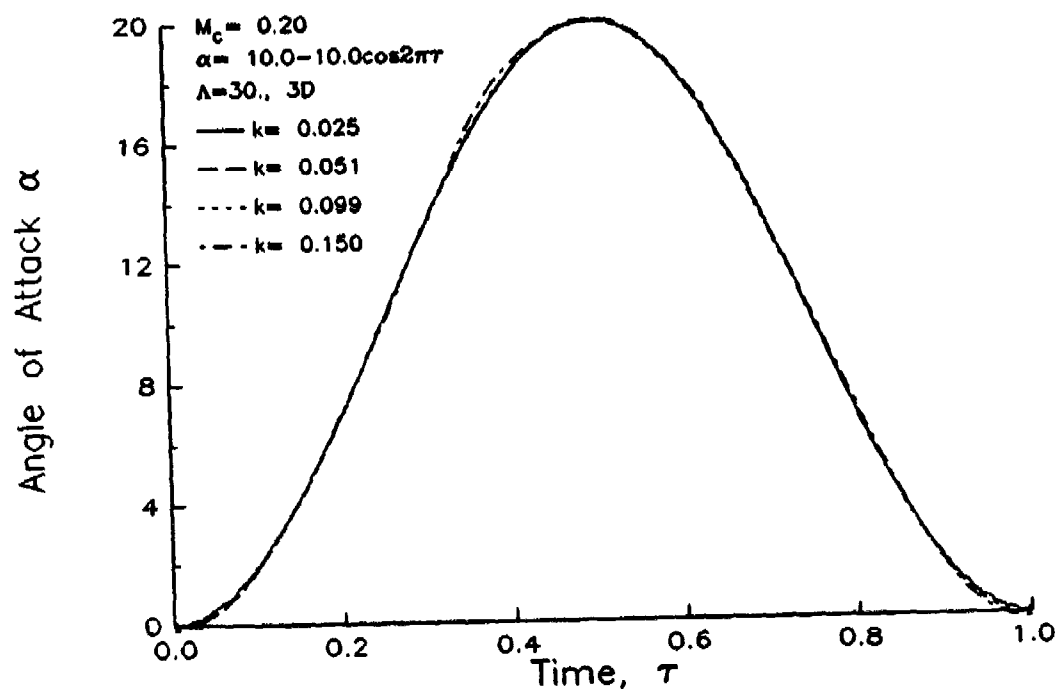


Fig. 8. Measured angle during sinusoidal motions.

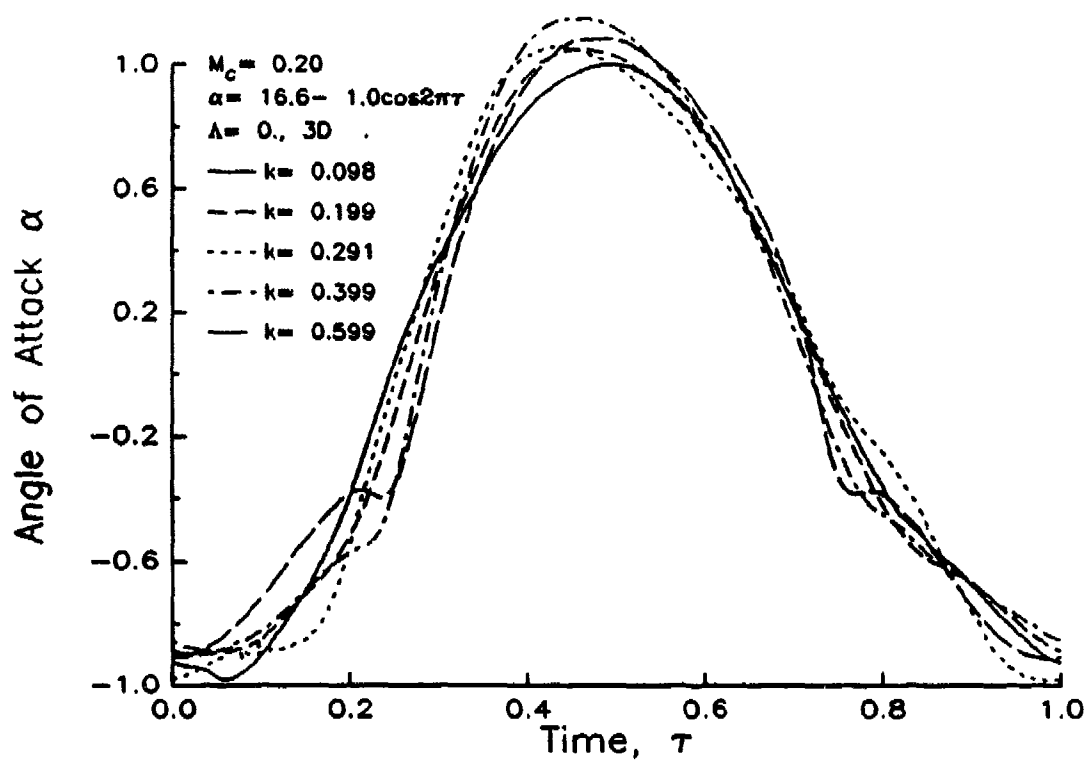


Fig. 9a. Measured angles during 1 deg amplitude sinusoids.

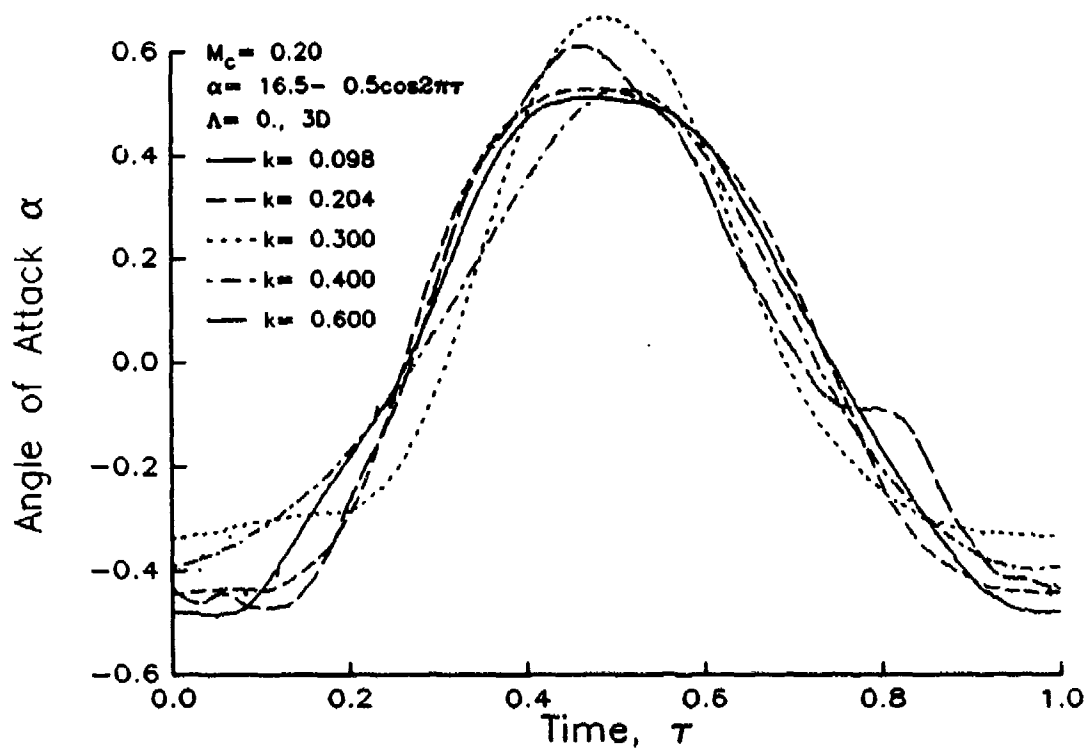


Fig. 9b. Measured angles during 0.5 deg amplitude sinusoids.

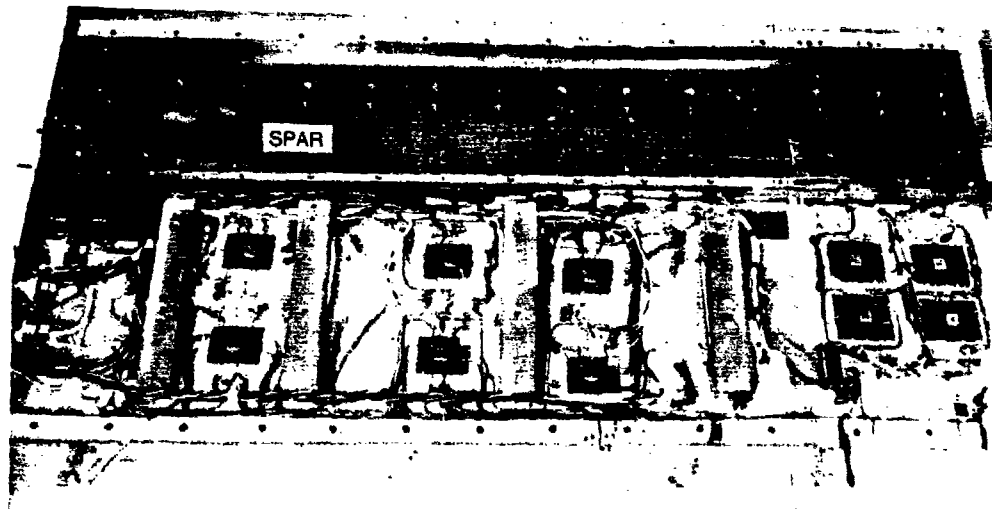


Fig. 10. Inside View of Model and Instrumentation

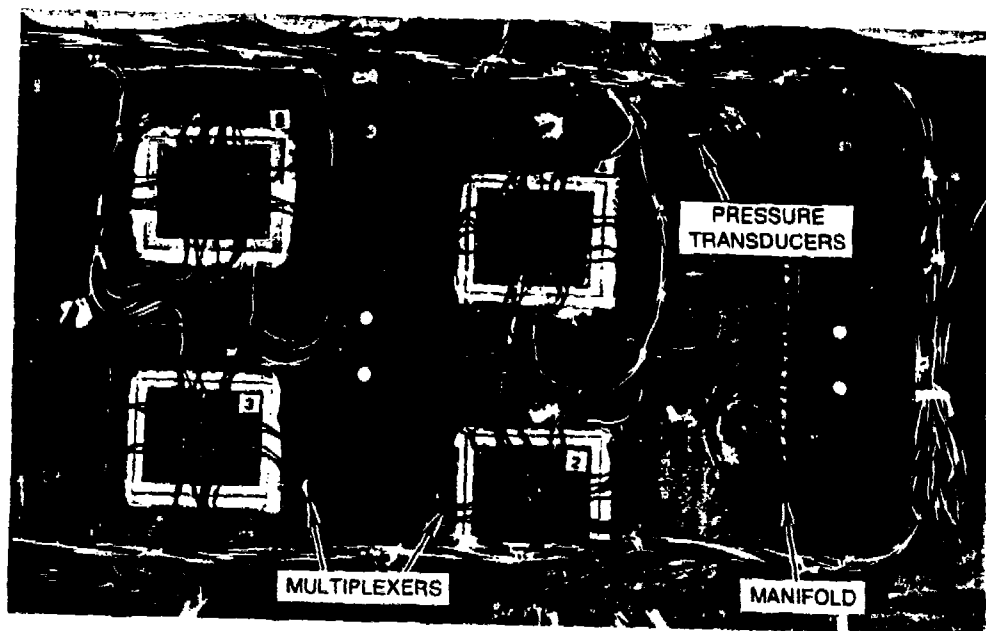


Fig. 11. Closeup View of Model

C90-213 B-18
86-197-D

92-11-7-3



Fig. 12. Wind Tunnel Control Room, Showing Unsteady Aerodynamics Data Acquisition System

**APPENDIX I
TEST MATRICES**

LARGE AMPLITUDE SINUSOIDS AT $A=0$

REDUCED FREQUENCY	MACH NUMBER				
	M=0.2	M=0.3	M=0.4	M=0.5	M=0.6
k=.025	6±6 10±10 20±10	10±10 20±10	6±6 10±10 12±6 14±6 16±6	4±4 6±6 8±6 10±6	4±4 5±5 6±6
k=.050	6±6 10±10 ^S 12±6 20±10 ^S 14±6 16±6 18±6 20±6 22±6 24±6	10±10 20±10	6±6 ^S 10±10 ^S 12±6 ^S 14±6 ^S 16±6 ^S	4±4 6±6 8±6 10±6	4±4 5±5
k=.054		12±8			
k=.075			10±10	4±4 6±6 8±6 10±6	4±4 5±5
k=.100	6±6 10±10 ^S 8±6 20±10 ^S 10±6 12±6 14±6 16±6 18±6 20±6 22±6 24±6	6±6 10±10 20±10	6±6 12±6 14±6		
k=.110		9±8			
k=.150	10±10 20±10				

MATCHING POINTS FOR AMES TEST, $A=0$ AND $M=0.28$

k=.040 15±2, 15±4, 15±5
k=.100 15±2, 15±4, 15±5

^S Square tip data in addition to round tip

LARGE AMPLITUDE SINUSOIDS AT $\Lambda=15$

REDUCED FREQUENCY	MACH NUMBER				
	M=0.2	M=0.3	M=0.4	M=0.5	M=0.6
k=.025	6±6 10±10 20±10	10±10 20±10	10±10	4±4 6±6 8±6 10±6	4±4 5±5 6±6
k=.050	6±6 10±10 ^s 20±10 ^s	10±10 20±10	6±6 ^s 10±10 ^s 10±6 12±6 ^s 14±6 ^s 16±6 ^s	4±4 6±6 8±6 10±6	4±4 5±5
k=.075			10±10	4±4 6±6 8±6 10±6	4±4 5±5
k=.100	6±6 10±10 ^s 8±6 20±10 ^s 10±6 12±6 14±6 16±6 18±6 20±6 22±6 24±6	6±6 10±10 20±10	6±6 10±6 12±6		
k=.150	10±10 20±10				

^s Square tip data in addition to round tip

$$k = \frac{\omega c}{2U_{\infty} \cos \Lambda}$$

$$M = \frac{U_{\infty} \cos \Lambda}{a_{\infty}}$$

LARGE AMPLITUDE SINUSOIDS AT $A=30$

REDUCED FREQUENCY	MACH NUMBER					
	M=0.2	M=0.3	M=0.4	M=0.5	M=0.6	
k=.025	6±6 10±10 20±10	10±10 20±10	6±6 10±10 10±6 12±6 14±6 16±6	4±4 6±6 8±6 10±6 12±6	4±4 5±5 6±6 7±6 8±6	
k=.050	6±6 10±10 ^S 8±6 20±10 ^S 10±6 12±6 14±6 20±6 16±6 22±6 18±6 24±6	10±10 20±10	6±6 ^S 10±10 ^S 10±6 ^S 12±6 ^S 14±6 ^S 16±6	4±4 6±6 8±6 10±6 12±6	4±4 5±5 6±6 7±6 8±6	
k=.054		12±8				
k=.075			6±6 10±10 10±6 12±6 14±6	4±4 6±6 8±6 10±6 12±6	4±4 5±5 6±6	
k=.100	6±6 10±10 ^S 8±6 20±10 ^S 10±6 12±6 14±6 20±6 16±6 22±6 18±6 24±6	6±6 10±10 20±10	6±6 10±6 12±6 14±6			
k=.110		9±8				
k=.150	6±6 10±10 8±6 20±10 10±6 12±6 14±6 20±6 16±6 22±6 18±6 24±6					

^S Square tip data in addition to round tip

RAMPS AT $\Lambda=0$

PITCH RATE	MACH NUMBER				
	M=0.2	M=0.3	M=0.4	M=0.5	M=0.6
A=.0010	0→10 0→30 ^S	0→30	0→10 0→20	0→10 0→16	0→6 0→10
A=.0025	0→30	0→30	0→20	0→16	0→10
A=.0050	0→10 0→30 ^S 10→20 12→22 14→24 16→26 18→28	0→10 0→20 0→30	0→10 0→20 0→25 ^S	0→8 0→16	
A=.0100	0→10 0→30 ^S	0→30	0→20 0→25	0→16	
A=.0200	0→30 ^S	0→30			
A=.0250	0→30				

RAMPS AT $\Lambda=15$

PITCH RATE	MACH NUMBER				
	M=0.2	M=0.3	M=0.4	M=0.5	M=0.6
A=.0010	0→10 0→30 ^S	0→30	0→20	0→16	0→10 0→12
A=.0025	0→30 ^S	0→30	0→20	0→16	0→12
A=.0050	0→10 0→30 ^S	0→10 0→30	0→10 0→20 ^S	0→8 0→16	0→12
A=.0100	0→10 0→30 ^S	0→30	0→20		
A=.0200	0→30 ^S	0→30			

^S Square tip data in addition to round tip

$$A = \frac{\partial \alpha}{\partial t} \frac{c}{2U_{\infty} \cos \Lambda} \quad M = \frac{U_{\infty} \cos \Lambda}{a_{\infty}}$$

RAMPS AT A=30

PITCH RATE	MACH NUMBER				
	M=0.2	M=0.3	M=0.4	M=0.5	M=0.6
A=.0010	0→10 0→30 ^s	0→30	0→20	0→18	0→12
A=.0025	0→30	0→30	0→20	0→18	0→12 0→13.5
A=.0050	0→10 0→30 ^s 10→20 12→22 14→24 16→26 18→28	0→10 0→30	0→10 0→20 ^s	0→8 0→18	0→13.5
A=.0100	0→10 0→30 ^s	0→30	0→20	0→18	
A=.0200	0→10 0→30 ^s	0→30			
A=.0250	0→30				

^s Square tip data in addition to round tip

$$A = \frac{\partial \alpha}{\partial t} \frac{c}{2U_{\infty} \cos \Lambda}$$

$$M = \frac{U_{\infty} \cos \Lambda}{a_{\infty}}$$

INCIPIENT STALL FLUTTER AT $\Lambda=0$

REDUCED FREQUENCY	MACH NUMBER								
	0.2			0.4			0.6		
0.10	14±.5	14±1	14±2		10±1		6±.5	6±1	6±2
	16.5±.5	16.5±1	16.5±2		11±1			7±1	
	18±.5	18±1	18±2	12±.5	12±1	12±2	8±.5	8±1	8±2
					13±1			9±1	
				14±.5	14±1	14±2	10±.5	10±1	
					15±1				
0.20				16±.5	16±1	16±2			
					17±1				
					18±1				
					17±1				
					16±1				
					15±1				
					14±1				
					13±1				
					12±1				
					11±1				
					10±1				
0.25									
0.30									
0.40									
0.60									

$$K = \frac{\omega c}{2U_{\infty} \cos \Lambda} \quad M = \frac{U_{\infty} \cos \Lambda}{a_{\infty}}$$

INCIPIENT STALL FLUTTER AT $A=15$

REDUCED FREQUENCY	MACH NUMBER		
	0.2	0.4	0.6
0.075		10 ± 1 11 ± 1 12 ± 1 13 ± 1 14 ± 1 15 ± 1 16 ± 1 17 ± 1 18 ± 1 19 ± 1	
0.20	10 ± 1 12 ± 1 14 ± 1 15 ± 1 16 ± 1 17 ± 1 18 ± 1 19 ± 1 20 ± 1 22 ± 1 24 ± 1		

INCIPIENT STALL FLUTTER AT $A=30$

REDUCED FREQUENCY	MACH NUMBER		
	0.2	0.4	0.6
0.10	$16 \pm .5$ 16 ± 1 16 ± 2 $18 \pm .5$ 18 ± 1 18 ± 2 $20 \pm .5$ 20 ± 1 20 ± 2	10 ± 1 11 ± 1 $12 \pm .5$ 12 ± 1 $13 \pm .5$ 13 ± 1 13 ± 2 $14 \pm .5$ 14 ± 1 $15 \pm .5$ 15 ± 1 15 ± 2 $16 \pm .5$ 16 ± 1 $17 \pm .5$ 17 ± 1 17 ± 2 $18 \pm .5$ 18 ± 1 19 ± 1 20 ± 1	$6 \pm .5$ 6 ± 1 6 ± 2 7 ± 1 $8 \pm .5$ 8 ± 1 8 ± 2 $9 \pm .5$ 9 ± 1 $10 \pm .5$ 10 ± 1 10 ± 2 $11 \pm .5$ 11 ± 1 $12 \pm .5$ 12 ± 1 $13 \pm .5$ 13 ± 1

INCIPIENT STALL FLUTTER AT $A=30$, con't.

REDUCED FREQUENCY	MACH NUMBER					
	0.2			0.4		0.6
0.20		10±1				6±.5 6±1
	12±.5	12±1	12±2			7±1
	14±.5	14±1	14±2			8±.5 8±1
		15±1				9±1
	16±.5	16±1	16±2			10±.5 10±1
			16.5±2			11±.5 11±1
	17±.5	17±1	17±2			12±.5 12±1
	17.5±.5	17.5±1				13±.5
	18±.5	18±1	18±2			
	18.5±.5	18.5±1				
	19±.5	19±1	19±2			
	20±.5	20±1	20±2			
		21±1				
		22±1	22±2			
		24±1				
		26±1				
		28±1				
0.25				13±.5 13±1 13±2		
				15±.5 15±1 15±2		
				17±.5 17±1		
0.30	16±.5	16±1	16±2			
		17±1				
		17.5				
	18±.5	18±1	18±2			
		18.5±1				
		19±1				
0.50	20±.5	20±1	20±2			
	16±.5	16±1	16±2			
		17±1				
0.60	18±.5	18±1	18±2			
		19±1				
	20±.5	20±1	20±2			
		21±1				
		22±1				
		23±1				

APPENDIX II
RUN LIST - 0 SWEEP

Mach	Waveform	Angle Range	Pitch Rate or Red Fr.	Run.Pt	Date	Remarks
0.2	Ramp	0→10	A=.0010 A=.0050 A=.0100 A=.0200	31.23 31.24 31.25 31.26	6/15	Attached Ramp
0.2	Ramp	0→30	A=.0010 A=.0025 A=.0050 A=.0100 A=.0200 A=.0250	31.27 31.36 31.37 31.38 31.39 35.43	6/15 6/22	Large Amplitude Ramp
0.2	Ramp	10→20 12→22 14→24 16→26 18→28	A=.0050	39.34 39.35 39.36 39.37 39.38	6/28	Vary Ramp Range
0.2	Sine	6±6	k=.025 k=.050 k=.100	31.41 35.35 31.42	6/15 6/22 6/15	Attached Sine
0.2	Sine	12±6 14±6 16±6 18±6 20±6 22±6 24±6	k=.050	35.36 35.37 35.38 35.39 35.40 35.41 35.42	6/22	Sine Mean Angle sweep
0.2	Sine	8±6 10±6 12±6 14±6 16±6 18±6 20±6 22±6 24±6	k=.100	31.43 31.44 31.45 31.46 31.47 31.48 31.49 31.50 31.51	6/15	Sine Mean Angle Sweep
0.2	Sine	10±10	k=.025 k=.050 k=.100 k=.150	32.09 32.11 32.13 32.15	6/18	Large Amplitude Sines
0.2	Sine	20±10	k=.025 k=.050 k=.100 k=.150	32.10 32.12 32.14 32.16	6/18	

RUN LIST - 0 SWEEP

Mach	Waveform	Angle Range	Pitch Rate or Red Fr.	Run.Pt	Date	Remarks
0.3	Ramp	0→10	A=.0050	32.42	6/18	Attached Flow Ramp
0.3	Ramp	0→20	A=.0050	33.18	6/20	
0.3	Ramp	0→30	A=.0010 A=.0025 A=.0050 A=.0100 A=.0200	32.43 32.44 32.46 32.47 32.48	6/18	Large Amplitude Ramps
0.3	Sine	6±6	k=.100	32.49	6/18	Attached Sine
0.3	Sine	10±10	k=.025 k=.050 k=.100	33.09 33.11 33.13	6/20	Large Amplitude Sines
0.3	Sine	20±10	k=.025 k=.050 k=.100	33.10 33.12 33.14	6/20	
0.3	Sine	9±8 12±8	k=.110 k=.054	33.16 33.17	6/20	SA Sine Repeat of 2D
0.4	Ramp	0→10	A=.0010 A=.0050	33.52 33.53	6/20	Attached ramp
0.4	Ramp	0→20	A=.0010 A=.0025 A=.0050 A=.0100	33.54 33.55 33.56 33.57	6/20	Large Ampl Ramp
		0→25	A=.0050 A=.0100	34.11 34.12	6/21	
0.4	Sine	6±6 12±6 14±6 16±6	k=.025	33.44 33.45 33.46 33.47	6/20	Sine Sweep
0.4	Sine	6±6 12±6 14±6 16±6	k=.050	33.48 33.49 33.50 33.51	6/20	Sine Sweep
0.4	Sine	6±6 12±6 14±6	k=.100	39.03 39.04 39.05	6/28	Sine Sweep
0.4	Sine	6±6 12±6 14±6 16±6	k=.050	34.07 34.08 34.09 34.10	6/21	Repeated by Mistake

RUN LIST - 0 SWEEP

Mach	Waveform	Angle Range	Pitch Rate or Red Fr.	Run.Pt	Date	Remarks
0.4	Sine	10±10	k=.025 k=.050 k=.075	34.04 34.05 34.06	6/21	Large Ampl Sine
0.5	Ramp	0→10 0→8	A=.0010 A=.0050	34.44 35.05	6/21 6/22	Attached Ramp
0.5	Ramp	0→16	A=.0010 A=.0025 A=.0050 A=.0100	35.06 35.07 35.08 35.09	6/22	Large Ramp
0.5	Sine	4±4	k=.025 k=.050 k=.075	34.32 34.36 34.40	6/21	Attached Sine
0.5	Sine	6±6 8±6 10±6	k=.025	34.33 34.34 34.35	6/21	Sine sweep
0.5	Sine	6±6 8±6 10±6	k=.050	34.37 34.38 34.39	6/21	Sine sweep
0.5	Sine	6±6 8±6 10±6	k=.075	34.41 34.42 34.43	6/21	Sine Sweep
0.6	Ramp	0→6	A=.0010	35.30	6/22	Attached ramp
0.6	Ramp	0→10 0→10	A=.0010 A=.0025	35.31 35.32	6/22	Large Ramp
0.6	Sine	4±4 5±5 6±6	k=.025	35.21 35.22 35.23	6/22	Sines
0.6	Sine	4±4 5±5	k=.050	35.26 35.27	6/22	Sines
0.6	Sine	4±4 5±5	k=.075	35.28 35.29	6/22	Sines
0.28	Sine	15±2 15±4 15±5 15±2 15±4 15±5	k=.040 k=.100	37.03 37.04 37.05 37.06 37.07 37.08	6/26	Match Army Ames Pts

RUN LIST - 0 SWEEP

Mach	Waveform	Angle Range	Pitch Rate or Red Fr.	Run.Pt	Date	Remarks
0.2	Ramp	0→30	A=.0010 A=.0050 A=.0100 A=.0200	40.05 40.03 40.18 40.04	6/29	Square Tip Ramp
0.2	Sine	10±10 20±10 10±10 20±10	k=.050 k=.050 k=.100 k=.100	40.06 40.07 40.08 40.09	6/29	Square Tip Sine
0.4	Ramp	0→25	A=.0050	40.16	6/29	Square Tip Ramp
0.4	Sine	10±10	k=.050	40.15	6/29	Square Tip Sine
0.4	Sine	6±6 12±6 14±6 16±6	k=.050	40.11 40.12 40.13 40.14	6/29	Square Tip Sine Sweep
0.2	Sine	10±1 12±1 14±1 15±1 16±1 16.5±1 17±1 18±1 20±1 22±1 24±1 26±1	k=.20	37.09 37.11 37.12 37.13 37.14 37.22 37.16 37.17 37.18 37.19 37.20 37.21	6/26	Incipient Sweep-10Hz
0.2	Sine	12±2 14±2 16±2 16.5±2 18±2 20±2	k=.20	37.23 37.24 37.25 37.55 37.26 37.27	6/26	
0.2	Sine	12±.5 14±.5 16±.5 16.5±.5 17±.5 18±.5 20±.5	k=.20	37.29 37.30 37.31 37.32 37.33 37.34 37.35	6/26	
0.2	Sine	14±.5 16.5±.5 18±.5	k=.10	37.56 37.57 37.58	6/26	Incipient at 5Hz

RUN LIST - 0 SWEEP

Mach	Waveform	Angle Range	Pitch Rate or Red Fr.	Run.Pt	Date	Remarks
0.2	Sine	14±1		38.03	6/27	
		16.5±1		38.04		
		18±1		38.05		
		14±2		38.06		
		16.5±2		38.07		
		18±2		38.08		
0.2	Sine	14±.5 k=.3		38.09	6/27	Incipient at 15Hz
		16.5±.5		38.10		
		18±.5		38.11		
		14±1		38.12	38.32	New Servo
		16.5±1		38.13	38.33	
		18±1		38.14	38.34	
		14±2		38.15		
		16.5±2		38.16		
		18±2		38.17		
0.2		14±.5 k=.4		38.19	6/27	Incipient at 20Hz
		16.5±.5		38.20		
		18±.5		38.21		
		14±1		38.22	38.29	New Servo
		16.5±1		38.23	38.30	
		18±1		38.24	38.31	
		14±2		38.25		
		16.5±2		38.26		
		18±2		38.27		
0.2		14±.5 k=.6		38.35	6/27	Incipient at 30Hz
		16.5±.5		38.36		
		18±.5		38.37		
		14±1		38.38		
		16.5±1		38.39		
		18±1		38.40		
0.4		10±1 k=.1		38.42	6/27	Incipient at 10Hz
		11±1		38.43		
		12±1		38.44		
		13±1		38.45		
		14±1		38.46		
		15±1		38.47		
		16±1		38.48		
		17±1		38.49		
		18±1		38.50		
0.4		12±.5 k=.1		38.55	6/27	Incipient at 10Hz
		14±.5		38.56		
		16±.5		38.57		
		18±.5		38.58		
		12±2		38.51		
		14±2		38.52		
		16±2		38.53		

RUN LIST - 0 SWEEP

Mach	Waveform	Angle Range	Pitch Rate or Red Fr.	Run.Pt	Date	Remarks
0.4		12±.5	k=.25	39.06	6/28	Incipient at 25Hz
		14±.5		39.07		
		16±.5		39.08		
		12±1		39.09		
		14±1		39.10		
		16±1		39.11		
		12±2		39.12		
		14±2		39.13		
		16±2		39.14		
0.6		6±1	k=.1	39.17	6/28	Incipient at 15Hz
		7±1		39.18		
		8±1		39.19		
		9±1		39.20		
		10±1		39.21		
0.6		6±.5	k=.1	39.22	6/28	Incipient at 15Hz
		8±.5		39.23		
		10±.5		39.24		
		6±2		39.25		
		8±2		39.26		
0.6		6±.5	k=.2	39.27	6/28	Incipient at 30Hz
		8±.5		39.28		
		10±.5		39.29		
		6±1		39.30		
		8±1		39.31		
		10±1		39.32		
0.2	Steady	0	0	31.02	6/15	First Steady Sweep
		2.3		32.03		
		4.2		32.04		
		6.0		32.05		
		7.9		31.06		
		10.0		31.07		
		12.0		31.08		
		14.0		31.09		
		16.5		31.10		
		18.0		31.11		
		20.0		31.12		
		21.2		31.13		
		22.0		31.14		
		22.9		31.15		
		24.7		31.16		
		26.0		31.17		
		27.3		31.18		
		28.5		31.19		
		29.4		31.20		
		30.7		31.21		
		0.0		31.22		

RUN LIST - 0 SWEEP

Mach	Waveform	Angle Range	Pitch Rate or Red Fr.	Run.Pt	Date	Remarks
0.2	Steady	16.2	0	31.30	6/15	Second Steady Sweep
		17.4		31.31		
		18.2		31.32		
		19.6		31.33		
		21.0		31.34		
		21.9		31.35		
0.2	Steady	0.0		37.36	6/26	Third Steady Sweep
		10.0		37.37		
		11.0		37.38		
		12.0		37.39		
		13.0		37.40		
		14.0		37.41		
		15.0		37.42		
		16.0		37.43		
		16.6		37.44		
		17.0		37.45		
		18.0		37.46		
		19.0		37.47		
		20.0		37.48		
		21.0		37.49		
		22.0		37.50		
		24.0		37.51		
		26.0		37.52		
		28.0		37.53		
		30.0		37.54		
0.3	Steady	0.0	0.	32.18	6/18	Steady Sweep
		2.1		32.19		
		4.1		32.20		
		6.3		32.21		
		8.0		32.22		
		10.0		32.23		
		12.0		32.24		
		13.2		32.25		
		14.0		32.26		
		14.9		32.27		
		15.9		32.28		
		16.8		32.29		
		18.0		32.30		
		18.9		32.31		
		20.0		32.32		
		21.0		32.33		
		22.2		32.34		
		23.0		32.35		
		24.0		32.36		
		25.8		32.37		
		28.0		32.38		
		30.0		32.39		
		0.0		33.07	6/20	Check pt

RUN LIST - 0 SWEEP

Mach	Waveform	Angle Range	Pitch Rate or Red Fr.	Run.Pt	Date	Remarks
0.4	Steady	0.0	0	33.21	6/20	Steady Sweep
		2.0		33.22		
		4.3		33.23		
		6.2		33.24		
		8.0		33.25		
		10.1		33.26		
		11.1		33.27		
		11.3		33.28		
0.4	Steady	12.1		33.29		
		13.0		33.30		
		14.0		33.31		
		15.0		33.32		
		16.0		33.33		
		17.1		33.34		
		18.0		33.35		
		19.0		33.36		
		20.0		33.37		
		20.8		33.38		
		23.1		33.39		
		24.5		33.40		
		0.0		33.43	6/20	Check pt
		0.0		34.02	6/21	Check pt
0.5	Steady	0.0		34.15	6/21	Steady
		1.8		34.16		
		4.0		34.17		
		6.0		34.18		
		8.0		34.19		
		8.9		34.20		
		10.0		34.21		
		11.1		34.29		
		12.0		34.23		
		13.0		34.24		
		14.0		34.25		
		14.9		34.26		
		16.0		34.27		
		17.1		34.28		
		0.0		34.13		Warm up
		0.0		34.31		Check pt
		0.0		35.04	6/22	Check pt
0.6	Steady	0.0	0	35.13	6/22	Steady
		1.8		35.14		
		3.9		35.15		
		6.0		35.16		
		8.1		35.17		
		9.0		35.18		
		10.0		35.19		
		11.0		35.20		
		0.0		35.12		Warm up

RUN LIST - 15 DEG SWEEP

Mach	Waveform	Angle Range	Pitch Rate or Red Fr.	Run.Pt	Date	Remarks
0.2	Ramp	0→10	A=.0010	41.55	7/5	Attached Ramp
			A=.0050	41.56		
			A=.0100	41.49		
			A=.0200	41.57		
			A=.0200	45.05	7/11	Spline Coupling
0.2	Ramp	0→30	A=.0010	41.58	7/5	Large Amplitude Ramp
			A=.0025	41.59		
			A=.0050	41.60		
			A=.0100	41.61		
			A=.0100	45.06	7/11	Spline Coupling
			A=.0200	45.07		
0.2	Sine	6±6	k=.025	41.34	7/5	Attached Sine
			k=.050	41.35		
			k=.100	41.36		
0.2	Sine	8±6	k=.100	41.37	7/5	Sine Mean Angle Sweep
		10±6		41.38		
		12±6		41.39		
		14±6		41.40		
		16±6		41.41		
		18±6		41.42		
		20±6		41.43		
		22±6		41.44		
		24±6		41.45		
2	ine	10±10	k=.025	41.62	7/5	Large Amplitude Sines
			k=.050	41.65		
			k=.100	42.03	7/6	
			k=.150	42.05		
0.2	Sine	20±10	k=.025	41.63	7/5	
			k=.050	41.64		
			k=.100	42.04	7/6	
			k=.150	42.06		
0.3	Ramp	0→10	A=.0050	42.30	7/6	Attached Flow Ramp
0.3	Ramp	0→30	A=.0010	42.31	7/6	Large Amplitude Ramps
			A=.0025	42.32		
			A=.0050	42.33		
			A=.0100	42.34		
			A=.0100	45.08	7/11	Spline Coupling
			A=.0200	45.09		
0.3	Sine	10±10	k=.025	42.36	7/6	Large Amplitude Sines
			k=.050	42.38		
			k=.100	42.40		

RUN LIST - 15 DEG SWEEP

Mach	Waveform	Angle Range	Pitch Rate or Red Fr.	Run.Pt	Date	Remarks
0.3	Sine	20±10	k=.025 k=.050 k=.100	42.37 42.39 42.41	7/6	
0.4	Ramp	0→10	A=.0050	42.68	7/6	Attached Flow Ramp
0.4	Ramp	0→20	A=.0010 A=.0025 A=.0050 A=.0100 A=.0100	42.69 43.03 43.04 43.05 45.10	7/6 7/9 7/11	Large Ampl Ramp Spline Coupling
0.4	Sine	6±6 10±6 12±6 14±6 16±6	k=.050	42.59 42.60 42.61 42.62 42.63	7/6	Sine Sweep
0.4	Sine	6±6 10±6 12±6	k=.100	42.64 42.65 42.66	7/6	Sine Sweep
0.4	Sine	10±10	k=.025 k=.050 k=.075	43.06 43.07 43.08	7/9	Large Ampl Sine
0.5	Ramp	0→ 8	A=.0050	44.03	7/10	Attached Ramp
0.5	Ramp	0→16	A=.0010 A=.0025 A=.0050	44.04 44.05 44.06	7/10	Large Ramp
0.5	Sine	4±4	k=.025 k=.050 k=.075	43.45 43.49 43.53	7/9	Attached Sine
0.5	Sine	6±6 8±6 10±6	k=.025	43.46 43.47 43.48	7/9	Sine sweep
0.5	Sine	6±6 8±6 10±6	k=.050	43.50 43.51 43.52	7/9	Sine sweep
0.5	Sine	6±6 8±6 10±6	k=.075	43.54 43.55 43.56	7/9	Sine Sweep

RUN LIST - 15 DEG SWEEP

Mach	Waveform	Angle Range	Pitch Rate or Red Fr.	Run.Pt	Date	Remarks
0.6	Ramp	0→10	A=.0010	44.28	7/10	Large Ramp
		0→12	A=.0012	44.29		
		0→12	A=.0025	44.30		
		0→12	A=.0050	44.31		
0.6	Sine	4±4	k=.025	44.20	7/10	Sines
		5±5		44.21		
		6±6		44.22		
0.6	Sine	4±4	k=.050	44.23	7/10	Sines
		5±5		44.25		
0.6	Sine	4±4	k=.075	44.26	7/10	Sines
		5±5		44.27		

0.2	Ramp	0→30	A=.0010	46.03	7/12	Square Tip Ramp
			A=.0050	46.04		
			A=.0100	46.06		
			A=.0200	46.07		
0.2	Sine	10±10	k=.050	46.08		Square Tip Sine
		20±10	k=.050	46.09		
		10±10	k=.100	46.10		
		20±10	k=.100	46.11		
0.4	Ramp	0→20	A=.0050	46.12		Square Tip Ramp
0.4	Sine	10±10	k=.050	46.17		Square Tip Sine
0.4	Sine	6±6	k=.050	46.13		Square Tip Sine Sweep
		12±6		46.14		
		14±6		46.15		
		16±6		46.16		
0.2	Sine	10±1	k=.20	43.20	7/9	Incipient Sweep-10Hz
		12±1		43.21		
		14±1		43.22		
		15±1		43.23		
		16±1		43.24		
		17±1		43.25		
		18±1		43.26		
		19±1		43.27		
		20±1		43.28		
		22±1		43.29		
		24±1		43.30		

RUN LIST - 15 DEG SWEEP

Mach	Waveform	Angle Range	Pitch Rate or Red Fr.	Run.Pt	Date	Remarks
0.4		10±1	k=.075	43.09	7/9	Incipient at 7.5Hz
		11±1		43.10		
		12±1		43.11		
		13±1		43.12		
		14±1		43.13		
		15±1		43.14		
		16±1		43.15		
		17±1		43.16		
		18±1		43.17		
		19±1		43.18		
0.2	Steady	0	0	41.08	7/5	Steady Sweep
		2.0		41.09		
		4.1		41.10		
		6.0		41.11		
		7.9		41.12		
		10.1		41.13		
		12.2		41.14		
		12.9		41.15		
		14.0		41.16		
		15.1		41.17		
		16.0		41.18		
		16.9		41.19		
		17.8		41.20		
		19.0		41.21		
		20.6		41.22		
		21.0		41.23		
		21.9		41.24		
		23.1		41.25		
		24.0		41.26		
		25.1		41.27		
		26.0		41.28		
		27.0		41.29		
		28.0		41.30		
		30.0		41.31		
		17.1		41.32		
		18.0		41.53		
0.3	Steady	0.0	0.	42.07	7/6	Steady Sweep
		2.1		42.08		
		4.0		42.09		
		6.1		42.10		
		8.0		42.11		
		10.0		42.12		
		12.0		42.13		
		13.0		42.14		
		14.0		42.15		
		15.0		42.16		
		16.0		42.17		
		17.0		42.18		

RUN LIST - 15 DEG SWEEP

Mach	Waveform	Angle Range	Pitch Rate or Red Fr.	Run.Pt	Date	Remarks
0.3	Steady	18.0		42.19		
		19.0		42.20		
		20.0		42.21		
		21.0		42.22		
		22.0		42.23		
		23.0		42.24		
		24.0		42.25		
		26.0		42.26		
		28.0		42.27		
		30.0		42.28		
0.4	Steady	0.0	0	42.43	7/6	Steady Sweep
		2.0		42.44		
		4.0		42.45		
		6.0		42.46		
		8.0		42.47		
		10.0		42.48		
		11.0		42.49		
		12.0		42.50		
		13.0		42.51		
		14.0		42.52		
		15.0		42.53		
		16.0		42.54		
		17.0		42.55		
		18.0		42.56		
		19.0		42.57		
		20.0		42.58		
0.5	Steady	0.0		43.32	7/9	Steady
		2.1		43.33		
		4.0		43.34		
		6.1		43.35		
		8.2		43.36		
		9.1		43.37		
		10.0		43.38		
		10.9		43.39		
		11.9		43.40		
		12.9		43.41		
		14.1		43.42		
		15.0		43.43		
		16.0		43.44		

RUN LIST - 15 DEG SWEEP

Mach	Waveform	Angle Range	Pitch Rate or Red Fr.	Run.Pt	Date	Remarks
0.6	Steady	0.0	0	44.08	7/10	Steady
		2.0		44.09		
		4.0		44.10		
		6.2		44.11		
		6.9		44.12		
		8.1		44.18		
		8.8		44.14		
		10.1		44.15		
		11.1		44.16		
		12.1		44.17		

RUN LIST - 30 DEG SWEEP

Mach	Waveform	Angle Range	Pitch Rate or Red Fr.	Run.Pt	Date	Remarks
0.2	Sine	6±6	k=.025	47.32	7/18	Attached Sine
			k=.050	47.33		
			k=.100	47.34		
			k=.150	47.35		
0.2	Sine	8±6	k=.050	47.36	7/18	Sine Mean Angle Sweep
		10±6		47.37		
		12±6		47.38		
		14±6		47.39		
		16±6		47.40		
		18±6		47.41		
		20±6		47.42		
		22±6		47.43		
		24±6		47.44		
0.2	Sine	8±6	k=.100	47.45	7/18	Sine Mean Angle Sweep
		10±6		47.46		
		12±6		47.47		
		14±6		47.48		
		16±6		47.49		
		18±6		47.50		
		20±6		47.51		
		22±6		47.52		
		24±6		47.53		
0.2	Sine	8±6	k=.150	48.37	7/19	Sine Mean Angle Sweep
		10±6		48.38		
		12±6		48.39		
		14±6		48.40		
		16±6		48.41		
		18±6		48.42		
		20±6		48.43		
		22±6		48.44		
		24±6		48.45		
0.2	Ramp	0→10	A=.0010	47.55	7/18	Attached Ramp
			A=.0050	47.56		
			A=.0100	47.57		
			A=.0100	55.03	7/30	Spline Coupling
			A=.0200	55.04		
0.2	Ramp	0→30	A=.0010	47.59	7/18	Large Amplitude Ramp
			A=.0025	47.60		
			A=.0050	48.03	7/19	
			A=.0100	48.04		
			A=.0100	55.05	7/30	Spline Coupling
			A=.0200	55.06		
			A=.0250	55.07		

RUN LIST - 30 DEG SWEEP

Mach	Waveform	Angle Range	Pitch Rate or Red Fr.	Run.Pt	Date	Remarks
0.2	Ramp	10→20 12→22 14→24 16→26 18→28	A=.0050	48.05 48.06 48.07 48.09 48.10	7/19	Vary Ramp Range
0.2	Sine	10±10	k=.025 k=.050 k=.100 k=.150	48.11 48.13 48.15 48.17	7/19	Large Amplitude Sines
0.2	Sine	20±10	k=.025 k=.050 k=.100 k=.150	48.12 48.14 48.16 48.18		
0.3	Ramp	0→10	A=.0050	49.27	7/20	Attached Flow Ramp
0.3	Ramp	0→30	A=.0010 A=.0025 A=.0050 A=.0100 A=.0200	49.28 49.29 49.30 49.31 55.08	7/20 7/30	Large Amplitude Ramps Spline Coupling
0.3	Sine	10±10	k=.025 k=.050 k=.100	49.32 49.34 49.37	7/20	Large Amplitude Sines
0.3	Sine	20±10	k=.025 k=.050 k=.100	49.33 49.35 49.38		
0.3	Sine	9±8 12±8	k=.110 (8Hz) k=.055 (4Hz)	49.39 49.40	7/20	SA 1976/86 Repeat
0.4	Ramp	0→10	A=.0050	49.59	7/20	Attached ramp
0.4	Ramp	0→20	A=.0010 A=.0025 A=.0050 A=.0050 A=.0100	49.60 50.03 50.04 55.11 55.12	7/20 7/21 7/30	Large Ampl Ramp Spline Coupling
0.4	Sine	6±6 10±6 12±6 14±6 16±6	k=.025	50.05 50.06 50.07 50.08 50.09	7/21	Sine Sweep

RUN LIST - 30 DEG SWEEP

Mach	Waveform	Angle Range	Pitch Rate or Red Fr.	Run.Pt	Date	Remarks
0.4	Sine	6±6 10±6 12±6 14±6 16±6	k=.050	50.10 50.11 50.12 50.13 50.14	7/21	Sine Sweep
0.4	Sine	6±6 10±6 12±6 14±6	k=.075	50.16 50.17 50.18 50.19	7/21	Sine Sweep
0.4	Sine	6±6 10±6 12±6 14±6	k=.100	50.20 50.21, 50.23 50.24 50.25	7/21	Sine Sweep
0.4	Sine	10±10	k=.025 k=.050 k=.075	50.26 50.27 50.28	7/21	Large Ampl Sine
0.5	Ramp	0→8	A=.0050	51.20	7/24	Attached Ramp
0.5	Ramp	0→18	A=.0010 A=.0025 A=.0050 A=.0100	51.21 51.23 51.24 55.13	7/24 7/30	Large Ramp Spline Coupling
0.5	Sine	4±4	k=.025 k=.050 k=.075	51.25 51.30 51.36	7/24	Attached Sine
0.5	Sine	6±6 8±6 10±6 12±6	k=.025	51.26 51.27 51.28 51.29	7/24	Sine sweep
0.5	Sine	6±6 8±6 10±6 12±6	k=.050	51.31 51.32 51.33 51.34	7/24	Sine sweep
0.5	Sine	6±6 8±6 10±6 12±6	k=.075	51.37 51.38 51.39 51.40	7/24	Sine Sweep

RUN LIST - 30 DEG SWEEP

Mach	Waveform	Angle Range	Pitch Rate or Red Fr.	Run.Pt	Date	Remarks
0.6	Sine	4±4	k=.025	53.17	7/26	Moderate Amplitude Sines
		5±5		53.18		
		6±6		53.19		
		7±6		53.20		
		8±6		53.21		
0.6	Sine	4±4	k=.050	53.22	7/26	Moderate Amplitude Sines
		5±5		53.23		
		6±6		53.24		
		7±6		53.25		
		8±6		53.26		
		4±4	k=.075	53.28	7/26	Moderate Amplitude Sines
		5±5		53.29		
		6±6		53.30		
0.6	Ramp	0→12	A=.0010	54.02	7/27	Large Ramp
		0→12	A=.0025	54.04		
		0→13.5	A=.0025	54.05		
		0→13.5	A=.0050	54.06		

0.2	Ramp	0→30	A=.0010	55.15	7/30	Square Tip Ramp
			A=.0050	55.16		
			A=.0100	55.17		
			A=.0200	56.03	7/31	
0.2	Sine	10±10	k=.050	56.04	7/31	Square Tip Sine
		20±10	k=.050	56.05		
		10±10	k=.100	56.06		
		20±10	k=.100	56.07		
0.4	Ramp	0→20	A=.0050	56.09	7/31	Square Tip Ramp
0.4	Sine	6±6	k=.050	56.11	7/31	Square Tip Sine
		12±6		56.12		
		14±6		56.13		
		16±6		56.14		
		10±10		56.15		

RUN LIST - 30 DEG SWEEP

Mach	Waveform	Angle Range	Pitch Rate or Red Fr.	Run.Pt	Date	Remarks
-----Incipient Stall Runs-----						
0.2	Sine	10±1	k=.20	48.20	7/19	1.0 deg at 10Hz
		12±1		48.21		
		14±1		48.22		
		16±1		48.23		
		17±1		48.24		
		17.5±1		48.34		
		18±1		48.25		
		18.5±1		48.35		
		19±1		48.26		
		19.5±1		48.36		
		20±1		48.27		
		21±1		48.28		
		22±1		48.29		
		24±1		48.30		
		26±1		48.31		
		28±1		48.32		
0.2	Sine	12±2	k=.20	52.11	7/25	2.0 deg at 10Hz
		14±2		52.12		
		16±2		52.13		
		16.5±2		52.19		
		17±2		52.14		
		18±2		52.15		
		19±2		52.16		
		20±2		52.17		
		22±2		52.18		
0.2	Sine	12±.5	k=.20	52.20	7/25	0.5 deg at 10Hz
		14±.5		52.21		
		16±.5		52.22		
		17±.5		52.23		
		17.5±.5		52.24		
		18±.5		52.25		
		18.5±.5		52.26		
		19±.5		52.27		
		20±.5		52.28		
0.2	Sine	16±.5	k=.10	52.30	7/25	0.5 deg at 5Hz
		18±.5		52.31		
		20±.5		52.32		
0.2	Sine	16±1	k=.10	52.33	7/25	1.0 deg at 5Hz
		18±1		52.34		
		20±1		52.35		
0.2	Sine	16±2	k=.10	52.36	7/25	2.0 deg at 5Hz
		18±2		52.37		
		20±2		52.38		

RUN LIST - 30 DEG SWEEP

Mach	Waveform	Angle Range	Pitch Rate or Red Fr.	Run.Pt	Date	Remarks
0.2	Sine	16±.5 18±.5 20±.5	k=.3	52.39 52.40 52.41	7/25	0.5 deg at 15Hz
0.2	Sine	16±1 17±1 17.5±1 18±1 18.5±1 19±1 20±1	k=.3	52.43 52.49 52.52 52.44 52.51 52.50 52.45	7/25	1.0 deg at 15Hz
0.2	Sine	16±2 18±2 20±2	k=.3	52.46 52.47 52.48	7/25	2.0 deg at 15Hz
0.2	Sine	16±.5 18±.5 20±.5	k=.5	52.54 52.55 52.56	7/25	0.5 deg at 25Hz
0.2	Sine	16±1 17±1 18±1 19±1 20±1	k=.5	52.57 52.58 52.59 52.60 52.61	7/25	1.0 deg at 25Hz
0.2	Sine	16±2 18±2 20±2	k=.5	52.62 52.63 52.64	7/25	2.0 deg at 25Hz
0.2	Sine	16±.5 17±.5 18±.5 19±.5 20±.5	k=.6	52.66 52.70 52.67 52.69 52.68	7/25	0.5 deg at 30Hz
0.2	Sine	16±1 17±1 18±1 19±1 20±1 21±1 22±1 23±1	k=.6	52.71 52.72 52.73 52.74 52.75 52.76 52.77 52.78	7/25	1.0 deg at 30Hz

RUN LIST - 30 DEG SWEEP

Mach	Waveform	Angle Range	Pitch Rate or Red Fr.	Run.Pt	Date	Remarks
0.4	Sine	10±1 11±1 12±1 13±1 14±1 15±1 16±1 17±1 18±1 19±1 20±1	k=.1	50.30 50.31 50.32 50.33 50.34 50.35 50.36 50.37 50.38 50.39 50.40	7/21	1.0 deg at 10Hz
0.4	Sine	12±.5 13±.5 14±.5 15±.5 16±.5 17±.5 18±.5	k=.1	51.48 51.42 51.43 51.44 51.45 51.46 51.47	7/24	0.5 deg at 10Hz
0.4	Sine	13±2 15±2 17±2	k=.1	51.49 51.50 51.51	7/24	2.0 deg at 10Hz
0.4	Sine	13±.5 15±.5 17±.5 13±1 15±1 17±1	k=.25	52.02 52.03 52.04 52.05 52.06 52.07	7/25	0.5 deg at 25Hz 1.0 deg at 25Hz
0.4	Sine	13±2 15±2	K=.25	52.09	7/25	2.0 deg at 25Hz
0.6	Sine	6±.5 8±.5 9±.5 10±.5 11±.5 12±.5 13±.5	k=.1	54.08 54.09 54.10 54.11 54.12 54.14 54.15	7/27	0.5 deg at 15Hz
0.6	Sine	6±1 7±1 8±1 9±1 10±1 11±1 12±1 13±1	k=.1	54.17 54.18 54.19 54.20 54.21 54.22 54.23 54.27	7/27	1.0 deg at 15Hz

RUN LIST - 30 DEG SWEEP

Mach	Waveform	Angle Range	Pitch Rate or Red Fr.	Run.Pt	Date	Remarks
0.6	Sine	6±2 8±2 10±2	k=.1	54.24 54.25 54.26	7/27	2.0deg at 15Hz
0.6	Sine	6±.5 8±.5 10±.5 11±.5 12±.5 13±.5	k=.2	54.29 54.30 54.31 54.32 54.33 54.34	7/27	0.5 deg at 30Hz
0.6	Sine	6±1 7±1 8±1 9±1 10±1 11±1 12±1	k=.2	54.35 54.36 54.37 54.38 54.39 54.40 54.41	7/27	1.0 deg at 30Hz

RUN LIST - 30 DEG SWEEP

Mach	Waveform	Angle Range	Pitch Rate or Red Fr.	Run.Pt	Date	Remarks
0.2	Steady	0		47.07	7/18	Steady Sweep
		2.1		47.08		
		4.1		47.09		
		6.1		47.10		
		8.0		47.11		
		10.0		47.12		
		12.1		47.13		
		13.1		47.14		
		14.0		47.15		
		14.8		47.16		
		16.0		47.17		
		17.0		47.18		
		17.9		47.19		
		19.0		47.20		
		20.1		47.21		
		20.9		47.22		
		22.0		47.23		
		23.0		47.24		
		24.0		47.25		
		25.0		47.26		
		26.0		47.27		
		27.0		47.28		
		28.0		47.29		
		30.0		47.30		
0.3	Steady	0.0		49.03	7/20	Steady Sweep
		2.0		49.04		
		3.8		49.05		
		6.1		49.06		
		8.1		49.07		
		10.2		49.08		
		12.2		49.09		
		13.1		49.10		
		14.0		49.11		
		15.0		49.12		
		16.1		49.13		
		16.9		49.14		
		18.0		49.15		
		19.0		49.16		
		19.9		49.17		
		21.0		49.18		
		22.0		49.19		
		23.1		49.20		
		24.1		49.21		
		25.0		49.22		
		26.0		49.23		
		28.0		49.24		
		30.0		49.25		

RUN LIST - 30 DEG SWEEP

Mach	Waveform	Angle Range	Pitch Rate or Red Fr.	Run.Pt	Date	Remarks
0.4	Steady	0.0		49.42	7/20	Steady Sweep
		1.9		49.43		
		3.8		49.44		
		6.0		49.45		
		8.0		49.46		
		10.0		49.47		
		11.2		49.48		
		12.0		49.49		
		12.9		49.50		
		13.9		49.51		
		15.0		49.52		
		16.0		49.53		
		17.0		49.54		
		18.0		49.55		
		19.0		49.56		
		20.0		49.57		
0.5	Steady	0.0		51.03	7/24	Steady Sweep
		2.0		51.04		
		4.0		51.05		
		6.0		51.06		
		8.0		51.07		
		8.9		51.09		
		10.1		51.10		
		11.1		51.11		
		11.9		51.12		
		13.0		51.13		
		14.1		51.14		
		15.0		51.15		
		16.0		51.16		
		17.0		51.17		
		18.0		51.18		
0.6	Steady	0.0	0	53.03	7/26	Steady
		2.0		53.04		
		4.1		53.05		
		6.1		53.06		
		6.9		53.07		
		8.0		53.08		
		9.0		53.09		
		10.0		53.10		
		11.1		53.11		
		12.0		53.12		
		12.5		53.13		
		13.0		53.14		
		13.5		53.15		

RUN LIST - 30 DEG SWEEP

Mach	Waveform	Angle Range	Pitch Rate or Red Fr.	Run.Pt	Date	Remarks
0.2	Steady	4 10 16 22 28			7/19	Steady Surface Oil Flow
0.4	Steady	6 12 15 18			7/31	Steady Surface Oil Flow
0.6	Steady	5			7/31	Steady Surface Oil Flow

RUN LIST - 1986 2D TEST (0 SWEEP)

Mach	Waveform	Angle Range	Pitch Rate or Red Fr.	Run.Pt	Date	Remarks
0.2	Steady		0	06.01-.18	6/17	Steady Sweep
0.2	Sine	5±5	k=.025	17.04	6/23	Station 04 Only
0.2	Sine	10±10	.025	17.05	6/23	Sta 04
			.050	17.06		
			.100	17.07		
0.2	Sine	20±10	.025	18.01	6/23	Sta 04
			.050	18.02		Sta 04,12,20, Hot Films
			.100	19.01	6/24	Sta 04
0.2	Ramp	0→20	A=.0010	07.03	6/17	Sta 04
			.0010	08.01	6/18	Sta 04, +Unavg. Data
			.0025	08.02		Sta 04
			.0050	08.03		
			.0100	08.04		
0.2	Ramp	0→10	A=.0010	07.01	6/17	Sta 04
			.0025	08.07	6/18	Sta 04, Unavg
			.0050	08.05		
			.0050	13.01	6/20	Sta 04,12,20, HF, Unavg
			.0100	08.06	6/18	Sta 04
0.2	Down Ramp	20→10	A=.0010	17.02	6/23	Sta 04,12,20, HF, Unavg
			.0100	17.03		
0.2	Ramp	0→30	A=.0010	09.04	6/18	Sta 04
			.0010	10.02	6/19	Sta 04,12,20, HF, Unavg
			.0025	09.05	6/18	Sta 04,12,20
			.0050	09.06		
			.0050	10.01	6/19	Sta 04,12,20, HF, Unavg
			.0100	09.07	6/18	Sta 04,12,20, Unavg
			.0200	15.02	6/23	Sta 04,12,20, HF
0.2	Down Ramp	30→0	A=.0010	13.02	6/20	Sta 04,12,20, HF, Unavg
			.0050	15.01	6/23	
0.2	Ramp	14→24	A=.0010	11.03	6/19	Sta 04,12,20, HF, Unavg
			.0050	12.04		Sta 04
			.0100	17.01	6/23	
0.2	Ramp	12→22	.0010	15.03	6/23	Sta 04
			.0050	11.04	6/19	Sta 04,12,20, HF, Unavg
			.0100	16.02	6/23	Sta 04

RUN LIST - 1986 2D TEST (O SWEEP)

Mach	Waveform	Angle Range	Pitch Rate or Red Fr.	Run.Pt	Date	Remarks
0.3	Sine	12±8 9±8	k=.054(4Hz) .110(8Hz)	22.01 22.02	6/24	Sta 04
0.3	Ramp	0→20 0→30	A=.0050 A=.0100	22.03 22.04	6/24	Sta 04
0.4	Ramp	0→10	A=.0010 .0050	19.02 19.03	6/24	Sta 04
0.4	Ramp	0→20	A=.0025 .0050 .0100	21.02 21.01 21.03	6/24	Sta 04
0.4	Down Ramp	20→0	A=.0100	21.04	6/24	Sta 04

APPENDIX III DOCUMENTATION OF THE EXPERIMENTAL DATA BASE

Ensemble Averaged Data Files

The primary data set consists of files (one per test condition) containing wind tunnel and model operating conditions and time histories of the ensemble averaged pressures, hot film signals, integrated section force and moment coefficients, and other time-dependent parameters. The initial lines of such a file are shown in Table III-1. Wind tunnel operating conditions are based upon an approximately 20 second average.

The unsteady measurements included in each file are listed in Table III-2. Each ensemble average contains 1024 samples. This corresponds to one period for sinusoidal motion, and the positive pitch rate portion for ramp motions. Steady-state data are provided in 'quasi-steady' files, with each sample corresponding to the time average of the results at the specified α . The first 112 measurements are from the wing pressure transducers. Each transducer is identified by an engineering names ('ENAME') of the form 'CPKnnSmm' (Coefficient of Pressure, Kulite, at spanwise station nn, Suction (or Pressure) surface chordwise station mm). As shown in Table III-1, the spanwise (z/c from the wing tip) and chordwise (x/c from the leading edge) positions are also provided. Thermal corrections and zero shift adjustments have been applied. Pressure measurements that have been further corrected by interpolation between neighboring stations are identified by the notation 'INTERP ALL', 'INTERP MEAN', or 'INTERP UNST' depending on whether the entire signal, only the time average, or only the unsteady portion have been interpolated.

The next 16 time histories in each file are the hot film gage output voltages, identified by 'SFGnnSmm' (Skin Friction Gage at spanwise position nn and chordwise position mm). The data are in the form of unscaled DC voltage levels. Section lift, pressure drag, and moment coefficient time histories follow. The ENAMES are of the form 'Cxnn' (Coefficient in x direction - Lift, Drag, Moment - at spanwise station nn). The remaining time histories are for the additional instrumentation, identified in Table 5 of the report.

Data Tape Format

Ensemble averaged data files are supplied on ASCII-formatted magnetic tapes. Each record is 80 Bytes long and corresponds to one line in Table III-1. The data file for each test condition is 19661 records (1.6 MB) in length. Seven 6250 BPI tapes contain the complete set of 607 unsteady and 15 quasi-steady test conditions (the steady-state data at the same sweep angle and Mach number have been collected into common files as functions of α), a total of 1.04 GB. The tapes are grouped into steady-state data, ramp motions, large amplitude sinusoidal motions, and small amplitude sinusoidal motions. The conditions on each tape are listed in Table III-3. A FORTRAN program 'READASCO' is supplied with the data files. This program was written in FORTRAN-77 on a Perkin Elmer computer, but it has also been successfully run on a Digital Equipment Corporation VAX using the VMS operating system. The utility 'ETAPE' is the

preferred means to read the data tapes into a VAX system, but any utility capable of reading unlabelled ASCII tapes should work. Note that the number of number of records (bytes) per block is longer than the default value on most systems, and must be reset. The READASCO program reads a formatted ASCII data file and places the data into a series of common areas. It may be used by itself to verify that the data has been read in correctly, converted to an input subroutine, or used as a model for writing a specialized program. More extensive documentation on the data files is included as comments in this program.

Data From 1986 2D Test

An eighth data tape contains results from the 1986 test of the 2D version of the model (Refs. 20-21 of the report). This tape contains steady-state data at $M_c = 0.2$, and unsteady sinusoidal and ramp data at $M_c = 0.2, 0.3$, and 0.4 . A run list of the 45 conditions is included in Appendix II. These files can also be read using READASCO, but the unsteady parameters differ from the 3D files. Some 2D files contain only pressures at station 04 ($z/c = 0.59$ on the 3D model), while other also have pressure data at stations 12 and 20 ($z/c = 1.06$ and 1.52 on the 3D model), and/or hot film data at station 06. (The station numbers are in inches, referenced to the end of the main instrumented panel.) There is no reliable steady data at $M_c = 0.3$ and 0.4 , and the overall confidence level in the 2D data is somewhat lower than in the more recent 3D data. For example, the noticeable difference between the values of $C_L(\alpha=0)$ at $M_c = 0.2$ and 0.4 may represent calibration shifts in the α sensor.

Unaveraged and Down Ramp Data

The complete set of 20 to 40 cycles of unaveraged digital data for each test condition has been archived as binary Perkin Elmer format tapes. The complete set of 60 tapes contains approximately 8 GB of binary integer and floating point data. If necessary, unaveraged ASCII data tapes can be produced for selected conditions. The format would be similar to that used for ensemble averaged tapes. Ensembled averaged data for the negative pitch rate portions of the ramp conditions are also available, but have not been included in the basic data set. Down ramp and unaveraged data for the 1986 2D experiment exist only for those conditions identified in Appendix II.

Summary Test Conditions

The set of conditions listed in Table III-4 are proposed to provide a summary of the results. These conditions emphasize the effects of the primary independent variables ($A, M_c, \Lambda, k, \alpha_0, \alpha_1$), and provide an overview of the data. These conditions are available as a single ASCII data tape (identified in Table III-3).

TABLE III-1.
EXAMPLE OF DATA FILE

```

*****
UTRC OSCILLATING WING DATA
*****
RUN 32.48      DATE 06/18/90 15:19:54
PART SPAN MODEL WITH SSCA09  AIRFOIL AT  0. DEG SWEEP
P TOTAL      2093.2PSF P STATIC      1964.7PSF Q DYNAMIC      125.65PSF
T TOTAL      87.6F  T STATIC      77.8F  RHO STATIC 0.002115SLG/FT3
DEWPOINT     58.5F  SOUND SPD      1139.7FPS WING CHORD      1.441FT
TUNNEL SPD    344.7FPS MACH #        0.302
CHRD SPEED    344.7FPS CHRD MACH      0.302  REYNOLDS # 3040101.
RAMP FROM     0.00 TO 30.00 DEG
RAMP PERIOD= 0.05464SEC,  PITCH UP RATE= 0.0200
MEAS. MEAN ANGLE= 15.00 MIN= 0.02 MAX= 30.61 INIT= 0.06 FIN= 29.82
#SPAN STA= 5 #PRS XDCRS=112 #HT FILMS= 16 #OTHER= 6
*****
ENSEMBLE AVERAGED OSCILLATING WING DATA
SAMPLES/REV      1024 REV/ENSEMBLE      20 TIME SHIFT      -0.121826
ALPHA (DEG)

0.02073  0.06721  0.05552  0.05432  0.05732  0.05822  0.05972  0.05972
0.05702  0.05732  0.06062  0.06002  0.05642  0.05912  0.06212  0.05912
0.05672  0.05882  0.06152  0.06122  0.06062  0.06002  0.05972  0.06272
0.06182  0.06572  0.06212  0.06092  0.06392  0.06122  0.06422  0.05972
.
.
30.48630 30.49802 30.50429 30.51479 30.52290 30.53250 30.54269 30.55139
30.56007 30.56638 30.57657 30.58287 30.59248 30.59877 30.60837 30.61256
*****
CPK04S1
X / CHORD      0.005 SPANWISE Z/C      0.59
0.54352  0.54513  0.54447  0.54459  0.54507  0.54459  0.54340  0.54352
0.54429  0.54483  0.54418  0.54400  0.54406  0.54477  0.54489  0.54435
0.54477  0.54560  0.54495  0.54477  0.54578  0.54519  0.54519  0.54578
.
.
-1.06701 -1.04647 -1.05701 -1.06552 -1.06826 -1.05957 -1.06927 -1.06665
-1.06379 -1.06873 -1.04510 -1.05522 -1.06481 -1.04599 -1.04665 -1.04010
*****
CPK04S2
X / CHORD      0.0256022 SPANWISE Z/C      0.59
-0.15138 -0.14964 -0.15138 -0.15242 -0.15200 -0.15124 -0.15221 -0.15214
-0.15186 -0.15269 -0.15207 -0.15228 -0.15221 -0.15290 -0.15269 -0.15117
-0.15165 -0.15200 -0.15242 -0.15131 -0.15165 -0.15193 -0.15158 -0.15152
.
.

```


TABLE III-2.
UNSTEADY MEASUREMENTS CONTAINED IN DATA FILES

ALPHA_E_1 (α)

CPK04S1	CPK04S2	CPK04S3	CPK04S4	CPK04S5	CPK04S6
CPK04S7	CPK04S8	CPK04S9	CPK04S10	CPK04S11	CPK04S12
CPK04S13	CPK04S14	CPK04S15	CPK04S16	CPK04S17	CPK04S18
CPK04P1	CPK04P2	CPK04P3	CPK04P4	CPK04P5	CPK04P6
CPK04P7	CPK04P8	CPK04P9	CPK04P10	CPK04P11	CPK04P12
CPK04P13	CPK04P14	CPK04P15	CPK04P16	CPK04P17	CPK04P18
CPK45S1	CPK45S2	CPK45S3	CPK45S4	CPK12S1	CPK12S2
CPK12S3	CPK12S4	CPK12S5	CPK12S6	CPK12S7	CPK12S8
CPK12S9	CPK12S10	CPK12P1	CPK12P2	CPK12P3	CPK12P4
CPK12P5	CPK12P6	CPK20S1	CPK20S2	CPK20S3	CPK20S4
CPK20S5	CPK20S6	CPK20S7	CPK20S8	CPK20S9	CPK20S10
CPK20P1	CPK20P2	CPK20P3	CPK20P4	CPK20P5	CPK20P6
CPKT1S1	CPKT1S2	CPKT1S3	CPKT1S4	CPKT1S5	CPKT1S6
CPKT1S7	CPKT1S8	CPKT1S9	CPKT1S10	CPKT1S11	CPKT1S12
CPKT1S13	CPKT1S14	CPKT1P1	CPKT1P2	CPKT1P3	CPKT1P4
CPKT1P5	CPKT1P6	CPKT2S1	CPKT2S2	CPKT2S3	CPKT2S4
CPKT2S5	CPKT2S6	CPKT2S7	CPKT2S8	CPKT2S9	CPKT2S10
CPKT2S11	CPKT2S12	CPKT2S13	CPKT2S14	CPKT2P1	CPKT2P2
CPKT2P3	CPKT2P4	CPKT2P5	CPKT2P6	SFG06S1	SFG06S2
SFG06S3	SFG06S4	SFG06S5	SFG06S6	SFG06S7	SFG06S8
SFGT1S1	SFGT1S2	SFGT1S3	SFGT1S4	SFGT2S1	SFGT2S2
SFGT2S3	SFGT2S4	STR_BEND_1	STR_TORS_1	STR_BEND_2	MODEL_Q_1
TUNL_TOTAL	TUNL_STATIC	CLT1	CDT1	CMT1	CLT2
CDT2	CMT2	CL04	CD04	CM04	CL12
CD12	CM12	CL20	CD20	CM20	

TABLE III-3.
DIRECTORY OF DATA TAPES

Tape 1: Steady-State, $\Lambda = 0$, 15° Ramps, $\Lambda = 30^\circ$ Ramps at $M_c = 0.2$ and 0.3

ASCOPYR1.CMD, READASCO.FTN,

90.02, 90.03, 90.04, 90.05, 90.06 (Steady $\Lambda = 0$ at $M_c = 0.2, \dots, 0.6$)
91.02, 91.03, 91.04, 91.05, 91.06 (Steady $\Lambda = 15$ at $M_c = 0.2, \dots, 0.6$)
92.02, 92.03, 92.04, 92.05, 92.06 (Steady $\Lambda = 30$ at $M_c = 0.2, \dots, 0.6$)
1.23, 31.24, 31.25, 31.26, 31.27, 31.36, 31.37, 31.38, 31.39, 35.43, 39.34,
39.35, 39.36, 39.37, 39.38, 32.42, 33.18, 32.43, 32.44, 32.46, 32.47, 32.48,
33.52, 33.53, 33.54, 33.55, 33.56, 33.57, 34.11, 34.12, 34.44, 35.05, 35.06,
35.07, 35.08, 35.09, 35.30, 35.31, 35.32, 41.55, 41.56, 41.49, 41.57, 45.05,
41.58, 41.59, 41.60, 41.61, 45.06, 45.07, 42.30, 42.31, 42.32, 42.33, 42.34,
45.08, 45.09, 42.68, 42.69, 43.03, 43.04, 43.05, 45.10, 44.03, 44.04, 44.05,
44.06, 44.28, 44.29, 44.30, 44.31, 47.55, 47.56, 47.57, 55.03, 55.04, 47.59,
47.60, 48.03, 48.04, 55.05, 55.06, 55.07, 48.05, 48.06, 48.08, 48.09, 48.10,
49.27, 49.28, 49.29, 49.30, 49.31, 55.08 (109 Data Files)

Tape 2: $\Lambda = 30^\circ$ Ramps at $M_c = 0.4, 0.5, 0.6$, $\Lambda = 0$ Sinusoids

ASCOPYR2.CMD, READASCO.FTN,

49.59, 49.60, 50.03, 50.04, 55.11, 55.12, 51.20, 51.21, 51.23, 51.24, 55.13,
54.02, 54.05, 54.05, 54.06, 31.41, 35.35, 31.42, 35.36, 35.37, 35.38, 35.39,
35.40, 35.41, 35.42, 31.43, 31.44, 31.45, 31.46, 31.47, 31.48, 31.49, 31.50,
31.51, 32.09, 32.11, 32.13, 32.15, 32.10, 32.12, 32.14, 32.16, 32.49, 33.09,
33.11, 33.13, 33.10, 33.12, 33.14, 33.16, 33.17, 33.44, 33.45, 33.46, 33.47,
33.48, 33.49, 33.50, 33.51, 39.03, 39.04, 39.05, 34.04, 34.05, 34.06, 34.32,
34.36, 34.40, 34.33, 34.34, 34.35, 34.37, 34.38, 34.39, 34.41, 34.42, 34.43,
35.21, 35.22, 35.23, 35.26, 35.27, 35.28, 35.29, 37.03, 37.04, 37.05, 37.06,
37.07, 37.08 (90 Data Files)

Tape 3: $\Lambda = 15^\circ$ Sinusoids, $\Lambda = 30^\circ$ Sinusoids at $M_c = 0.2, 0.3, 0.4$

ASCOPYR3.CMD, READASCO.FTN,

41.34, 41.35, 41.36, 41.37, 41.38, 41.39, 41.40, 41.41, 41.42, 41.43, 41.44,
41.45, 41.62, 41.65, 42.03, 42.05, 41.63, 41.64, 42.04, 42.06, 42.36, 42.38,
42.40, 42.37, 42.39, 42.41, 42.59, 42.60, 42.61, 42.62, 42.63, 42.64, 42.65,
42.66, 43.06, 43.07, 43.08, 43.45, 43.49, 43.53, 43.46, 43.47, 43.48, 43.50,
43.51, 43.52, 43.54, 43.55, 43.56, 44.20, 44.21, 44.22, 44.23, 44.25, 44.26,
44.27, 48.11, 48.13, 48.15, 48.17, 48.12, 48.14, 48.16, 48.18, 49.32, 49.34,
49.37, 49.33, 49.35, 49.38, 49.39, 49.40, 50.05, 50.06, 50.07, 50.08, 50.09,
50.10, 50.11, 50.12, 50.13, 50.14, 50.16, 50.17, 50.18, 50.19, 50.20, 50.21,
50.23, 50.24, 50.25, 50.26, 50.27, 50.28 (94 Data Files)

Tape 4: $\Lambda = 30^\circ$ Sinusoids at $M_c = 0.5, 0.6$, Square Tip at $\Lambda = 0, 15, 30^\circ$,
Incipient Stall Flutter at $\Lambda = 15^\circ$

ASCOPYR4.CMD, READASCO.FTN,

51.25, 51.30, 51.36, 51.26, 51.27, 51.28, 51.29, 51.31, 51.32, 51.33, 51.34,
51.37, 51.38, 51.39, 51.40, 53.17, 53.18, 53.19, 53.20, 53.21, 53.22, 53.23,
53.24, 53.25, 53.26, 53.28, 53.29, 53.30, 40.05, 40.03, 40.18, 40.04, 40.06,
40.07, 40.08, 40.09, 40.16, 40.15, 40.11, 40.12, 40.13, 40.14, 46.03, 46.04,
46.06, 46.07, 46.08, 46.09, 46.10, 46.11, 46.12, 46.17, 46.13, 46.14, 46.15,
46.16, 55.15, 55.16, 55.17, 56.03, 56.04, 56.05, 56.06, 56.07, 56.09, 56.11,
56.12, 56.13, 56.14, 56.15, 43.20, 43.21, 43.22, 43.23, 43.24, 43.25, 43.26,
43.27, 43.28, 43.29, 43.30, 43.09, 43.10, 43.11, 43.12, 43.13, 43.14, 43.15,
43.16, 43.17, 43.18 (91 Data Files)

Tape 5: Incipient Stall Flutter at $\Lambda = 0$

ASCOPYR5.CMD, READASCO.FTN,

37.09, 37.11, 37.12, 37.13, 37.14, 37.22, 37.16, 37.17, 37.18, 37.19, 37.20,
37.21, 37.23, 37.24, 37.25, 37.55, 37.26, 37.27, 37.29, 37.30, 37.31, 37.32,
37.33, 37.34, 37.35, 37.56, 37.57, 37.58, 38.03, 38.04, 38.05, 38.06, 38.07,
38.09, 38.10, 38.11, 38.12, 38.13, 38.14, 38.15, 38.16, 38.17, 38.19, 38.20,
38.21, 38.22, 38.23, 38.24, 38.25, 38.26, 38.27, 38.35, 38.36, 38.37, 38.38,
38.39, 38.40, 38.42, 38.43, 38.44, 38.45, 38.46, 38.47, 38.48, 38.49, 38.50,
38.55, 38.56, 38.57, 38.58, 38.51, 38.52, 38.53, 39.06, 39.07, 39.08, 39.09,
39.10, 39.11, 39.12, 39.13, 39.14, 39.17, 39.18, 39.19, 39.20, 39.21, 39.22,
39.23, 39.24, 39.25, 39.26, 39.27, 39.28, 39.29, 39.30, 39.31, 39.32
(98 Data Files) [39.31 and 39.32 may be missing, see Tape 7]

Tape 6: Incipient Stall Flutter at $\Lambda = 30^\circ$ at $M_c = 0.2, 0.4$ at $k=0.1, \alpha_0=1^\circ$

ASCOPYR6.CMD, READASCO.FTN,

48.20, 48.21, 48.22, 48.23, 48.24, 48.34, 48.25, 48.35, 48.26, 48.36, 48.27,
48.28, 48.29, 48.30, 48.31, 48.32, 52.11, 52.12, 52.13, 52.19, 52.14, 52.15,
52.16, 52.17, 52.18, 52.20, 52.21, 52.22, 52.23, 52.24, 52.25, 52.26, 52.27,
52.28, 52.30, 52.31, 52.32, 52.33, 52.34, 52.35, 52.36, 52.37, 52.38, 52.39,
52.40, 52.41, 52.43, 52.49, 52.52, 52.44, 52.51, 52.50, 52.45, 52.46, 52.47,
52.48, 52.54, 52.55, 52.56, 52.57, 52.58, 52.59, 52.60, 52.61, 52.62, 52.63,
52.64, 52.66, 52.70, 52.67, 52.69, 52.68, 52.71, 52.72, 52.73, 52.74, 52.75,
52.76, 52.77, 52.78, 50.30, 50.31, 50.32, 50.33, 50.34, 50.35, 50.36, 50.37,
50.38, 50.39, 50.40 (91 Data Files)

Tape 7: Incipient Stall Flutter at $\Lambda = 30^\circ$

ASCOPYR5.CMD, READASCO.FTN,

51.48, 51.42, 51.43, 51.44, 51.45, 51.46, 51.47, 51.49, 51.50, 51.51, 52.02,
52.03, 52.04, 52.05, 52.06, 52.07, 52.09, 52.10, 54.08, 54.09, 54.10, 54.11,
54.12, 54.14, 54.15, 54.17, 54.18, 54.19, 54.20, 54.21, 54.22, 54.23, 54.27,
54.24, 54.25, 54.26, 54.29, 54.30, 54.31, 54.32, 54.33, 54.34, 53.35, 54.36,
54.37, 54.38, 54.39, 54.40, 54.41, 39.29, 39.30, 39.31, 39.32 (53 Data Files)

Tape 8: 2D Data from 1986 Experiment

ASCOPYR8.CMD, READASCO.FTN

90.00, 17.04, 17.05, 17.06, 17.07, 18.01, 18.02, 19.01, 07.03, 08.01, 08.02,
08.03, 08.04, 07.01, 08.07, 08.05, 13.01, 08.06, 17.02, 17.03, 09.04, 10.02,
09.05, 09.06, 10.01, 09.07, 15.02, 13.02, 15.01, 11.03, 12.04, 17.01, 15.03,
11.04, 16.02, 22.01, 22.02, 22.03, 22.04, 19.02, 19.03, 21.02, 21.01, 21.03,
21.04 (45 Data Files)

Tape 0: Summary Tape of 3D Data

ASCOPYR0.CMD, READASCO.FTN

90.02, 90.03, 90.04, 90.05, 90.06 (Steady $\Lambda = 0$ at $M_c = 0.2, \dots, 0.6$)
91.02, 91.03, 91.04, 91.05, 91.06 (Steady $\Lambda = 15$ at $M_c = 0.2, \dots, 0.6$)
92.02, 92.03, 92.04, 92.05, 92.06 (Steady $\Lambda = 30$ at $M_c = 0.2, \dots, 0.6$)
33.09, 33.10, 33.11, 33.12, 33.13, 33.14, 32.13, 32.14, 32.15, 32.16, 34.05,
34.39, 35.27, 34.06, 34.43, 35.29, 40.09, 40.15, 42.40, 42.41, 42.03, 42.04,
43.08, 43.52, 44.25, 49.37, 49.38, 48.15, 48.18, 50.28, 51.39, 51.40, 53.29,
53.30, 32.43, 32.44, 32.46, 32.47, 32.48, 31.38, 35.43, 34.12, 33.56, 35.09,
35.32, 40.18, 40.16, 42.31, 42.32, 42.33, 45.08, 45.09, 45.10, 43.04, 44.06,
49.28, 49.29, 49.30, 49.31, 55.08, 55.05, 55.07, 55.12, 55.11, 55.13, 54.06,
55.17, 56.09, 48.20, 48.21, 48.22, 48.23, 48.24, 48.34, 48.25, 48.35, 48.26,
48.36, 48.27, 48.28, 48.29, 48.30, 48.31, 48.32 (99 Data Files)

TABLE III-4.
CONDITIONS ON SUMMARY TAPE

Run	A	Mc	Type	k	α	Run	A	Mc	Type	A	α
90.02	0	0.2	Steady	-	-	32.43	0	0.3	Ramp	.0010	0→30
90.03	0	0.3	Steady	-	-	32.44				.0025	
90.04	0	0.4	Steady	-	-	32.46				.0050	
90.05	0	0.5	Steady	-	-	32.47				.0100	
90.06	0	0.6	Steady	-	-	32.48				.0200	
91.02	15	0.2	Steady	-	-	31.38	0	0.2	Ramp	.0100	0→30
91.03	15	0.3	Steady	-	-	35.43				.0250	
91.04	15	0.4	Steady	-	-	34.12	0	0.4	Ramp	.0100	0→25
91.05	15	0.5	Steady	-	-	33.56				.0050	
91.06	15	0.6	Steady	-	-	35.09	0	0.5	Ramp	.0100	0→16
92.02	30	0.2	Steady	-	-	35.32	0	0.6	Ramp	.0025	0→10
92.03	30	0.3	Steady	-	-	40.18	0	0.2	R(Sqr)	.0100	0→30
92.04	30	0.4	Steady	-	-	40.16	0	0.4	R(Sqr)	.0050	0→25
92.05	30	0.5	Steady	-	-	42.31	15	0.3	Ramp	.0010	0→30
92.06	30	0.6	Steady	-	-	42.32				.0025	
33.09	0	0.3	Sine	.025	10±10	42.33				.0050	
33.10					20±10	45.08				.0100	
33.11				.050	10±10	45.09				.0200	
33.12					20±10	45.10	15	0.4	Ramp	.0100	0→20
33.13				.100	10±10	43.04				.0050	
33.14					20±10	44.06	15	0.5	Ramp	.0050	0→16
32.13	0	0.2	Sine	.100	10±10	49.28	30	0.3	Ramp	.0010	0→30
32.14					20±10	49.29				.0025	
32.15				.150	10±10	49.30				.0050	
32.16					20±10	49.31				.0100	
34.05	0	0.4	Sine	.050	10±10	55.08				.0200	
34.39		0.5			10±6	55.05	30	0.2	Ramp	.0100	0→30
35.27		0.6			5±5	55.07				.0250	
34.06	0	0.4	Sine	.075	10±10	55.12	30	0.4	Ramp	.0100	0→20
34.43		0.5			10±6	55.11				.0050	
35.29		0.6			5±5	55.13	30	0.5	Ramp	.0050	0→18
40.09	0	0.2	Sin(SqT)	.100	20±10	54.06	30	0.6	Ramp	.0050	0→13.5
40.15		0.4		.050	10±10	55.17	30	0.2	R(Sqr)	.0100	0→30
42.40	15	0.3	Sine	.100	10±10	56.09	30	0.4	R(Sqr)	.0050	0→20
42.41					20±10	48.20	30	0.2	Sine	k=.20	10±1
42.03	15	0.2	Sine	.100	10±10	48.21					12±1
42.04					20±10	48.22					14±1
43.08	15	0.4	Sine	.075	10±10	48.23					16±1
43.52		0.5			10±6	48.24					17±1
44.25		0.6			5±5	48.34					17.5±1
49.37	30	0.3	Sine	.100	10±10	48.25					18±1
49.38					20±10	48.35					18.5±1
48.15	30	0.2	Sine	.100	10±10	48.26					19±1
48.18					20±10	48.36					19.5±1
50.28	30	0.4	Sine	.075	10±10	48.27					20±1
51.39		0.5			10±6	48.28					21±1
51.40		0.5			12±6	48.29					22±1
53.29		0.6			5±5	48.30					24±1
53.30		0.6			6±6	48.31					26±1
48.32					28±1						

APPENDIX IV
INCIPIENT TORSIONAL STALL FLUTTER AERODYNAMIC EXPERIMENTS
ON A SWEEPED THREE-DIMENSIONAL WING

AIAA-91-0935-CP

Peter F. Lorber* and Franklin O. Carta**
United Technologies Research Center
East Hartford, CT 06108

ABSTRACT

The aerodynamics of small amplitude pitching motions near stall have been studied experimentally in order to improve understanding of the torsional stall flutter problem for propeller blades. A model wing was oscillated in pitch at several small amplitudes over a wide and representative range of conditions. Unsteady surface pressures were measured and integrated to determine the aerodynamic damping at five spanwise stations. Attached flow damping was positive and, for moderate Mach numbers and frequencies, in good agreement with thin airfoil theory. Strong negative damping was found for motions centered near static stall for all studied reduced frequencies, Mach numbers, and sweep angles. The 30° swept back configuration was found to become negatively damped over the entire span nearly simultaneously, while the unswept model exhibited local regions of negative damping that moved toward the wing tip as the mean angle of attack was increased.

NOMENCLATURE

A pitch rate, $\dot{\alpha}/2U_c$
c airfoil chord, m
 C_L section lift coefficient, L/qc
 C_M section pitching moment coefficient
about $x/c = 0.25$, M/qc
 C_p pressure coefficient, $(P-P_\infty)/q$
 C_{p*} pressure coefficient for locally sonic
chordwise velocity
k reduced frequency, $\omega c/2U_c$
L aerodynamic lift, Nt
M aerodynamic moment, Nt-m
 M_c chordwise Mach number, $M_\infty \cos \Lambda$
 M_∞ freestream Mach number
q dynamic pressure, $0.5 \rho_\infty U_c^2$
t time, s
T oscillation period, s
Re Reynolds number, cU/v
 U_c chordwise component of freestream velocity,
 $U_\infty \cos \Lambda$, m/s
 U_∞ freestream velocity, m/s
x distance along chord from leading edge, m
z distance along span from tip leading edge, m

 α geometric angle of attack, $\alpha = \alpha_0 - \alpha_1 \cos \omega t$
 α_1 amplitude of oscillation, deg
 α_0 time-mean angle of attack, deg
 α_{ss} steady state stall angle, deg
 Λ sweep-back angle, deg
 ν kinematic viscosity, m^2/s
 Ξ damping coefficient, $-dC_M/d\alpha / \pi \alpha_1^2$
 ρ_∞ freestream density
 τ nondimensional time, t/T
 ω circular frequency, $2\pi/T$
 ϕ phase lag relative to α , deg

INTRODUCTION

An experiment has been performed to investigate the aerodynamics of small amplitude pitching oscillations near static stall. The motivation for this research is the self-induced torsional stall flutter problem experienced by propeller blades. The instability may be encountered during high thrust static testing or at the start of the takeoff roll, when the blades are operating at high angles of attack. The characteristic behavior includes a small amplitude initiation, a rapid growth to a large amplitude, and a reduction in growth rate to establish a constant amplitude, limit-cycle oscillation. Early phenomenological studies [1-3] used strain gages to record the decay or growth of the airfoil torsional response, but were unable to determine the actual aerodynamic damping or characterize the underlying physical mechanism. The related problem of dynamic stall of helicopter rotor blades was studied, starting in the 1960's, by measuring aerodynamic loads during forced large amplitude motions [4-6]. Accurate unsteady blade pressure measurements may now be used to obtain instantaneous pressure distributions and aerodynamic damping coefficients. A preliminary experiment [7] made such pressure measurements on a two-dimensional airfoil model oscillating in pitch at amplitudes of 0.5, 2.0, and 4.0°. The strongest negative (unstable) damping coefficients were found near the static stall angle for amplitudes of 0.5 and 2.0°. The measured damping coefficients were then applied in a simple model problem to compute the behavior of a single degree-of-freedom torsional oscillation. The predicted rapid growth to a limit cycle oscillation was similar to the early stall flutter results.

The initial experiment [7] used a two-dimensional model, and was limited to relatively low Reynolds number, Mach number, and frequency ($Re = 650,000$, $M_\infty = 0.18$, and $k \leq 0.16$). The small wind tunnel had less than ideal flow quality (relatively high turbulence level and unknown angularity), resulting in an early static stall (at 9.5°). A much more sophisticated experiment has now been conducted with a larger model and wind tunnel, with significantly improved instrumentation, and over a much wider range of conditions. This paper describes the new experiment and presents a selection of the results. The effects of six independent parameters (Mach number, mean angle of attack, oscillation amplitude, reduced frequency, sweep angle, and spanwise position) are discussed, and a conceptual model is provided. It is hoped that this information will facilitate the design of lightweight propellers that avoid potential instabilities but do not require excessive stiffness.

* Research Engineer. Member AIAA.

** Supervisor, Experimental and Analytical Aeromechanics. Associate Fellow AIAA.

DESCRIPTION OF EXPERIMENT

The current model is a straight, untwisted, semi-span wing of 17.3 in. (44 cm) chord and 48 in. (122 cm) span (Fig. 1), producing an aspect ratio of 5.6. The wing consists of a steel spar and fiberglass airfoil panels, and uses a Sikorsky SSC-A09 9% thickness cambered airfoil section (Fig. 2). The tip is rounded into an approximate body of revolution. The wing is mounted at sweep angles of 0, 15, and 30° from the side wall of the 8 ft (2.4 m) octagonal test section of the UTRC Large Subsonic Wind Tunnel. Additional airfoil panels are added to the spar at higher sweep angles in order to keep the wing tip 1/4 chord at the tunnel centerline (Fig. 1). At $\Lambda = 30^\circ$ the span is thus increased to 55 in., an aspect ratio of 6.4. A hydraulic drive is used to oscillate the model in pitch about the line connecting the root and tip 1/4 chord.

Unsteady surface pressure measurements were made on the wing model using 112 miniature transducers distributed among five spanwise stations.

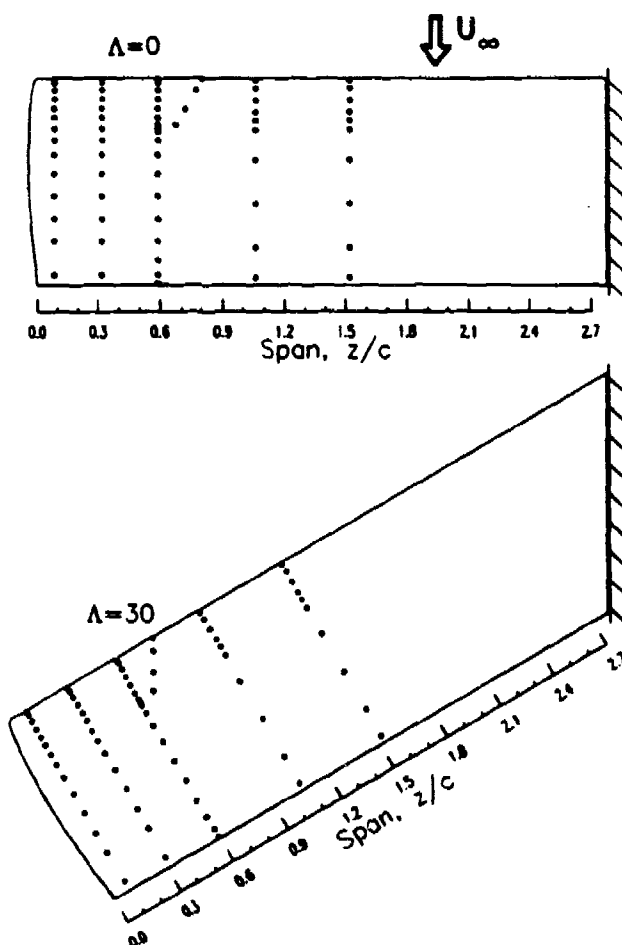


Fig. 1 Wing planform and transducer locations.

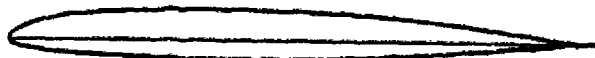


Fig. 2 SSC-A09 airfoil section.

The suction surface transducer locations are shown by the dots in Fig. 1. The frequency response of the installed transducers has been measured by comparing their response to white noise with that of a reference microphone [8]. The initial resonance is typically between 4 and 12 kHz, well above the current range of interest (fundamental frequencies of up to 30 Hz). Steady state calibration was performed over the full range of pressures (+2.5 to -12.5 psi) and temperatures (50 to 110 F) expected. This procedure [8-9] results in a steady-state calibration accuracy of better than 0.5% of the full scale pressure range. Two bending and one torsional strain gage bridges were mounted on the spar to verify that limit stresses were not exceeded and to allow wing deflections to be estimated. (The deflections were not significant for the conditions reported here.) The output of each sensor was digitized 1024 times during each of 40 pitching oscillations, recorded on digital magnetic tape, ensemble averaged, and converted to coefficient form. The pressures were integrated along the chord at each of the five spanwise stations to determine the unsteady lift, pressure drag, and pitching moment coefficients.

The incipient stall flutter work reported in this paper is an element of a continuing program that is also studying large amplitude dynamic stall with application to helicopter rotors and maneuvering aircraft [9-10]. Table 1 shows the test matrix for the 260 incipient stall flutter data points. The test envelope included chordwise Mach numbers of 0.2, 0.4, and 0.6, corresponding to Reynolds numbers of 2, 4, and 6×10^6 . Oscillation amplitudes of $\alpha_1 = 0.5, 1.0, \text{ and } 2.0^\circ$ were used. (Additional steady state and $\alpha_1 = 6^\circ$ results are also included in this paper for comparison.) The maximum oscillation frequency at these amplitudes was 30 Hz, corresponding to a reduced frequency of $k = 0.6$ at $M_\infty = 0.2$ and $k = 0.2$ at $M_\infty = 0.6$. These parameters are much more representative of the propeller operating environment than those used during the previous experiment [7]. Application of standard correction procedures [11] to this model and wind tunnel generates a correction of $0.54^\circ C_L$ to be added to the angle of attack measurements to approximate free flight. (This correction has not been applied to the results in this paper.) The test conditions at each combination of M_∞ , Λ , and k were either sets of up to 11 mean angles at a fixed amplitude (at the primary conditions), or (at secondary conditions) surveys of three mean angles (above, below, and equal to α_{ss}) at each amplitude.

Table 1 Test matrix
Number of amplitude and mean angle pairs

k	$\Lambda=0$			$\Lambda=15$			$\Lambda=30$		
	$M_\infty = .2$.4	.6	.2	.4	.6	.2	.4	.6
0.075							10		
0.10	9	15	10	11			9	21	18
0.20	25		6				34		13
0.25		9						8	
0.30	9						13		
0.40	9								
0.50							11		
0.60	4						13		

STEADY STATE RESULTS

Steady state pressure distributions were measured at each Mach number and sweep angle, from zero angle of attack to beyond stall. In general the results are in agreement with those expected for a simple subsonic wing. Of most relevance here are the effects of Mach number, sweep angle, and spanwise position on the stall characteristics. Figure 3 shows lift and pitching moment curves for the unswept wing at three Mach numbers for the furthest inboard station, $z/c = 1.5$. (Note that spanwise positions have been referenced to the wing tip to maintain constant values at the different sweep angles.) The stall angle, as determined from the break in the lift and moment curves, drops from 16.5° at $M_c = 0.2$, to 13° at $M_c = 0.4$, and to 10° at $M_c = 0.6$.

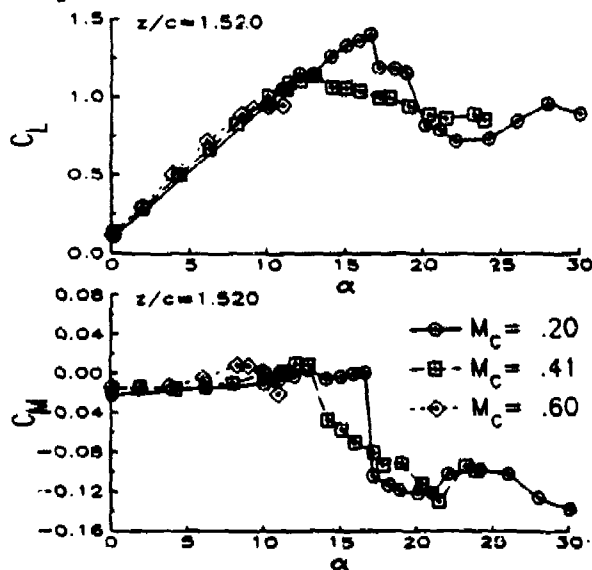


Fig. 3 Mach effects on steady lift and moment at $\Lambda=0$ and $z/c=1.52$.

The standard infinite swept wing normalization was found to collapse C_L to a single curve for the inboard ($z/c \geq 0.3$) stations up to stall and at lower Mach numbers ($M_c < 0.4$). An example is shown in Fig. 4a for $M_c = 0.2$ and $z/c = 1.06$. Above stall, very close to the tip, or at higher Mach number, differences appear that are not accounted for by the simple normalization. For example, the moment at $z/c = 0.08$ (Fig. 4b) shows a gradually increasing negative moment at $\Lambda = 0$ (caused by the tip vortex increasing the suction on the upper surface near the trailing edge), while at $\Lambda = 15$ and 30° the tip vortex effects are much weaker.

The static stall angles were determined from the lift and moment curves at each combination of M_c and Λ . As shown in Table 2, the stall angle is significantly altered by the induced flow of the tip vortex: at $\Lambda = 0$ stall occurs from $\alpha = 2$ to 4° higher at $z/c = 0.3$ than at $z/c = 1.5$. At $z/c = 0.08$ no stall was observed on the unswept wing over the range of tested angles of attack. At higher sweep angles the combination of spanwise flow and the inboard translation (Fig. 1) of the tip trailing edge relative to the leading edge causes the vortex to be quickly convected away. At $\Lambda = 30^\circ$ the variation of the stall angle with spanwise position is less than 1° .

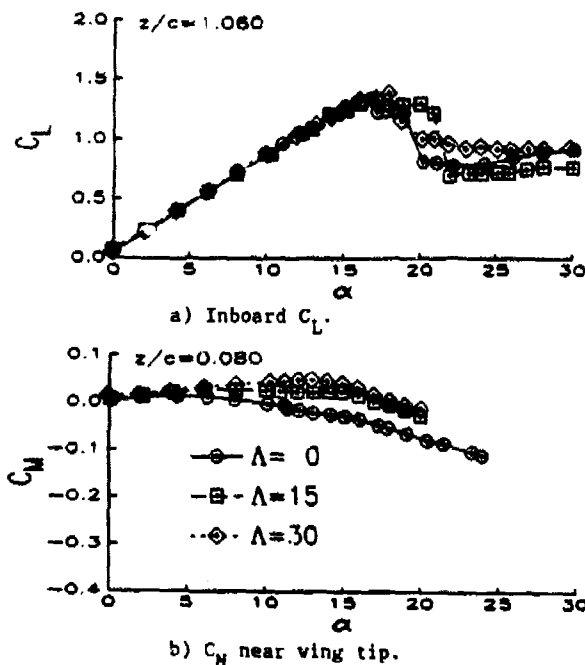


Fig. 4 Sweep effects on steady lift and moment at $M_c=0.2$.

Table 2 Steady-state stall angles

z/c	$\Lambda=0$			$\Lambda=15$			$\Lambda=30$		
	$M_c=.2$.4	.6	.2	.4	.6	.2	.4	.6
1.52	16.5	13	10	17	14.5	18	14	13	8
1.06	17	13.5	10	17	14.5	18	13	13	9
0.59	18	16	10.5	18	14.5	18	13	13	9
0.30	19	17	>11	18	15	18	13	13	9
0.08	>30	>30	>11	18	16	17.5	13	13	9

ATTACHED-FLOW OSCILLATIONS

Small subsonic pitching oscillations that do not include penetration into stall are generally stable. The unsteady component of the flow can usually be described using thin airfoil theory. For the simplest circumstances (two dimensional, inviscid, and incompressible flow) Theodorsen's method [12-13] predicts an unsteady pitching moment about the quarter-chord of

$$C_H = -\alpha_1 k \frac{\pi}{2} [\sin \omega t + \frac{3}{8} k \cos \omega t].$$

The out of phase first harmonic response ($\sin \omega t$) term makes the only contribution to the aerodynamic damping [5], which is therefore $\delta = nk/2$.

An example of an attached flow result of the current experiment is shown in Fig. 5. The conditions are $\alpha = 14^\circ$, $M_c = 0.2$, $\Lambda = 30^\circ$, $k = 0.2$, and $z/c = 0.08$. The mean pressure distribution is smooth, with a strong suction peak of $C_p = -6.8$. Unsteady pressures (not shown) for this condition are characterized by smooth sinusoidal vari-

ations that are in phase with the angle of attack on the lower surface and 180° out of phase on the upper surface. The moment loop is elliptical, and exhibits counterclockwise motion (shown by the arrows), which corresponds to positive damping and stability [5]. The close match between the experimental unsteady moment and the thin airfoil result (the dashed ellipse) is typical of results at lower Mach numbers, lower reduced frequencies and inboard stations. (Note that the experimental mean C_M has been added to the thin airfoil result since the theory predicts a zero steady moment component.)

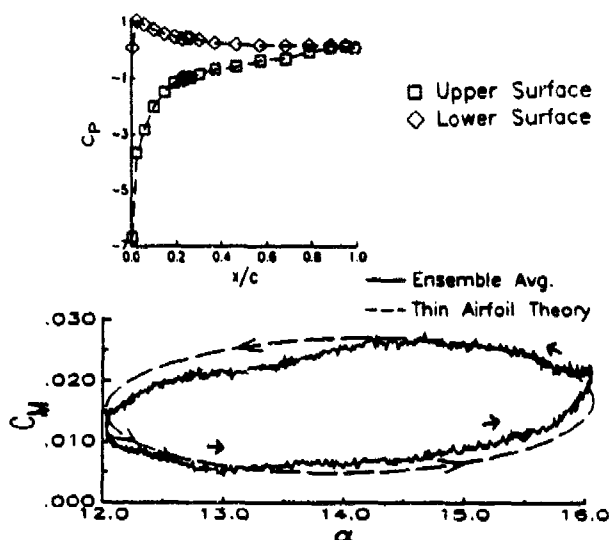


Fig. 5 Mean pressures and moment loop for attached flow at $\alpha = 14 - 2\cos 2\pi t$, $M_c = 0.2$, $k = 0.2$, $\Lambda = 30^\circ$, $z/c = .59$

Measured damping coefficients for several representative attached flow conditions are shown as symbols and dashed lines in Fig. 6. The theoretical prediction ($\pi k/2$) is a straight solid line. The experimental results at $M_c = 0.2$ and 0.4 follow the theory very well for $k \leq 0.4$, for all three amplitudes, but the experimental damping is substantially higher than the theory at $k = 0.6$, perhaps because the straight line wake model is no longer adequate [13]. The experimental damping at $M_c = 0.6$ is also much higher than $\pi k/2$, a likely result of the alteration of the pressure distributions by the presence of local supersonic flow. Very close to the wing tip, at $z/c = 0.08$, the ex-

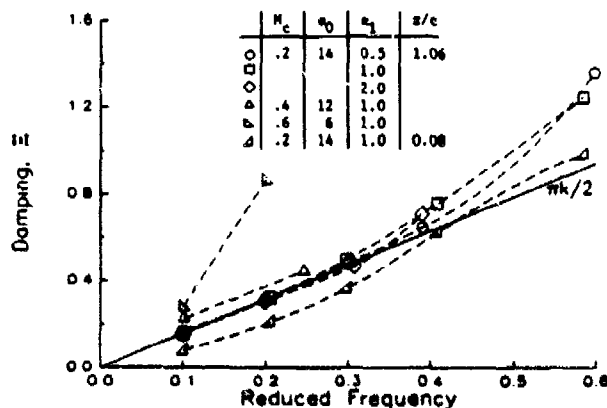


Fig. 6 Attached flow damping coefficients at $\Lambda = 0$.

perimental damping is smaller than the inboard result. These results have demonstrated a relatively wide range of conditions beyond incompressible, two-dimensional flow for which the simple theory continues to give acceptable results. (More sophisticated three dimensional and high subsonic analytical and numerical methods are available to extend Theodorsen's approach.)

OSCILLATIONS NEAR STATIC STALL

The situation changes abruptly when the flow contains substantial separation over a portion of the oscillation. As discussed in Ref. 7, the least stable conditions (the highest negative aerodynamic damping) are small amplitude oscillations centered about the static stall angle. This section will examine such a condition. Figure 7 shows the moment loop and pressure distributions for a 2° amplitude oscillation about the static stall angle of 18° , at $M_c = 0.2$, $k = 0.3$, $\Lambda = 30^\circ$, and $z/c = .59$. ($\Lambda = 30^\circ$ was chosen for clarity because the static stall angle is less dependent on spanwise position, reducing three-dimensional effects.) The experimental moment loop (the solid curve) shows a relatively constant moment ($C_M = -0.05$) during the increase in angle from 16 to 20° , followed by a rapid drop to $C_M = -0.14$ as the angle returns to 19° . The moment then recovers to $C_M = -0.08$ by $\alpha = 16^\circ$. In comparison with the small ellipse predicted by thin airfoil theory (the dotted line), the experimental loop is much larger and in the opposite (clockwise or unstable) sense.

The instantaneous pressure distributions in Fig. 7 illustrate the aerodynamic mechanism. Each is related to the corresponding point on the moment loop by the numbers 1 to 6. Near the start of the cycle, at $t = 0.1$ (#1), the pressure distributions are similar to those in steady attached flow. The high pitch rate allows a suction peak of up to $C_p = -5.8$ to be maintained at angles above static stall (#2). This is the same basic mechanism that generates dynamic lift overshoots during large amplitude motions [9]. Since the instantaneous pitch rate for a sinusoidal oscillation is $A = a_1 k \sin \omega t$, at maximum angle of attack the pitch rate is zero, and attached flow can no longer be maintained. The flow then separates near the leading edge (#3). The separation propagates back along the chord (#4) in the form of a small stall vortex, leading to massive separation by (#5). As the angle of attack drops further, reattachment occurs (#6), and the cycle repeats.

The primary effect of separation is to create a negative (nose-down) moment during the second half of the cycle by removing the suction peak (which had contributed a nose-up moment), and increasing the loading at the trailing edge, (which adds a nose-down moment). The components of a strong instability are therefore: 1) a minimum angle of attack low enough to maintain at least a locally attached flow at the leading edge during the initial portion of the cycle, 2) a pitch rate high enough to delay separation until the maximum angle is nearly reached, 3) a maximum angle high enough so that when the positive pitch rate is removed, the flow separates and remains separated during much of the remainder of the cycle. If the pitch rate is too low, the flow will separate and reattach near α_{st} , and the required hysteresis will not be established. If the maximum and/or minimum

angles are too high, the flow will either separate before the maximum angle is reached, or not reattach. In neither case will the necessary hysteresis be present. Since pitch rate is determined by the combination of frequency and oscillation amplitude, since the minimum and maximum angles are determined by both mean angle and amplitude, and since the static stall angle is determined by Mach number, sweep, airfoil geometry, and three-dimensionality, it is understandable that the experimental damping results exhibit complex dependencies.

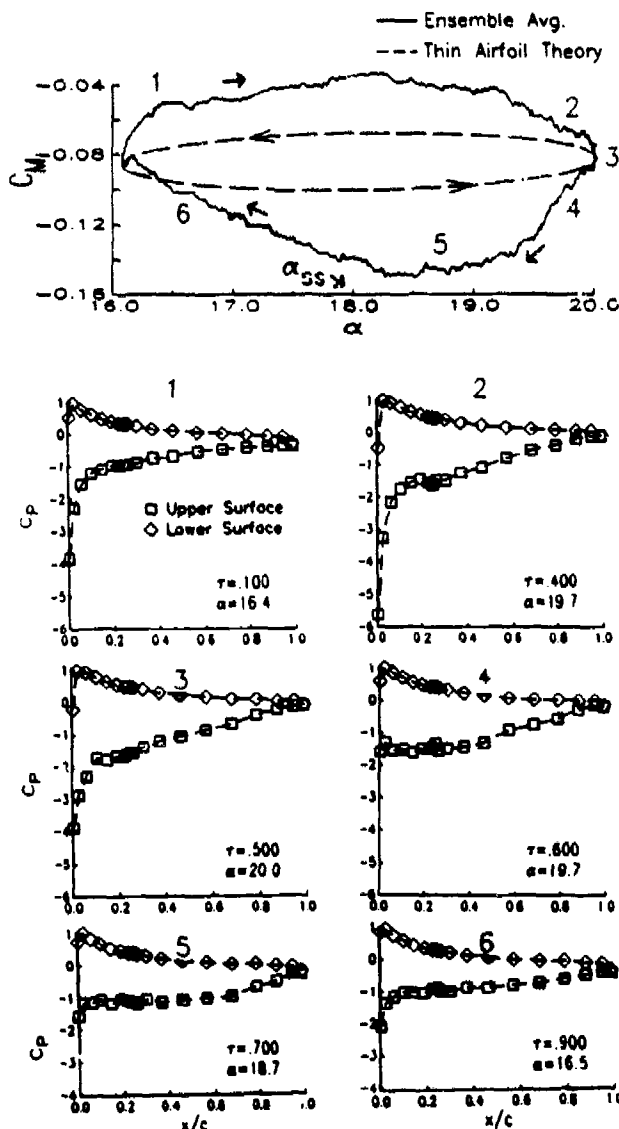


Fig. 7 Moment loop and instantaneous pressures for separating flow at $\alpha = 18 - 2 \cos 2\pi\tau$, $M_c = 0.2$, $k = 0.3$, $\Lambda = 30^\circ$, and $z/c = 0.59$.

MEAN ANGLE AND AMPLITUDE EFFECTS

Both the mean angle and the amplitude have a major influence on the damping. Figure 8 illustrates this using curves of damping vs. mean angle at $k = 0.2$, $M_c = 0.2$, $\Lambda = 30^\circ$, and $z/c = 0.59$ for three amplitudes: $\alpha_1 = 0.5$, 1, and 2° , and, at $k = 0.15$, for $\alpha_1 = 6^\circ$. At the lowest amplitude ($\alpha_1 = 0.5^\circ$) the region of negative damping is narrow and

not very intense. Maximum negative damping values of $\Xi = -0.2$ to -0.5 are typically found in a band approximately 0.5 to 1° wide that ends at $\alpha_o = \alpha_{ss}$. At amplitudes of $\alpha_1 = 1$ and 2° the negative damping band is wider (2 to 4°) and more intense ($\Xi = -1.5$ to -2). At higher amplitudes ($\alpha_1 \geq 6^\circ$) a less intense ($\Xi = -0.5$) band of negative damping covers a 6 to 8° wide region centered about α_{ss} . At all amplitudes considered here, the damping below the initial penetration into stall approaches a common value close to $\pi k/2$. The qualitative characteristics described here were also observed during the earlier experiment (cf. Fig. 9 in [7]). Both sets of data indicate that the most unstable motions are 1 - 2° amplitude oscillations centered about α_{ss} .

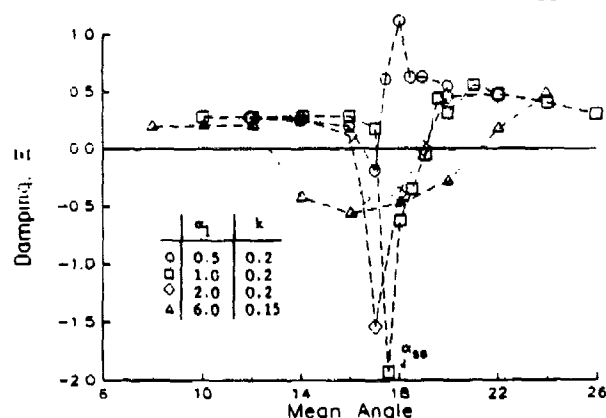


Fig. 8 Damping vs. mean angle at several amplitudes for $M_c = 0.2$, $k = 0.2$, $\Lambda = 30^\circ$, and $z/c = 0.59$.

Once the flow remains massively separated throughout the cycle, the damping is positive, and approaches a value slightly higher than in attached flow. This similarity between two very different flow regimes is somewhat surprising and worthy of further examination. The damping computed for the attached potential flow stems from three primary assumptions: a) vorticity is shed from the trailing edge to maintain zero net circulation as the lift varies; b) a Kutta condition is satisfied at the trailing edge; and c) an undistorted straight wake is convected downstream from the trailing edge at the freestream velocity.

The applicability of these three assumptions to small amplitude motions in separated flow will now be examined. a) As shown in Fig. 9, lift variations of similar magnitude occur in both attached ($\alpha = 16^\circ$) and separated ($\alpha = 22^\circ$) conditions. Vorticity must therefore still be shed into the wake (although the shedding may not be restricted to the trailing edge). The 'quasi-steady' lift variation (the α -dependent response obtained by averaging the increasing and decreasing pitch halves of the cycle) is reduced at $\alpha = 22^\circ$. This is compensated for by increased hysteresis (the minor axis of the

Expressions of this condition include finite trailing edge velocities, surface streamlines that are bounded by the airfoil trailing edge angles, a smooth approach to zero pressure difference between the upper and lower surfaces, and an 'extended Kutta condition,' [14], that relates the difference in the upper and lower surface velocities to the time derivative of the circulation.

ellipse is larger). b) The unsteady pressure results from the current experiment, as well as results [15] for a massively separated airfoil subject to flow angle oscillations at frequencies between $k = 0.5$ and 6.4 , indicate that the unsteady pressures smoothly approach a common value at the trailing edge, satisfying at least one form of Kutta condition. c) An undistorted wake geometry is the least plausible assumption. Even in attached flow, the wake distorts significantly from a straight line at high frequencies or large amplitudes. In massively separated flows vorticity is shed not in a thin wake emanating from the trailing edge, but throughout a broad region starting at the forward separation point.

It appears that even though there are violations in detail of the assumptions underlying the potential flow damping calculation, the fundamental similarities of shed vorticity and satisfaction of a trailing edge condition are sufficient to generate damping values similar to attached flow.

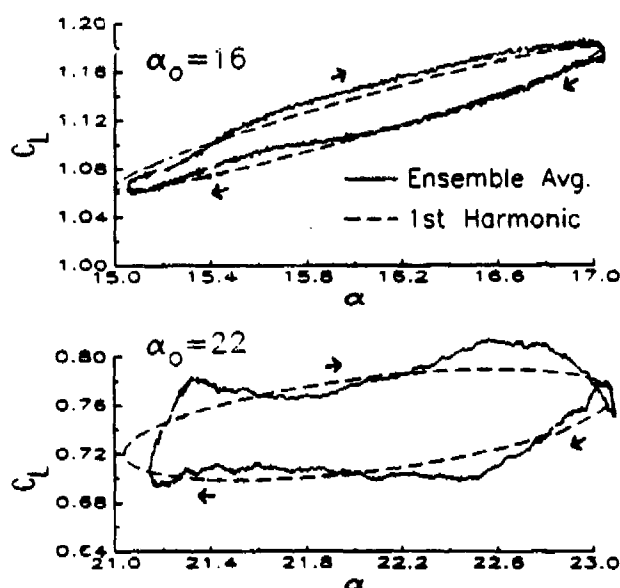


Fig. 9 Lift loops in attached ($\alpha_0 = 16$) and separated ($\alpha_0 = 22$) flow at $\alpha = \alpha_0 - 1 \cos 2\pi t$, $M_c = 0.2$, $k = 0.2$, $\Lambda = 30^\circ$, and $z/c = 0.59$.

FREQUENCY EFFECTS

Increasing the reduced frequency of attached flow oscillations was shown previously (Fig. 6) produce a consistent and benign increase in damping. Such consistency is not present for unstable oscillations about the stall angle. This is illustrated in Fig. 10, which shows maximum negative damping coefficients plotted versus k . Each point represents the maximum measured negative damping over all values of α for a given combination of α_1 , z/c , Λ , and M_c . Separate symbols are provided only for the different values of Λ . Figure 10 is not intended to provide comprehensive quantitative information, it is instead intended to illustrate trends: a) For all reduced frequencies, damping coefficients of $\Xi \leq -1$ could be found for some com-

binations of α_1 and α_2 . b) The negative damping is generally weakest ($\Xi \approx -1$) at $k = 0.1$, when the unsteady hysteresis is low. c) The maximum negative damping is increased at $k = 0.2-0.3$ ($\Xi \approx -1.5$ to -2). d) For $k = 0.4, 0.5$, and for most of the $k = 0.6$ data, the damping returns to $\Xi \approx -1.5$.

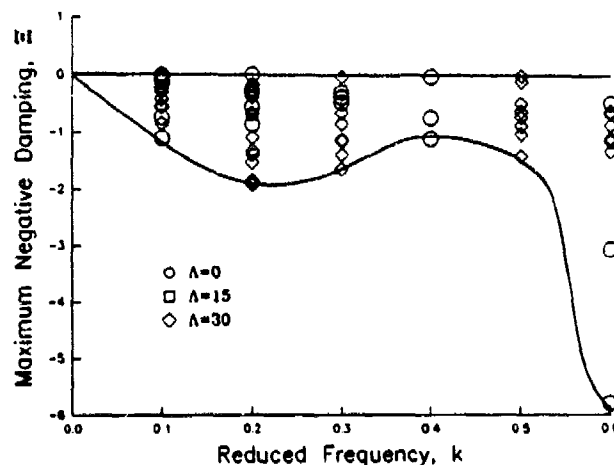


Fig. 10 Maximum negative damping coefficients as a function of reduced frequency.

A somewhat different mechanism is involved in producing the very strong negative damping ($\Xi = -3$ and -5.8) measured at $k = 0.6$ and $\Lambda = 0$ (Fig. 10). At this frequency the maximum pitch rate is high enough ($A = 0.01$ for $\alpha_1 = 1^\circ$) to generate a substantial stall vortex. If the dynamics are similar to those at large amplitude [9], the vortex forms near $x_{sep}/c = 0.15$ and convects downstream at a velocity, $V = 0.3U_\infty$. It will therefore remain above the airfoil for a time of approximately

$$\Delta t = \Delta x/V, \text{ or } \Delta \tau = \frac{k}{2\pi} \frac{[1 - x_{sep}/c]}{V/U_\infty} \approx 0.3.$$

The effect of the stall vortex on the pressure distributions is shown in Fig. 11. Separation occurs after $\tau = 0.4$, and by $\tau = 0.8$ the vortex is above the trailing edge, generating large trailing edge suction and a nose-down moment and exacerbating the instability.

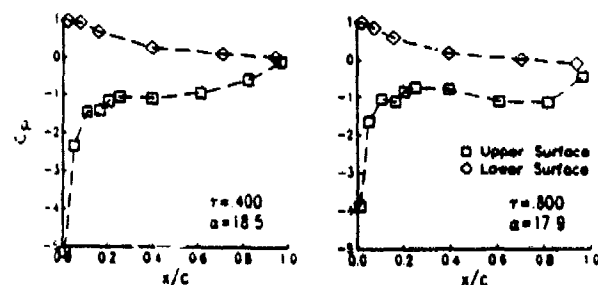


Fig. 11 Instantaneous pressure distributions showing the effect of a strong stall vortex at $M_c = 0.2$, $k = 0.6$, $\Lambda = 0$, $z/c = 1.52$, and $\alpha = 18 - 0.5 \cos 2\pi t$.

MACH NUMBER EFFECTS

In attached flow (Fig. 6) the damping at $M_c = 0.4$ is very similar both to the $M_c = 0.2$ data and to incompressible theory, while the damping at $M_c = 0.6$ is larger. As illustrated in Fig. 12, it is difficult to identify such a clear dependence on Mach number for the maximum negative damping in separated flow. As in Fig. 10, each point represents the maximum over a range of α at a particular combination of α , z/c , Λ , and k . The data are for $k = 0.1$ and 0.2 . The principal conclusion drawn from Fig. 12 is that maximum negative values of $\Xi = -1$ to -2 occur at all studied Mach numbers.

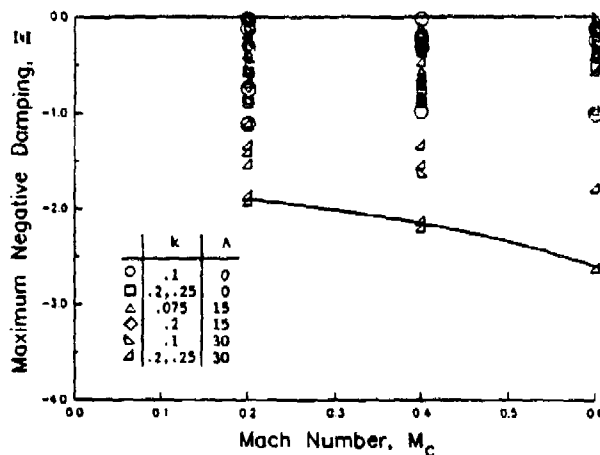


Fig. 12 Maximum negative damping coefficients as a function of Mach number.

The mechanism for instability at higher Mach number is fundamentally the same as at lower Mach number. The details of the pressure distributions are, however, different. Figure 13 shows pressures at two instants during an $\alpha = 15 \pm 2^\circ$ oscillation at $k=0.25$, $\Lambda = 30^\circ$, and $M_c = 0.4$. There is a small region of mild supersonic flow ($C_p < C_{p^*}$) near the leading edge at $\tau = 0.2$. The flow separates over the forward 40% of chord at $\tau = 0.4$, and reattaches by $\tau = 0.8$ (not shown). Except for a reduction in the chordwise extent of the separation, these results are similar to those at $M_c = 0.2$ (Fig. 7).

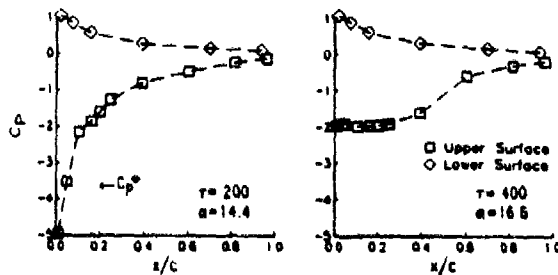


Fig. 13 Instantaneous pressure distributions for separating flow at $M_c=0.4$, $k=0.25$, $\Lambda=30^\circ$, $z/c=1.06$, and $\alpha=15-2\cos 2\pi\tau$.

At $M_c = 0.6$ there is a sizable supersonic region in high angle of attack attached flow, as shown in Fig. 14, for $\alpha = 9 \pm 1^\circ$ at $k=0.2$. For $\tau \leq 0.2$ a maximum local chordwise Mach number of 1.5 is attained in a region that covers the front 20% of the chord. The region is terminated by a strong shock. A nose-up moment is created since the shock is ahead of $x/c = 0.25$. (This positive moment is also present in steady flow, Fig. 3.) At $\tau = 0.5$ the flow has separated, and the shock is replaced by a region of highly random flow having (on average) a linear pressure gradient between $x/c = 0.05$ and 0.6 . This change creates a nose-down moment. The flow reattaches near $\tau = 0.9$.

In terms of the moment loops, the detailed differences between the pressures at different values of M_c primarily alter the quasi-steady and higher harmonic components. As shown in Fig. 15, the first harmonic response at $M_c = 0.4$ and 0.6 shows a clockwise loop with substantial hysteresis, similar to the results at $M_c = 0.2$. Since the damping depends only on the first harmonic, the damping is also similar: $\Xi = -1.3$, -1.4 , and -1.0 at $M_c = 0.2$, 0.4 , and 0.6 , respectively. The higher harmonic portion of Fig. 15 differs from the $M_c = 0.2$ results. These differences are caused both by the

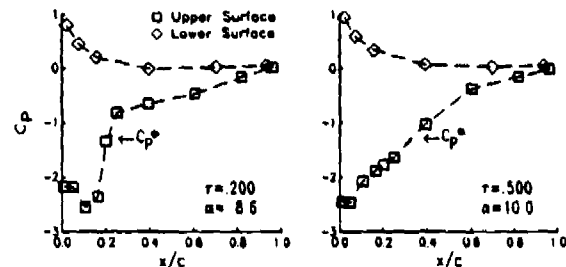


Fig. 14 Instantaneous pressure distributions for separating flow at $M_c=0.6$, $k=0.2$, $\Lambda=30^\circ$, $z/c=1.06$, and $\alpha=9-1\cos 2\pi\tau$.

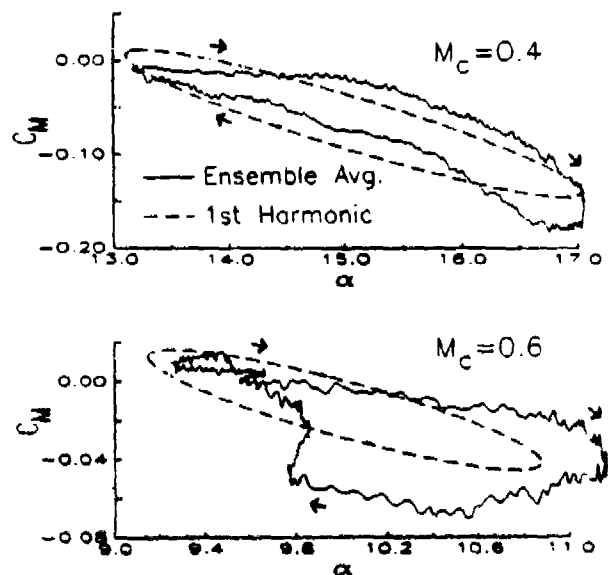


Fig. 15 Moment loops at $M_c=0.4$ and 0.6 . Test conditions are as in Figs. 14 and 15.

aerodynamics and by the distortion of the pitching waveform at higher frequency. It must be recognized that even though the strength of the instability is similar over the Mach number range studied, it occurs at much lower angles of attack at higher Mach number, simply because the steady stall angle is lower (Table 2).

A second Mach effect may develop at higher reduced frequencies ($k \geq 0.6$). At large amplitude compressibility weakens the dynamic stall vortex [9]. If a similar weakening occurs at small amplitudes, the high negative damping observed at $k = 0.6$ and $M_\infty = 0.2$ may not be present for $M_\infty \geq 0.4$. (No data for such conditions could be obtained by this experiment.)

SWEEP AND 3-DIMENSIONALITY EFFECTS

The fundamental requirement for negative damping is that the angle of attack passes through the steady stall angle during the cycle. It is thus not surprising that the differences in α_{ss} with spanwise position and sweep angle (Table 2) have a substantial influence on the local damping. Results for the unswept wing will be discussed first. Figure 16a shows curves of damping vs. z/c for several values of α_0 at $\Lambda = 0$, $M_\infty = 0.2$, $k = 0.2$, and $\alpha_1 = 1^\circ$. The filled-in symbols indicate when $\alpha = \alpha_{ss}(M_\infty, \Lambda, z)$. As α_0 is increased, negative damping first occurs inboard (at $\alpha = 16.6^\circ$), and then moves outboard (to $z/c = 0.30$ at $\alpha_0 = 22^\circ$). The region near the tip has a lower effective angle of attack because of the tip vortex. The entire wing is never simultaneously unstable, because the inboard region has returned to positive damping before the outboard region stalls. The maximum instability lags the α_{ss} by approximately 1° . The station closest to the tip ($z/c = 0.08$) never stalls, and always has positive damping.

Results for equivalent conditions at $\Lambda = 15^\circ$ are shown in Fig. 16b. The instability again begins inboard, but for $\alpha_0 = 18$ and 19° the entire region outboard of $z/c = 1$ is unstable. The maximum instability lags approximately 1° behind α_{ss} . At $\Lambda = 30^\circ$ (Fig. 16c) the entire wing has negative damping for $17 \leq \alpha_0 \leq 19^\circ$, a much more general instability than at lower sweep angles. The influence of the tip vortex is much weaker so that the local effective angles of attack are more uniform. The $z/c = 0.08$ station has significant negative damping. Further, the maximum negative damping is increased at all spanwise stations, and the lag of the maximum behind α_{ss} is reduced or eliminated. These may be results of the simultaneity of stall intensifying the local instabilities observed with no sweep.

MIDCHORD MOMENTS AND DAMPING

The preceding discussion has been concerned with the damping coefficient computed using the pitching moment about $x/c = 0.25$. This was the model axis of rotation and the aerodynamic center of the SSC-A09 airfoil. However, the elastic axis for many propeller and turbomachinery blades is near $x/c = 0.50$. Therefore damping information for midchord oscillations would be quite useful. Since the axis of rotation of our apparatus could not be moved, this section attempts to extrapolate from quarterchord results using previous analytical and

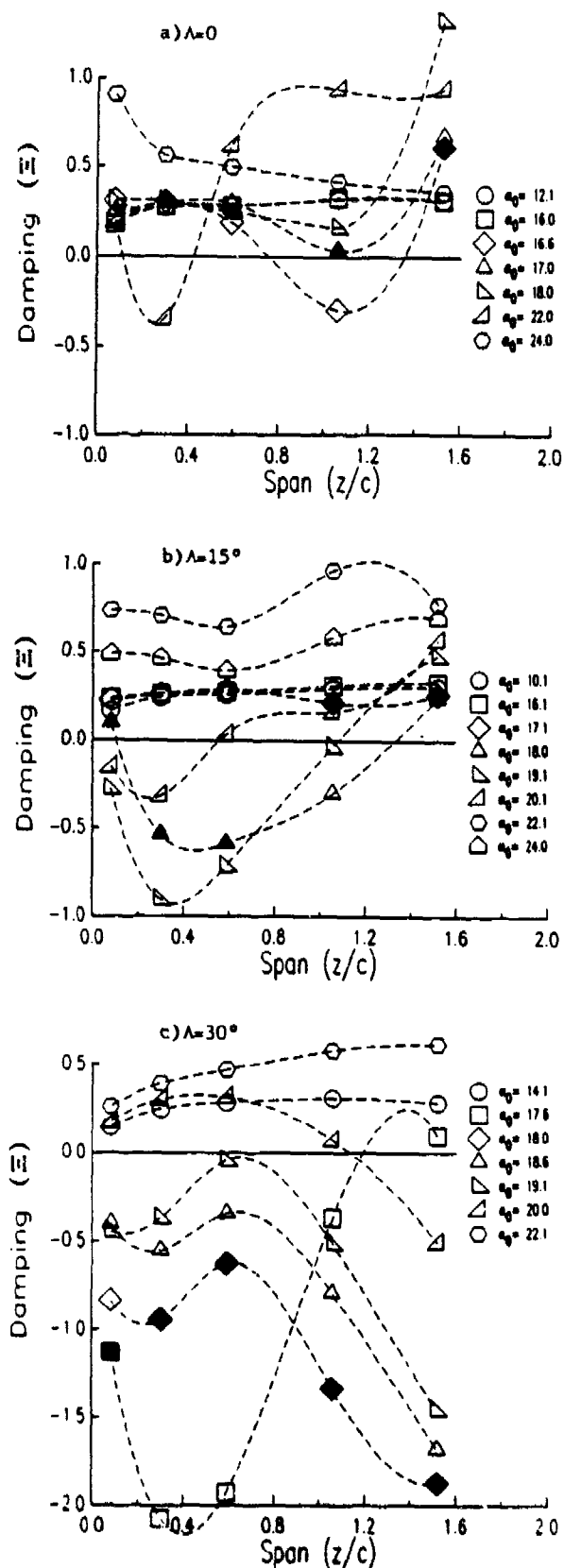


Fig. 16 Damping coefficients vs. spanwise position for several mean angles, at $\alpha = \alpha_0 - 1 \cos 2\pi \tau$, $M_\infty = 0.2$, and $k = 0.2$.

experimental results. In order to estimate the effects of changing the axis, the influence of two factors must be considered. The first is the reference point about which the moment is computed. The second is the actual axis of rotation.

The change in reference point adds $\Delta x/c = 0.25$ times the normal force coefficient to the instantaneous quarterchord C_n . The quasi-steady effect is to generate a moment that increases linearly with α prior to stall. In unsteady attached flow the effect is to reduce the positive damping, since normal force and lift loops generally have a clockwise sense, as shown in Fig. 9. The addition of a lift component is reflected in the analytical expression for the pitching moment [13] by the introduction of additional terms proportional to $C(k)$, the Theodorsen lift deficiency function [12]. The attached flow damping for oscillations about $x/c = 0.25$, using the moment referenced to $x/c = 0.5$ is:

$$\Xi_{.25,.50} = 0.5\pi (k(0.5 - F(k)) - G(k)),$$

where F and G are the real and imaginary parts of $C(k)$. Since $G(k)$ is negative, and $F(k)$ is between 0.5 and 1.0, the theoretical $\Xi_{.25,.50}$ will always be positive.

The corresponding attached flow damping coefficient for oscillations about $x/c = 0.50$ using the moment referenced to $x/c = 0.50$ is:

$$\Xi_{.50,.50} = 0.5\pi (0.5k(1.0 - F(k)) - G(k)).$$

The three analytical damping coefficients are shown in Table 3 at several reduced frequencies. While all three indicate stability, there are sizable differences in the values, particularly at higher k , where $\Xi = 1.57k$, $\Xi_{.50,.50} \rightarrow 0.4k$, and $\Xi_{.25,.50} \rightarrow 0$. Pitch axis and moment reference locations are thus both significant for computing quantitative attached flow damping.

Table 3 Computed attached flow damping

k	Pitch about $x/c = .25$		Pitch about $x/c = 0.50$
	Ξ	$\Xi_{.25,.50}$	$\Xi_{.50,.50}$
0.1	0.16	0.23	0.30
0.2	0.31	0.21	0.32
0.4	0.63	0.13	0.32
0.6	0.94	0.11	0.38
1.0	1.57	0.09	0.51

The effects of changing the moment reference point to midchord and recomputing the damping for the current experiment are illustrated in Fig. 17 for the same condition ($M_\infty = 0.2$, $k = 0.2$, $\Lambda = 30^\circ$) used in Fig. 8. The primary changes are a reduction in the attached flow damping (in agreement with Table 3), an earlier onset (by $\leq 1^\circ$) of negative damping, a small increase in the maximum negative damping, a broadening of the negative damping region above α_{ss} , and a reduction in the positive damping in post-stall region. In general, changing the moment reference to midchord makes the aerodynamic damping more negative, but does not change the essential character of the phenomenon.

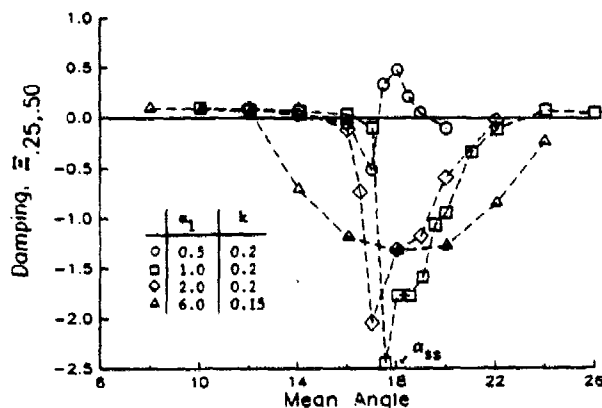


Fig. 17 Damping coefficient based upon midchord moment vs. mean angle, at several amplitudes for $M_\infty = 0.2$, $k = 0.2$, $\Lambda = 30^\circ$, and $z/c = 0.59$.

The effects of moving the rotation axis in separating flow have been studied previously at large amplitude. Ham and Garelick [16] reported that the maximum unsteady airload increments (and hence the strength of the stall vortex) were not seriously changed by moving the pitch axis between $x/c = -.25$ and $+.75$. Stall was delayed the longest with the axis at the leading edge, and least with the axis at $x/c = 0.75$. In contrast, the more recent experiment of Helin and Walker [17] found that an aft axis location delayed dynamic stall and strengthened the vortex. The theoretical and analytical work of Jumper, et al. [18] and the computational results of Visbal [19] indicate that at moderate pitch rates ($\Lambda \leq 0.025$) moving the pitch axis aft delayed stall, but did not appreciably change the unsteady airloads.

The consensus appears to be that for moderate pitching rates aft motion of the pitching axis will delay stall but leave the basic phenomenon relatively untouched. This implies that damping coefficients for motion about midchord should be similar to the quarter-chord results, but the mean angles of attack for maximum negative damping may be several degrees higher.

CONCLUSIONS

The primary results of this study of small amplitude pitching motions of a three-dimensional wing model are:

1) The aerodynamic damping is positive for all studied motions where the instantaneous angle of attack always remains below the steady stall angle, α_{ss} . For $k \leq 0.4$ and $M_\infty \leq 0.4$, the damping agrees with the results of incompressible thin airfoil theory, $\Xi = \pi k/2$. At higher frequencies or at $M_\infty = 0.6$, the damping is higher than $\pi k/2$. Very close to the wing tip, the damping is lower.

2) Small amplitude oscillations that include α_{ss} are usually unstable. The conditions for strong negative damping ($\Xi < -1$) include a positive pitch rate that delays stall beyond α_{ss} , a maximum angle high enough to cause separation, and a minimum angle low enough to permit reattachment. The strongest negative damping was observed for 1 to 2° amplitude oscillations centered about α_{ss} , at reduced frequencies of $k \geq 0.2$.

3) For $k = 0.6$, the dynamic stall vortex is strong enough at low amplitude to significantly increase the trailing edge loading. This generates a strong transient nose-down moment and increases the negative damping to $\Xi \leq -3$.

4) In fully separated flow the damping is positive, and somewhat larger in magnitude than in attached flow. This implies a degree of independence between the periodic, mean, and random flow fields.

5) Only differences in detail were observed between the $M = 0.2$, 0.4 , and 0.6 results; the fundamental aerodynamic mechanism leading to negative damping is unchanged.

6) Sweep and spanwise position alter the aerodynamic damping primarily through changes in the local steady stall angle. For the unswept wing, stall and regions of negative damping occur at lower mean angles on the inboard portion of the wing (one chord or greater from the tip). As mean angle increases, stall moves outboard. Negative damping was never observed at the same instant over the entire wing. However, at $\Lambda = 30^\circ$, the wing stalled over its entire span within an angle of attack range of 1° . At $M = 0.2$, damping was negative over the entire span for a 2° wide band centered at the static stall angle (18°).

In summation, this experiment has verified that torsional instability near stall occurs at realistic scales, and over a wide range of conditions. The underlying aerodynamic mechanism is sufficiently basic that negative aerodynamic pitch damping is possible whenever the local angle of attack is close to the local steady stall angle. Actual flutter will occur only if an initial excitation is present and if the structural natural frequency, stiffness, and damping permit. If the wing (or blade) is designed so that the stall angle varies sufficiently over its span (as was true for the unswept model here), it may be possible to avoid global instabilities.

ACKNOWLEDGMENTS.

This research was funded by the NASA Lewis Research Center, as part of U.S. Army Research Office Contract DAAL03-89-C-0013. The authors would like to thank Alfred Covino for instrumenting the model and operating the data acquisition system during the test. We also thank John Ayer and the UTRC wind tunnel staff for their assistance.

REFERENCES

1. Baker, J.E., "The Effects of Various Parameters, Including Mach Number, on Propeller-Blade Flutter, with Emphasis on Stall Flutter," NACA RML50L12b, 1950; reissued as NACA TN3557, 1955.
2. Fanti, R., Carta, F.O., and Pitt, W.R., "Stall Flutter Characteristics of Several 16-Series Cantilevered Airfoil Models," United Aircraft Corporation Research Department Report R-23624-2, East Hartford, CT, May 1954.
3. Lemnios, A.Z., "Aerodynamic Damping Tests of Propeller Blade Airfoil Sections," United Aircraft Corporation Research Department Report R-0997-1, East Hartford, CT, Oct. 1957.

4. Ham, N.D., "Stall Flutter of Helicopter Rotor Blades: A Special Case of the Dynamic Stall Phenomenon," Journal of the American Helicopter Society, Vol. 12, No. 4, Oct 1967.
5. Carta, F.O., and Niebanck, C.F., "Prediction of Rotor Instabilities at High Forward Flight Speeds. Volume III. Stall Flutter." USAAVLABS TR 68-18C, Ft. Eustis, VA, Feb. 1969.
6. McCroskey, W.J., and Pucci, S.L., "Viscous Inviscid Interaction on Oscillating Airfoils in Subsonic Flow," AIAA paper 81-0051, Jan. 1981.
7. Carta, F.O., and Lorber, P.F., "Experimental Study of the Aerodynamics of Incipient Torsional Stall Flutter," Journal of Propulsion and Power, Vol. 3, March-April 1987, pp. 164-170.
8. Marcolini, M.A., Lorber, P.F., Miller, W.T., and Covino, A.F. Jr., "Frequency Response Calibration of Recess-Mounted Pressure Transducers," Instrumentation Society of America 37th Annual Instrumentation Symposium, San Diego, CA, May 1991.
9. Lorber, P.F., and Carta, F.O., "Airfoil Dynamic Stall at Constant Pitch Rate and High Reynolds Number," Journal of Aircraft, Vol. 25, June 1988, pp. 548-556.
10. Lorber, P.F., Covino, A.F. Jr., and Carta, F.O., "Dynamic Stall Experiments on a Swept Three-Dimensional Wing in Compressible Flow," AIAA Paper 91-1795, 22nd Fluid Dynamics, Plasma Dynamics, and Lasers Conference, Honolulu, HI, June 1991.
11. Rae, W.H., and Pope, A., Low-Speed Wind Tunnel Testing, 2nd Edition, John Wiley & Sons, NY 1984.
12. Theodorsen, T., General Theory of Aerodynamic Instability and the prediction of Flutter, NACA Report 496, 1935.
13. Bisplinghoff, R.L., Ashley, H., and Halfman, R.L., Aeroelasticity, Addison-Wesley, Reading, MA, 1955.
14. Sears, W.R., "Unsteady Motion of Airfoils with Boundary Layer Separation," AIAA Journal, Vol. 14, 1, pp. 57-63, Jan. 1976.
15. Covert E.E., Lorber, P.F., and Vaczy, C.M., "Flow Separation Induced by Periodic Aerodynamic Interference," Proceedings of the AFOSR/FJSRL/U. Colorado Workshop on Unsteady Separated Flows, Aug. 1983.
16. Ham, N.D., and Garelick, M.S., "Dynamic Stall Considerations in Helicopter Rotors," Journal of the American Helicopter Society, Vol. 13, No. 2, April 1968, pp. 49-55.
17. Helin, H.E., and Walker, J.M., "Interrelated Effects of Pitch Rate and Pivot Point on Airfoil Dynamic Stall," AIAA Paper 85-0130, Jan. 1985.
18. Jumper, E.J., Dimmick, R.L., and Allaire, A.J.S., "The Effect of Pitch Location on Dynamic Stall," Forum on Unsteady Flow Separation, FED - Vol. 52, The American Society of Mechanical Engineers, New York, 1987, pp. 201-208.
19. Visbal, M.R., "On Some Physical Aspects of Airfoil Dynamic Stall," ASME Symposium on Non-Steady Fluid Dynamics, Toronto, Canada, June 1990.

APPENDIX V

DYNAMIC STALL EXPERIMENTS ON A SWEEP THREE-DIMENSIONAL WING IN COMPRESSIBLE FLOW

Peter F. Lorber*, Alfred F. Covino Jr., and Franklin O. Carta†
United Technologies Research Center
East Hartford, CT 06108

ABSTRACT

An experiment has been performed to investigate the transient aerodynamic response of a three-dimensional wing undergoing pitching motions to angles of attack above static stall. The experimental parameters included sweep angles of 0, 15, and 30°, Mach numbers from $M_c = 0.2$ to 0.6, and pitch rates from $\dot{\alpha}/2U_c = 0.001$ to 0.025. Data were obtained from 112 surface pressure transducers for steady flow, sinusoidal oscillations, and constant rate ramps. This paper describes the experiment and discusses the dependence of the aerodynamic loads on the test parameters. Where conditions overlap, the current results were found to be consistent with previous work. Significant quantitative changes in the dynamic stall process were, however, observed upon the introduction of higher Mach number, three-dimensionality, and sweep. Of particular interest were the effect of locally supersonic flow on stall inception, and the interactions between the tip vortex and the stall vortex.

NOMENCLATURE

A	pitch rate, $\dot{\alpha}/2U_c$
c	airfoil chord
C_D	section pressure drag coefficient, D/qc
C_L	section lift coefficient, L/qc
C_L^{max}	maximum lift coefficient
C_M	section $\frac{1}{4}$ chord moment coefficient, M/qc^2
C_P	pressure coefficient, $(P - P_\infty)/q$
C_P^*	pressure coefficient for locally sonic chordwise velocity
k	reduced frequency, $\omega c/2U_c$
M_c	chordwise Mach number, $M_\infty \cos \Lambda$
M_∞	freestream Mach number
P_∞	freestream static pressure
q	dynamic pressure, $\frac{1}{2}\rho_\infty U_c^2$
QS	quasisteady load coefficient
t	time
T	oscillation period
Re	Reynolds number, cU_c/ν
U_c	chordwise component of freestream velocity, $U_\infty \cos \Lambda$
U_∞	freestream velocity
v	velocity of vortex propagation along chord
x	distance along chord from leading edge
z	distance along span from tip leading edge

* Research Engineer. Member AIAA.

** Leader, Electronic Technicians.

† Supervisor, Experimental and Analytical Aeromechanics. Associate Fellow AIAA.

Copyright ©1991 by United Technologies Corporation.
Published by the American Institute of Aeronautics and
Astronautics, Inc., with permission.

$\dot{\alpha}$	pitch rate, rad/sec
α	geometric angle of attack
	$\alpha = \alpha_{min} + 2(\tau - 0.125)(\alpha_{max} - \alpha_{min})$
α_s	unsteady stall angle
α_{ss}	steady state stall angle
Λ	sweep-back angle
ν	kinematic viscosity
ρ_∞	freestream density
τ	nondimensional time, t/T
ω	circular frequency, $2\pi/T$

INTRODUCTION

Dynamic stall has been extensively studied by numerous researchers using a wide variety of experimental, analytical, and computational techniques.¹⁻¹⁸ Various methods, such as force balances,¹⁴ flow visualization,^{6,7-9,12} interferometers,¹⁰ laser velocimeters, and surface pressure transducers^{1-6,11,13} have been used to measure characteristics of the flow field and loads on the aerodynamic surfaces. Model geometries and test conditions have been quite diverse. Models have included two-dimensional (2D) airfoils,^{1-3,8-11,13} three-dimensional (3D) wings,^{4-5,12} and complex multi-element configurations.⁷ Test conditions are defined by the parameters that quantify the relative motion between the surface and the fluid: Mach number, Reynolds number, type of unsteadiness (plunging, pitching, or translation), waveform (sinusoid, constant-rate ramp, or arbitrary), amplitude, and frequency (or pitch rate). Each study usually concentrates on a relatively small region of this multi-dimensional space. The listed references provide a selection of recent work, and illustrate the considerable information that has been uncovered. A unified picture of the inception and progression of dynamic stall that encompasses conditions of both practical and academic interest has, however, still not been developed.

The present experiment is concerned with a sizable, but still limited, subset of dynamic stall. The geometry was a rectangular semi-span wing pitching about its quarter chord. The approach was to measure surface pressures at 112 locations and integrate to obtain the aerodynamic force and moment at five spanwise stations, within 1.6 chord lengths of the tip. The objective was straightforward: to examine in a single experiment the influence on the aerodynamic loads of Mach number, frequency, waveform, and wing sweep. The experiment was conducted at physical scales representative of practical applications such as helicopter rotors or maneuvering aircraft.

Test Mach numbers ranged from $M_c = 0.2$ to 0.6, sweep angles from $\Lambda = 0$ to 30°, and pitch rates from $A = 0.001$ to

0.025. The model chord was typical of a full-scale helicopter main rotor, and resulted in Reynolds numbers of 2 to 6×10^6 . The appropriateness of these conditions was confirmed by a recent wind tunnel test of a pressure-instrumented model helicopter rotor.¹⁹ For moderate speed forward flight, dynamic stall occurred on the inboard region of the rotor blade at local pitch rates between $\Lambda = 0.01$ and 0.015 and Mach numbers between 0.2 and 0.4 . Qualitative features of stall were very similar to oscillating airfoil results.²⁰⁻²¹

This paper describes the experiment and discusses the dependence of the surface pressures and aerodynamic loads (lift, pitching moment, and pressure drag) on the test parameters. This work is part of a continuing research program. Unswept tunnel-spanning wing (2D) results for this model have been presented in Refs. 20-21. Computational simulations of the 2D experiment were described in Refs. 15-16. An earlier version of the UTRC oscillating wing was tested in a swept 2D configuration.¹⁻² A complementary study is also being conducted of small amplitude oscillations, with application to the torsional stall flutter of propeller blades.²² Full documentation will be provided in a final contract report.²³

DESCRIPTION OF EXPERIMENT

The model was a straight, rectangular, untwisted, semi-span wing of 17.3 in. (44 cm) chord and 48 in. (122 cm) span (Fig. 1). The aspect ratio of a full wing would be 5.6 . The wing consisted of a steel spar and fiberglass airfoil panels, and had a Sikorsky SSC-A09 9% thickness cambered airfoil section (Fig. 2). Airfoil coordinates have been provided in Ref. 21. The majority of the data were acquired with a tip cap rounded into an approximate body of revolution. Limited data were also acquired using a square tip cap. The wing was mounted at sweep angles of 0 , 15 , and 30° from the side wall of the 8 ft (2.4 m) octagonal test section of the UTRC Large Subsonic Wind Tunnel. Additional airfoil panels were added to the spar at higher sweep angles in order to keep the wing tip $\frac{1}{4}$ chord at the tunnel centerline (Fig. 1). At $\Lambda = 30^\circ$ the span was thus increased to 55 in., an aspect ratio of 6.4 .

Application of standard wind tunnel wall correction procedures²⁴ to this geometry produces a small correction of $\Delta\alpha = 0.54^\circ \times C_L$ to approximate free flight. (This correction was not applied in this paper.) A minimal gap of $0.005c$ was maintained between the wing root and the wind tunnel wall at $\Lambda = 0$. The maximum gaps in the swept configuration were larger (up to $0.02c$) and varied with α . Oil visualization in steady-state showed the primary effect of the wall on the surface flow vectors to be a corner vortex which covered a triangular region having an extent at the trailing edge of $0.2c$. Beyond this region, the oil pattern did not show obvious wall influence.

A hydraulic rotary drive was used to oscillate the model in pitch about the line connecting the root and tip $\frac{1}{4}$ chord. Two pitching waveforms were used, sinusoids and ramps. The ramps began at a steady-state condition (typically $\alpha = 0$), increased at constant rate to a maximum angle, main-

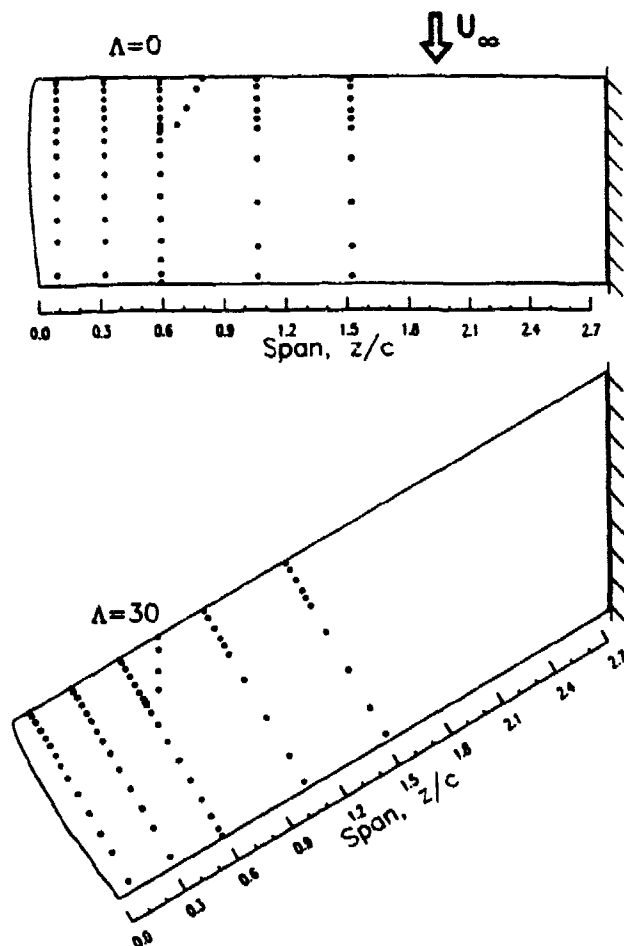


Fig. 1 Wing planforms and upper surface transducer locations.

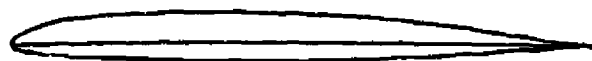


Fig. 2 SSC-A09 airfoil section.

tained that maximum for a short time, and then returned to the initial condition. A time delay of $2-4$ sec was imposed between ramps to regain steady-state. The sufficiency of the time delay was verified using an unsteady pitot-static probe located $2.8c$ above the tip $\frac{1}{4}$ chord. The sinusoids were performed at frequencies from 1.25 to 12 Hz ($0.025 \leq k \leq 0.15$), at amplitudes primarily of 6 and 10° , and at numerous mean angles. The maximum ramp angles were 30° at $M_c = 0.2$ and 0.3 , 20 or 25° at $M_c = 0.4$, 16 or 18° at $M_c = 0.5$, and 10 , 12 , or 13.5° at $M_c = 0.6$. The upper limits for the ramps were determined by the stall characteristics and structural loads at each Mach number and sweep angle. Stall penetration was achieved at each Mach number. The nondimensional pitch rates were selected between $\Lambda = \dot{\alpha}c/2U_\infty$ of 0.001 and 0.025 , bounded by a limiting dimensional pitch rate of $560^\circ/\text{sec}$. Typical ramp time histories were shown in Ref. 20. The primary departure from an ideal constant-rate motion was rounding of the ramp corners at higher rates. At rates near the $560^\circ/\text{sec}$ limit, the impulsive start of the ramp caused a measurable torsional

oscillation of the model at its natural frequency of 20 Hz. Below the limiting rate, the structural deflections (as measured by spar strain gages) were not significant.

Data were obtained for a total of 259 large amplitude sinusoids, 120 ramps, and 295 steady-state conditions. Table 1 shows the test matrix for ramps at $\Lambda = 30^\circ$. Matrices for the other two sweep angles are similar. Only results for the positive pitch rate portions of selected ramps will be presented here. The complete data set will be documented in technical reports and digital data tapes.²³

Table 1. Test Matrix of Ramps at $\Lambda = 30^\circ$

Pitch Rate	Mach Number				
	$M_c = 0.2$	$M_c = 0.3$	$M_c = 0.4$	$M_c = 0.5$	$M_c = 0.6$
A=.0010	0 → 10				
	0 → 30°	0 → 30	0 → 20	0 → 18	0 → 12
A=.0025	0 → 30	0 → 30	0 → 20	0 → 18	0 → 12
					0 → 13.5
A=.0050	0 → 10	0 → 10	0 → 10	0 → 8	
	0 → 30°	0 → 30	0 → 20°	0 → 18	0 → 13.5
	10 → 20				
	12 → 22				
	14 → 24				
	16 → 26				
	18 → 28				
A=.0100	0 → 10				
	0 → 30°	0 → 30	0 → 20	0 → 18	
A=.0200	0 → 10				
	0 → 30°	0 → 30			
A=.0250	0 → 30				

* Square tip data in addition to round tip

Unsteady surface pressure measurements were made on the wing model using 112 miniature transducers distributed among five spanwise stations. The suction surface transducer locations are shown by the dots in Fig. 1. The chordwise arrays on the upper surface had 10, 14, or 18 transducers each. The lower surface arrays were less dense, containing 6 or 18 transducers each. The frequency response of the installed transducers has been measured by comparing their response to white noise with that of a reference microphone.²⁵ The initial resonance is typically between 4 and 12 kHz, well above the current range of interest (fundamental frequencies of up to 12 Hz). Steady state calibration was performed over the full range of pressures (+2.5 to -12.5 psi) and temperatures (50 to 110 F) expected. This procedure results in a steady-state calibration accuracy of better than 0.5% of the full scale pressure range.^{21,25}

Additional instrumentation included 16 surface hot film gages to determine transition and separation locations, three spar strain gage bridges to verify that limit stresses were not exceeded, a spar angle of attack sensor, and an unsteady pitot-static probe mounted below the upper wind tunnel wall to identify far field disturbances. The output of each sensor was amplified, passed through a 10 kHz low pass filter, and digitized (to 15 bit accuracy) at a rate of 1024 samples per period (T). The data from 20 pitching oscillations were recorded on digital magnetic tape, ensemble

averaged, and converted to coefficient form. The pressures were integrated along the chord at each of the five spanwise stations to determine the unsteady lift, pressure drag, and pitching moment coefficients. All parameters were available for on-line analysis. Standard wind tunnel instruments were used to measure total and static pressures, total temperature, and dewpoint.

STEADY STATE RESULTS

Steady state pressure distributions were measured at each Mach number and sweep angle. In general the results are in agreement with those expected for a simple subsonic wing. Of most relevance here are the effects of Mach number, sweep angle, and spanwise position on the stall characteristics. Figure 3 shows lift and pitching moment curves for the unswept wing at five Mach numbers for the furthest in-board station, $z/c = 1.52$. (Note that z has been defined as the distance from the wing tip (Fig. 1) to make the value of z for each transducer array independent of sweep.) The stall angle, as determined from the break in the lift and moment curves, drops from 16.5° at $M_c = 0.2$, to 13° at $M_c = 0.4$, and to 10° at $M_c = 0.6$. The maximum lift coefficient is reduced from 1.4 at $M_c = 0.2$ to 0.9 at $M_c = 0.6$, and the sharpness of the changes in lift and moment after stall are also reduced. The load curves before stall are very similar at all five Mach numbers, with the exception of the increase in lift curve slope (as predicted by the Prandtl-Glauert relation²⁶). The lift curve slopes for the 3D wing are reduced from the 2D values.²⁰ The steady-state slope at $z/c = 1.52$ is 23% less than the 2D slope, in reasonable agreement with the 27% reduction predicted by Weissinger's incompressible lifting line theory.²⁶

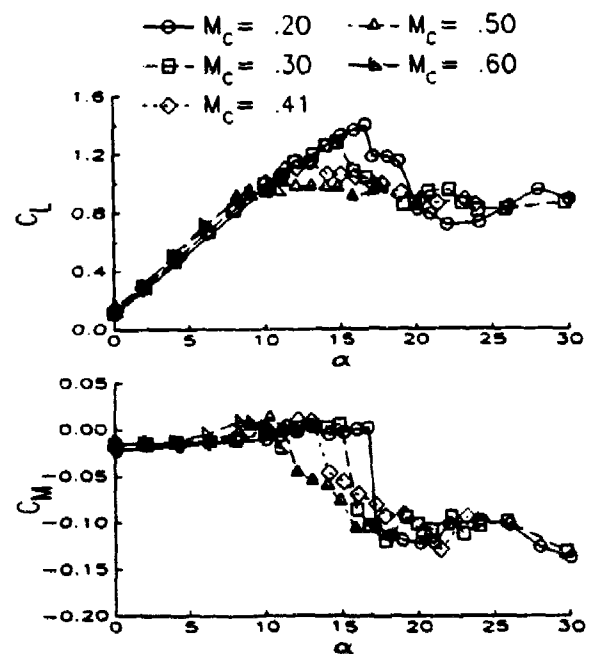


Fig. 3 Effect of Mach number on steady-state lift and moment at $\Lambda = 0$ and $z/c = 1.52$.

The standard infinite swept wing normalization (division by the chordwise component of freestream dynamic pressure, $q_\infty \cos^2 \Lambda$) was found to collapse C_L to a single curve for the inboard ($z/c \geq 0.3$) stations, at lower Mach numbers, and below stall. An example is shown in Fig. 4a for $M_c = 0.3$ and $z/c = 1.06$. Close to the wing tip, the influence of the tip vortex is very strong, and additional differences with sweep are present. For example, at $M_c = 0.3$ the moment at $z/c = 0.08$ on the unswept wing (Fig. 4b) gradually becomes more negative for $\alpha > 4^\circ$. This behavior is caused by the tip vortex rolling up over the tip and increasing the suction pressure on the aft portion of the chord. At $\Lambda = 15$ and 30° the vortex does not roll up over the chord, and the moment remains positive until stall.

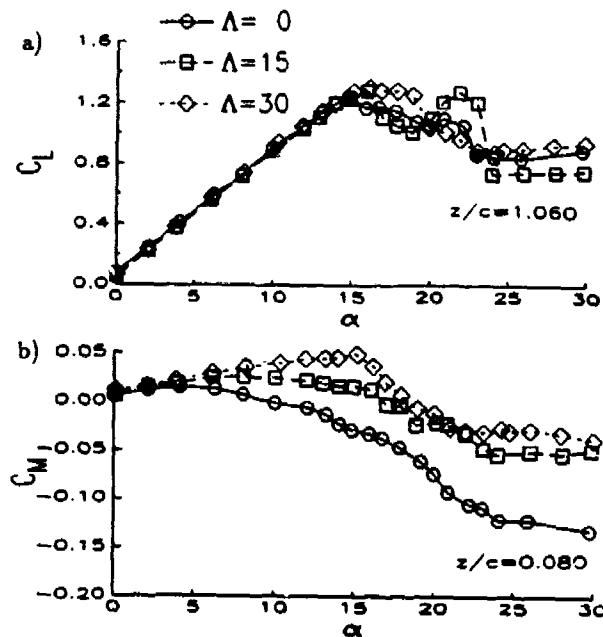


Fig. 4 Effect of sweep on steady-state inboard lift and tip moment at $M_c = 0.3$.

Spanwise load distributions are strongly influenced by wing sweep. Figure 5 shows contours of the steady-state C_L as a function of spanwise position and angle of attack at $M_c = 0.3$. The $\Lambda = 0$ results are in Fig. 5a, and the $\Lambda = 30^\circ$ results are in Fig. 5b. Since load contours will be used several times in this paper, it may be helpful to point out how various characteristics appear. A region without spanwise gradients will have straight vertical contour lines. If the spacing between these lines is constant, then the load increases linearly with angle of attack. If the contour lines are horizontal, then the load is locally independent of angle of attack, and only spanwise gradients are present. For the unswept wing (Fig. 5a) the contour lines are uniformly spaced for $\alpha < 13^\circ$ (the region of attached flow and constant lift curve slope), and approach vertical as z/c increases. Strong spanwise gradients are present for $z/c < 0.4$. The lift smoothly approaches zero at the tip ($z = 0$). A maximum lift plateau ($C_L \approx 1.25$) is formed near $\alpha = 14$ to 15° for $z/c \geq 1.0$. Closer to the tip, maximum lift and stall are delayed by up to 5° .

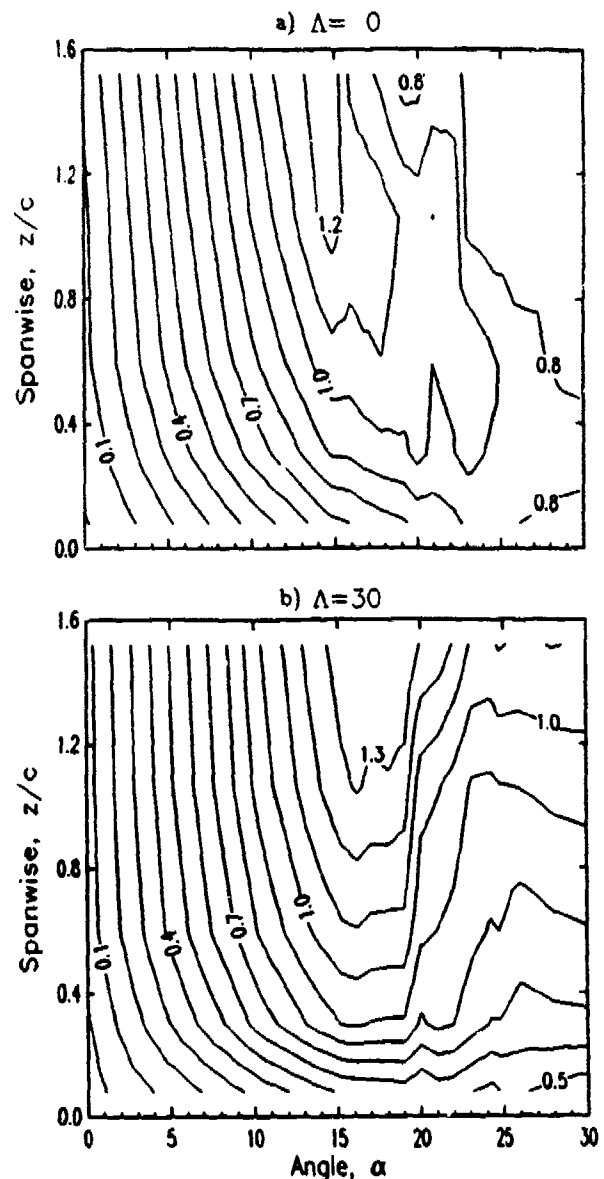


Fig. 5 Steady-state lift contours at $\Lambda = 0$ and 30° , $M_c = 0.3$.

At $\Lambda = 30^\circ$ (Fig. 5b) the attached flow contour lines for $\alpha \leq 10^\circ$ are more nearly vertical for $z/c \geq 0.6$, indicating a reduced influence of the tip vortex. The lift plateau is also higher ($C_L \approx 1.4$) and broader ($15 \leq \alpha \leq 19^\circ$). Stall is delayed relative to $\Lambda = 0$, and occurs nearly simultaneously over almost the entire span. Many of these effects of sweep and three-dimensionality will also be important during unsteady motions.

UNSTEADY PRESSURE RESULTS

Pressure data for a single condition, a $0 \rightarrow 30^\circ$ ramp with $\Lambda = 0.02$, $M_c = 0.3$, and $\Lambda = 0$, will be examined in some detail to identify the characteristics of lower Mach number dynamic stall. Figure 6 shows ensemble-averaged pressures

at $z/c = 0.59$ for 6 instants during the ramp. At $\tau = 0.47$ and $\alpha = 20.2^\circ$ (Fig. 6a) there is a strong leading edge suction peak ($C_p \approx -9$), and no indication of separation. There is a small region of supersonic flow ($M \approx 1.2$) near the leading edge, indicated by the C_p^* arrow near $x/c=0.005$. Separation begins as the suction peak shrinks (Fig. 6b at $\alpha = 20.8^\circ$). The leading edge separation plateau then widens and lowers (Figs. 6c-f at $\alpha = 21.4, 22.6, 24.9$, and 27.7°), as the dynamic stall vortex convects downstream. The process concludes with massive separation (Fig. 6g at $\alpha = 30^\circ$).

The chordwise pressure distributions also illustrate the strong effects of spanwise position on the stall process. Figure 7 shows instantaneous pressures at $\tau = 0.525$ ($\alpha = 23.5^\circ$) for all five stations. At $z/c = 1.52$, the upper surface separation plateau extends to $x/c = 0.6$. At $z/c = 1.06$, the plateau ends near $x/c = 0.4$, and at $x/c = 0.59$ it ends near $x/c = 0.2$. No evidence of separation is present at $z/c = 0.3$ and 0.08 . The pressures at $z/c = 0.08$ are distorted by the roll-up of the tip vortex, which induces high suction loads on the upper surface trailing edge.

Another view of the stall process is provided by time histories of the pressures. Figure 8 shows stacks of the ensemble-averaged upper surface pressures for the conditions of Fig. 6. Results for the furthest inboard station ($z/c \approx 1.52$) are shown in Fig. 8a. The $x/c = 0.01$ transducer is at the bottom, with the scale shown at the lower

right. Successive transducers are offset vertically, with the origins indicated along the left axis. Both τ and α scales are included along the horizontal axis. Separation is identified by the sharp loss of suction at $x/c = 0.01$ and $\tau \approx 0.43$ ($\alpha \approx 18^\circ$). The sharp negative pressure peak associated with the dynamic stall vortex is first observed at $x/c = 0.049$. The peak moves back along the chord and widens. These time histories are very similar to those obtained at $z/c = 1.06$ (not shown), and are qualitatively similar to other results with strong dynamic stall obtained from this experiment, from the 2D experiment,²⁰ and by other researchers.⁴⁻⁷

Closer to the wing tip, the pressure signature of dynamic stall is delayed and diffused. As shown by the time histories at $z/c=0.59$ (Fig. 8b) and $z/c=0.08$ (Fig. 8c), leading edge separation occurs later in the cycle, the initial strength of the pressure peak associated with the stall vortex is reduced, and the peak weakens earlier. Separation occurs at $\alpha \approx 21^\circ$ for $z/c=0.59$, and at $\alpha \approx 26.5^\circ$ for $z/c=0.08$, delays of 3 and 8.5° relative to $z/c=1.52$. This delay is attributed to lower effective angles of attack caused by proximity to the tip vortex. At $z/c=0.59$ the negative pressure peak near $x/c = 0.1$ remains relatively strong at $\Delta C_p \approx 1.6$, while at $z/c = 0.30$ (not shown), the initial peak is reduced to $\Delta C_p \approx 0.8$, and at $z/c = 0.08$ (Fig. 8c) the maximum strength is only $\Delta C_p \approx 0.6$. As the vortex moves downstream, the surface pressure peaks become diffuse and difficult to identify for $x/c \geq 0.4$ at $z/c=0.59$ and for $x/c \geq 0.2$ at $z/c=0.08$. The weakening at the tip is probably related to interaction with the tip vortex. Steady-state surface oil flow visualization indicates that the vortex rolls

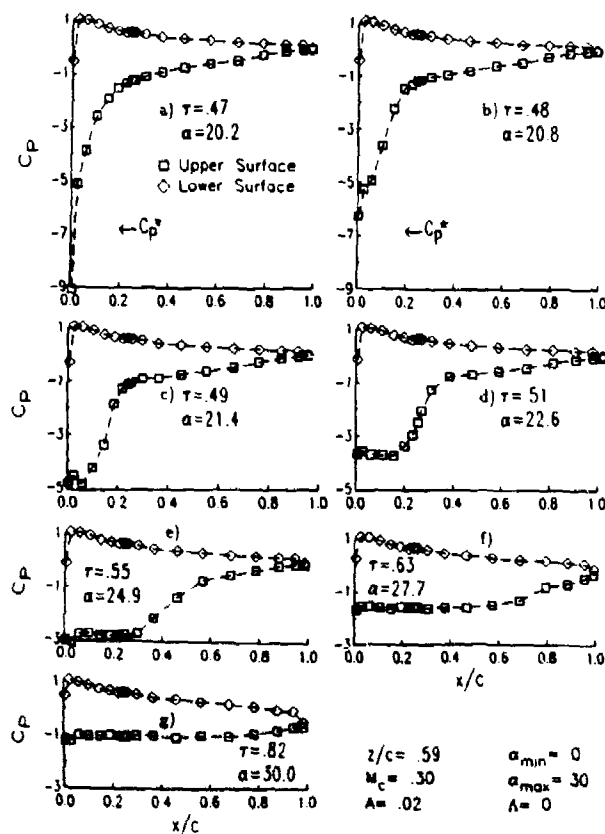


Fig. 6 Pressure distributions during a $0 \rightarrow 30^\circ$ ramp at $A=0.02$, $\Lambda = 0$, $M_c = 0.3$, and $z/c=0.59$.

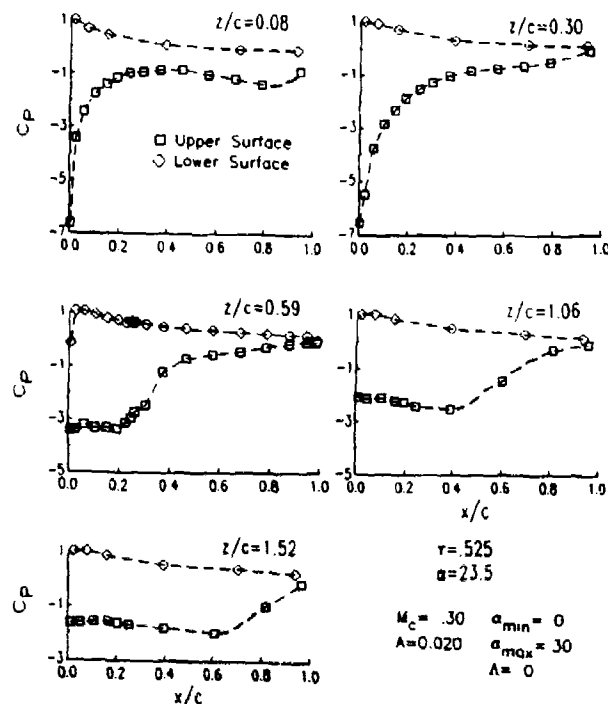


Fig. 7 Spanwise differences in pressure distributions at $\alpha = 23.5^\circ$ during a $0 \rightarrow 30^\circ$ ramp at $A=0.02$, $\Lambda = 0$, and $M_c = 0.3$.

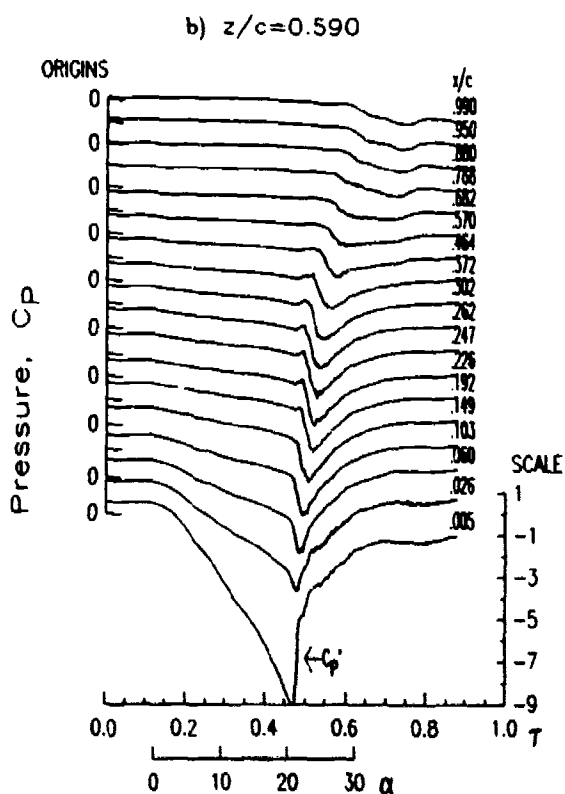
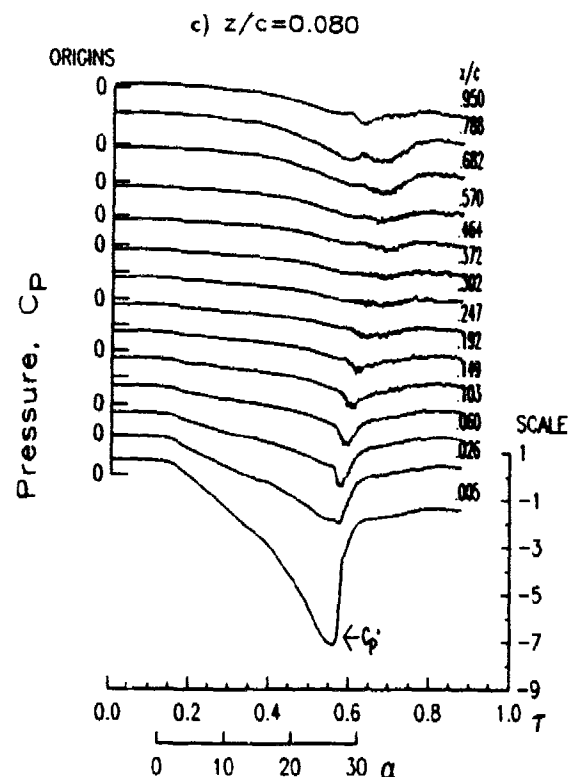
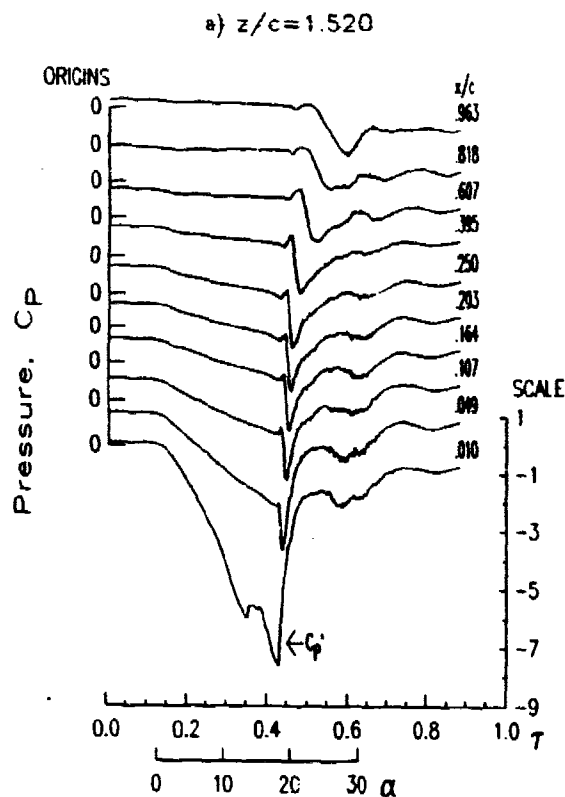


Fig. 8 Pressure time histories during a $0 \rightarrow 30^\circ$ ramp at $A=0.02$, $\Lambda = 0$, and $M_c = 0.3$.

up over the wing in a roughly 30° triangle beginning at the tip leading edge.

The effect of spanwise position on the initiation and propagation of the stall vortex is shown in Fig. 9. Assuming that the minimum C_p at each transducer is associated with passage of the stall vortex, a least-squares fit of the times of these minima as a function of chordwise position may be used to estimate the vortex propagation speed.²⁰ In the initial region of constant speed, the estimates for this particular $A=0.02$ condition range from $0.25U_c$ at $z/c = 1.52$ to $0.15U_c$ at $z/c = 0.08$. For comparison, speed estimates for similar conditions from the 2D experiment include $0.33U_c$ at $M_c = 0.2$ and $A = 0.02$, and $0.20U_c$ at $M_c = 0.4$ and $A = 0.01$.²⁰ The inboard results thus resemble the 2D results, while the propagation speeds near the tip are substantially lower. As shown in Fig. 9, the region of constant speed extends from $x/c \approx 0.05$ to $x/c \approx 0.8$ inboard, but only to $x/c \approx 0.5$ near the tip. Two effects may contribute to this change. The first is the tip vortex interaction discussed above. A second possibility is suggested by the observation that the region of constant propagation speed ends at roughly the same time that the pitching motion stops ($\tau \approx 0.625$). In 2D, when motion ended before the stall vortex passed the trailing edge, there was a pause, followed by a resumption of vortex propagation at nearly the same speed.²⁰ Such behavior is observed in 3D at $z/c=0.59$ (Fig. 9), but closer to the tip, constant speed propagation of the vortex does not resume.

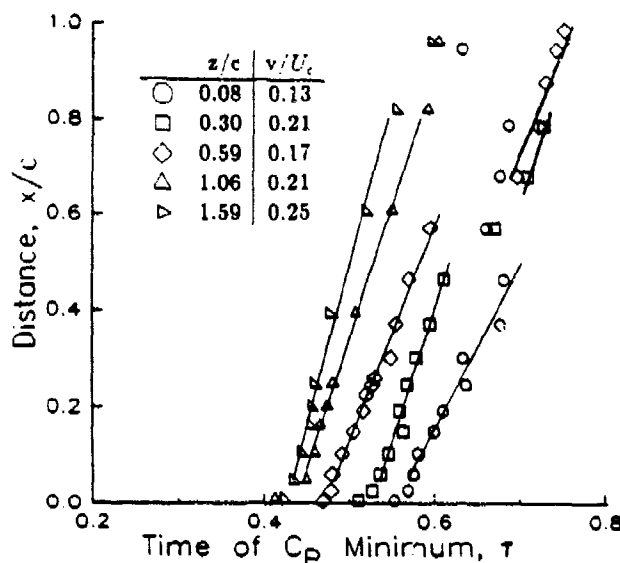


Fig. 9 Estimated stall vortex convection during a $0 \rightarrow 30^\circ$ ramp at $A=0.02$, $\Lambda=0$, and $M_c=0.3$

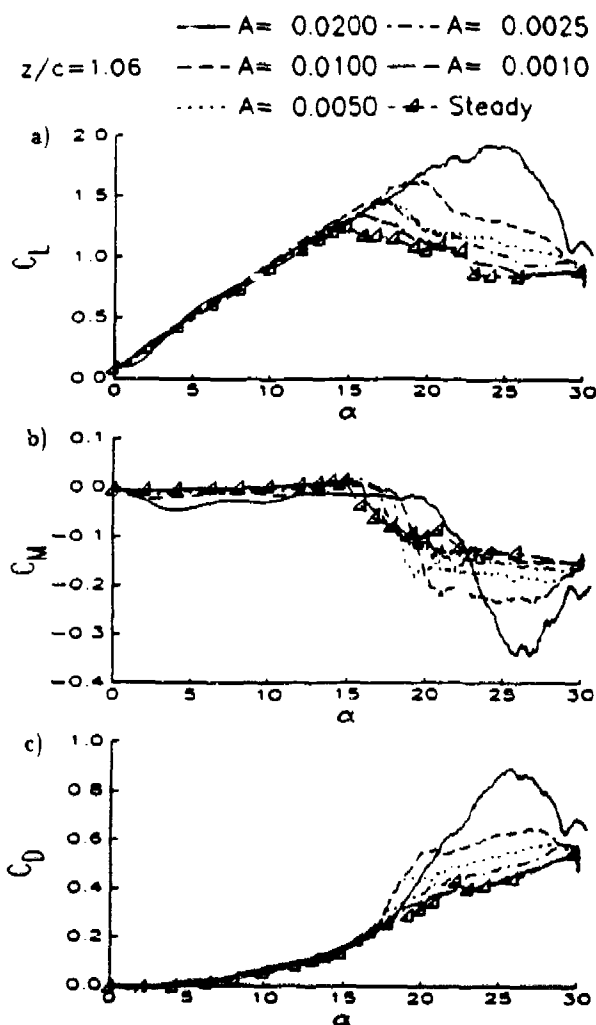


Fig. 10 Pitch rate effects on the aerodynamic loads at $z/c=1.06$, for $0 \rightarrow 30^\circ$ ramps at $\Lambda=0$, and $M_c=0.3$.

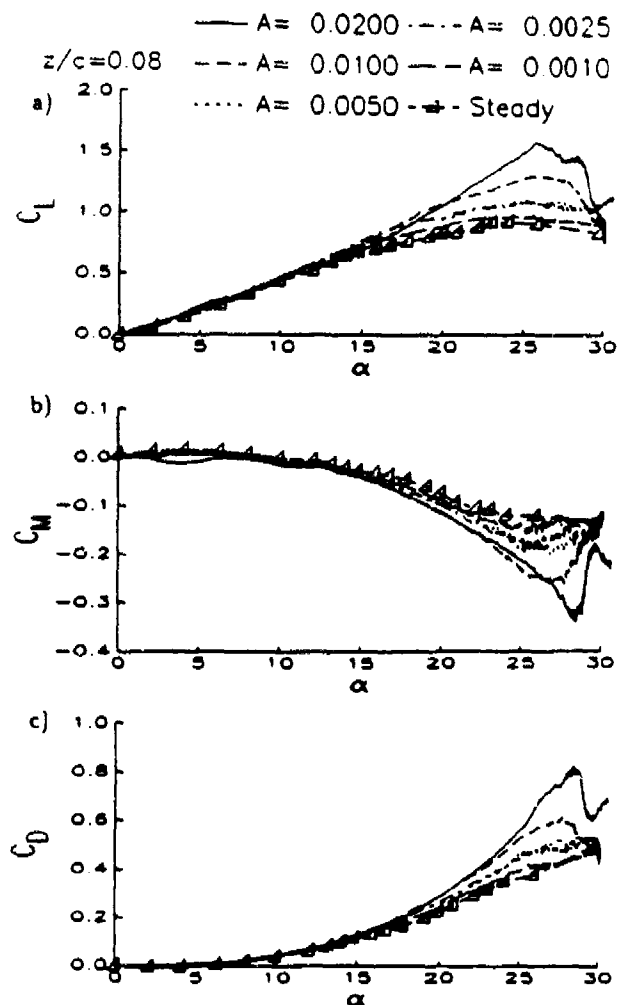


Fig. 11 Pitch rate effects on the aerodynamic loads at $z/c=0.08$, for $0 \rightarrow 30^\circ$ ramps at $\Lambda=0$, and $M_c=0.3$.

FORCE AND MOMENT RESULTS

Integrated sectional aerodynamic loads exhibit strong dependence on spanwise position and pitch rate. Figures 10 and 11 contain unsteady airloads versus α for $0 \rightarrow 30^\circ$ ramps at $M_c=0.3$ and $\Lambda=0$ for 5 pitch rates: $A=0.02$, 0.01 , 0.005 , 0.0025 , and 0.001 . Lift, moment and drag results at $z/c=1.06$ are shown in Fig. 10, and at $z/c=0.08$ in Fig. 11. The symbols represent the steady-state results. The qualitative unsteady characteristics are as expected²⁰: as pitch rate increases stall is delayed and the peak C_L , C_M , and C_D are increased. At $A=0.02$ the delay is approximately 10° and the increase in the unsteady load maxima are up to 60% of the steady maxima. At lower pitch rates the effects are smaller, but still measurable, even at $A=0.001$. Below stall, the lift and drag results differ only slightly from the steady-state values, while the unsteady moment shows the negative offset predicted from thin airfoil theory.²⁰ The primary qualitative difference at $z/c=0.08$ is the gradual increase in the negative pitching moment (Fig. 11b), rather than the sharp break observed further inboard (Fig. 10b).

This is similar to the steady-state results (Fig. 4), and thus appears to be a quasi-steady rather than unsteady effect.

In agreement with the pressure results (Fig. 7-5), at $M_c = 0.3$ the quantitative effects of the proximity to the wing tip include delaying stall and reducing the absolute levels of the unsteady load increments. This can be seen in Fig. 12, which plots the difference between the unsteady and quasi-steady (QS) lift. (The QS lift was determined by interpolation of the steady-state values.) At both $z/c = 1.52$ and 0.08 , substantial unsteady loads are first generated after $\alpha \approx 15^\circ$. The loads increase much more rapidly at $z/c = 1.52$, reaching an initial peak between $\alpha \approx 16$ to 19° (depending on pitch rate). At the highest rate, $A = 0.02$, the largest increment, $C_L - QS \approx 1.1$, occurs at $\alpha \approx 24^\circ$. The unsteady loads increase more gradually at $z/c = 0.08$, with the maximum ($C_L - QS \approx 0.7$ at $A = 0.02$) not occurring until $\alpha \approx 26^\circ$. (Note that the maximum of $C_L - QS$ is generally larger than the increase in C_L^{max} , since the delay in stall causes the maximum unsteady lift to occur at a time when the QS lift has dropped below its maximum.)

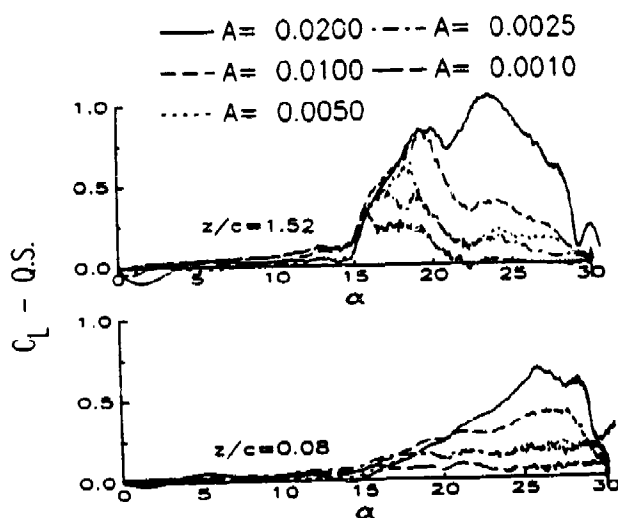


Fig. 12 Pitch rate effects on the unsteady increment to the loads for a $0 \rightarrow 30^\circ$ ramps at $A = 0$, and $M_c = 0.3$.

An overview of the spanwise unsteady airloads is provided by contour plots. Figure 13 shows C_L and C_M contours for the $A = 0.02$ ramp. The primary horizontal scale is time (τ), with an auxiliary scale showing the values of α during the ramp. In comparison with the steady-state contours (Fig. 5), the C_L contours at $A = 0.02$ (Fig. 13a) show a region of high lift ($C_L \geq 1.0$) that is stronger and extends further towards the wing tip. The unsteady moment contours (Fig. 13b) can be roughly divided into three regions. a) $z/c \geq 1$, where there are only small spanwise gradients, b) $0.3 \leq z/c \leq 1$, where the negative moments induced by stall are increasingly delayed, and c) $z/c < 0.3$, where the tip vortex roll-up exerts the primary influence.

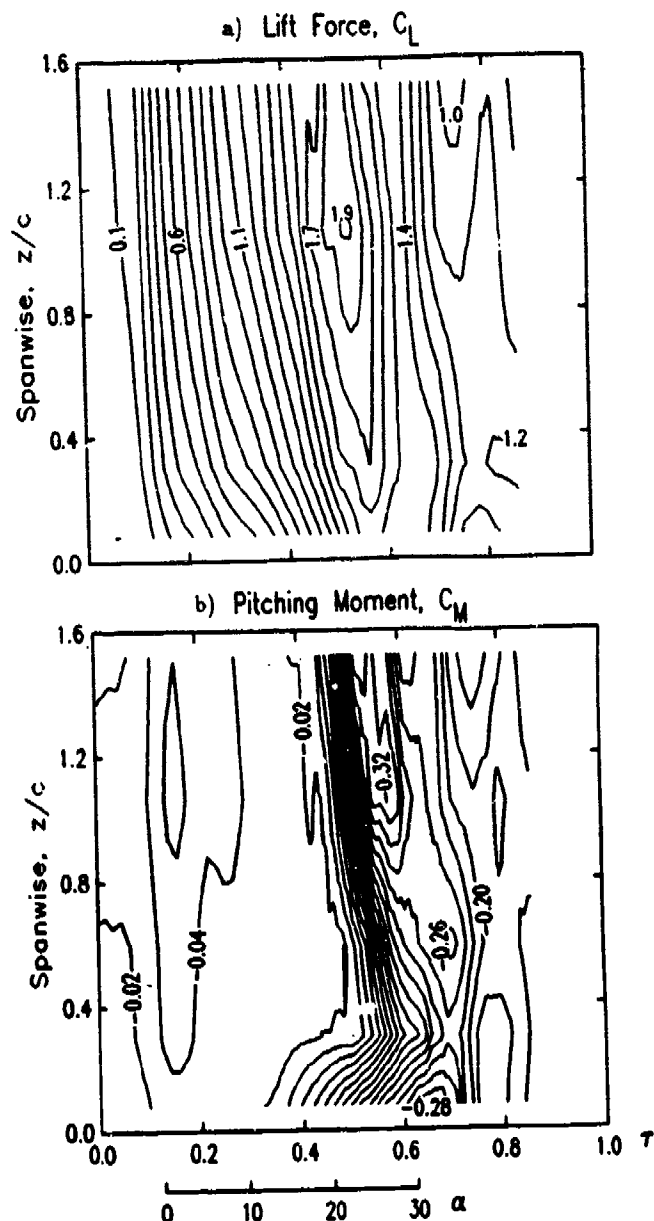


Fig. 13 Lift and moment contours for a $0 \rightarrow 30^\circ$ ramp at $A = 0$, $A = 0.02$, and $M_c = 0.3$.

There may appear to be a contradiction near the tip between the enhanced unsteady lift shown in the contour plot (Fig. 13), the weakened stall vortex (Fig. 8), and the reduced levels of $C_L - QS$ (Fig. 12). The explanation is that while the absolute levels of the unsteady increments are reduced at the tip, the unsteady increments at the tip are larger relative to the local QS loads. (The QS tip loads reflect the lower effective angle of attack induced by the tip vortex.) The unsteady enhancement of the tip lift has been previously noted by Robinson and Wissler at lower speed ($M_c \leq 0.08$, $6 \times 10^4 \leq Re \leq 2 \times 10^5$).⁵⁻⁶ Their conclusion that the enhancement is a result of the tip vortex inhibiting convection of the stall vortex is supported by the reduced convection velocities measured near the tip in the current experiment (Fig. 9).

MACH NUMBER EFFECTS

Mach number effects on the unsteady aerodynamic loads are illustrated in Fig. 14 using ramps at $M_c = 0.2, 0.3, 0.4,$ and 0.5 . Each curve is for $A = 0.01, A = 0,$ and $z/c = 0.59$. The characteristics of the $C_L, C_M,$ and C_D curves show similarities to the steady-state results (Fig. 3) and to the previous 2D unsteady results at $M_c = 0.2$ and 0.4 .²⁰ Below stall the primary difference with M_c is the increase of lift curve slope noted in steady-state. At all Mach numbers, the unsteady motion causes a delay in stall and an increase in the peak C_L, C_D and C_M . These effects are, however, significantly reduced at higher Mach numbers.

The data can also be presented in terms of the difference between the unsteady, $A = 0.01$ loads and the quasi-steady loads at the same $\alpha, M_c,$ and z/c . Figure 15 shows this for $C_L, C_M,$ and C_D . (The small negative increments to C_L for $\alpha \leq 4^\circ$ result from drive system lags associated with the sudden initiation of the motion.) The unsteady increments to C_M (Fig. 15c) are particularly interesting since there is first the small ($C_M - QS \approx 0.015$) negative increment in attached flow²⁰, then a positive increment (up to $C_M - QS \approx 0.12$) caused by the delay in stall, and finally the negative

increment (up to $C_M - QS \approx 0.12$) caused by propagation of the stall vortex aft along the chord.

The stall delays and maximum unsteady load increments for the five ramps are given in Table 2. The C_L stall angle identified in the table is the angle at which the lift either reaches its maximum or (near the tip) at which the lift slope is abruptly reduced. C_M stall is identified by the break in the moment curve. ΔC_L^{max} is the increase in the maximum lift above the steady maximum, while $max(C_L - QS)$ is the maximum value of the difference between the unsteady and quasi-steady coefficients (Fig. 15). Both positive and negative values are given for $C_M - QS$. Because of experimental uncertainty and because determining the stall angle was somewhat arbitrary, Table 2 is intended to illustrate trends rather than to provide precise quantitative numbers.

A particularly interesting result is that, at $M_c = 0.2$ and $0.3, \Delta C_L^{max}$ is larger near the tip (in agreement with Ref. 5 and with the $A=0.02$ results discussed above), while for $M_c \geq 0.4, \Delta C_L^{max}$ is larger inboard. The $max(C_L - QS)$, however, is larger inboard at all M_c . Since the relative enhancement of the tip lift was attributed earlier to interactions between the tip and stall vortices, this observation implies that compressibility has a significant effect on this interaction. Another notable result is that the unsteady ef-

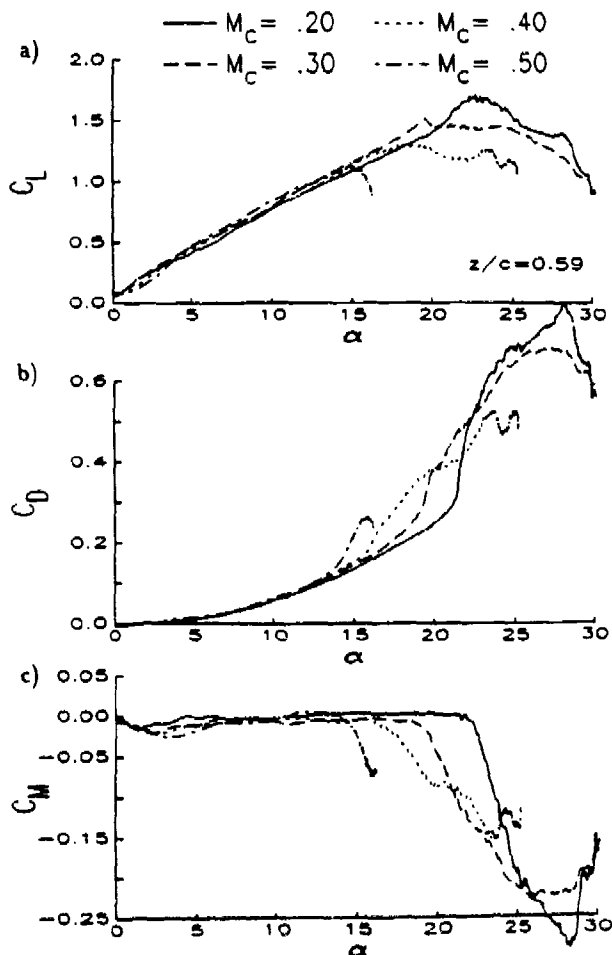


Fig. 14 Mach number effects on the aerodynamic loads at $z/c=0.59$, for $A=0.01$ and $A = 0$.

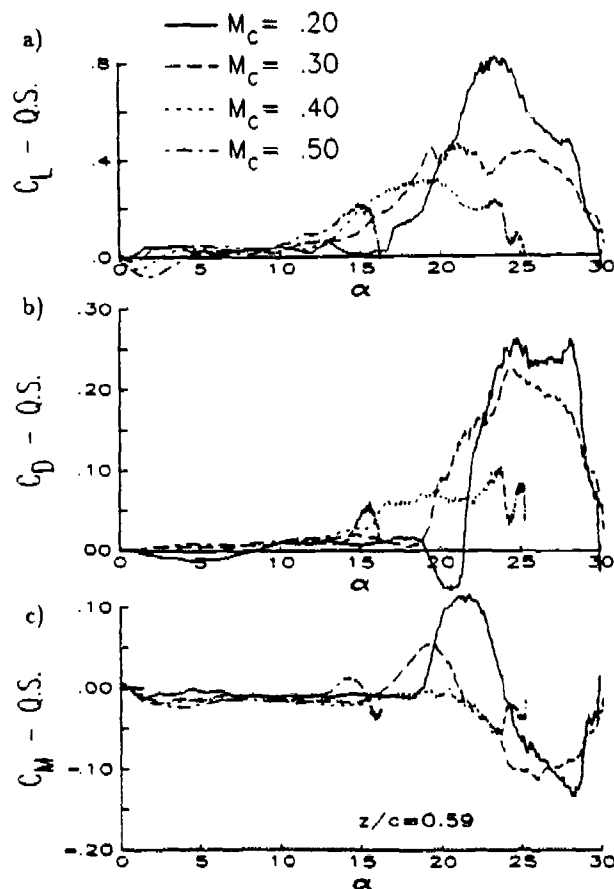


Fig. 15 Mach number effects on the unsteady increment to the loads at $z/c=0.59$, for $A=0.01$ and $A = 0$.

Table 2. Stall Delays and Load Increments
at $A=0.01$ and $A=C$

$z/c=1.52$	α_s		$\alpha_s - \alpha_{ss}$		ΔC_L^{max}	$max(C_x - QS)$		
	C_L	C_M	C_L	C_M		C_L	C_M	C_D
$M_c=0.2$	22	21	5	4	.30	1.00	+ .10, -.22	.39
$M_c=0.3$	19	17	4	2	.35	.80	+ .09, -.14	.26
$M_c=0.4$	17	16	4	3	.30	.45	+ .04, -.09	.17
$M_c=0.5$	14.5	13	4.5	2	.25	.30	+ .04, -.02	.03
$z/c=1.06$								
$M_c=0.2$	23	21	6	5	.45	1.05	+ .12, -.17	.37
$M_c=0.3$	19	18	4	3	.35	.55	+ .06, -.13	.23
$M_c=0.4$	17	16	4	3	.30	.45	+ .02, -.08	.13
$M_c=0.5$	14.5	13	3	1	.20	.27	+ .04, -.01	.05
$z/c=0.59$								
$M_c=0.2$	23	22	5	3	.55	.80	+ .12, -.12	.25
$M_c=0.3$	19	18	3	2	.40	.45	+ .05, -.10	.22
$M_c=0.4$	18	16.5	5	1	.25	.30	+ .06, -.06	.09
$M_c=0.5$	15	14	3	1	.15	.20	+ .01, -.04	.05
$z/c=0.30$								
$M_c=0.2$	23	23	5	3	.60	.80	+ .07, -.07	.17
$M_c=0.3$	22	20	7	2	.30	.35	+ .04, -.06	.13
$M_c=0.4$	18	17.5	5	.5	.15	.30	+ .02, -.04	.06
$M_c=0.5$	15.5	15	3.5	1	.10	.18	+ .03, -.03	.04
$z/c=0.08$								
$M_c=0.2$	26	-	7	-	.50	.55	+ .17, -.22	.22
$M_c=0.3$	26	-	6	-	.40	.40	+ .12, -.16	.16
$M_c=0.4$	23	-	-	-	.20	.18	+ .07, -.08	.08
$M_c=0.5$	16	-	-	-	.10	.15	+ .06, -.06	.04

fect on the moment differs from the effect on the lift and drag. The maximum negative $C_M - QS$ is nearly as strong at $z/c=0.08$ as it is inboard, even at higher M_c . Interaction with the tip vortex is again a likely suspect, since it has a dominant effect on the tip moments (Figs. 4, 10, and 11). A more extensive study of the relation between the load increments and the stall delays at each M_c is clearly required.

Instantaneous pressure distributions provide information on the inception and progress of dynamic stall at higher M_c . Chordwise pressures for $A = 0.01$ ramps near the time of maximum suction (shortly before stall) are shown in Fig. 16. The results are for the same conditions and location used in Figs. 14 and 15. As Mach number increases, the peak suction pressure coefficient drops from $C_p \approx -11.3$ at $M_c=0.2$, to -3.8 at $M_c=0.5$. At the same time the region of leading edge supersonic flow expands from less than 1% of chord at $M_c=0.3$, to 5% at $M_c=0.4$, and to 8% at $M_c=0.5$. A clear shock is visible at $M_c=0.5$. Also shown in Fig. 16 is a pressure distribution for an $A = 0.0025$ ramp at $M_c=0.6$. At this condition the peak local Mach number is 1.6, and the shock occurs at $x/c \approx 0.15$.

The effect of compressibility on the stall process is illustrated in Fig. 17, which contains pressure distributions during an $A = 0.01$ ramp at $M_c = 0.5$. Maximum suction ($C_p \approx -3.8$ and $M \approx 1.5$) occurs near $\alpha = 13.1^\circ$ (Fig. 17a). At higher α , the increase in C_L (Fig. 14) is accounted for by broadening the peak (Fig. 17b). The supersonic region remains, but the shock becomes indistinct, and the leading edge pressure distribution assumes a triangular shape (Fig.

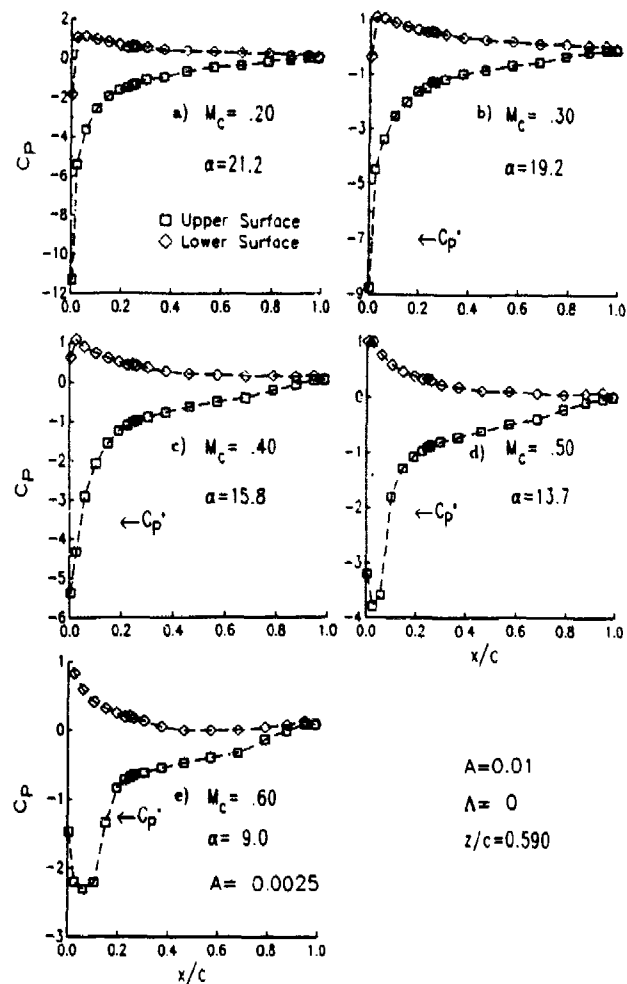


Fig. 16 Mach number effects on the pressure distributions at the time of maximum suction during ramps at $z/c=0.59$ and $A = 0$. The $M_c = 0.6$ ramp is at $A=0.0025$; the remainder are at $A=0.01$.

17 c-d). Individual cycle time histories (not shown) indicate that the triangular shape is an accurate representation of the pressure distribution, and is not caused by ensemble averaging of a randomly moving shock. Above $\alpha \approx 15^\circ$ the lift begins to drop, and a separation pressure plateau forms just below sonic velocity (Figs. 17e-f). This plateau extends back to approximately $x/c = 0.2$. The same basic pressure distribution is maintained through the end of the motion at $\alpha = 16^\circ$ (not shown).

Neither surface pressure distributions nor pressure time histories (not shown) provide evidence of multiple shocks, as were observed at moderate α by Schlieren measurements⁹ of the field about a NACA 0012 airfoil pitching at $A = 0.016$ and $M = 0.45$. While it is possible (but not likely) that shifts between supersonic and subsonic flow could occur between the pressure transducer locations, a more plausible explanation is that the behavior of a NACA 0012 at $Re \approx 9 \times 10^5$ differs from that of an SSC-A09 at $Re \approx 5 \times 10^6$. Steady flow visualizations (Figs. 245-249 of Ref. 27) show

a succession of lambda shocks on an airfoil with a laminar boundary layer, but only a single normal shock when the boundary layer is turbulent. Surface hot film results for the current experiment indicate that transition occurs upstream of the shock at $M_c = 0.5$. The multiple shocks of Ref. 9 may be a result of larger regions of laminar flow at the lower Reynolds number.

A comparison between the $M_c = 0.5$ pressures in Fig. 17 and the $M_c = 0.3$ results in Fig. 6 reveals several differences in the stall process. First, at low M_c the suction pressures keep increasing until stall, while at higher M_c , maximum suction occurs well before stall. Second, although a leading edge separation plateau is formed at both conditions, it is limited to $x/c \approx 0.25$ at $M_c = 0.5$. The rapid replacement of the shock by the triangular pressure distribution, followed by the retreat of the suction pressures below C_p^* are also interesting, if as yet unexplained. There is clearly a strong correlation between the extent of supersonic flow, the strength of the shock, the stall process, the strength of the stall vortex, and the reduction in the unsteady load increments at higher M_c . Speculations on the mechanism have been presented,^{9,18,20,28} but the issue remains unresolved.

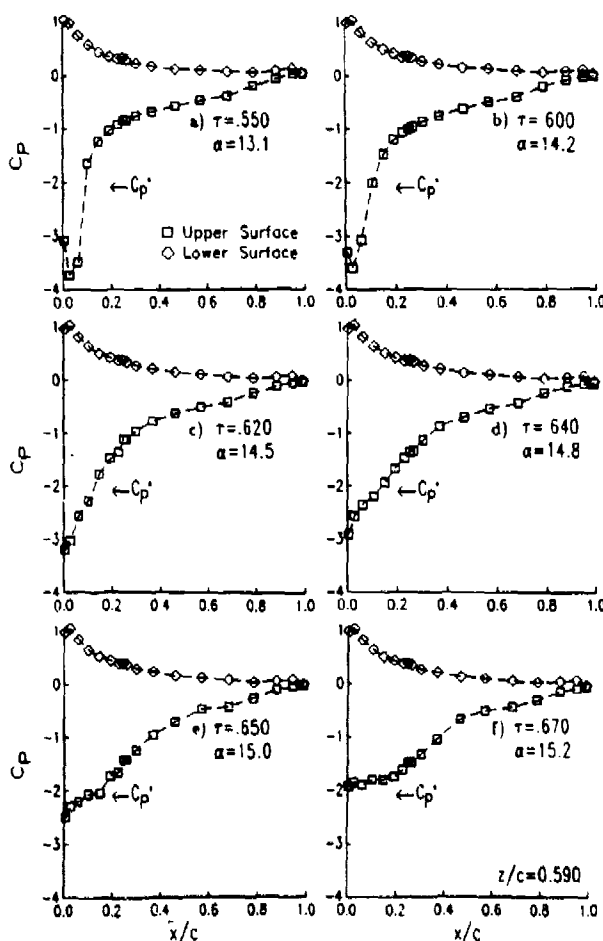


Fig. 17 Pressure distributions during a $0 \rightarrow 16^\circ$ ramp at $A=0.01$, $\Lambda = 0$, $M_c = 0.5$, and $z/c=0.59$.

The effect of sweep on the load coefficients at $z/c=1.06$ is shown in Fig. 18 for constant rate ramps at $A = 0.02$ and $M_c = 0.3$. As was true in steady-state (Fig. 4), the loads at $\Lambda = 0, 15$, and 30° collapse approximately to a single curve prior to stall. This includes the $\Delta C_M \approx -0.03$ offset in attached flow. At this condition and location, C_L^{max} is somewhat lower at $\Lambda = 15$ and 30° (Fig. 18a), and occurs at a lower α . The break in the moment curve (Fig. 18b) is also sharper and earlier. These differences become more pronounced closer to the tip. At $z/c = 0.08$ (Fig. 19) the peak C_L , C_M , and C_D are substantially less at higher Λ . C_L^{max} occurs 1° earlier at $\Lambda = 15^\circ$ (Fig. 19a), and an additional 2° earlier at $\Lambda = 30^\circ$. The C_M curve (Fig. 19b) also has a sharper and earlier break at positive sweep.

Many of these features are qualitatively similar to the steady-state results (Fig. 4). Figure 20 isolates the effects of sweep on the unsteady increments to the load by plotting the difference between the $C_L - QS$ and $C_M - QS$ for the $A = 0.02$ ramps. At all three sweep angles, large unsteady increments are first observed near $\alpha = 15^\circ$. At $z/c = 1.06$ the maximum unsteady increment to C_L (Fig. 20a) is approximately 1 at $\Lambda = 0$ but only 0.7 at $\Lambda = 15$ and 30° . The positive and negative unsteady moment increments (Fig. 20b)

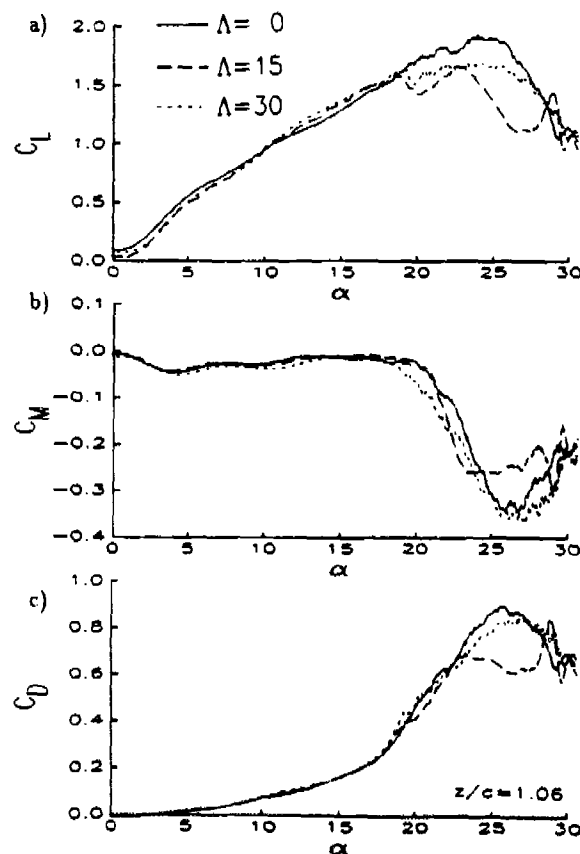


Fig. 18 Sweep effects on the aerodynamic loads at $z/c=1.06$, during $0 \rightarrow 30^\circ$ ramps with $A = 0.02$, and $M_c = 0.3$.

are also slightly smaller for the swept wing. At $z/c = 0.08$, $C_L - QS$ (Fig. 20c) is approximately 0.6 at $\Lambda = 0$ and 15° , and 0.4 at $\Lambda = 30^\circ$.

The largest effect of sweep occurs in the moment increments at $z/c = 0.08$ (Fig. 20d). The negative offset predicted by thin airfoil theory is present at all sweep angles below $\alpha \approx 15^\circ$. Above this angle the unsteady moment increment gradually becomes more negative at $\Lambda = 0$, reaching a peak of $C_M - QS \approx -0.20$ at $\alpha = 28^\circ$. At $\Lambda = 15^\circ$ there is a small positive increment ($C_M - QS \approx 0.01$) caused by the unsteady delay of stall, followed by a negative increment of up to $C_M - QS \approx -0.15$ caused by the stall vortex. At $\Lambda = 30^\circ$, the unsteady moment increments are similar to those occurring further inboard at lower sweep angles: a large positive increment ($C_M - QS \approx 0.05$), followed by a negative increment of $C_M - QS \approx -0.07$. Differences with spanwise position are substantially reduced at $\Lambda = 30^\circ$.

The effects discussed above seem to be primarily the result of a lessened influence of the tip vortex for the swept wing. Since sweep moves the aft portion of the wing away from the vortex, the effective angle of attack near the tip is increased. Stall occurs earlier, and the resulting dynamic stall vortex may be somewhat weaker. After stall, more complex interactions are likely between the tip vortex, the stall vortex, and (possibly) the corner vortex at the wall.

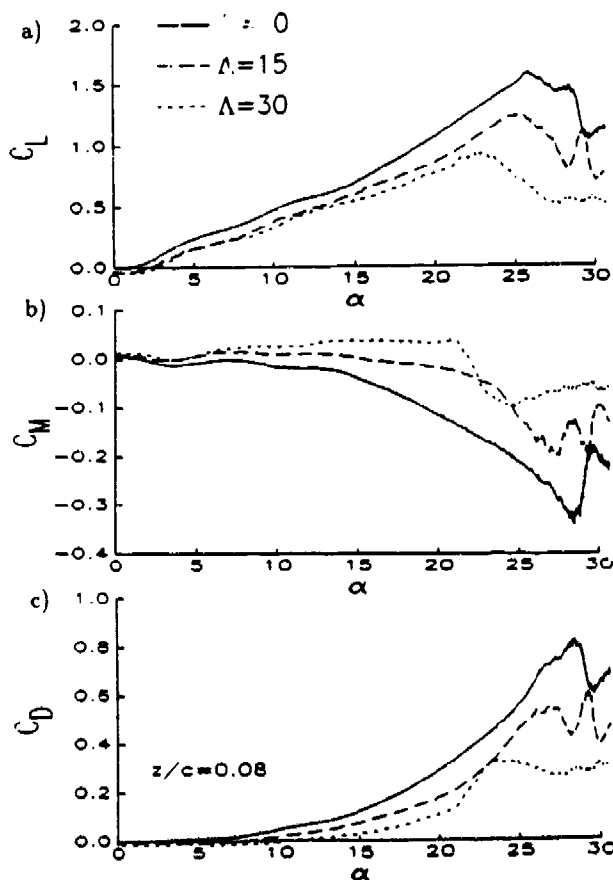


Fig. 19 Sweep effects on the aerodynamic loads at $z/c=0.08$, during $0 \rightarrow 30^\circ$ ramps with $\Lambda = 0.02$, and $M_c = 0.3$.

One example is the three post-stall peaks in $C_L - QS$ at $\Lambda = 15^\circ$ (Fig. 20a). This type of strong oscillation occurred at several other test conditions at this sweep angle. Weaker post-stall oscillations were more common at $\Lambda = 0$ and 30° . Strong oscillations associated with periodic vortex shedding were previously observed during 2-D testing at higher pitch rate.²⁰ The connection between sweep, tip effects, and post-stall oscillations is not yet apparent.

Lift and moment contours for $\Lambda = 0.02$ ramps at $M_c = 0.3$ are shown in Figs. 13 (for $\Lambda = 0^\circ$), 21 (for $\Lambda = 15^\circ$), and 22 (for $\Lambda = 30^\circ$). The C_L contours will be discussed first. For $z/c \leq 1$ there are major differences with sweep both during and after stall. Maximum lift occurs earlier (at lower α) inboard at $\Lambda = 0^\circ$ (Fig. 13a), but earlier near the tip at $\Lambda = 30^\circ$ (Fig. 22a). The high lift ($C_L \geq 1.4$) plateau extends over the complete span at $\Lambda = 0$, but only out to $z/c \approx 0.3$ at $\Lambda = 15^\circ$ (Fig. 21a) and to $z/c \approx 0.5$ at $\Lambda = 30^\circ$.

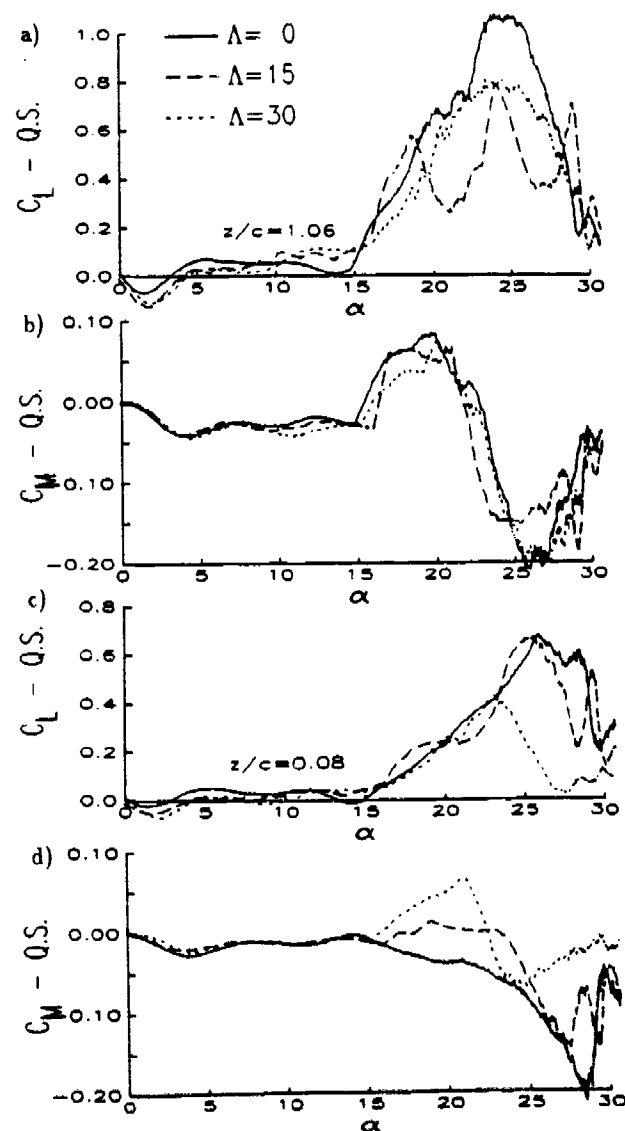
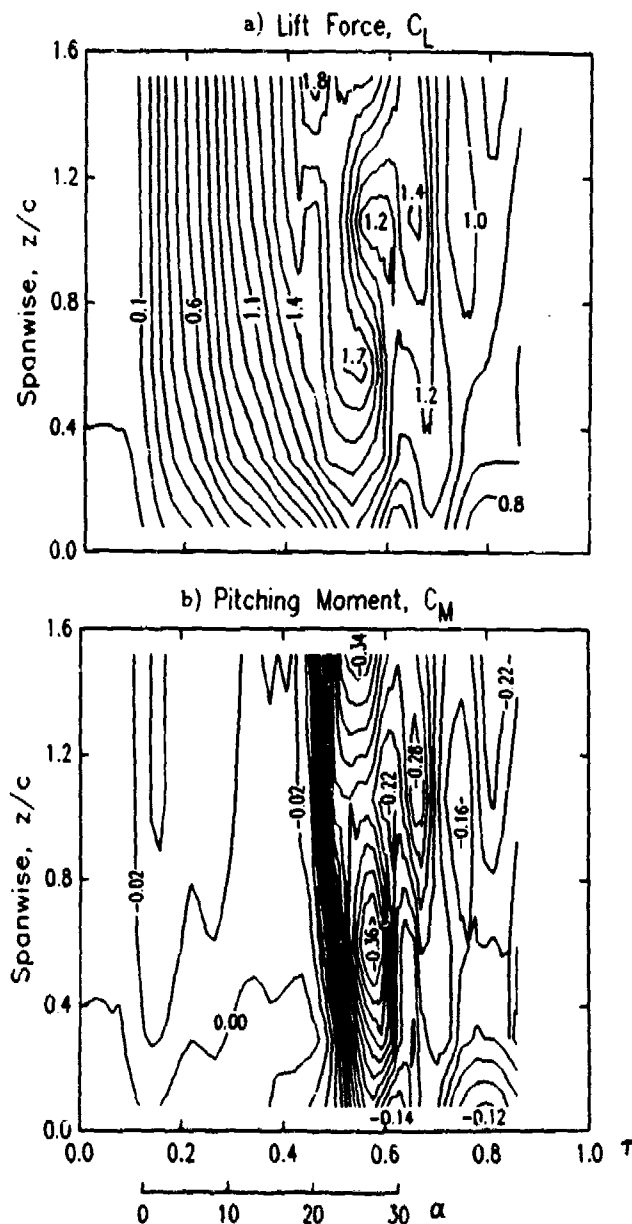


Fig. 20 Sweep effects on the unsteady increment to the loads at $z/c=1.06$ and 0.08 , during $0 \rightarrow 30^\circ$ ramps with $\Lambda=0.02$, and $M_c = 0.3$.

This is a result of the reduced unsteady lift increments for the swept wing (Fig. 20), and indicates that the enhanced tip lift observed on unswept wings⁵ may vanish with sweep.

In the post-stall region, both the C_L and C_M contours exhibit large qualitative differences with sweep. At $\Lambda = 0$ (Fig. 13) the contours are widely spaced, indicating small spanwise and temporal gradients. At $\Lambda = 15^\circ$ (Fig. 21) the contours are mostly vertical (independent of spanwise position), but show a strong oscillation with time. Finally, at $\Lambda = 30^\circ$ (Fig. 22), the contours are approaching horizontal, implying a strong spanwise gradient in a largely steady flow.

The differences in stall characteristics are most apparent in the moment contours. The distortion of the contours for $z/c < 0.3$ caused by the tip vortex of the unswept wing (Fig. 13b) has largely vanished at $\Lambda = 15^\circ$ (Fig. 21b). At this Λ there is still a slight slant in the contour lines from upper left to lower right for $z/c \geq 1$, corresponding to the delay in stall. At $\Lambda = 30^\circ$ (Fig. 22b) the slant is reduced, implying nearly simultaneous stall over the entire span. A peak negative moment of $C_M \approx -0.38$ occurs inboard for $\Lambda = 30^\circ$, in comparison with a peak of -0.32 at $\Lambda = 0$. There is also a much larger spanwise moment gradient after stall at $\Lambda = 30^\circ$. C_M changes smoothly from -0.38 at $z/c = 1.52$ to $C_M \approx -0.05$ at $z/c = 0.08$.



TIP CAP GEOMETRY EFFECTS

The final parameter change to be discussed is removing the approximate body of revolution ('round') tip end cap (Fig. 1), and substituting a flat plate at $z/c = 0$. As shown in Table 1, a small number of conditions were repeated with the square tip cap. Figure 23 shows a typical comparison. At $z/c = 0.59$ (Fig. 23a) the lift curves for ramps at $M_c = 0.2$, $\Lambda = 0.01$, and $\Lambda = 0$ show only minor differences between the two geometries. (The symbols represent steady-state data for the round tip.) This independence from tip cap geometry is characteristic of results for $z/c > 0.08$. At $z/c = 0.08$ (Fig. 23b), the square tip increases the lift during the entire motion. C_L^{max} is increased from 1.4 to 1.8. Pressure time histories (not shown) indicate that the tip vortex has a stronger and more concentrated effect on the pressures over the aft 40% of chord. This leads to a substantial increase in the negative pitching moment, as shown in Fig. 20c. One consequence of the higher tip load is a somewhat earlier stall, by $\Delta\alpha \approx 2^\circ$.

An earlier experiment²⁰ on an unswept wing tip oscillating at low amplitude and Mach number also showed much stronger tip vortex effects for $z/c \leq 0.05$ with a square tip. Similar results were also measured on a hovering (steady) helicopter rotor model.³⁰ Two effects may contribute to the differences in the tip loads. First, the sharp corners of the square tip will define a fixed separation point for the spanwise flow, and concentrate the vorticity. Second, steady-state oil flow visualizations (not shown) indicate that the tip vortex rolls up near the midchord of the round tip cap. At this location the round tip extends out to $z/c \approx -0.04$, so the vortex is farther from the measuring station at $z/c = 0.08$.

The tip geometry effects are substantially eliminated at $\Lambda = 30^\circ$. As shown in Fig. 22d, the unsteady lift coefficients for the $\Lambda = 0.01$, $M_c = 0.3$ ramps are virtually the same. The only difference is a small change in the quantitative behavior near stall. This is consistent with the previous observation that sweep moves the tip away from the vortex, so that changes to the vortex will have much less influence on the wing.

CONCLUSIONS

Initial examination of the data from this experiment has produced the following conclusions:

1. The steady-state aerodynamic load characteristics of this model, including the effects of sweep, compressibility, and spanwise position, are as expected for a simple subsonic wing.
2. The dynamic stall phenomenon on the inboard portion of the wing is qualitatively similar to that observed in 2D. The unsteady increments to the loads and the delay in stall increased with increasing pitch rate and decreased with increasing Mach number.

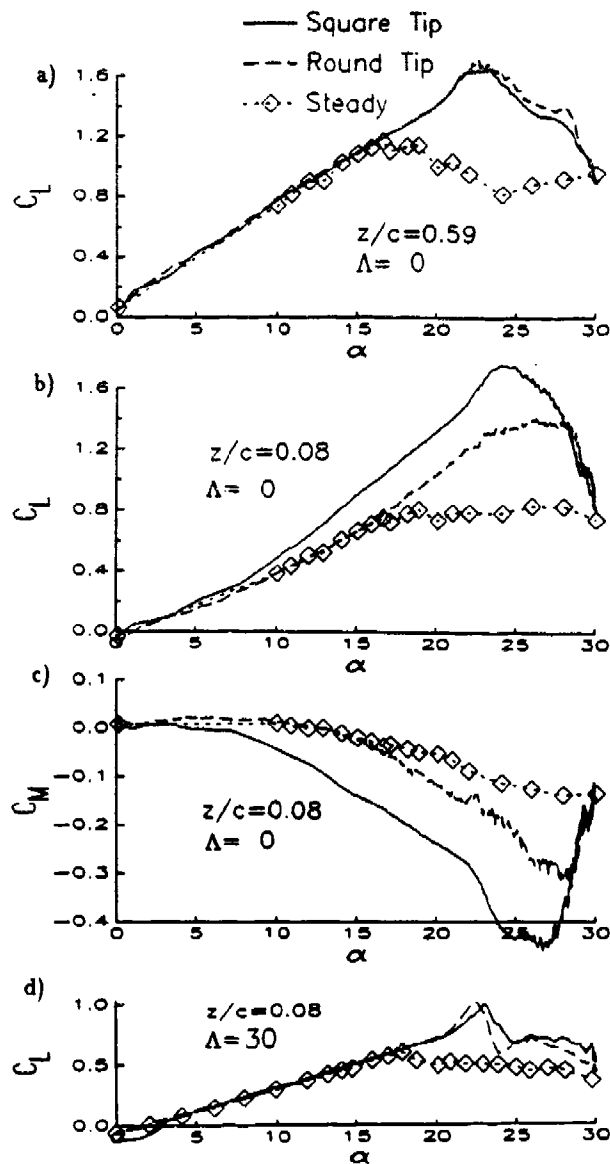


Fig. 23 Effect of tip cap geometry on the aerodynamic loads at $z/c=0.59$ and 0.08 , during $0 \rightarrow 30^\circ$ ramps at $\Lambda = 0$ and 30° , $\Lambda=0.01$, and $M_c = 0.2$.

3. Data for Mach numbers up to $M_c = 0.6$ indicate that even though the dynamic stall process is weakened by a region of local supersonic flow terminated by a shock, measurable stall delays and unsteady load increments persist.
4. For the unswept wing, the tip vortex reduces the effective angle of attack, delays dynamic stall, and, at $M_c \leq 0.3$, interacts with the stall vortex to enhance the unsteady airloads near the tip. This enhancement relative to the inboard loads is reduced at higher Mach numbers.

5. For the swept wing, the interaction between the tip vortex and the wing is reduced. Dynamic stall occurs nearly simultaneously over the entire span, and the unsteady increments to the tip loads are less than those inboard. Post-stall characteristics, including temporal oscillations and spanwise gradients are very different at $\Lambda = 0, 15$, and 30° .
6. Replacing the round tip cap with a flat plate produces strong tip vortex effects and increases the lift near the tip. This effect is important only near $\Lambda = 0$.

The results presented in this paper have provided a broad survey of the acquired data. The emphasis has been on the large scale effects of the major parameters. Future publications will include a more detailed examination of the pressure measurements (including stall vortex formation and propagation characteristics), results for sinusoidal motions and for the negative pitch rate portions of the ramps, results from the unsteady transition measurements, and a more extensive examination of the interactions between the parameters.

ACKNOWLEDGMENTS

The instrumented model, the wind tunnel test, and the analysis of the results were funded by the U.S. Army Research Office and the U.S. Air Force Office of Scientific Research, under Contract DAAL03-89-C-0013. Dr. Thomas J. Doligalski of ARO was the technical monitor. Dr. Hank E. Helin of AFOSR was instrumental in initiating the program. The model support and drive system was supplied by the Sikorsky Aircraft Division of United Technologies. The authors thank John Ayer and the staff of the UTRC LSWT for their assistance during the test.

REFERENCES

1. St. Hilaire, A.O., Carta, F.O., Fink, M.R., and Jepson, W.D., "The Influence of Sweep on the Aerodynamic Loading of an Oscillating NACA 0012 Airfoil," NASA CR-3092, 1979.
2. St. Hilaire, A.O. and Carta, F.O., "Analysis of Unswept and Swept Wing Chordwise Pressure Data from an Oscillating NACA 0012 Airfoil Experiment," NASA CR 3567, 1983.
3. Walker, J.M., Helin, H.E., and Chou, D.C., "Unsteady Surface Pressure Measurements on a Pitching Airfoil," AIAA Paper 85-0532, March 1985.
4. Robinson, M.C. and Wissler, J.B., "Unsteady Surface Pressure Measurements on a Pitching Rectangular Wing," AIAA Paper 88-0328, Jan. 1988.
5. Robinson, M.C. and Wissler, J.B., "Pitch Rate and Reynolds Number Effects on a Pitching Rectangular Wing," AIAA Paper 88-2577-CP, 1988.
6. Albertson, J.A., Troutt, T.R., and Kedzie, C.R., "Unsteady Aerodynamic Forces at Low Airfoil Pitching Rates," AIAA Paper 88-2579-CP, 1988.
7. Walker, J.M. and Robinson, M.C., "Dynamic Stall Development Dependence on Wing Planform," 4th Symposium on Numerical and Physical Aspects of Aerodynamic Flows, Long Beach, CA, Jan. 1989.
8. Chandrasekhara, M.S. and Carr, L.W., "Flow Visualization Studies of the Mach Number Effects on the Dynamic Stall of an Oscillating Airfoil," *Journal of Aircraft*, Vol. 27, June 1990, pp. 516-522.
9. Chandrasekhara, M.S., Ahmed, S., and Carr, L.W., "Schlieren Studies of Compressibility Effects on Dynamic Stall of Airfoils in Transient Pitching Motion," AIAA Paper 90-3038-CP, 8th AIAA Applied Aerodynamics Conference, Portland, OR, 1990.
10. Carr, L.W., Chandrasekhara, M.S., Ahmed, S., and Brock, N.J., "A Study of Dynamic Stall Using Real Time Interferometry," AIAA Paper 91-0007, 29th Aerospace Sciences Meeting, Reno, NV, Jan 1991.
11. Jumper, E.J., and Stephen, E.J., "Toward Unsteady Lift Augmentation: An Assessment of the Role of Competing Phenomena in Dynamic Stall," 2nd AFOSR Workshop on Unsteady Separated Flows, USAF Academy, CO, July 1987.
12. Freymuth, P., "Vortex Patterns of Dynamic Separation," Chapter 11 of the Encyclopedia of Fluid mechanics, N.P. Chermisinoff, Ed., Gulf Publishing Co., Vol 8., 1989.
13. Strickland, J.H., and Graham, G.M., "Dynamic Stall Inception Correlation for Airfoils Undergoing Constant Pitch Rate Motions," *AIAA Journal*, Vol. 24, April 1986, pp. 678-680.
14. Favier, D., Agnes, A., Barbi, C., and Maresca, C., "Combined Translation/Pitch Motion: A New Airfoil Dynamic Stall Simulation," *Journal of Aircraft*, Vol. 25, Sept. 1988, pp. 805-814.
15. Patterson, M.T., and Lorber, P.F., "Computational and Experimental Studies of Compressible Dynamic Stall," *Journal of Fluids and Structures*, Vol. 4, 1990, pp.259-285.
16. Ekaterinaris, J., "Compressible Studies of Dynamic Stall," AIAA Paper 89-0024, 27th Aerospace Sciences Meeting, Reno, NV, Jan. 1989.
17. Visbal, M.R., "Effect of Compressibility on Dynamic Stall of a Pitching Airfoil," AIAA Paper 88-0132, 26th Aerospace Sciences Meeting, Reno, NV, Jan 1988.
18. Visbal, M.R., "On Some Physical Aspects of Airfoil Dynamic Stall," ASME Symposium on Non-Steady Fluid Dynamics, Toronto, Canada, June 1990.

19. Lorber, P.F., "Aerodynamic Results of a Pressure-Instrumented Model Rotor Test at the DNW," American Helicopter Society 46th Annual Forum, Washington DC, May 1990, to be published in AHS Journal, July 1991.
20. Lorber, P.F., and Carta, F.O., "Airfoil Dynamic Stall at Constant Pitch Rate and High Reynolds Number," *Journal of Aircraft*, Vol. 25, June 1988, pp. 548-556.
21. Lorber, P.F., and Carta, F.O., "Unsteady Stall Penetration Experiments at High Reynolds Number", AFOSR TR-87-1202, April 1987.
22. Lorber, P.F., and Carta, F.O., "Incipient Torsional Stall Flutter Experiments on a Swept Three-Dimensional Wing," AIAA Paper 91-0935, 32nd Structures, Structural Dynamics, and Materials Conference, Baltimore, MD, April 1991.
23. Lorber, P.F., Carta, F.O., and Covino, A.F., Jr., "Sweep, Compressibility, Rate, and Geometry Effects on the Dynamic Stall of a Three-Dimensional Wing," UTRC Report 958325-91-4, Nov. 1991.
24. Rae, W.H., and Pope, A., *Low-Speed Wind Tunnel Testing*, 2nd Edition, John Wiley & Sons, NY 1984.
25. Marcolini, M.A., Lorber, P.F., Miller, W.T., and Covino, A.F. Jr., "Frequency Response Calibration of Recess-Mounted Pressure Transducers," Instrumentation Society of America 37th Annual Instrumentation Symposium, San Diego, CA, May 1991.
26. Schlichting, H., and Truckenbrodt, E., *Aerodynamics of the Airplane*, McGraw Hill International Book Co. New York, 1979.
27. Van Dyke, M., *An Album of Fluid Motion*, Parabolic Press, Stanford, CA, 1982.
28. Fung, K.Y., and Carr, L.W., "Effects of Compressibility on Dynamic Stall", *AIAA Journal* Vol. 29, February 1991, pp. 306-308.
29. Triebstein, H., "Unsteady Pressure Measurements on Rotor Blade Tips with Incidence," *AIAA Journal* Vol 17, May 1979, pp. 514-518.
30. Gray, R.B., McMahon, H.M., Shenoy, K.R., and Hammer, M.L., "Surface Pressure Measurements at Two Tips of a Model Helicopter Rotor in Hover," NASA CR 3281, May 1980.

UNSTEADY TRANSITION MEASUREMENTS ON A PITCHING THREE-DIMENSIONAL WING

Peter F. Lorber and Franklin O. Carta

United Technologies Research Center
East Hartford, CT 06108

ABSTRACT

Boundary layer transition measurements have been made during an experimental study of the aerodynamics of a rectangular wing undergoing unsteady pitching motions. The wing was tested at chordwise Mach numbers between 0.2 and 0.6, at sweep angles of 0, 15, and 30°, and for steady state, sinusoidal, and constant pitch rate motions. The model was scaled to represent a full size helicopter rotor blade, with chord Reynolds numbers between 2 and 6×10^6 . Sixteen surface hot film gages were located along three spanwise stations: 0.08, 0.27, and 0.70 chords from the wing tip. Qualitative heat transfer information was obtained to identify the unsteady motion of the point of transition to turbulence. In combination with simultaneous measurements of the unsteady surface pressure distributions, the results illustrate the effects of compressibility, sweep, pitch rate, and proximity to the wing tip on the transition and relaminarization locations.

NOMENCLATURE

A	pitch rate, $\dot{\alpha}c/2U_c$
c	airfoil chord (17.3 in.)
C_p	pressure coefficient, $(P - P_\infty)/q$
C_p^*	pressure coefficient for locally sonic chordwise velocity
k	reduced frequency, $\omega c/2U_c$
M_c	chordwise Mach number, $M_\infty \cos \Lambda$
M_∞	freestream Mach number
P_∞	freestream static pressure
q	dynamic pressure, $\frac{1}{2}\rho_\infty U_c^2$
t	time
T	oscillation period
Re	Reynolds number, cU_c/ν
U_c	chordwise component of freestream velocity, $U_\infty \cos \Lambda$
U_∞	freestream velocity
x	distance along chord from leading edge
z	distance along span from tip leading edge
$\dot{\alpha}$	pitch rate, rad/sec
α	geometric angle of attack
ramp: $\alpha = \alpha_{min}, \tau \leq 0.125$	
$\alpha = \alpha_{min} + 2(\tau - 0.125)(\alpha_{max} - \alpha_{min}),$	
$0.125 \leq \tau \leq 0.625$	
$\alpha = \alpha_{max}, \tau \geq 0.625$	
sine: $\alpha = \alpha_0 + \alpha_1 \cos 2\pi\tau$	

α_{ss}	steady state stall angle
Λ	sweep-back angle
ν	kinematic viscosity
ρ_∞	freestream density
τ	nondimensional time, t/T
ω	circular frequency, $2\pi/T$

INTRODUCTION

Knowledge of the state of the boundary layer is a prerequisite to understanding the aerodynamics of airfoils and wings in unsteady motion. In particular, the response during dynamic stall (pitching motion penetrating beyond the steady-state stall angle) may differ substantially, depending upon whether the boundary layer prior to separation is laminar or turbulent, completely subsonic or locally supersonic, fully attached or containing regions of reversed flow. The boundary layer state is in turn influenced by the Reynolds and Mach numbers of the external flow, airfoil contours and surface roughness, freestream turbulence level, and the presence of sweep and three-dimensionality.

Numerous investigations of dynamic stall have been conducted, at Reynolds numbers from 10^3 to 10^7 , at Mach numbers from essentially incompressible to nearly transonic, and for a wide variety of two- and three-dimensional geometries. Most have concentrated on measurements of either the aerodynamic forces (surface pressures or overall model loads) or the flow field characteristics (using various visualization techniques). Only a few studies have included measurements of the boundary layer state. The most informative approach is to obtain complete boundary layer profiles at numerous stations by means of hot wire anemometry¹ or laser velocimetry.² This is usually a difficult and time-consuming process. A simpler approach is to use surface-mounted instrumentation to obtain qualitative characteristics. Sublimation, surface visualization, and shear-sensitive liquid crystal techniques have proven useful in steady or slowly varying flow. For higher frequency ($f \approx 10\text{Hz}$) conditions, and when data can only be efficiently acquired electronically, the surface hot film gage is preferred.³⁻⁶

This paper presents the results of such surface hot film gage measurements of the state of the boundary layer on a three-dimensional wing model. The model was scaled to be representative of a full scale helicopter main rotor, with Reynolds numbers of $2-6 \times 10^6$. It was tested at freestream Mach numbers between 0.2 and 0.6, and in both swept and unswept configurations. Previous publications⁵⁻¹⁰ have described the surface pressure and integrated aerodynamic

Presented at the Fifth Symposium on Numerical and Physical Aspects of Aerodynamic Flows, Long Beach, CA, January 13-15, 1992.

load results from the current experiment and from an earlier experiment using a two-dimensional (tunnel-spanning) version of this model. The boundary layer state measurements described in the current paper should contribute to the understanding of the previous results. The measured transition locations should also be useful for computational simulation of the experiment.

DESCRIPTION OF EXPERIMENT

The model was a straight, rectangular, untwisted, semi-span wing of 17.3 in. (44 cm) chord and 48 in. (122 cm) span (Fig. 1). The aspect ratio of a full wing would be 3.6. The wing consisted of a steel spar and fiberglass airfoil panels, and had a Sikorsky SSC-A09 9% thickness cambered section (Fig. 2). Airfoil coordinates have been provided in Ref. 6. The surface was kept smooth, with no artificial roughness added to alter the transition characteristics. The wing was mounted at sweep angles of 0, 15, and 30° from the side wall of the 8 ft (2.4 m) octagonal test section of the UTRC Large Subsonic Wind Tunnel. Additional airfoil panels were added to the spar at non-zero sweep angles in order to keep the wing tip $\frac{1}{4}$ chord at the tunnel centerline. The experiment was conducted at five chordwise Mach numbers, $M_c = 0.2, 0.3, 0.4, 0.5$, and 0.6 . Based upon the model chord and the fact that this wind tunnel is vented to atmosphere in the stilling section, the chord Reynolds numbers for these experiments were approximately equal to $10^7 \times M_c$. Longitudinal turbulence levels have been measured in this facility using an LDV system to be between 0.7 and 1.2% of the freestream velocity¹¹. Measurements with an unsteady pitot-static probe during the current experiment indicated root-mean-square unsteadiness equivalent to 0.35–0.5% of the freestream velocity for $0.3 \leq M_c \leq 0.6$, and 0.9% at $M_c = 0.2$.

A hydraulic rotary drive oscillated the model in pitch about the line connecting the root and tip $\frac{1}{4}$ chord. Two

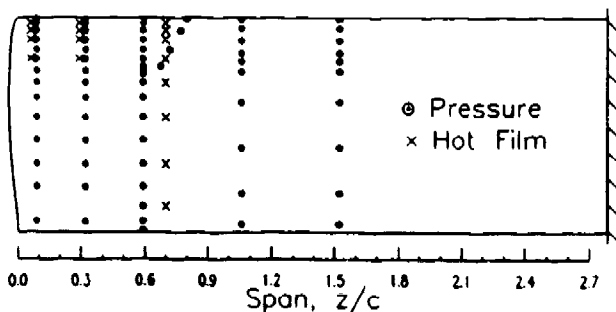


Fig. 1. Wing planform and instrumentation locations.

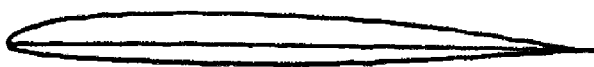


Fig. 2. SSC-A09 airfoil section.

pitching waveforms were used, sinusoids and ramps. The sinusoids were performed at frequencies from 1.25 to 12 Hz ($0.025 \leq k \leq 0.15$), at amplitudes primarily of 6 and 10°, and at numerous mean angles. The ramps began at a steady-state condition (usually $\alpha = 0$), increased at constant rate to a maximum angle, maintained that maximum for a short time, and then returned to the initial condition. The maximum pitch angles were 30° at $M_c = 0.2$ and 0.3 , 25° at $M_c = 0.4$, 18° at $M_c = 0.5$, and 13.5° at $M_c = 0.6$. The nondimensional pitch rates were selected between $A = \dot{\alpha}c/2U_\infty$ of 0.001 and 0.025, bounded by a limiting dimensional rate of 560°/sec. Data were obtained for a total of 259 large amplitude sinusoids, 120 ramps, 260 small amplitude sinusoids, and 295 steady-state conditions. The complete data set will be made available in a technical report and a set of digital data tapes.

Unsteady surface pressure measurements were made on the wing model by 112 miniature transducers distributed among five spanwise stations. The suction surface transducer locations are shown by the dots in Fig. 1. The chordwise arrays on the upper surface had 10, 14, or 18 transducers each. The lower surface arrays were less dense, containing 6 or 18 transducers each. The transducers were installed so as to retain a smooth surface contour and achieve a flat frequency response to at least 4 kHz. The pressures were integrated along the chord at each spanwise station to determine the unsteady lift, pressure drag, and pitching moment coefficients.

Sixteen flush-mounted surface hot film gages were used to determine transition and separation locations. As shown by the x-marks in Fig. 1, the gages were located in chordwise arrays at three spanwise stations, $z/c = 0.08, 0.27$, and 0.70 . (Note that $z = 0$ is at the wing tip.) The chordwise stations were $x/c = 0.026, 0.060, 0.103, 0.192, 0.302, 0.464, 0.682$, and 0.880 . All eight chordwise stations were used at $z/c = 0.70$, while only the forward four stations were used at $z/c = 0.08$ and 0.27 . The $x/c = 0.026$ and 0.103 gages at $z/c = 0.70$ were offset by 1 in. (to $z/c = 0.65$) to reduce the chance for thermal interference. TSI model 1268 gages were installed in holes drilled through the fiberglass airfoil skins. Each gage consists of a heated element deposited on the end of a 0.15 in. (0.38 cm) diameter quartz rod. The hot films were operated in the constant-temperature mode, at a nominal operating temperature of 225°C, corresponding to an overheat ratio (hot to cold gage resistance) of 1.35. The output voltage will increase with the heat transfer from the gage, and therefore, by the Reynolds analogy, with the shear stress at the wall. The anemometer circuits were mounted immediately outside of the wind tunnel wall to minimize lead resistance and noise.

The output voltages from both the pressure transducers and hot film gages were passed through a 10 kHz low pass filter, and digitized (to 15 bit accuracy) at a rate of 1024 samples per oscillation period (T). Ensemble-averaged time histories were computed using data from 20 pitching oscillations. Both the individual oscillations and the ensemble averages were recorded on digital magnetic tape.

The hot film results were intended to provide only qualitative information on transition and separation locations. When the flow over the hot film gage is laminar, the heat transfer is generally low, with little random unsteadiness. Movement of transition past the gage is indicated by a rapid rise in heat transfer, accompanied by an increase in the higher frequency, random portion of the signal. Separation is indicated by a low level of average heat transfer, but a high level of unsteadiness. Interpretation of hot film signals is simplified in a periodic unsteady flow because the changes from one flow state to another can be more readily identified than the characteristics of a steady-state flow. It is particularly difficult to determine if an individual signal with moderate unsteadiness is turbulent, separated, or transitional.

No attempt was made to obtain quantitative values of skin friction. Calibration of multiple surface mounted gages for unsteady flow is quite difficult, because of the need to either a) calibrate all probes in a reference unsteady flow prior to installation, b) provide a reference flow at each probe, or c) calibrate the probes by comparison to a traceable and portable reference probe. Surface-mounted quartz substrate gages (such as used here) have been shown to have limitations in unsteady flow, including different steady and unsteady calibrations^{12,13}. The difficulties are created because heat is transferred not only from the active element to the fluid, but also from the element to the substrate, from the substrate to the model, and from the substrate to the fluid. The characteristic lengths and times for these various processes differ, resulting in different steady and unsteady responses.¹² Surface gages with a cavity below the heated element have been more successful in obtaining quantitative unsteady data.^{14,15} The qualitative information at the relatively low frequencies (1-10Hz) of interest here should, however, be valid.

Transition information may also be obtained from the surface pressure data. As described in Refs. 1, 5, 6, and 16, transition is frequently accompanied by an increase in the higher frequency random component of the pressure, and by a small shift in the ensemble-average. The problem with this technique is that transition is not the only source of such pressure changes. The pressure information is most useful in confirming or extending transition information obtained from other means. For example, several hot film gages were not operating properly during the unswept portion of this experiment. The data from adjacent pressure transducers was used to cover the resulting gaps between functional hot films. Comparison between hot film and pressure information at other stations confirmed that the pressure changes were actually caused by transition.

STEADY CHARACTERISTICS

For each steady (fixed α) condition, hot film gage voltages were recorded over a 5 second period and averaged. Results for each value of α during a particular test series (at fixed M_c and Λ) were used to form a 'quasi-steady' data

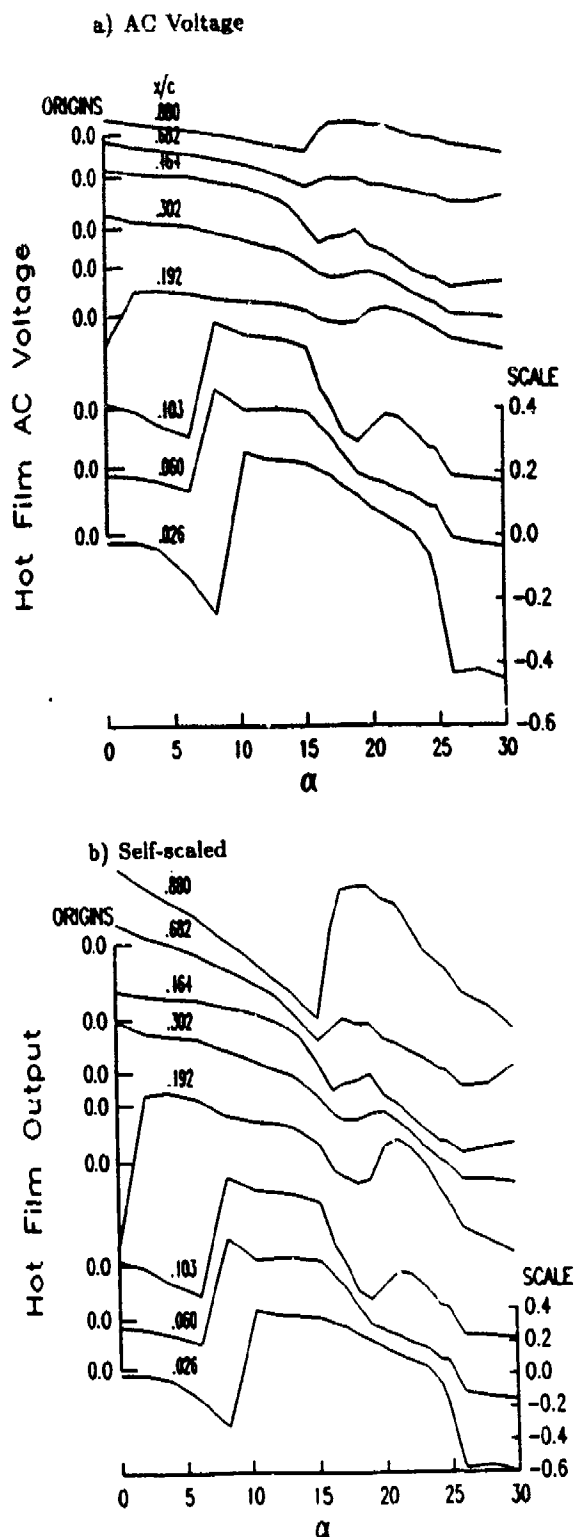


Fig. 3. Steady hot film results at $M_c = 0.3$, $\Lambda = 30$, and $z/c = 0.7$.

file containing hot film outputs as a function of α . Figure 3 shows an example for $M_c = 0.3$ and $\Lambda = 30^\circ$. The results for the 8 gages at $z/c = 0.7$ (the station furthest from the wing tip) are shown in two formats: as AC voltages (Fig. 3a)

and self-scaled to a peak-to-peak value of 1 (Fig. 3b). The AC voltage illustrates the magnitude of the output variations, while the self-scaled output allows regions of change to be easily identified and provides a clear qualitative picture. (Since the gages are not calibrated, quantitative comparisons between gages are not possible.) The origins for the output at each chordwise position (x/c) are along the left of the figure, and the scale is at the lower right. Because data points were only acquired every 1 or 2°, the quasi-steady series appear somewhat rough.

At $x/c = 0.026$ the sharp increase in heat transfer corresponding to the passage of the transition point over the gage occurs between $\alpha = 8$ and 10° . Similar sharp increases are also present for the $x/c = 0.06, 0.10$, and 0.19 gages, but at successively lower values of α . This indicates that at $\alpha = 0$, transition occurs between the $x/c = 0.19$ and 0.30 gages, and as α increases the transition point moves forward, occurring upstream of the $x/c = 0.026$ gage for $\alpha \geq 10^\circ$. Away from transition, the heat transfer decreases with increasing α in both laminar and turbulent regions prior to separation. This decrease is a consequence of the thickening of the boundary layer. It is present for $0 \leq \alpha \leq 8^\circ$ and $10^\circ \leq \alpha \leq 20^\circ$ at $x/c = 0.026$, and at $\alpha \leq 15^\circ$ for $x/c = 0.682$.

Separation is manifested by the sharp drop in heat transfer that occurs after $\alpha = 15^\circ$, most noticeably at $x/c = 0.06, 0.10$, and 0.19 . This sharp drop does not occur at the $x/c = 0.026$ station until $\alpha \approx 25^\circ$. On the aft portion of the wing, where the boundary layer is never laminar, the self-scaling emphasizes a 'bump' of increased heat transfer that occurs while the separation process is underway (between its initiation at $\alpha \approx 15^\circ$ and completion at $\alpha \approx 26^\circ$). A possible explanation is that the turbulent boundary layer near the trailing edge is already quite thick at $\alpha = 15^\circ$, and in fact may have thin regions of reversed flow. The resulting heat transfer from the hot film gages would be quite low. The vorticity shed during separation energizes the trailing edge flow, increasing the heat transfer. Once the process is completed and the flow has separated over the entire section, the average output returns to a low level. (The random variations, not shown here, remain high.)

A more quantitative picture of the effect of changes in Mach number, sweep angle, and spanwise position on steady flow transition is provided in Fig. 4. The symbols represent the angle of attack, α , at which the transition point moves past the hot film gage at each chordwise position, x/c . The selected value of α was that corresponding to the most rapid increase of hot film output, which generally occurred 20-40% of the way from the start to the finish of the transition process. Figure 4a illustrates the effect of Mach number at fixed spanwise position ($z/c = 0.70$) and sweep angle ($\Lambda = 30^\circ$). At $M_c = 0.2$ transition occurs near $x/c = 0.3$ at $\alpha \approx 0$, and moves forward of $x/c = 0.026$ by $\alpha = 10^\circ$. At $M_c = 0.3$ transition is always forward of $x/c = 0.3$, and moves past the $x/c = 0.19, 0.10, 0.06$, and 0.026 gages at somewhat lower angles of attack than at $M_c = 0.2$. This trend continues at $M_c = 0.4$, as transition always occurs before $x/c = 0.19$,

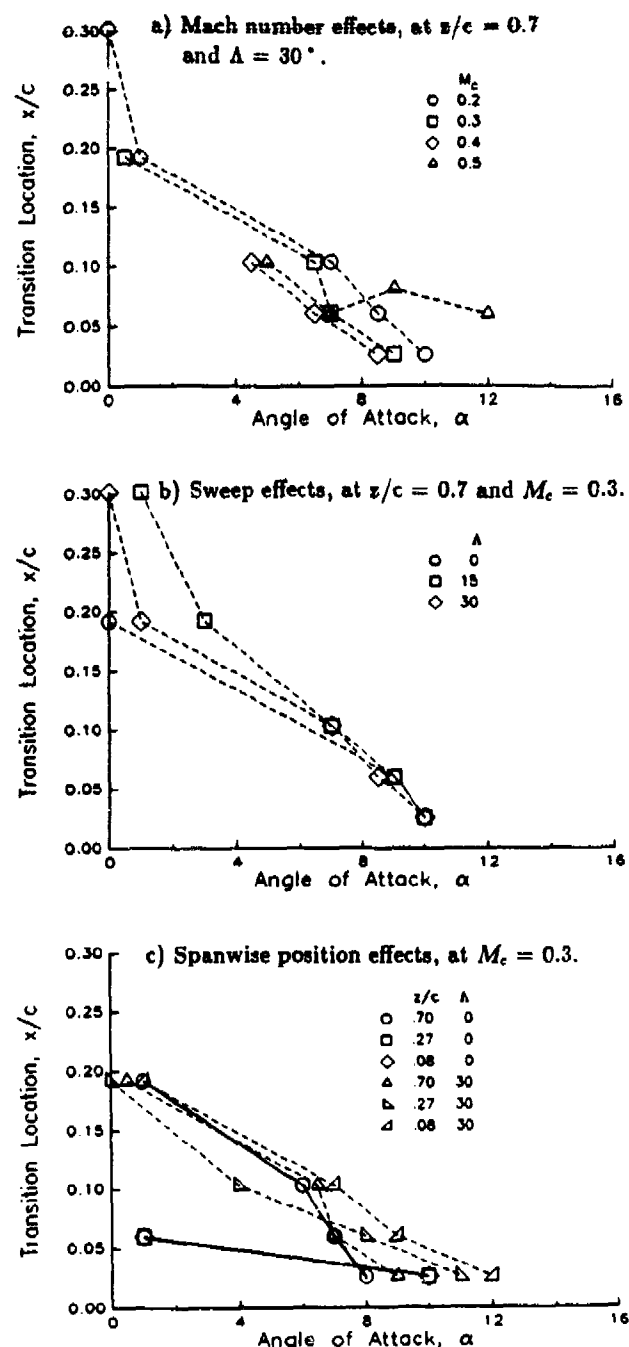


Fig. 4. Mach number, sweep angle, and spanwise position effects on transition locations in steady flow.

and moves forward of $x/c = 0.026$ at $\alpha \approx 8.5^\circ$, a value approximately 1.5° less than at $M_c = 0.2$. These results are consistent with previous data from the unswept 2-D version of this model at $M_c = 0.2$ and 0.4 .⁶ The primary difference is that the lower effective angle of attack of the 3-D model (a result of the wing tip vortex⁹) delays the forward motion of transition to slightly higher geometric angles. The final data shown on Fig. 4a are at $M_c = 0.5$. The transition point ceases forward motion near $x/c = 0.06$ at $\alpha \approx 7^\circ$. The shock effects responsible for this will be discussed in the section on Mach number effects on unsteady transition.

Figure 4b illustrates the effect of sweep angle for fixed spanwise location ($z/c = 0.7$) and Mach number ($M_c = 0.3$). At lower angles of attack ($\alpha \leq 6^\circ$), transition is delayed by non-zero sweep. At $\alpha = 0$ transition on the swept wing occurs near $x/c = 0.3$, approximately 10% of chord further downstream than at $\Lambda = 0$. The forward motion of transition is delayed by up to 3° in α at $\Lambda = 15^\circ$, and by up to 1° at $\Lambda = 30^\circ$, in comparison to the $\Lambda = 0$ results. As α increases this difference is reduced. The motion of the transition point past the $x/c = 0.026$ gage occurs at $\alpha \approx 10^\circ$ for all three sweep angles.

The effect of spanwise position is illustrated in Fig. 4c at fixed Mach number ($M_c = 0.3$) and at two sweep angles ($\Lambda = 0$ and 30°). At $\Lambda = 0$ (the solid lines) there is a substantial difference between the inboard ($z/c = 0.7$) and tip ($z/c = 0.27$ and 0.08) stations. Compared to the inboard results, transition near the tip occurs further forward (at $x/c \approx 0.06$) at low α but moves forward more slowly (passing $x/c = 0.026$ at 2° higher α). Several mechanisms appear to be involved. Proximity to the wing tip implies proximity to the tip vortex, which reduces the effective angle of attack. This would tend to delay forward motion of transition. In contrast, transition may be promoted by the three-dimensionality and unsteadiness introduced by the tip vortex. It is possible that at low α this second mechanism causes early transition, while the forward motion of transition is delayed by the reduced effective angle of attack. These differences do not appear at $\Lambda = 30^\circ$, or at $\Lambda = 15^\circ$ (not shown). This is plausible since the tip vortex has less influence on the aerodynamic loading when the wing is swept.⁹

The simplest example of transition in unsteady flow is provided by data obtained during constant pitch rate ramps. Figure 5 shows ensemble averaged hot film and pressure time histories for an $\alpha = 0$ to 30° ramp at $M_c = 0.2$, $\Lambda = 15^\circ$, and $A = 0.005$. The series of pressure coefficient time histories at $z/c = 0.59$ shown at the left of the figure show a smooth increase in pressure until an abrupt separation occurs at a nondimensional time of $\tau = 0.45$ (corresponding to $\alpha = 20^\circ$). After separation a negative pressure peak associated with the dynamic stall vortex travels aft along the chord. This is followed by a region of constant pressure indicating massive separation. Further details on the pressure measurements during dynamic stall are provided in Refs. 6, 9, and 10.

The corresponding hot film time gage time histories at $z/c = 0.7$ are shown at the lower right of Fig. 5. Note that because data are acquired 1024 times over the period, T , the temporal resolution of the unsteady measurements is much greater than that of the quasisteady measurements (Fig. 3). Thus the movement of transition past the gages

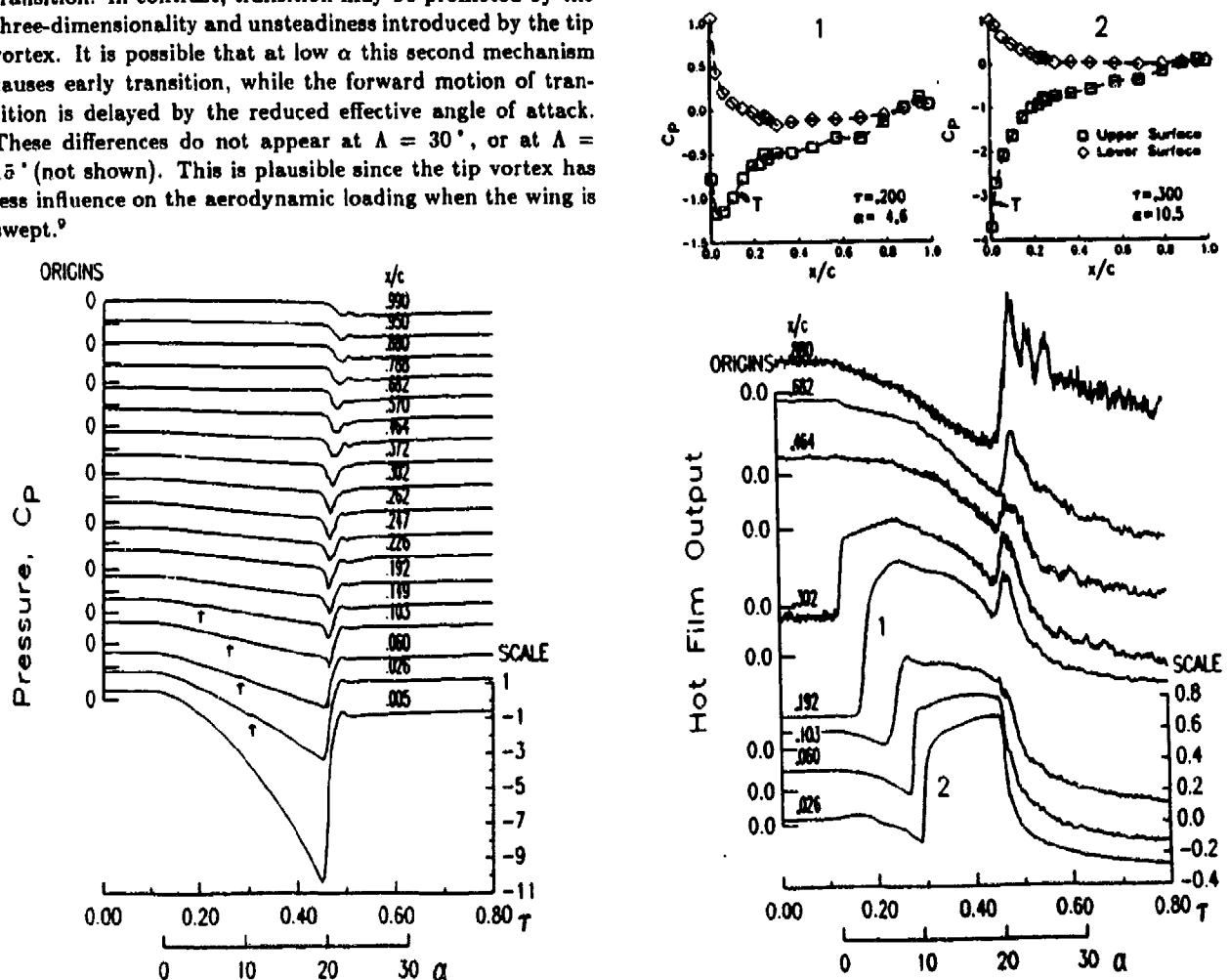


Fig. 5. Pressure and hot film time histories and chordwise pressure distributions at $M_c = 0.2$, for a ramp at $A = 0.005$, $\Lambda = 15^\circ$, and $z/c = 0.7$.

is very sharply defined. Over the initial (steady state, $\alpha = 0$) portion of the cycle, transition occurs just aft of the $x/c = 0.30$ gage, but once the pitching motion begins at $\tau = 0.125$, transition immediately moves forward. The motion continues until $\tau = 0.3$ ($\alpha \approx 10^\circ$), when transition occurs ahead of the $x/c = 0.026$ gage. As shown by the chord-wise pressure distributions at $\tau = 0.2$ (number 1 in Fig. 5) and at $\tau = 0.3$ (number 2), transition (indicated by the 'T') typically occurs shortly after the suction peak. This is in agreement with the experimental and theoretical work reported in Ref. 17 for incompressible flow over airfoils at a Reynolds number range of $10^5 \leq Re \leq 10^6$. The strong adverse pressure gradient downstream of the suction pressure peak was found to induce transition within 1-2% of chord aft of the peak.

The series of arrows on the pressure time histories (the left portion of Fig. 5) indicate local pressure increases that approximately correspond to the transition measurements obtained with the hot film gages (the right portion of the figure). The pressure increases are quite small, and are only apparent between $x/c = 0.026$ and 0.149. They generally occur slightly after the hot film gage output rises, i.e. when transition is complete.

The results in Fig. 5 indicate that transition has moved very close to the leading edge by $\tau = 0.3$, well before the onset of separation at $\tau = 0.45$ ($\alpha = 20^\circ$). There is no indication of a significant transitional separation bubble. This implies that dynamic stall for the SSC-A09 section at Reynolds numbers greater than 2×10^5 is a result of turbulent boundary layer separation. This differs from the observations reported in Refs. 1 and 2, for the NACA 0012 airfoil at lower Reynolds numbers (approximately $3-5 \times 10^4$). For those conditions, the transitional separation bubble appears to be a key participant in the dynamic stall process. The sequence observed in the current experiment, laminar boundary layer - turbulent boundary layer - separation, has also been observed during other high Reynolds number experiments, such as Refs. 3 and 4. The separation process for the current model is discussed at greater length in Ref. 10.

The preceding paragraphs have described the general behavior of transition during an unsteady pitching motion. This behavior is similar to that observed at other pitch rates, sweep angles, spanwise positions, and Mach numbers (at least when local supersonic flow effects are minimal). The actual location of the transition point, and its motion as α is increased is, however, dependent on all of these parameters. These dependencies will be discussed next.

Pitch Rate Effects

The effect of pitch rate on the location of transition is illustrated in Fig. 6. Figure 6a shows results at the inboard station, $z/c = 0.7$, for ramps at a series of five pitch rates between $A = 0.001$ and 0.02, at fixed Mach number ($M_c = 0.3$) and sweep angle ($\Lambda = 0$). Steady results are also included. Note that the results at $x/c = 0.10$ and 0.149 were obtained using RMS pressure data, because of the problems with the 0.10 hot film gage described above. (There is no

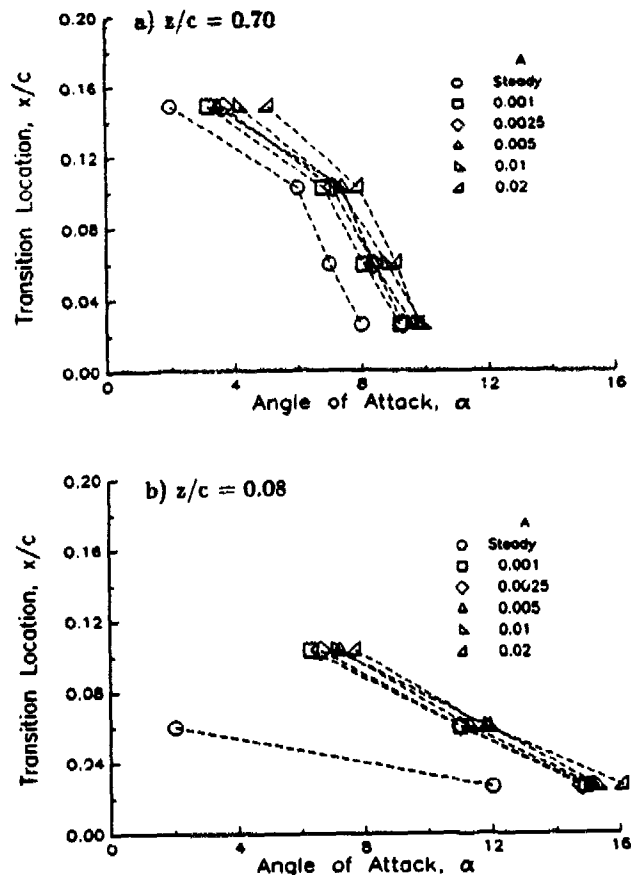


Fig. 6. Effect of pitch rate on transition locations for ramp motions at $M_c = 0.3$, and $\Lambda = 0$.

hot film at $x/c = 0.149$). The primary effect of increasing the pitch rate is to delay forward motion of the transition point. There is a delay of approximately 0.8° between the steady and $A = 0.001$ conditions, and an additional delay of approximately 1.2° from $A = 0.001$ to $A = 0.02$. The unsteady delays are consistent with the results for the 2-D model⁶. Data at $z/c = 0.027$ and at other pitch rates and sweep angles (not shown) exhibit similar lags with increased pitch rate.

Close to the wing tip, at $z/c = 0.08$ (Fig. 6b), there is still a transition delay associated with increased pitch rate, but there is also a substantial difference between the steady and unsteady response. In steady flow the transition point moves from $x/c = 0.06$ at $\alpha \approx 2^\circ$ to $x/c = 0.026$ at $\alpha = 10^\circ$. This behavior has been discussed above in connection with Fig. 4c. In unsteady flow transition occurs considerably further aft, between $x/c = 0.10$ and 0.19 at low α , and moves forward of $x/c = 0.026$ only at $\alpha = 15-16^\circ$, a delay of at least 5° compared to the steady results. Since the relatively early transition in the steady flow was attributed to unsteadiness and three-dimensionality associated with the tip vortex, it is possible that these disturbances do not develop rapidly enough during the unsteady ramp to cause early transition.

Sweep Effects.

Figure 7 illustrates the effect of sweep angle on the transition location during ramps at $A = 0.01$ and $M_c = 0.3$. At the inboard location of $z/c = 0.70$ (Fig. 7a), the effect of sweep appears limited to a somewhat earlier transition at low α for the unswept wing. For $\alpha \geq 8^\circ$, the transition location exhibits no dependence on sweep. This is consistent with the steady-state, $M_c = 0.2$ data shown in Fig. 4b, and with pressure data⁹ showing little effect of sweep on the inboard portion of the wing prior to stall. At $z/c = 0.08$ (Fig. 7b) sweep effects are more significant. Transition on the unswept wing occurs further forward for $\alpha \leq 8^\circ$, and further aft for $\alpha \geq 10^\circ$. This is also consistent with the steady-state results (Fig. 4c).

Mach Number Effects.

The effect of Mach number will be illustrated using ramp data for the $\Lambda = 15^\circ$ wing, at a nondimensional pitch rate of $A = 0.005$, and at the $z/c = 0.70$ station. Ensemble averaged hot film time histories and instantaneous chordwise pressure distributions will be discussed at $M_c = 0.2$, 0.3, 0.4, 0.5, and 0.6. This sweep angle and spanwise position was selected for in-depth discussion because the spanwise variations appear relatively low. The pitch rate of 0.005 was selected because it was the highest value that was within

the drive system limits at all Mach numbers. Qualitatively similar variations with M_c were measured at other test conditions.

At $M_c = 0.3$ (Fig. 8) the results are generally similar to those already described at $M_c = 0.2$ (Fig. 5), with two differences. The first is that the initial transition location is somewhat further forward, near the $x/c = 0.19$ gage rather than at the $x/c = 0.30$ gage. As shown by the chordwise pressure distribution at $\tau = 0.2$ ($\alpha = 4.7^\circ$, number 1 in Fig. 8), the transition location (indicated by the 'T') is still slightly downstream of the suction peak. A more interesting difference from the $M_c = 0.2$ results is the rapid drop in hot film output prior to transition present at $x/c = 0.026$. This drop is sharper than the gradual reduction that typically occurs as increases in α cause the boundary layer to thicken and thereby reduce the heat transfer. More rapid reductions tend to occur at $M_c \geq 0.3$, both in the current experiment and also in the earlier two-dimensional unswept experiment⁶. The cause appears to be compressibility. The minimum hot film output is at $\tau = 0.275$ and $\alpha = 9.1^\circ$.

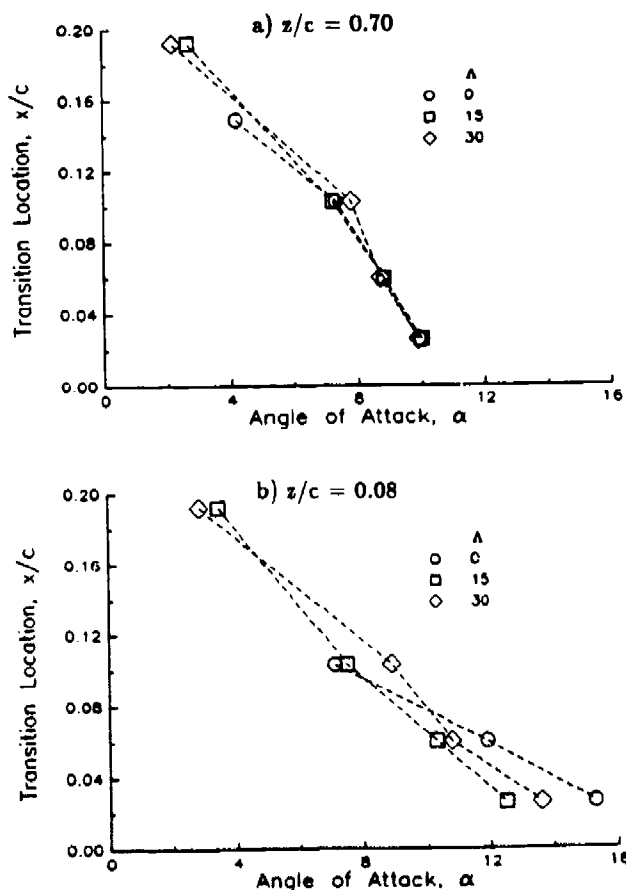


Fig. 7. Effect of sweep on transition locations for ramp motions at $M_c = 0.3$, and $A = 0.01$.

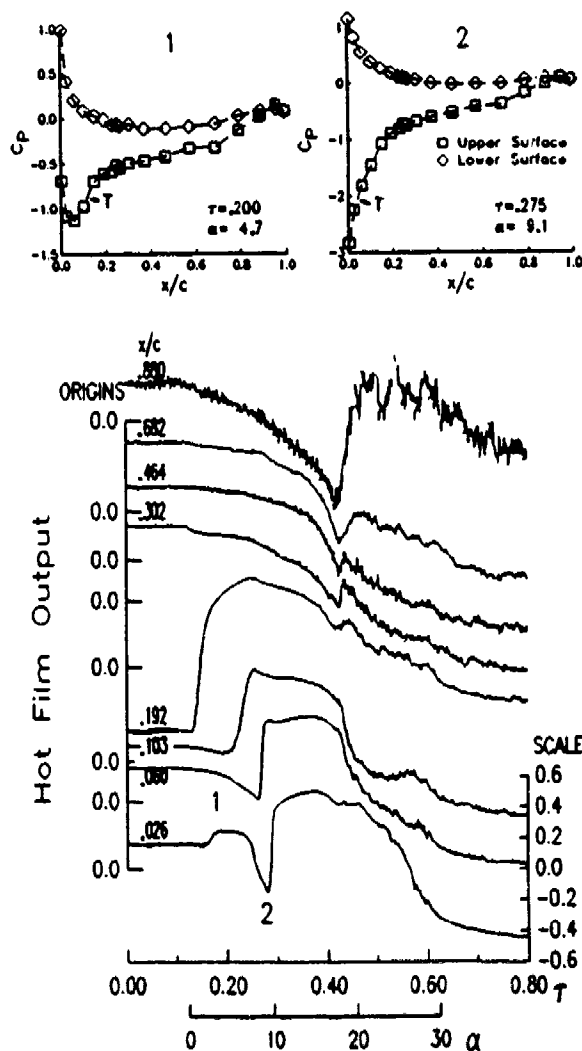


Fig. 8. Hot film time histories and chordwise pressure distributions at $M_c = 0.3$, for a ramp at $A = 0.005$, $\Lambda = 15^\circ$, and $z/c = 0.7$.

Based upon the measured pressure distribution (number 2 in Fig. 8) and the steady isentropic relations, the maximum local Mach number at this time is approximately 0.6, double the freestream value. Increasing the local Mach number generally increases the temperature, increases boundary layer thickness, reduces the density, and increases the molecular viscosity and thermal conductivity.¹⁸ The first three effects will tend to reduce the heat transfer from the heated element to the air (and therefore to decrease hot film output), while the increase in conductivity will tend to increase heat transfer. The actual balance between the effects in this unsteady, variable pressure gradient flow is not known, but it appears that the effects tending to decrease heat transfer are stronger. There is in general a good correlation between rapid drops in hot film output and regions of high subsonic local Mach numbers. No evidence has been found for the other possible cause of the decreased heat transfer, a laminar separation bubble. Neither the surface pressure distributions, the magnitude of random unsteadiness in the hot film and pressure signals, nor limited surface oil flow visualization indicate separation at these low angles of attack ($\alpha \leq 10^\circ$).

At $M_c = 0.4$ (Fig. 9) the drop in the heat transfer near the leading edge prior to transition is more pronounced. The maximum local Mach number at $\tau = 0.35$, the time of minimum hot film output, is 0.83. The sequence of events is quite compressed for this condition. First, the transition point moves forward of $x/c = 0.026$ at $\tau = .37$ ($\alpha = 9.7^\circ$), as shown by pressure distribution number 1 in Fig. 9). Next, the flow becomes locally supersonic at $\tau \approx 0.4$ ($\alpha = 10.9^\circ$).

This is indicated in pressure distribution number 2 by the C_p^* arrow. The supersonic bubble expands past $x/c = 0.060$ at $\tau = 0.475$ ($\alpha = 13.9^\circ$, pressure distribution number 3), with a maximum local Mach number of 1.27. This is almost immediately followed by separation, as indicated by the loss of leading edge suction starting at $\tau = 0.5$ ($\alpha = 14.9^\circ$, pressure distribution number 4). The separation appears to initiate near $x/c = 0.02-0.10$ (as indicated by the earliest drop in heat transfer). The rapid sequence of transition, supersonic flow, and separation in a very compact region near the leading edge illustrates the complexity of the flow and demonstrates the need for high spatial and temporal resolution in both experimental or computational experiments.

At $M_c = 0.5$ the region of supersonic flow is more extensive, leading to the more complex hot film response shown in Fig. 10. At lower α the flow remains subsonic, and the behavior is similar to that at lower M_c . The transition point moves forward from its initial position near $x/c = 0.19$, and passes $x/c = 0.10$ at $\tau = 0.3$. Pressure distribution number 1 (at $\alpha = 7.1^\circ$) in Fig. 10 illustrates this portion of the cycle. By $\tau = 0.4$ ($\alpha = 8.8^\circ$, pressure distribution number 2), the flow ahead of $x/c = 0.06$ has become supersonic. Although the maximum local Mach number is quite low (1.05) at $\tau = 0.4$, it increases rapidly, reaching a maximum of 1.4 at $\tau = 0.5$ ($\alpha = 12^\circ$, pressure distribution number 3). The hot film time histories reflect the formation of the shock at $\tau \approx 0.4$ by the rapid drop in heat transfer at the $x/c = 0.026$ gage and the rapid increase in heat transfer at the $x/c = 0.06$ gage. The decrease at the $x/c = 0.026$ gage is similar to the decreases caused by compressibility that were previ-

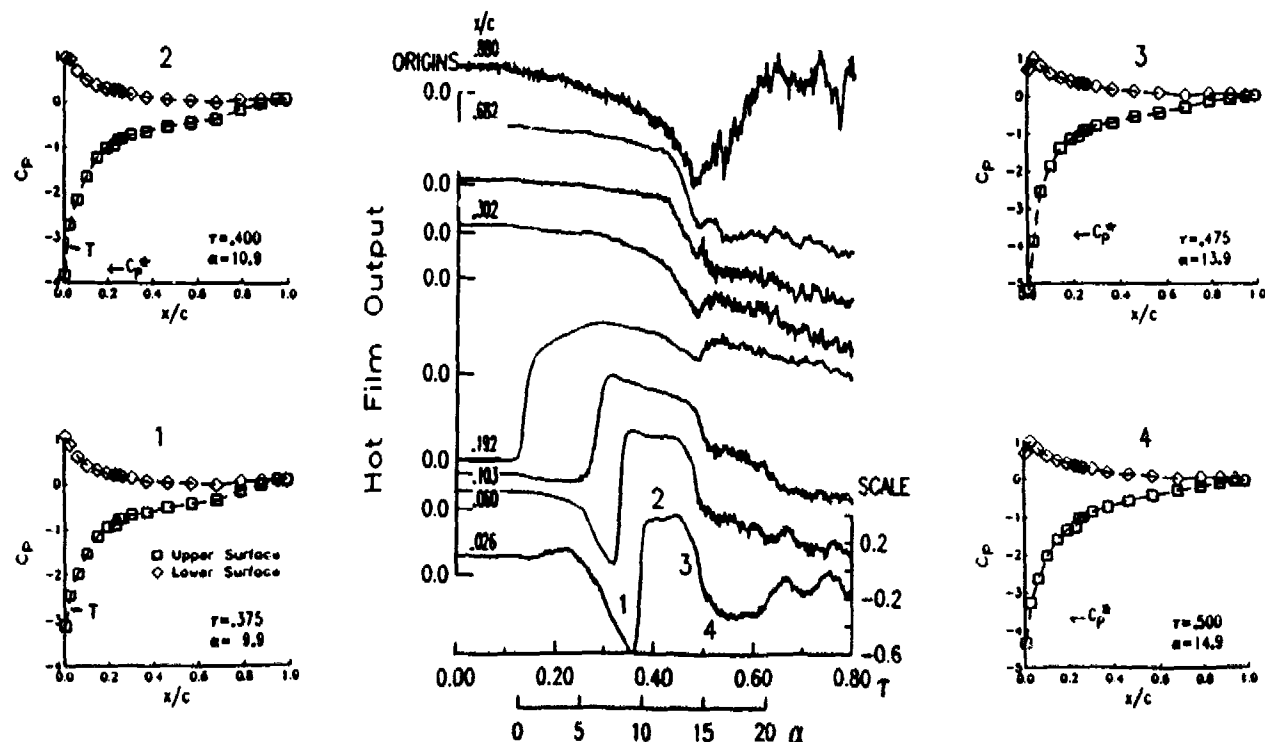


Fig. 9. Hot film time histories and chordwise pressure distributions at $M_c = 0.4$, for a ramp at $A = 0.005$, $\Lambda = 15^\circ$, and $z/c = 0.7$.

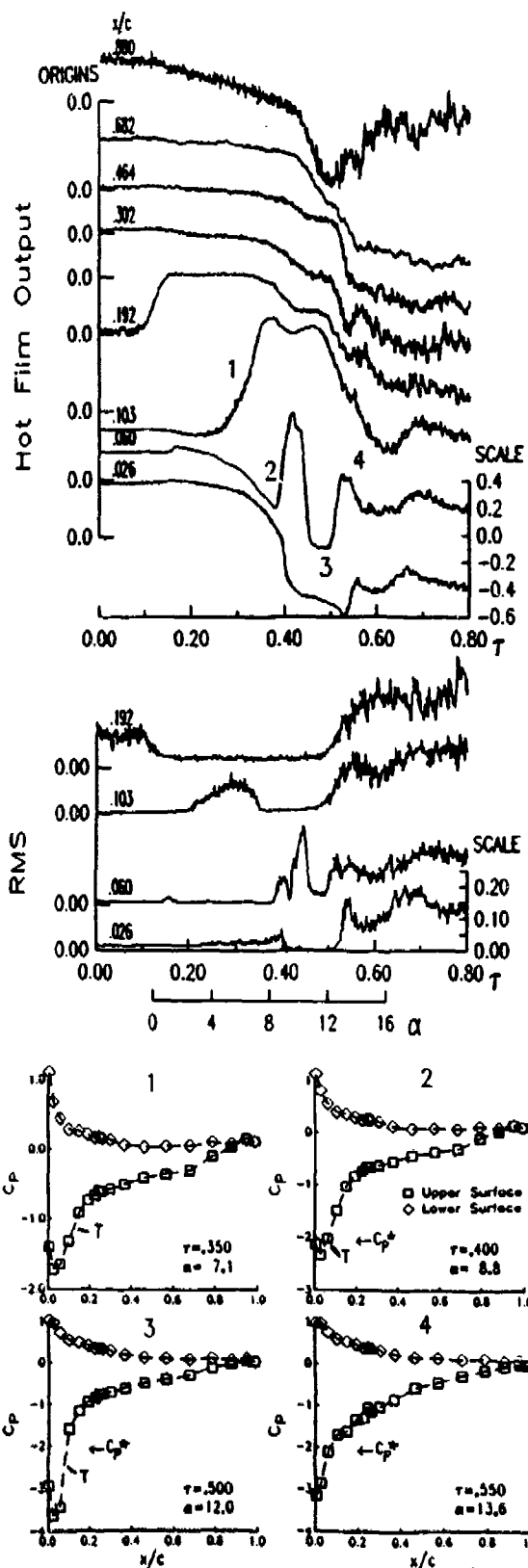


Fig. 10. Hot film time histories and chordwise pressure distributions at $M_c = 0.5$, for a ramp at $A = 0.005$, $A = 15^\circ$, and $z/c = 0.7$.

ously described at lower M_c . The increase at $x/c = 0.06$, which is now downstream of a shock, appears to be a combination of two factors. The first is transition, induced at the shock, and the second is the increase in density behind the shock (a 50% increase is predicted by the normal shock relations). An increase in temperature will also occur behind the shock, tending to reduce heat transfer from the hot film, but the effects of the density increase and of transition are apparently dominant.

As α increases further, the supersonic region expands aft past the $x/c = 0.06$ gage at $\tau \approx 0.45$. The heat transfer from this gage drops since it is now in the supersonic flow ahead of the shock. Pressure distribution number 3 in Fig. 10, at $\tau = 0.5$ and $\alpha = 12.0^\circ$, illustrates this situation. It is likely that the transition point has returned aft with the shock, to between the $x/c = 0.06$ and 0.10 gages. RMS hot film time histories (shown at the center of Fig. 10) support this hypotheses. The RMS is the variation at each value of τ of the data for 20 individual cycles about the ensemble average. The RMS at the $x/c = 0.06$ gage is considerably lower at $\tau \approx 0.4$ and 0.5 , when the ensemble averaged output is low (and the flow is presumed to be laminar at this gage), than at $\tau \approx 0.425$, when the ensemble averaged output is high (and transition is presumed to be forward of the gage). At $\tau = 0.55$ ($\alpha = 13.6^\circ$, pressure distribution number 4) the boundary layer has begun to separate near the shock. The time and location of the separation are indicated by the initial reductions in heat transfer and suction pressure. Pressure distribution number 4 clearly shows the loss of suction and the disappearance of a sharply defined shock. The flow very quickly becomes massively separated over the entire upper surface. This process is more completely described in Refs. 9 and 10.

At the highest Mach number, $M_c = 0.6$, compressibility effects are even more dominant. As shown by pressure distribution 1 in Fig. 11, locally supersonic flow begins at $\tau \approx 0.3$ and $\alpha = 4.5^\circ$. Transition occurs between the $x/c \approx 0.10$ and 0.19 gages, just aft of the suction pressure peak. Transition moves forward past the $x/c = 0.10$ gage at $\tau = 0.35$ ($\alpha = 5.5^\circ$, pressure distribution number 2). While the maximum local Mach number at $M_c = 0.6$ is 1.45, almost the same as the value measured at $M_c = 0.5$, the supersonic region extends further aft, to $x/c = 0.19$ at $\tau = 0.45$ ($\alpha = 7.6^\circ$, pressure distribution number 3). As at $M_c = 0.5$, there is reduced heat transfer from the hot film gage ahead of the shock and increased transfer from the gage behind the shock. Transition is again linked with the shock, and appears to move aft as the supersonic zone strengthens between $\tau = 0.35$ and 0.45 . Separation occurs starting at $\tau \approx 0.55$, as indicated by drops in the ensemble averaged hot film output, increased randomness, and the disappearance of a sharply defined shock. This last effect is shown in pressure distribution number 4, at $\tau = 0.6$ and $\alpha = 11.1^\circ$. At $M_c = 0.6$ the loss of leading edge suction is not as sudden as at $M_c = 0.5$, and massive separation of the entire upper surface is somewhat delayed. Further details on the separation process are provided in Ref. 10.

The transition results described in this section are summarized in the form of a transition location versus angle of attack plot in Fig. 12. The low angle of attack ($\alpha \leq 4^\circ$) data indicate that as M_c increases, the transition point moves forward earlier. Motion past the $x/c = 0.19$ gage occurs at approximately 4° earlier at $M_c = 0.6$ than at $M_c = 0.2$. The earlier transition at higher M_c may be at least in part a result of increased Reynolds number. At low angle

of attack the adverse pressure gradient aft of the suction peak is relatively weak, so transition may be induced by the amplification of natural disturbances, similar to the process on a flat plate. The concept of a critical Reynolds number based on x , $\frac{U_\infty x}{\nu}$, is applicable. For the 0.4-1% freestream turbulence levels present in this experiment, a critical Reynolds number of approximately 5×10^5 is likely.¹⁹ The value of x/c yielding this Reynolds number varies from $x/c = 0.25$ at $M_c = 0.2$ to $x/c = 0.08$ at $M_c = 0.6$. The $M_c \leq 0.4$ data in Fig. 12 are in rough agreement with this trend, but at $M_c = 0.5$ and 0.6 , the experimental transition locations are considerably further aft.

At higher angles of attack ($6 \leq \alpha \leq 10^\circ$), the dependence of the transition location on M_c is reduced (Fig. 12), as long as the regions of supersonic flow are very small and weak. Under these conditions ($M_c \leq 0.4$), transition appears to be initiated by the adverse pressure gradient immediately aft of the suction peak. As shown by the pressure distributions in Figs. 5, 8, and 9, the position of the suction peak does not vary strongly with M_c .

For $M_c = 0.5$ and 0.6 , sizable regions of supersonic flow develop at moderate angles of attack. The shock terminating these regions becomes the initiator of transition. As shown in Fig. 12, at $M_c = 0.5$ this link between the transition point and the shock causes the forward motion of the transition point to be halted near $x/c = 0.06-0.10$ at $\alpha \approx 10^\circ$. At $M_c = 0.6$, the transition point also remains near the shock ($x/c \geq 0.1$) for $\alpha \geq 5^\circ$. The chordwise resolution of the hot film measurements is too coarse to determine whether transition occurs immediately following or preceding the shock. The results only indicate laminar conditions forward of the shock and turbulence aft. There is no clear indication of the separation that is the classic response of a laminar boundary layer to the presence of a shock. There is also no evidence of the multiple 'lambda' shocks that are commonly observed with laminar boundary layers.^{20,21} It must be emphasized that there are potentially significant differences between the current experiment and the traditional results. This experiment is at a low freestream Mach

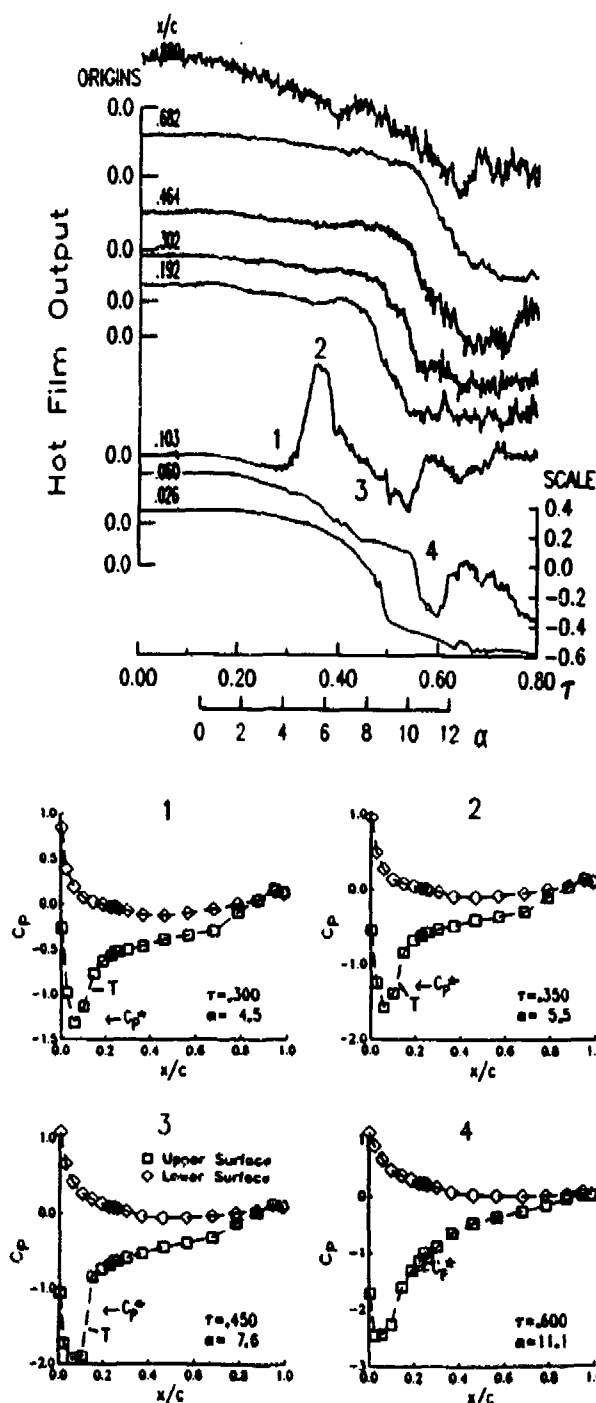


Fig. 11. Hot film time histories and chordwise pressure distributions at $M_c = 0.6$, for a ramp at $A = 0.005$, $\Lambda = 15^\circ$, and $z/c = 0.7$.

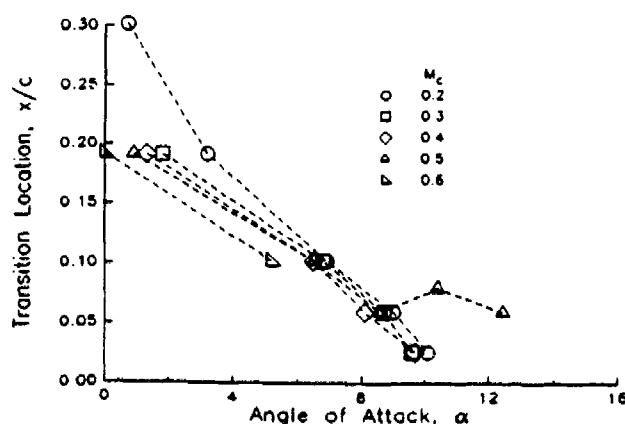


Fig. 12. Effect of Mach number on transition locations for ramp motions at $A = 0.005$ and $\Lambda = 15^\circ$.

number and moderate angle of attack, generating a thin supersonic region near the highly curved leading edge, while the traditional experiments were typically performed at low angle of attack and higher freestream Mach number, generating a thick region of supersonic flow over the aft (low curvature) region of an airfoil or plate. The combination of a relatively weak shock ($M \approx 1.3-1.4$), a thin supersonic region, and a curved surface may result in a shock that induces transition, but, at least temporarily, no significant separation. At higher angle of attack ($\alpha \geq 12^\circ$ at $M_\infty = 0.5$) the dynamic separation process does begin in the vicinity of the shock.^{9,10}

TRANSITION AND RELAMINARIZATION DURING SINUSOIDAL MOTIONS

The previous sections have described the transition process at steady state and during constant pitch rate ramps. This section will discuss results obtained for periodic sinusoidal pitching motions. The primary differences are the introduction of a time-varying pitch rate, and a periodic wake. The pitch-down portion of the sinusoidal motion also allows reattachment and relaminarization to be studied.

Figure 13 provides an example of the hot film and pressure results during sinusoidal motion. The conditions are $\alpha = 10^\circ - 10^\circ \cos \omega t$, $M_\infty = 0.2$, $k = 0.05$, $A = 15^\circ$, and $z/c = 0.7$. The pressure results (Fig. 13a) show a generally smooth response, punctuated by a sharp separation at $\tau \approx 0.46$. The separation occurs at $\alpha \approx 19.8^\circ$, after the pitch rate has dropped substantially from its maximum value of $A = 0.009$. The negative pressure peak associated with the dynamic stall vortex propagates aft, followed by a constant pressure region indicating massive separation. Reattachment begins near the leading edge at $\tau \approx 0.67$ ($\alpha \approx 15^\circ$).

The hot film time histories (Fig. 13b) are qualitatively quite similar during pitch-up to the ramp results at $M_\infty = 0.2$ shown in Fig. 5. As with the ramp, the transition point moves forward from $x/c \geq 0.30$ at $\alpha = 0$ past $x/c = 0.026$ at $\alpha \approx 10.7^\circ$. The region of low heat transfer caused by separation corresponds to the constant pressure region shown in Fig. 13a. Starting at $\tau \approx 0.66$, the boundary layer reattaches from the leading edge aft, as shown by the rapid increase in heat transfer at the $x/c = 0.026, 0.06$, and 0.10 gages (Fig. 13b). The high level indicates that the flow reattaches as a turbulent boundary layer. The subsequent drop in heat transfer, starting at the $x/c = 0.026$ gage at $\tau \approx 0.74$ ($\alpha = 10.9^\circ$), corresponds to a relaminarization of the boundary layer, again moving from the leading edge aft. The relaminarization at $x/c = 0.026$ occurs at approximately the same value of α as transition. This symmetry is not present for separation and reattachment, since at $x/c = 0.026$ separation occurs at $\alpha = 19.8^\circ$ and reattachment at $\alpha = 15^\circ$. The symmetry of transition and relaminarization does not persist through the conclusion of relaminarization. The transition point moves aft past $x/c = 0.30$ at $\tau = 0.97$ ($\alpha = 0.2^\circ$), but does not return forward until $\tau = 0.07$ ($\alpha = 0.9^\circ$).

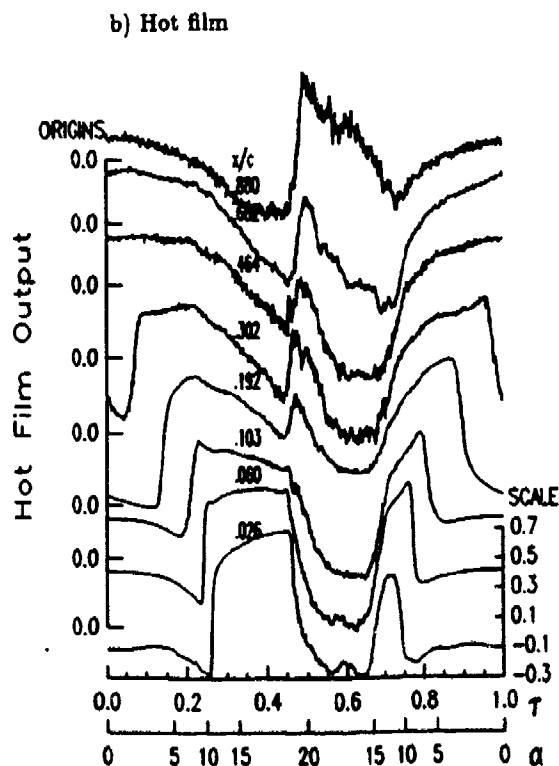
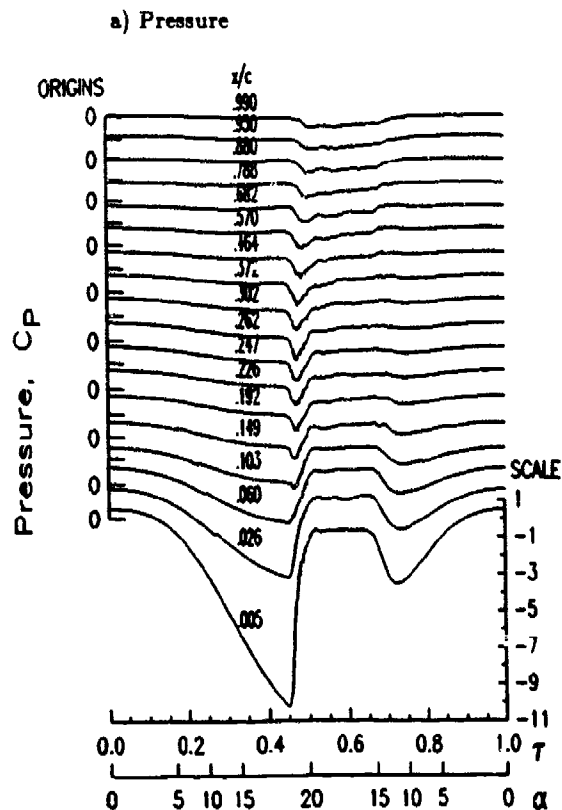


Fig. 13. Hot film and pressure time histories for sinusoidal oscillation at $\alpha = 10^\circ - 10^\circ \cos \omega t$, $M_\infty = 0.2$, $k = 0.05$, $A = 15^\circ$, and $z/c = 0.7$.

Transition and relaminarization locations for a series of sinusoidal oscillations at reduced frequencies of $k = 0.025, 0.05, 0.1, \text{ and } 0.15$ are shown in Fig. 14. The Mach number, sweep angle, and spanwise position are the same as in Fig. 13. These results show significant hysteresis in the transition-relaminarization cycle at higher frequency. At a given chordwise position, relaminarization generally occurs at a lower α than transition. The largest measured difference is at $x/c = 0.19$, where data at $k = 0.15$ show a 3.6° lower relaminarization angle. The hysteresis decreases at higher α , as the transition point approaches the leading edge, to a maximum of 1.8° at $x/c = 0.103$ and 0.9° at $x/c = 0.026$. At higher α , transition is primarily influenced by the strong adverse pressure gradient immediately aft of the suction peak. Thus there is less variation in transition location than at lower α , where transition occurs further aft, in a region with a more moderate pressure gradient. The hysteresis observed in Fig. 14 for $\alpha = 10^\circ - 10^\circ \cos \omega t$ motions, in which there are large regions of flow separation, is also present in Fig. 15 for $\alpha = 6^\circ - 6^\circ \cos \omega t$ motions, in which the boundary layers always remain attached. Separation is therefore not an essential requirement for hysteresis.

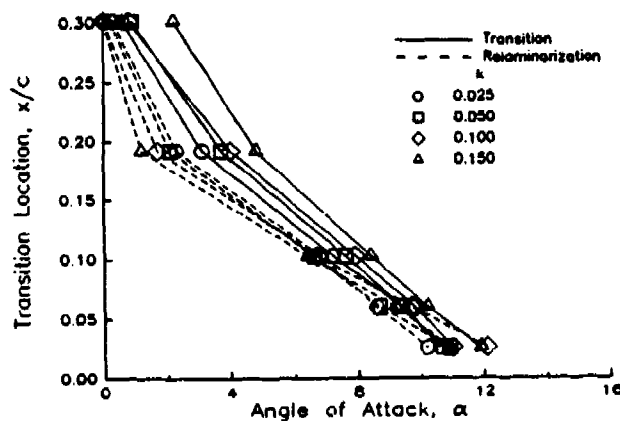


Fig. 14. Transition and relaminarization locations for sinusoidal motions at $\alpha = 10^\circ - 10^\circ \cos \omega t$, $M_c = 0.2$, $\Lambda = 15^\circ$, and $z/c = 0.7$.

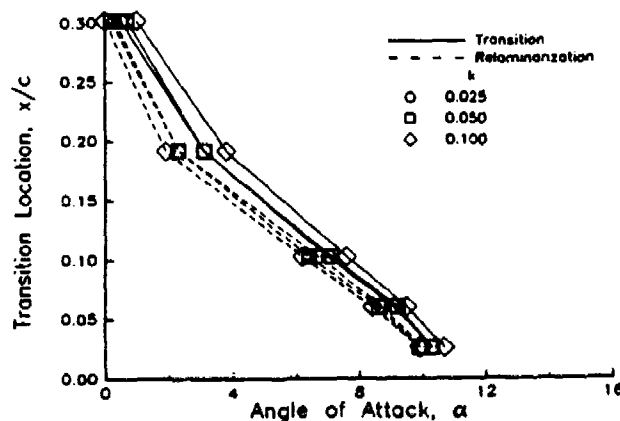


Fig. 15. Transition and relaminarization locations for sinusoidal motions at $\alpha = 6^\circ - 6^\circ \cos \omega t$, $M_c = 0.2$, $\Lambda = 15^\circ$, and $z/c = 0.7$.

Time histories at higher Mach number, $M_c = 0.5$, are shown in Fig. 16, for an $\alpha = 6^\circ - 6^\circ \cos \omega t$ oscillation at $k = 0.05$. The pressure time histories (Fig. 16a) show a flow

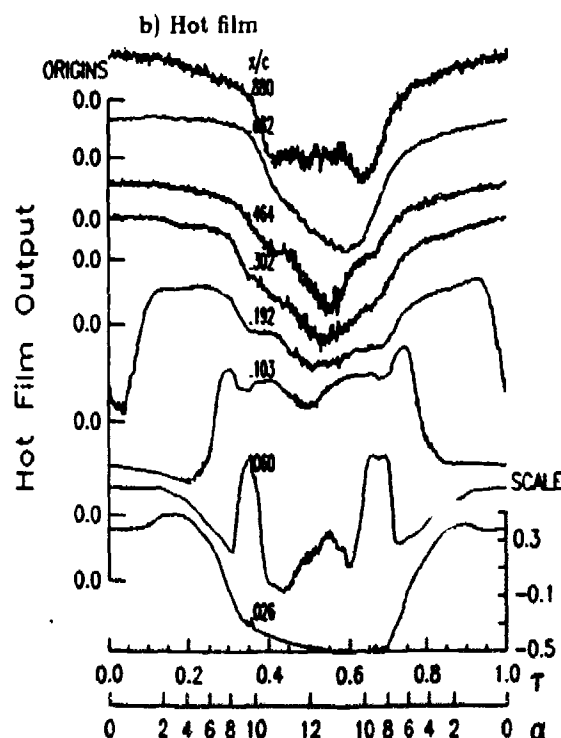
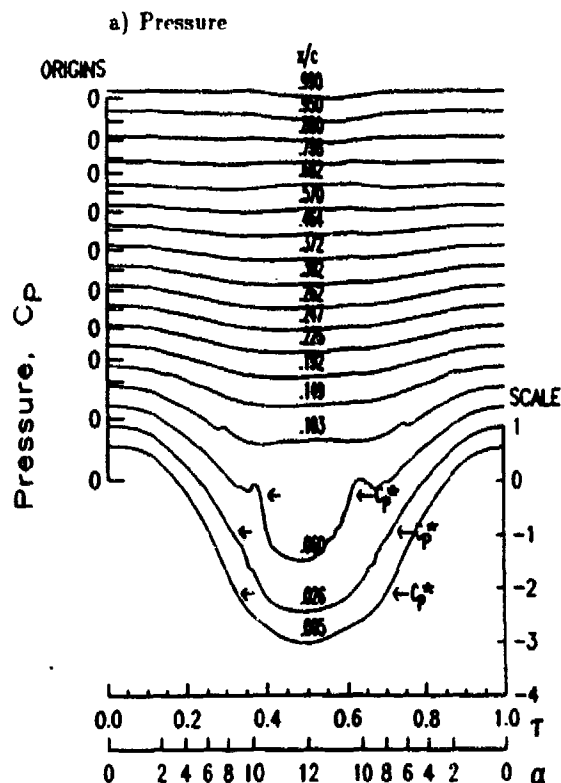


Fig. 16. Hot film and pressure time histories for sinusoidal oscillation at $\alpha = 6^\circ - 6^\circ \cos \omega t$, $M_c = 0.5$, $k = 0.05$, $\Lambda = 15^\circ$, and $z/c = 0.7$.

that remains attached, but becomes supersonic for $x/c = 0.026$ and 0.06 at $\tau = 0.3$ and $\alpha \approx 8^\circ$. The expansion of the supersonic region and rearward movement of the shock past $x/c = 0.06$ at $\tau = 0.38$ distorts the pressure time history by creating a rapid pressure drop. The hot film time histories (Fig. 16b) during the pitch-up portion of the cycle appear quite similar to the ramp results at this Mach number (Fig. 10). The increase in heat transfer at the $x/c = 0.06$ gage between $\tau = 0.32$ and 0.38 correlates closely with the pressure time histories (Fig. 16a), which indicate that the shock forms upstream of $x/c = 0.06$, and then moves aft past this position. A similar, but reversed, sequence occurs during the pitch-down.

Transition and relaminarization locations are shown in Fig. 17 for $M_c = 0.5$ sinusoids at $k = 0.025, 0.05$, and 0.1 . As at $M_c = 0.2$, there is significant hysteresis (up to 1.6°) involved in the movement of the transition between $x/c = 0.19$ and 0.06 . The differences between the transition and relaminarization angles for $\alpha \geq 9^\circ$ are reduced to less than 0.5° . Under these conditions, the shock is believed to be the primary determinant of the transition location.

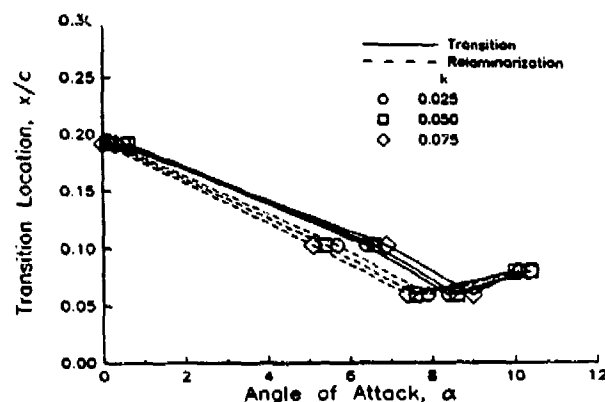


Fig. 17. Transition and relaminarization locations for sinusoidal motions at $\alpha = 6^\circ - 6^\circ \cos \omega t$, $M_c = 0.5$, $\Delta = 15^\circ$, and $z/c \approx 0.7$.

CONCLUSIONS

Experimental measurements of transition locations on a rectangular wing model during steady-state and unsteady pitching motions at Mach numbers between 0.2 and 0.6 and Reynolds numbers of $2-6 \times 10^6$ have resulted in the following observations.

1. At low angle of attack ($\alpha \leq 4^\circ$) transition generally occurs between $x/c = 0.14$ and 0.3 . Transition occurs furthest aft at $M_c = 0.2$, and closest to the leading edge at $M_c = 0.6$. Under these conditions, where the adverse pressure gradient is relatively mild, the occurrence of transition may be associated with reaching a critical Reynolds number, based on x , of approximately 5×10^5 .

2. As α is increased, the adverse pressure gradient increases and the transition point moves forward. For $\alpha \geq 6-8^\circ$, transition occurs a very short distance aft of the suction pressure peak. Under these conditions, the dependence on M_c (and therefore also Reynolds number) is reduced, for $M_c \leq 0.4$. Transition moves forward of the first hot film gage ($x/c = 0.026$) at $\alpha \approx 10-12^\circ$.
3. For the relatively high Reynolds number range of this experiment, the boundary layer becomes essentially turbulent prior to separation. There is no indication of the transitional separation bubble frequently observed at lower Reynolds number.
4. At $M_c = 0.5-0.6$, significant regions of supersonic flow develop near the leading edge at $\alpha \geq 7-10^\circ$, with maximum local Mach numbers of $1.3-1.4$. Transition is initiated at the shock that terminates the supersonic region at $x/c \approx 0.1-0.15$. There does not appear to be any substantial shock-induced separation at these moderate angles of attack.
5. Increasing pitch rate from $A = 0.001$ to 0.02 introduces a lag in the forward motion of the transition point, by up to $\Delta\alpha = 2^\circ$.
6. Wing sweep angles of $\Lambda = 0, 15$, and 30° do not substantially alter the transition locations at the inboard station ($z/c = 0.7$ chords from the tip). However, very close to the wing tip, transition occurs earlier for the unswept wing at low α than for the swept wing, possibly because of disturbances induced by the tip vortex.
7. During sinusoidal pitching motions, the transition point moves forward as α increases, and aft as α decreases. At higher reduced frequency, a significant hysteresis of up to 3.6° develops between the values of α for transition and relaminarization. The hysteresis is much stronger near $x/c = 0.15-0.30$ than it is closer to the leading edge.

ACKNOWLEDGMENTS

The instrumented model, the wind tunnel test, and the analysis of the results were funded by the U.S. Army Research Office and the U.S. Air Force Office of Scientific Research, under Contract DAAL03-89-C-0013. Dr. Thomas Doligalski of ARO was the technical monitor. Capt. Hank Helin and Maj. Daniel Fant were the AFOSR representatives. The model support and drive system was supplied by the Sikorsky Aircraft Division of United Technologies. The authors thank Alfred Covino, John Ayer, and the staff of the UTRC LSMT for their assistance during the test.

REFERENCES

1. De Ruyck, J., Hazarika, B., and Hirsch, C., "Transition and Turbulence Structure in the Boundary Layers of an Oscillating Airfoil," Vrije Univ. Brussels Report STR-16, Dec. 1989.
2. Chandrasekhara, M.S., and Ahmed, S., "Laser Velocimetry Measurements of Oscillating Airfoil Dynamic Stall Flow Field," AIAA Paper 91-1799, 22nd Fluid Dynamics, Plasma Dynamics, and Lasers Conference, Honolulu HI, June 1991.
3. Carr, L.W., McCroskey, W.J., McAlister, K.W., Pucci, S.L., and Lambert, O., "An Experimental Study of Dynamic Stall on Advanced Airfoil Sections, Volume 3: Hot-Wire and Hot-Film Measurements," NASA TM 84245, Dec. 1982.
4. Carta, F.O., "Dynamic Stall of Swept and Unswept Oscillating Airfoils, AGARD FDP Symposium on Unsteady Aerodynamics," May 1985.
5. Lorber, P.F., and Carta, F.O., "Airfoil Dynamic Stall at Constant Pitch Rate and High Reynolds Number," *Journal of Aircraft*, Vol. 25, June 1988, pp. 548-556.
6. Lorber, P.F., and Carta, F.O., "Unsteady Stall Penetration Experiments at High Reynolds Number," AFOSR TR-87-1202, April 1987.
7. Patterson, M.T., and Lorber, P.F., "Computational and Experimental Studies of Compressible Dynamic Stall," *Journal of Fluids and Structures*, Vol. 4, 1990, pp. 259-285.
8. Lorber, P.F., and Carta, F.O., "Incipient Torsional Stall Flutter Experiments on a Swept Three-Dimensional Wing," AIAA Paper 91-0935, 32nd Structures, Structural Dynamics, and Materials Conference, Baltimore MD, April 1991.
9. Lorber, P.F., Carta, F.O., and Covino, A.F. Jr., "Dynamic Stall Experiments on a Swept Three-Dimensional Wing in Compressible Flow," AIAA Paper 91-1795, 22nd Fluid Dynamics, Plasma Dynamics, and Lasers Conference, Honolulu HI, June 1991.
10. Lorber, P.F., "Sweep and Compressibility effects on the Dynamic Stall of a Three-Dimensional Wing," AIAA Paper 92-0191, 30th Aerospace Sciences Meeting, Reno NV, Jan. 1992.
11. Williams, M.C., Pratt & Whitney Aircraft Internal Correspondence, September 1988.
12. Haritonidis, J.H., "The Measurement of Wall Shear Stress," *Advances in Fluid Mechanics Measurements, Lecture Notes in Engineering* (ed. M. Gad-el-Hak), Springer-Verlag, pp. 229-261, 1989.
13. Cook, W., "Response of Hot Element Wall Shear Stress Gages in Unsteady Turbulent Flows," AIAA Paper 91-0167, 29th Aerospace Sciences Meeting, Reno NV, Jan. 1991.
14. Houdeville, R., Juillen, J.C., and Cousteix, J., "Skin Friction Measurements with Hot-Element Gages," *Recherche Aerospaciale*, Vol. 1, 1984, pp. 67-79.
15. Flutie, K.J., and Covert, E.E., "Unsteady Measurement of Skin Friction in Adverse Pressure Gradients; A New Approach to a Well-Known Gauge," AIAA Paper 91-0168, 29th Aerospace Sciences Meeting, Reno NV, Jan. 1991.
16. Greff, E., "In-Flight Measurement of Static Pressures and Boundary-Layer State with Integrated Sensors," *Journal of Aircraft*, Vol. 28, pp. 289-299, May 1991.
17. Schlichting, H., *Boundary Layer Theory*, Seventh Edition, McGraw Hill Book Co., New York NY, 1979, pp. 496-502.
18. Ibid., pp. 719-723.
19. Ibid., pg. 476.
20. Ibid., pp. 358-372.
21. Van Dyke, M., *An Album of Fluid Motion*, Parabolic Press, Stanford CA, 1982, pp. 150-152.

APPENDIX VII

COMPRESSIBILITY EFFECTS ON THE DYNAMIC STALL OF A THREE-DIMENSIONAL WING

Peter F. Lorber*

United Technologies Research Center
East Hartford, CT 06108

ABSTRACT

Experimental measurements have been made of the unsteady separation process on a pitching three-dimensional wing. Surface pressure transducers and hot film sensors were used to provide a detailed description of the events prior to and during separation. The geometric and flow conditions were selected to approximate the Reynolds number, Mach number, pitch rate, and angle of attack range of a full scale helicopter main rotor blade. Separation characteristics are described at five Mach numbers between 0.2 and 0.6. At $M_c = 0.2$ the local velocities always remain subsonic, and an abrupt separation of the turbulent boundary layer occurs starting near 10% of chord. A well defined stall vortex is formed and propagates aft along the chord. At $M_c = 0.3$ the small region of supersonic flow at the leading edge initiates a high frequency instability, resulting in an earlier, but less abrupt, stall. At $M_c = 0.4-0.6$ a significant shock develops. Flow separation at the shock causes stall to occur at considerably lower angles of attack. The stall is more gradual, and results in a more diffuse stall vortex.

NOMENCLATURE

A	pitch rate, $\dot{\alpha}c/2U_c$
c	airfoil chord (17.3 in.)
C_L	section lift coefficient, L/qc
C_M	section $\frac{1}{4}$ chord moment coefficient, M/qc^2
C_P	pressure coefficient, $(P - P_\infty)/q$
C_P^*	pressure coefficient for locally sonic chordwise velocity
M_c	chordwise Mach number, $M_\infty \cos \Lambda$
M_∞	freestream Mach number
P_∞	freestream static pressure
q	dynamic pressure, $\frac{1}{2}\rho_\infty U_c^2$
t	time
T	acquisition period
Re	Reynolds number, cU_c/ν
U_c	chordwise component of freestream velocity, $U_\infty \cos \Lambda$
U_∞	freestream velocity
x	distance along chord from leading edge
z	distance along span from tip leading edge

$\dot{\alpha}$	pitch rate, rad/sec
α	geometric angle of attack
ramp: $\alpha = \alpha_{min}, \tau \leq 0.125$	
$\alpha = \alpha_{min} + 2(\tau - 0.125)(\alpha_{max} - \alpha_{min}),$	
$0.125 \leq \tau \leq 0.625$	
$\alpha = \alpha_{max}, \tau \geq 0.625$	
Λ	sweep-back angle
ν	kinematic viscosity
ρ_∞	freestream density
τ	nondimensional time, t/T

INTRODUCTION

It has long been recognized that compressibility can have a significant effect on dynamic stall. Aerodynamic load measurements¹⁻⁴ have shown that two of the primary dynamic stall characteristics, the delay in stall and the increase in lift and moment beyond the steady state maxima, are reduced at Mach numbers of 0.4 and higher. Surface pressure measurements^{5,6} indicate that, at Mach numbers of 0.2-0.4, a region of high subsonic or supersonic velocities may develop near the leading edge at high angle of attack. Peak suction pressures are constrained by compressibility,^{7,8} and do not reach the extreme values of $C_P \approx -12$ to -14 attained under incompressible or low subsonic conditions. The structure and propagation characteristics of the dynamic stall vortex are also altered at increased Mach number.⁹⁻¹¹ Analytical¹² and computational¹³⁻¹⁶ studies of the effect of compressibility have also indicated the presence of a supersonic leading edge bubble, a limitation on the maximum unsteady loads, and an alteration in the unsteady separation characteristics. The appearance of a strong shock in computations at Mach numbers of 0.5-0.6 has been found to trigger a 'massive shock-induced separation.'¹⁷

In-depth information on the unsteady separation during the dynamic stall of a wing is difficult to obtain because of the small length and time scales involved. Experimental data on the flow field away from the surface have usually been limited to sub-scale Reynolds numbers, two-dimensional geometries, and/or relatively low velocities. Both hot wire measurements¹⁸ for a NACA 0012 airfoil at $Re = 3 \times 10^5$, and the interferometric⁸ and laser velocimetry¹⁹ measurements of the same section (at a different facility) at $Re = 4 - 9 \times 10^5$ show a laminar separation bubble near the leading edge. These bubbles, which are quite common at lower Reynolds numbers, may have a substantial impact on unsteady separation. Such a 'bubble-bursting' mechanism does not seem to be dominant at the

*Research Engineer, Member AIAA

Copyright ©1992 by United Technologies Corporation. Published by the American Institute of Aeronautics and Astronautics, Inc., with permission.

higher Reynolds numbers ($Re \geq 2 - 3 \times 10^6$) characteristic of full-scale applications. Surface pressure and hot film data at such Reynolds numbers^{5,6,20} indicate that laminar separation bubbles are of only secondary importance; the primary mechanism seems to be separation of the turbulent boundary layer near the leading edge. The fact that the unsteady separation appears to originate near the leading edge is also significant, since forward expansion of a trailing edge separation is common in steady flow at high Reynolds number.^{5,20} A region of reversed flow near the airfoil surface that propagates forward from the trailing edge is a common prediction of both steady and unsteady computations at moderate Mach number.^{15,17}

The object of the current paper is to describe, based upon experimental data, the unsteady separation and dynamic stall process on a pitching wing at high Reynolds number. The particular areas of interest are the events leading to separation and the development of the local separation into dynamic stall. The experiment was designed to simulate (as closely as practical on a single, non-rotating wing) the conditions on a full-scale helicopter main rotor. This required attempting to match Reynolds number, Mach number, pitch rate, airfoil section, sweep angle, and angle of attack range. The resulting geometric and flow conditions should also be relevant to the study of the unsteady aerodynamics of maneuvering aircraft. High temporal resolution surface pressure measurements are combined with boundary layer state information from surface hot film gages to identify separation characteristics. The effects of compressibility are examined by comparing results at Mach numbers of 0.2, 0.3, 0.4, 0.5, and 0.6, with other parameters held constant.

This work is a continuation of the analysis of the results obtained during an extensive study of the aerodynamics of a pitching three dimensional wing. A description of the experiment and a survey of the characteristics of the aerodynamic load results for constant pitch rate motions is provided in Ref. 21. This reference concentrates on the dependence of the surface pressures and loads upon the test parameters (pitch rate, wing sweep, Mach number, spanwise position, and tip geometry). Transition measurements are described in Ref. 22. Results for small amplitude oscillations, simulating stall flutter, are given in Ref. 23. Results for a two-dimensional version of the experiment were provided in Refs. 6 and 24.

DESCRIPTION OF EXPERIMENT

The model was a straight, rectangular, untwisted, semi-span wing of 17.3 in. (44 cm) chord and 48 in. (122 cm) span (Fig. 1). The aspect ratio of a full-span wing would be 5.6. The wing consisted of a steel spar and fiberglass airfoil panels, and had a Sikorsky SSC-A09 9% thickness cambered section. Airfoil coordinates have been provided in Ref. 24. The wing was mounted at sweep angles of 0, 15, and 30° from the side wall of the 8 ft (2.4 m) octagonal test section of the UTRC Large Subsonic Wind Tunnel. Additional airfoil panels were added at non-zero sweep angles

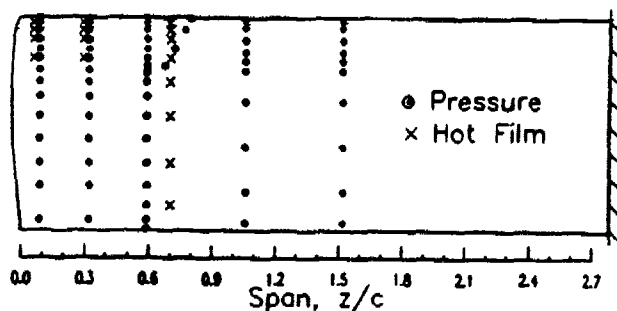


Fig. 1. Wing planform and instrumentation locations.

in order to keep the wing tip $\frac{1}{4}$ chord at the tunnel centerline. For this geometry, the Mach and Reynolds numbers are approximately related by $Re = M_c \times 10^7$.

A hydraulic rotary drive oscillated the model in pitch about the line connecting the root and tip $\frac{1}{4}$ chord. Two pitching waveforms were used, sinusoids and ramps. Each cycle of ramp motion began at a steady-state condition (usually $\alpha = 0$), increased at constant rate to a maximum angle, maintained that maximum for a short time, and then returned to the initial condition. The nondimensional pitch rates were selected between $A = \dot{\alpha}c/2U_\infty$ of 0.001 and 0.025, bounded by a limiting dimensional rate of 560°/sec. The complete data set (674 steady and unsteady conditions) will be made available in a technical report and a set of digital data tapes.

Unsteady surface pressure measurements were made on the wing model by 112 miniature transducers distributed among five spanwise stations. The suction surface transducer locations are shown by the dots in Fig. 1. The chordwise arrays on the upper surface had 10, 14, or 18 transducers each. The lower surface arrays were less dense, containing 6 or 18 transducers each. The transducers were installed so as to retain a smooth surface contour and achieve a flat frequency response to at least 4 kHz. The pressures were integrated along the chord at each spanwise station to determine the unsteady lift, pressure drag, and pitching moment coefficients.

Sixteen flush-mounted surface hot film gages were used to determine transition and separation locations. As shown by the x-marks in Fig. 1, the gages were located in chordwise arrays at three spanwise stations. The output voltage increases with the heat transfer from the gage, which may in turn be related by the Reynolds analogy to the shear stress at the wall.

The output voltages from both the pressure transducers and hot film gages were passed through a 10 kHz low pass filter, and digitized (to 15 bit accuracy) at a rate of 1024 samples per oscillation period (T). Ensemble-averaged time histories were computed using data from 20 pitching cycles. Both the individual cycle data and the ensemble averages were recorded on digital magnetic tape. Note that all conversions to coefficient use the chordwise velocity component, $U_c = U_\infty \cos \Delta$. A more complete description of the experiment is provided in Refs. 21 and 22.

The fundamental characteristics of dynamic stall at low Mach numbers have been well established.¹⁻⁶ Representative aerodynamic load curves are shown in Fig. 2 for constant rate ($A = 0.01$) pitching motions from $\alpha = 0$ to 30° at $M_c = 0.2$, $z/c = 0.59$, and three sweep angles, $\Lambda = 0, 15$, and 30° . Also shown are the steady state results for $\Lambda = 30^\circ$. The unsteady aerodynamic loads exhibit the expected delay in stall beyond the steady-state value, accompanied by an increase in the maximum lift coefficient. Upon separation, vorticity previously contained within the boundary layer near the leading edge is released, and moves aft (as the 'dynamic stall vortex') along the chord. This temporarily maintains high lift, but generates a very large nose-down pitching moment. Once the vortex has passed the trailing edge, the loads begin to relax towards the steady-state values for massively separated flow. The stall delays and the unsteady increments to the loads at the different sweep angles shown in Fig. 2 are similar, but the detailed characteristics after stall differ. (See Ref. 21 for additional information on the parameter dependence of the loads.)

As a first step in the illustration of the unsteady separation process observed during this experiment, results for a single condition will be explored in depth. The $M_c =$

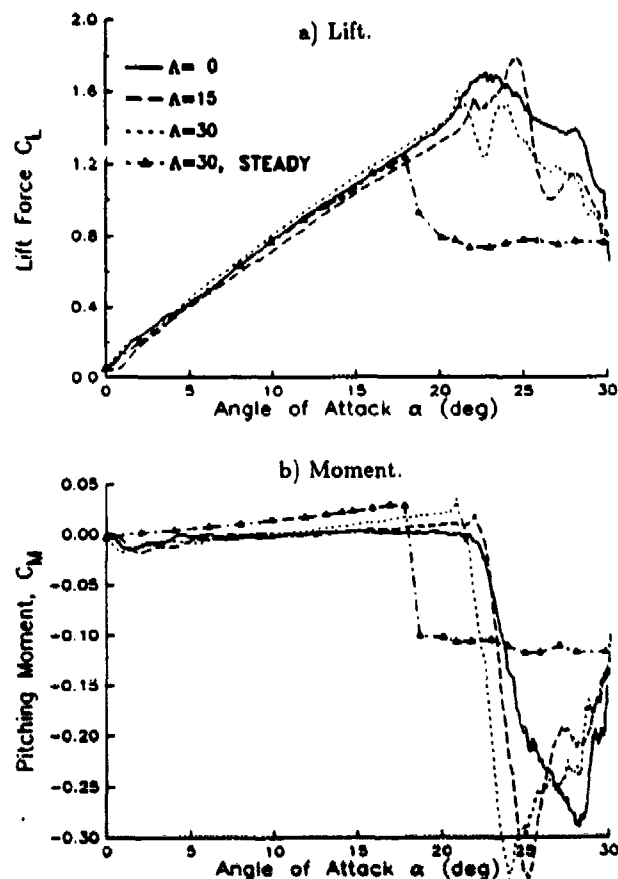


Fig. 2. Lift and pitching moment at $z/c = 0.59$, during $A = 0.01$ ramps at $M_c = 0.2$.

0.2 , $A = 0.01$, $\Lambda = 30^\circ$ condition from Fig. 2 was selected for initial examination for the following reasons. First, the low freestream Mach number minimizes compressibility effects. Second, the pitch rate is moderate, but representative of rates experienced on helicopter rotors.²⁶ Third, the 30° sweep angle minimizes the influence of the wing tip vortex, and reduces the spanwise gradients. The results at the other sweep angles (not shown) are fundamentally similar through the initial stages of stall. Results at $z/c = 0.59$ from the tip are presented because this station has the highest instrumentation density, and because it is relatively distant from both the wing tip and from the wind tunnel wall. The data will be presented using several different formats, each of which emphasizes different aspects of the separation and stall process.

Chordwise Pressure Distributions

The pressure data from this condition will first be presented as a series of chordwise distributions. Each distribution in Fig. 3 represents the ensemble average of 20 cycles at a particular instant in the cycle, and is identified both by the nondimensional time, τ , and by the angle of attack, α . The first distribution (Fig. 3a) is at $\alpha = 18^\circ$, the steady stall angle. The upper surface pressures are quite smooth, with a peak suction pressure of $C_p = -9$ at $x/c = 0.005$. As shown in Fig. 2, the lift at this time is only slightly greater than the steady-state value. As α increases (Figs. 3b-d), the suction peak strengthens, reaching a maximum of $C_p = -11.8$ at $\alpha = 20.8^\circ$ (Fig. 3d). Small distortions in the pressure distributions are developing between $x/c = 0.1$ and 0.2 . At $\alpha = 21^\circ$ (Fig. 3e) these distortions increase, and the suction peak starts to collapse. This is the time of maximum lift, and the beginning of the drop in pitching moment (Fig. 2).

At $\alpha = 21.3^\circ$ (Fig. 3f), the leading edge suction peak has collapsed to $C_p = -4.8$, and the negative pressure region associated with the stall vortex has formed at $x/c = 0.06-0.10$. This region broadens, weakens, and moves downstream for $\alpha = 21.4-21.8^\circ$ (Fig. 3g-i). By $\alpha = 22.2^\circ$ (Fig. 3j) the negative pressure region extends over the forward 50% of chord, and does not seem to reflect a compact, sharply defined vortex. This is in agreement with the interferometric results reported in Ref. 8. During this portion of the cycle, the lift remains above the steady state maximum (Fig. 2), but (at this sweep angle) contains a small oscillation. The broadening and weakening of the stall vorticity continues for $\alpha = 23^\circ$ (Fig. 3k). The maximum negative moment ($C_M = -0.33$) occurs shortly thereafter, at $\alpha = 24^\circ$ (Fig. 2). The lift and moment then relax towards their steady-state values, as the pressure distribution corresponds to massive stall (Fig. 3l).

Pressure Time Histories

A second way of presenting the pressure results for this condition is by means of time histories of the ensemble averages. Figure 4a shows time histories for all 18 upper surface transducers during the period $0.1 \leq \tau \leq 0.7$, which includes the entire $\alpha = 0-30^\circ$ ramp. Both τ and α scales are provided

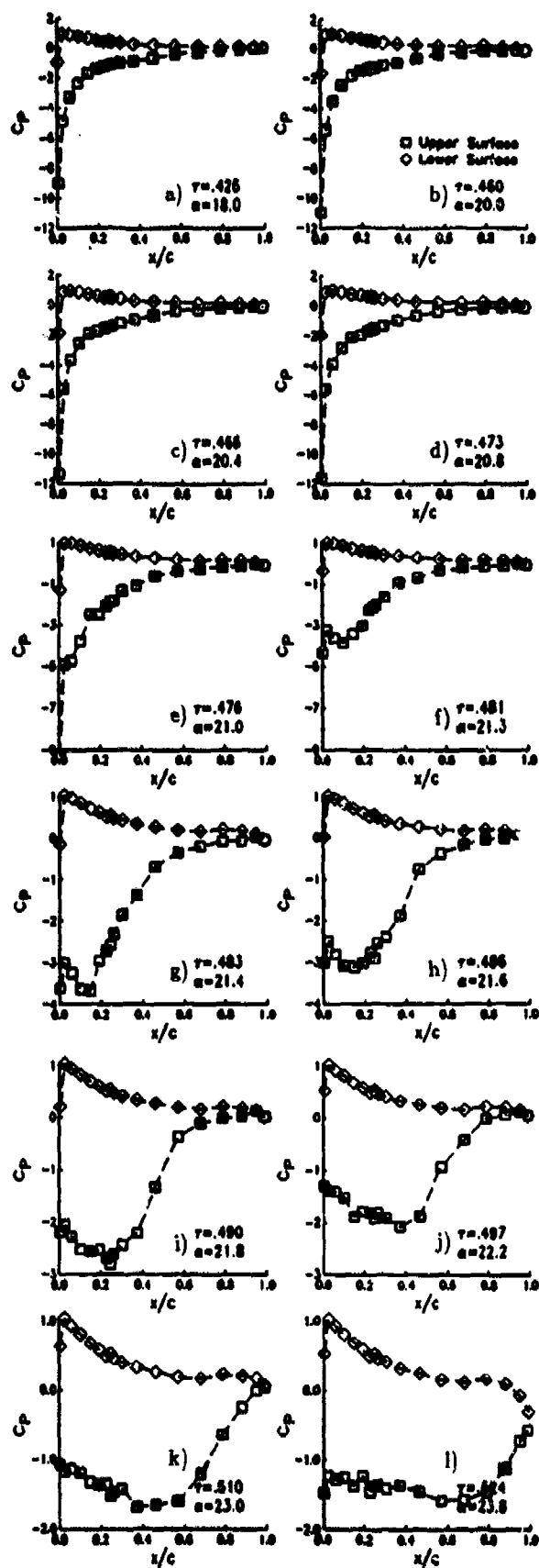


Fig. 3. Chordwise pressure distributions at $z/c = 0.59$, during an $A = 0.01$ ramp at $M_c = 0.2$ and $\Lambda = 30^\circ$.

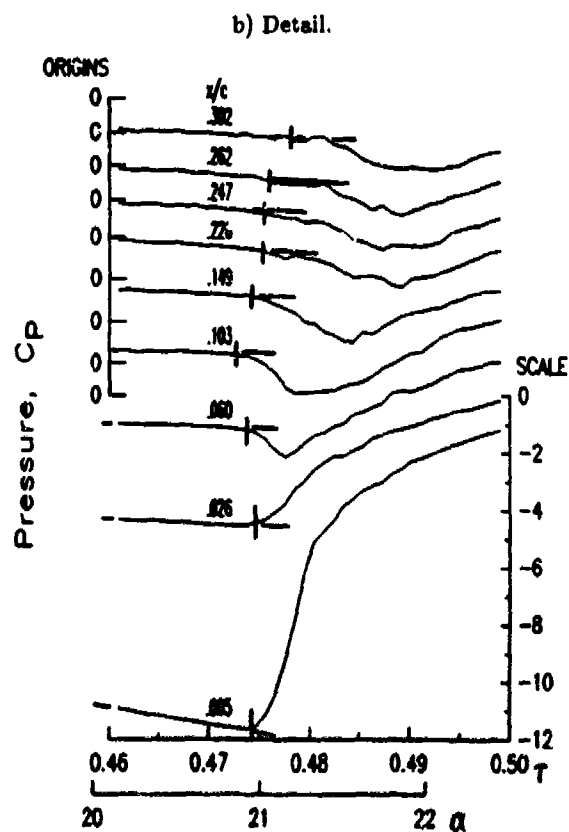
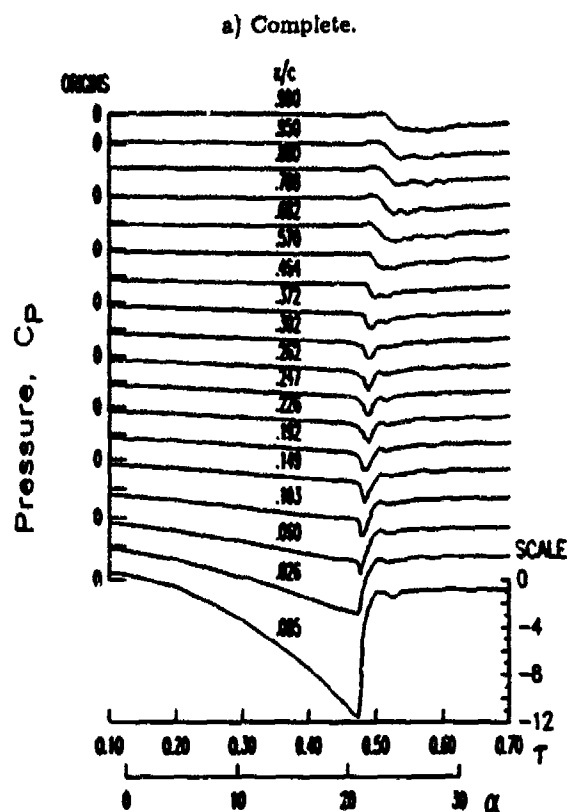


Fig. 4. Pressure time histories at $z/c = 0.59$, during an $A = 0.01$ ramp at $M_c = 0.2$ and $\Lambda = 30^\circ$.

along the horizontal axis. The data at $x/c = 0.005$ is at the bottom and corresponds to the scale at the lower right. The origins for each successive curve are offset along the left vertical axis. At $x/c = 0.005$ and 0.026 , the suction is abruptly removed at stall, and the pressure increases monotonically until the relatively uniform values characteristic of massive stall are attained. For $0.060 \leq x/c \leq 0.464$, there is an initial valley of negative pressure (associated with the stall vortex) prior to massive stall. For $x/c \geq 0.57$, the pressure first increases, and then drops. The negative pressure valleys are quite mild and broad, in comparison with the sharp valleys observed closer to the leading edge. Note that a sharp valley in Fig. 4 implies an event which is compact in time (it passes rapidly over a particular location), while sharpness in Fig. 3 implies spatial compactness (an event which extends over only a small portion of the chord at a particular time). These two characteristics are frequently, but not necessarily, related.

In order to concentrate on the separation process, Fig. 4b shows an expanded picture of the region from $0.46 \leq \tau \leq 0.5$ ($20^\circ \leq \alpha \leq 22.5^\circ$), for $x/c \leq 0.3$. At $x/c = 0.005$, there is an initial rapid pressure rise from $C_p = -11.8$ at $\tau = 0.475$ to $C_p = -5$ at $\tau = 0.48$, followed by a period of more gradual increase. A similar, but less extreme, pressure increase occurs at $x/c = 0.026$. For $x/c \geq 0.06$ the pressures initially become more negative at separation, and then recover. The straight, approximately horizontal, lines on each curve in Fig. 4b indicate the linear trends for $0.46 \leq \tau \leq 0.47$ (which are assumed to correspond to attached flow), while the vertical marks show the initial departure of the pressures from this linear trend. This departure provides an indication of separation. As shown by the marks, the earliest indication of separation is at $x/c = 0.1$ and $\tau = 0.472$. (Note that, in this discussion, separation refers to detachment of the boundary layer at a particular location, while stall refers to a change in the overall aerodynamic characteristics, such as a leveling off or drop in lift, or the introduction of a strong negative pitching moment.) The disturbance then spreads forward and aft by $\tau = 0.473$ to include the region $0.06 \leq x/c \leq 0.15$, and reaches $x/c = 0.005$ by 0.474 . This time interval, $\Delta\tau = 0.002$, corresponds to an angular increment of $\Delta\alpha = 0.12^\circ$, and a convection time increment of $U_c/c = 0.1$. (A disturbance traveling at U_c would move $0.1c$ in this time interval.) An additional interval of equal duration is required for the initial indication of separation to appear at $x/c = 0.3$.

Hot Film Results

Time histories of the hot film gage signals are shown in Fig. 5. These signals provide qualitative information on the state of the boundary layer. Each has been self-scaled to a peak-to-peak value of 1. Figure 5a shows ensemble averaged results for the complete ramp motion. Figure 5b shows the root-mean-square (RMS) variation of the 20 cycles about the ensemble average. Each RMS time history has been scaled using the same factors as the ensemble average; an RMS of 0.1 therefore represents 10% of the peak-to-peak of the ensemble average. At the start of the motion ($\alpha = 0$) the

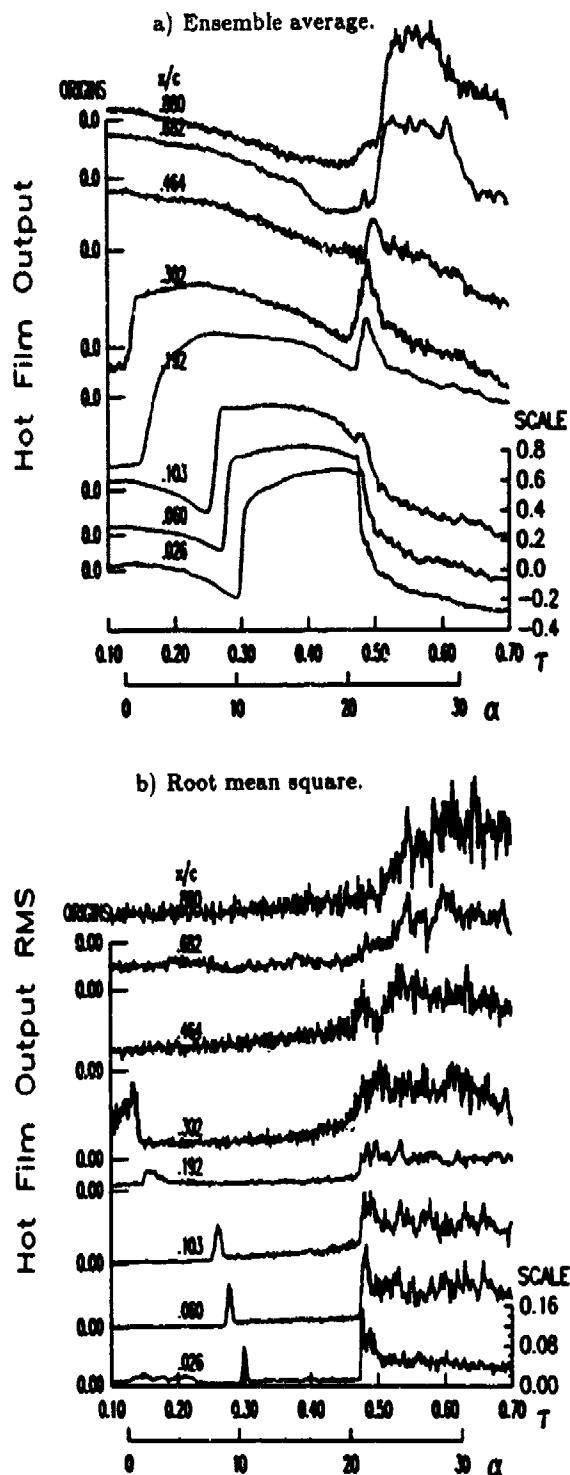


Fig. 5. Hot film gage time histories at $x/c = 0.7$, during an $A = 0.01$ ramp at $M_c = 0.2$ and $A = 30^\circ$.

point of transition from laminar to turbulent flow is near $x/c = 0.3$. Forward of this position, both the ensemble average (Fig. 5a) and the RMS (Fig. 5b) are low, indicating laminar flow. Aft of $x/c = 0.3$, both the ensemble average and the RMS are high, indicating an attached turbulent boundary layer. At the $x/c = 0.3$ gage, the ensemble average is

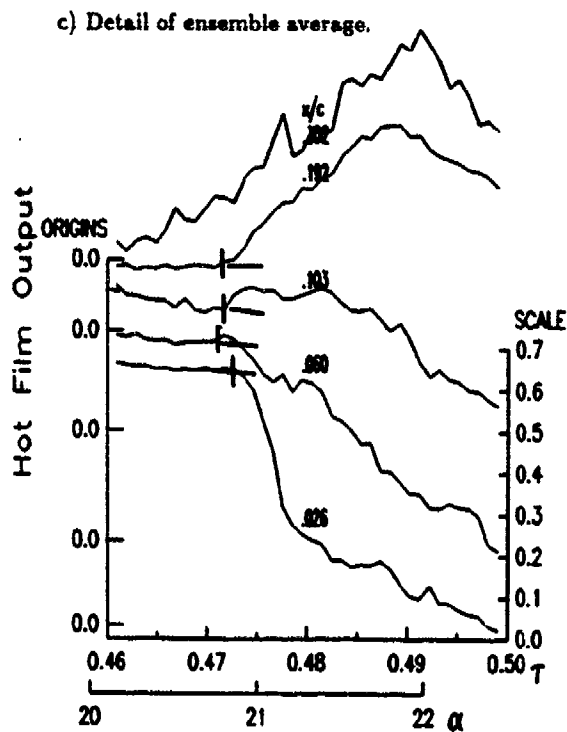


Fig. 5, cont. Hot film gage time histories at $x/c = 0.7$, during an $A = 0.01$ ramp at $M_c = 0.2$ and $\Delta = 30^\circ$.

low but the RMS is significant. This local intermittency implies that at $\alpha = 0$, transition is taking place at this sensor. As α increases, the transition point moves forward, as indicated by the succession of rapid increases in ensemble averaged heat transfer, accompanied by narrow peaks in the RMS. After the RMS peak during transition, the RMS returns to a lower, but non-zero, level characteristic of a turbulent boundary layer. Transition moves forward of the $x/c = 0.026$ gage at $\alpha \approx 10^\circ$. Much more information on transition is contained in Ref. 22, including a more complete description of the process and its dependence on compressibility, sweep, pitch rate, and spanwise position. The results of primary current interest are that, at $Re = 2 \times 10^6$, the boundary layer has become essentially turbulent well before separation, and there are no signs of a laminar separation bubble.

The hot film response near stall is highly dependent on chordwise position. At $x/c = 0.026$ and 0.06 there is a sharp drop in ensemble averaged heat transfer (Fig. 5a) and an increase in the RMS (Fig. 5b), corresponding to separation of a turbulent boundary layer. The expanded view of the $0.46 \leq \tau \leq 0.5$, $x/c \leq 0.3$ region shown in Fig. 5c indicates that this occurs at $\tau \approx 0.473$, the time when suction pressure is lost near the leading edge (Fig. 4b). (Note that small timing differences are possible because the hot film gages are 0.11 chord lengths inboard of the pressure transducers.) At $x/c = 0.1$ the hot film response is similar, but there is a small region of increased heat transfer for $0.475 \leq \tau \leq 0.49$ (Fig. 5a,c), which corresponds to the negative pressure valley associated with the formation of the stall vortex (Fig. 4b).

Further aft, for $x/c = 0.19$ to 0.46 , the increase in heat transfer (Fig. 5a) caused by the stall vortex is much stronger, and the subsequent reduction is relatively small. The RMS signals (Fig. 5b) also show a more gradual decrease after the vortex has passed, in comparison to that observed further forward. This behavior is even more pronounced at $x/c = 0.68$ and 0.88 . As α increases prior to stall, for $0.2 \leq \tau \leq 0.45$, the ensemble-averaged heat transfer for the aft four gages ($x/c \geq 0.3$) decreases and the RMS increases, characteristic of a thickening turbulent boundary layer.

It is in fact likely, but not proven, that the flow near the trailing edge becomes reversed and/or separated at higher angles of attack. The reduction in ensemble-averaged heat transfer (Fig. 5a) at the $x/c = 0.68$ gage at $\tau \approx 0.4$ may be related to this. Corroborating evidence was provided by surface oil flow visualization for several steady-state conditions. For $\alpha \geq 10^\circ$, the oil drops (not shown) moved very little, implying minimal surface shear. Trailing edge flow reversals or separations have previously been observed both experimentally^{18,20} and computationally.¹⁷ As observed during these earlier studies, there is no indication here that a trailing edge separation is connected to, or plays a significant role in, the separation near the leading edge that causes dynamic stall. Neither the ensemble averaged pressure results (Figs. 3 and 4) nor the RMS pressures (not shown) exhibit any effects of a trailing edge separation.

Pressure Contours

Contour plots of the ensemble-averaged pressure provide a different perspective on the separation process. Figure 6a shows the complete process, from $\tau = 0.1$ to 0.7 along the horizontal axis, and from $x/c = 0$ to 1 along the vertical axis. The isobars are generally quite smooth prior to stall ($\tau \leq 0.47$), with two exceptions. The first is the $C_p = 0.0$ contour near the trailing edge, which turns vertical near $\tau = 0.4$, possibly as a result of a trailing edge separation. The second is the region of strong gradients at the suction peak, very close to the leading edge. The dominant feature of the plot is, however, the dense pattern of isobars that traces the motion of the stall vortex from $\tau = 0.47$ and $x/c \approx 0.1$ to $\tau \approx 0.52$ near the trailing edge. Ref. 9 describe how such contours were used to identify vortex propagation characteristics. In this paper, the contours serve a primarily qualitative purpose.

Figure 6b shows a close-up of the isobars on the forward half of the chord during separation and stall ($0.46 \leq \tau \leq 0.50$). Although the contour plot provides a useful picture of the process, caution is needed to avoid being misled by the contouring algorithm. In particular, since there are only six transducers between $x/c = 0$ and 0.2 , much of the apparent fine detail results from interpolation. As evident from the earlier presentations of the pressure data (Figs. 3 and 4), the first indications of separation appear near $x/c \approx 0.1$, and the disturbance then spreads forward (collapsing the suction peak) and aft (forming the stall vortex). The aft propagation of the vortex is indicated by the dotted line in Fig. 6b, which represents the least squares fit to the times of minimum pressure at each transducer.⁶ Based upon the

slope of this line, the influence of the vortex propagates at a speed of approximately $\frac{\partial z}{\partial t} = 0.32U_c$.

Individual Cycles

The preceding description has used ensemble averaged data. Ensemble averages generally provide a satisfactory perspective on the basic features of the stall process. At time scales representative of the overall motion ($\geq 0.02\tau$), the variations between individual cycles (realizations) are small.⁶ However, at the relatively fine time scales used here to examine the details of separation, differences between

individual cycles become apparent. Figure 7 provides examples using pressure time histories at two locations. The upper curve in each set (labeled 'AVG') is the ensemble average of 20 cycles (as in Fig. 4), and the lower five curves (labeled #1, #2,...) are individual cycles. At $x/c = 0.005$

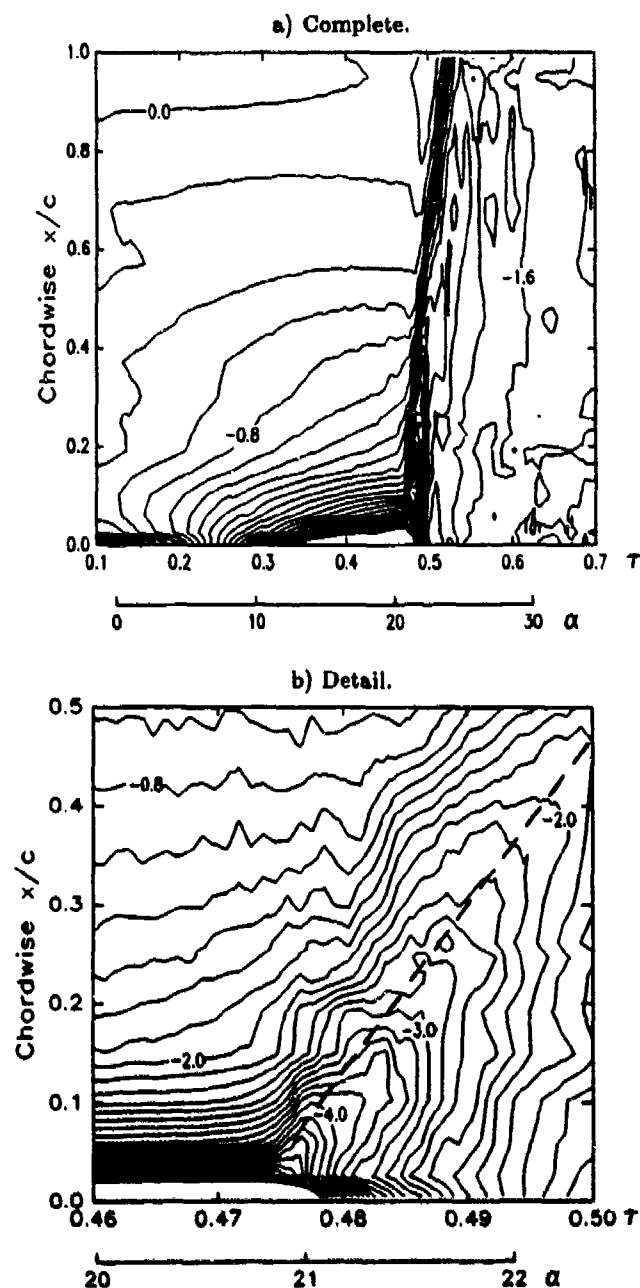


Fig. 6. Pressure contours at $z/c = 0.59$, during an $A = 0.01$ ramp at $M_c = 0.2$ and $\Lambda = 30^\circ$.

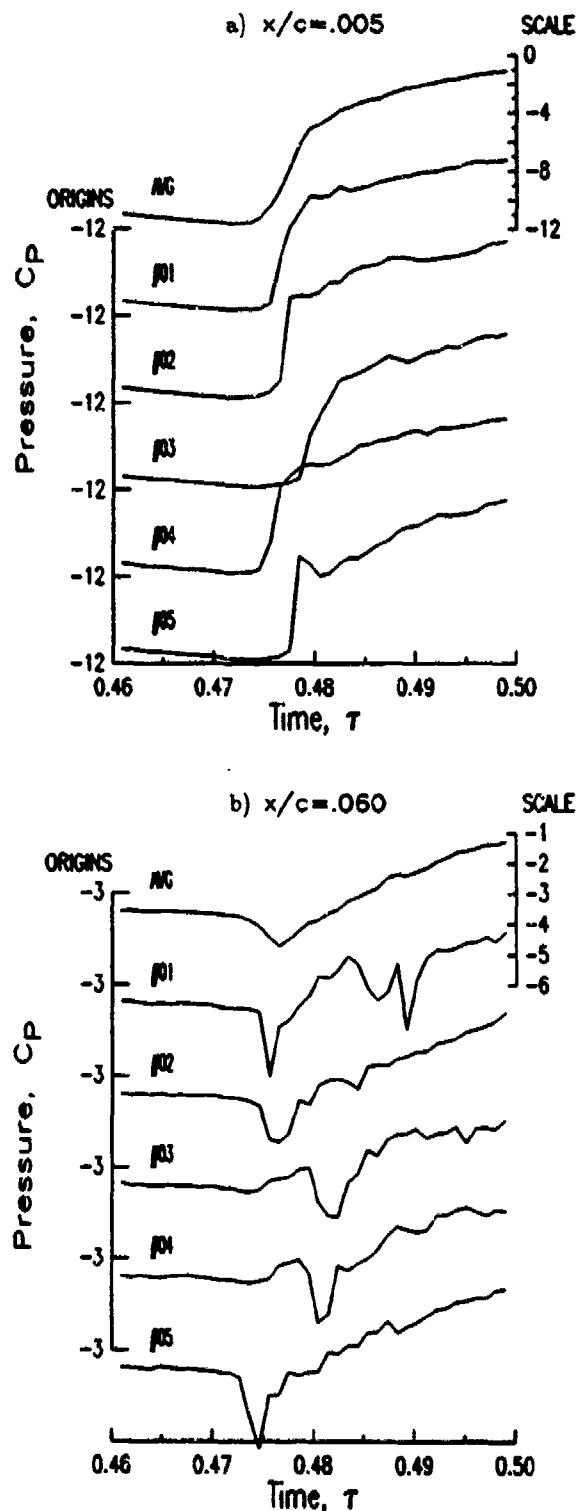


Fig. 7. Individual cycle and ensemble averaged pressure data at $z/c = 0.59$, during an $A = 0.01$ ramp at $M_c = 0.2$ and $\Lambda = 30^\circ$.

(Fig. 7a), cycles 01 and 04 resemble the average, while cycles 02 and 05 have a much steeper loss of suction. Cycle 04 appears to separate earlier than the average, while cycle 03 separates later. Angle of attack time histories (not shown) provide no indication of any substantial variation of $\alpha(r)$ from cycle to cycle, implying that these differences represent variations in the aerodynamic response rather than in the geometric boundary conditions. At $x/c = 0.06$ (Fig. 7b), the negative pressure peaks at cycles 01, 02, and 05 occur at approximately the same time as the average (at $r = 0.475$), but they are sharper and stronger. The negative peaks at cycles 03 and 04 occur later (at $r = 0.481$), although there is an increase in pressure near $r = 0.475$. There is a second strong negative peak at $r = 0.49$ for cycle 01. (Note that because the pressure transducers were divided among eight multiplexer positions,⁶ individual cycle data for different transducers cannot, in general, be correlated: cycle 01 at $x/c = 0.005$ is not the same event as cycle 01 at $x/c = 0.060$.)

Results such as these suggest that substantial cycle-to-cycle variations should be considered while interpreting ensemble-averaged results, since the averaging will smooth out the sharp changes that may be present in any individual realization. There are two implications for detailed studies of separation. First, simultaneous measurement of the same event at all relevant sensors is desirable. Second, laser velocimetry data, which are inherently ensemble-averaged, should be interpreted with care.

$M_c = 0.3$ RESULTS

The effects of compressibility on the aerodynamic loads on this model in steady state and during dynamic stall have been described in Ref. 21. As M_c increases, stall generally occurs more gradually and at lower α . Further, the delays in stall and increases in loads caused by unsteady motion are reduced in magnitude (but not eliminated). Figure 8 shows lift and moment coefficient curves at Mach numbers between 0.2 and 0.6, at fixed sweep angle ($\Lambda = 30^\circ$), pitch rate ($\dot{\Lambda} = 0.01$), and spanwise position ($z/c = 0.59$). The $M_c = 0.2$ condition is that described in the previous section. The maximum lift coefficient is reduced from 1.6 at $M_c = 0.2$ to 1.0 at $M_c = 0.6$, and the angle at which the negative pitching moment starts to develop (often referred to as the 'moment-stall' angle) drops from 21° to 11° . The remainder of this paper will describe the changes in the unsteady separation process that are responsible.

At $M_c = 0.3$, the unsteady chordwise pressure distributions are very similar to those at $M_c = 0.2$ prior to the onset of stall, but quite different thereafter. As shown in Fig. 9a, the pressure distribution at $\alpha = 17^\circ$ is quite smooth. As indicated by the C_p arrow, the chordwise velocity component near the leading edge is just becoming supersonic. Surface hot film data²² indicate that, as at $M_c = 0.2$, the point of transition to turbulence has moved forward of $x/c = 0.026$ by $\alpha \approx 10^\circ$, so the boundary layer has become essentially turbulent. At $\alpha = 18^\circ$ the pressure distribution at $M_c =$

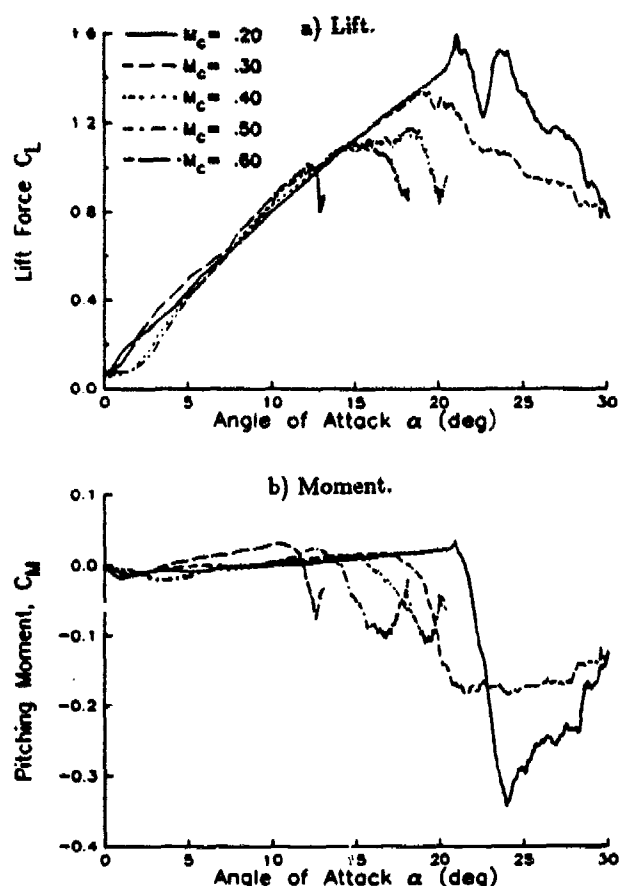


Fig. 8. Mach number effects on lift and pitching moment at $z/c = 0.59$, for $\Lambda = 0.01$ ramps at $\Lambda = 30^\circ$.

0.3 (Fig. 9b) remains virtually identical to that at $M_c = 0.2$ (Fig. 3a), with the exception of a slightly lower suction peak. The peak of $C_p = -8.2$ corresponds to a slightly supersonic chordwise Mach number of 1.1. Distortions to the pressure distribution first appear near $x/c = 0.1-0.2$ at $\alpha = 18.6^\circ$ (Fig. 9c). This is the same chordwise position where distortions appeared at $M_c = 0.2$, but they now occur at approximately 2° lower α . The disturbed region of the chord widens as α increases to 18.8° (Fig. 9d) and 19° (Fig. 9e), but the suction peak does not immediately collapse. In fact, the Mach number at $x/c = 0.005$ remains sonic until 19.2° (Fig. 9f). The region of negative pressure caused by the propagation of stall vorticity is also not as strong as at $M_c = 0.2$. At $\alpha \approx 20^\circ$ the moment is at its most negative (Fig. 8), but the pressure distribution (Fig. 9g) shows only a general thickening near the trailing edge. The pressure distribution becomes flat by $\alpha = 22^\circ$ (Fig. 9h), again with the exception of $x/c = 0.005$. The leading edge suction is not eliminated until $\alpha = 26^\circ$ (not shown).

Time histories of the ensemble-averaged pressures during stall at $M_c = 0.3$ (Fig. 10), show a more gradual loss of suction near the leading edge ($x/c = 0.005-0.06$) than at $M_c = 0.2$ (Fig. 4b). (Note that the time scale in Fig. 10 covers twice the period of that in Fig. 4b) The negative pressure valley associated with the formation of the stall vortex is not

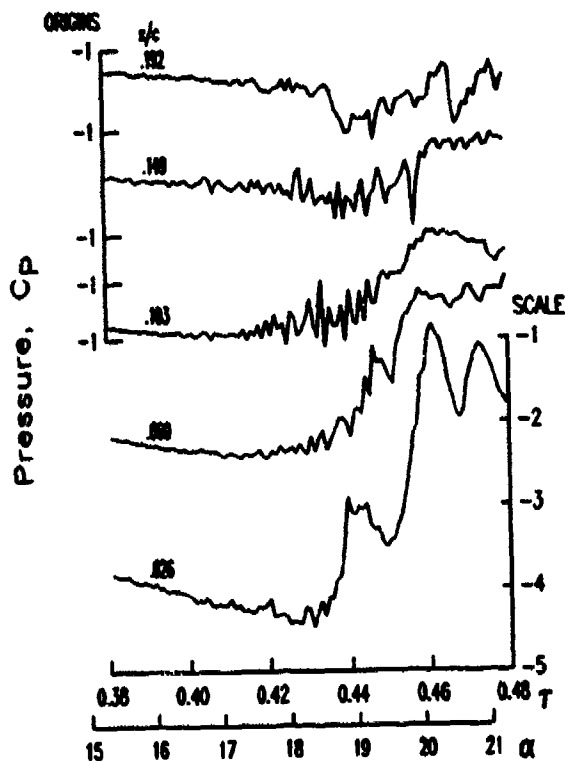


Fig. 12. Individual cycle pressure time histories at $z/c = 0.59$, during an $A = 0.01$ ramp at $M_c = 0.3$ and $\Lambda = 30^\circ$.

differences in the timing of the stall events observed at $M_c = 0.2$ (Fig. 7), the more gradual stall at $M_c = 0.3$ apparently leads to a more repeatable process. No such oscillations are apparent at $M_c = 0.2$ (Fig. 7), but they are present at $M_c = 0.3$ for the other two sweep angles, $\Lambda = 0$ and 15° (not shown).

Beyond a circumstantial attribution to compressibility, the source of this oscillation has not been identified. Besides Mach number, the only difference between the $M_c = 0.3$ and 0.2 conditions is Reynolds number (3 rather than 2×10^6). The nondimensional pitch rates, sweep angles, and geometries are the same, as are the ensemble-averaged C_p distributions prior to the onset of the oscillation (Figs. 3 and 9). Without the oscillation, the flow at $M_c = 0.2$ remains attached to 2° higher α than at $M_c = 0.3$. The only apparent change at $M_c = 0.3$ is the existence of a supersonic region. It is, however, quite weak ($M \leq 1.1$), and ends ahead of $x/c = 0.026$ (Fig. 9). While it is plausible that the oscillation originates at a (very weak) shock and then strengthens as it convects downstream to $x/c = 0.1$, no solid evidence for this exists. The connection between the oscillation and the early separation is clear, and results at higher M_c (to be discussed below) will solidify the links between the supersonic region, the oscillations, and separation.

$M_c = 0.4$ RESULTS

At $M_c = 0.4$, compressibility and shock effects become increasingly important. Figure 13 shows chordwise pressure

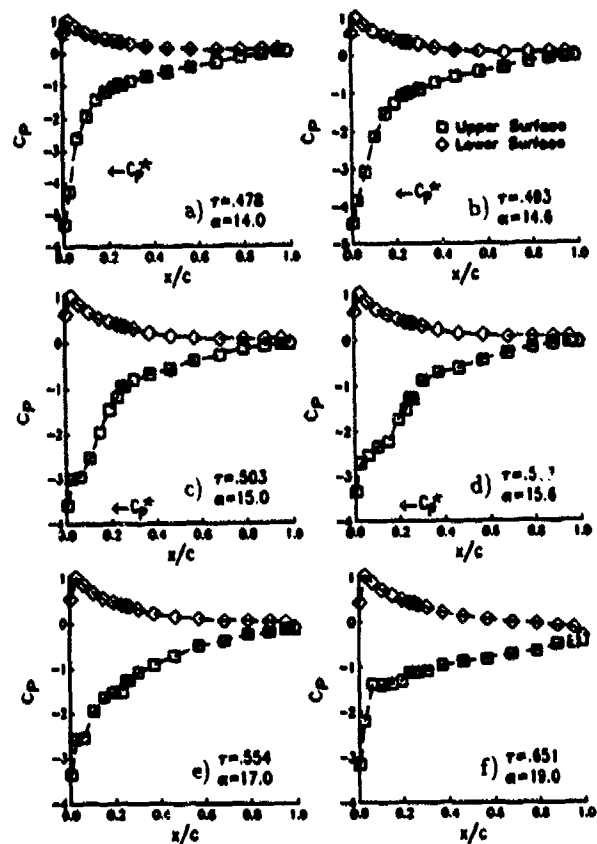


Fig. 13. Chordwise pressure distributions at $z/c = 0.59$, during an $A = 0.01$ ramp at $M_c = 0.4$ and $\Lambda = 30^\circ$.

distributions for the $A = 0.01$ ramp for $\Lambda = 30^\circ$ at this Mach number. The chordwise velocity first becomes supersonic near $\alpha = 11^\circ$, and at $\alpha = 14^\circ$ (Fig. 13a) maximum suction ($C_p = -5.3$), maximum local Mach number ($M = 1.3$), and maximum lift ($C_L = 1.1$, Fig. 8) are reached. At this time, the boundary between supersonic and subsonic velocities occurs between $x/c = 0.06$ and 0.1 . The sharp gradient implies the presence of a shock. As α increases beyond 14° , the lift remains relatively constant (Fig. 8), and, as shown in Fig. 13b at $\alpha = 14.6^\circ$, the suction peak is reduced. The gradient (shock) is weakened, but there are no clear signs of separation in the pressure distribution. At $\alpha = 15^\circ$ (Fig. 13c) the velocities at $x/c = 0.005$ have become subsonic, and there is a constant pressure plateau at $x/c = 0.026-0.06$. The pressure distribution over the forward 25% of chord continues to fatten by $\alpha = 15.6^\circ$ (Fig. 13d), reflecting the presence of the stall vorticity. This distortion is not as strong at $\alpha = 17^\circ$ (Fig. 13e), the time of peak negative pitching moment (Fig. 8). It is interesting to note that even though the flow is now largely separated, and (as will be shown below) contains considerable random unsteadiness, the ensemble averaged pressure distribution does not look very different from an attached flow distribution. By $\alpha = 19^\circ$ (Fig. 13f) this is changed, and there is a more conventional constant pressure plateau at $0.06 \leq x/c \leq 0.2$. Some leading edge suction still persists.

The sequence of events during the formation of the supersonic region and the subsequent separation are shown using ensemble averaged time histories in Fig. 14. The horizontal scale has again been expanded, to approximately twice the angle of attack range used at $M_c = 0.3$ (four times the range used in Fig. 4b at $M_c = 0.2$). The first event of interest is the bump in the pressure at $x/c = 0.026$ that occurs at $\tau \approx 0.38$ ($\alpha = 10^\circ$). As described in Ref. 22, this bump occurs at the same time as a rapid increase in hot film output, and indicates motion of the transition point forward of $x/c = 0.026$. The chordwise velocity becomes supersonic first at $x/c = 0.005$ and $\tau = 0.4$, and then at $x/c = 0.026$ and $\tau = 0.45$. The relatively rapid drop in pressure at $x/c = 0.026$ between $\tau = 0.44$ and 0.47 is caused by the motion of the shock aft past the transducer. At $\tau = 0.48$ ($\alpha = 14.1^\circ$), the pressures at $x/c = 0.005$ and 0.026 level off, and the pressure at $x/c = 0.060$ starts to become more negative. This is the first indication of separation in this plot. At $\tau = 0.49$ ($\alpha = 14.5^\circ$), the pressure begins to increase at $x/c = 0.026$ and decrease at $x/c = 0.1$ and 0.149 . This behavior looks similar to the loss of leading edge suction and formation of the stall vorticity observed at lower Mach number. In fact, the contour plot in Fig. 15 shows the pattern of a stall vortex in the region $0.1 \leq x/c \leq 0.4$ and $0.5 \leq \tau \leq 0.55$. In contrast to the results at lower Mach number (Figs. 6 and 11), no recognizable vortex pattern is evident further aft. A similar disappearance of a strong vortex signature at $M_c = 0.4$ was observed during the 2D experiment.⁶

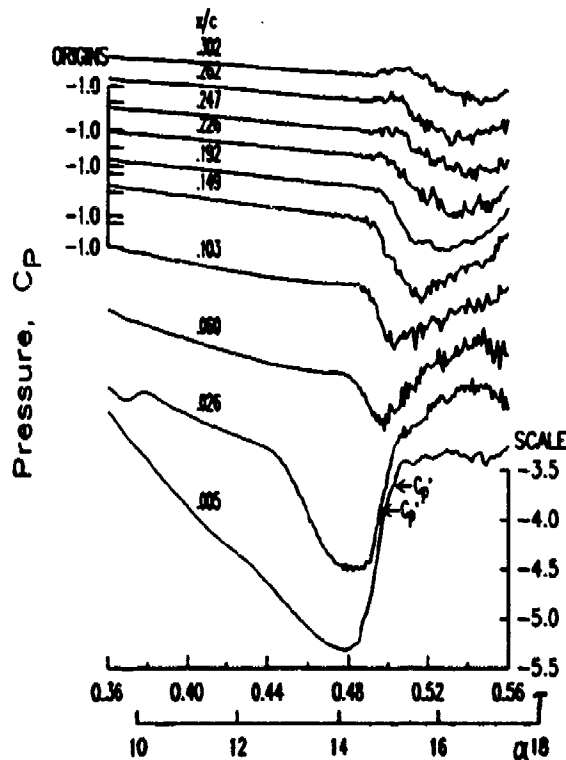


Fig. 14. Pressure time histories at $z/c = 0.59$, during an $A = 0.01$ ramp at $M_c = 0.4$ and $A = 30^\circ$.

The small high frequency oscillations that have survived ensemble averaging to appear in Fig. 14 hint that a high degree of unsteadiness is likely in individual realizations. As shown in Fig. 16, this takes several forms. The first is a small amplitude, higher frequency (approximately 2300 Hz) oscillation that appears at $x/c = 0.026$ and 0.06 at $\tau \approx 0.47$. The frequency is somewhat higher than at $M_c = 0.3$ (Fig. 12) and the first appearance of the oscillation is further forward, at $x/c = 0.06$ instead of 0.1 . This location is immediately

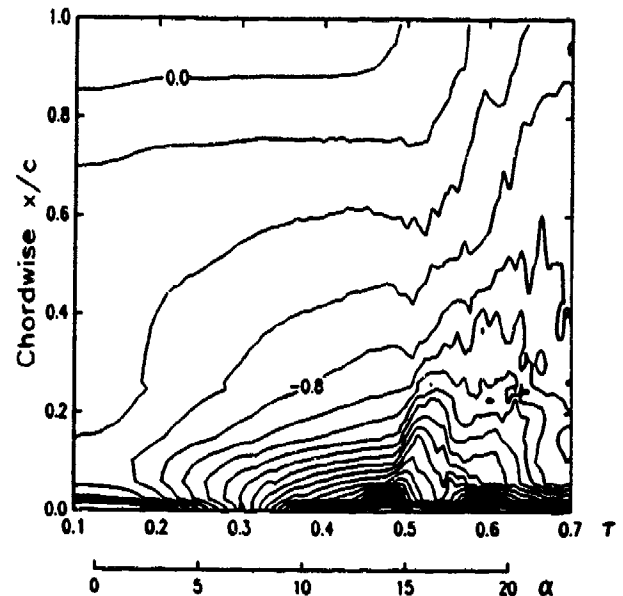


Fig. 15. Pressure contours at $z/c = 0.59$, during an $A = 0.01$ ramp at $M_c = 0.4$ and $A = 30^\circ$.

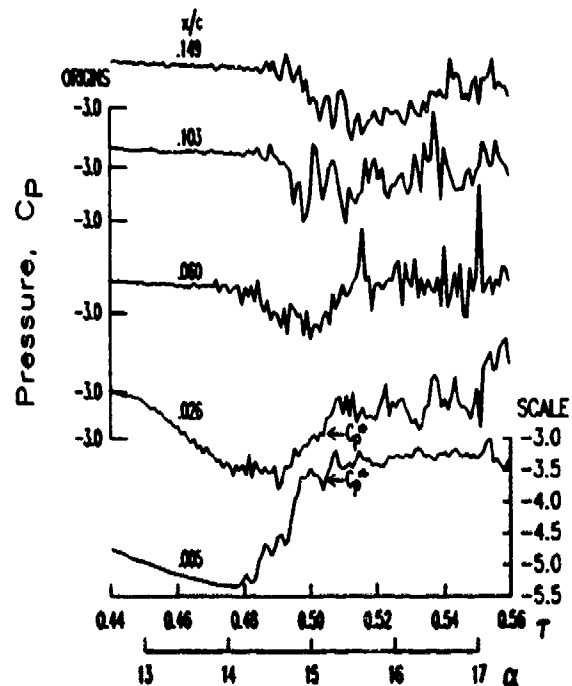


Fig. 16. Individual cycle pressure time histories at $z/c = 0.59$, during an $A = 0.01$ ramp at $M_c = 0.4$ and $A = 30^\circ$.

downstream of the shock (as indicated by the C_p arrows and Fig. 13a), improving the case for a shock-induced separation. Once the flow has separated (at $\tau \approx 0.48$) the oscillation amplitude is greatly increased, and the primary frequency is reduced. Frequencies near 1200 and 480 Hz have been identified for different chordwise positions and cycles. Note that these frequencies, while lower than those observed at $M_c = 0.3$, are still much higher than the vortex shedding frequencies of 38–70 Hz that were identified in the post-stall flow over the 2D model.⁶

$M_c = 0.5$ RESULTS

Chordwise pressure distributions for the $M_c = 0.5$ condition are shown in Fig. 17. These data are again for $A = 0.01$ and $\Lambda = 30^\circ$. At $\alpha = 9^\circ$ (Fig. 17a) a weak supersonic region ($M < 1.1$) has developed over the forward 6% of chord. Surface hot film results shown in Ref. 22 show that by this time the point of transition to turbulence has moved forward to $x/c \approx 0.06$. By $\alpha = 11^\circ$ (Fig. 17b) the maximum local Mach number has increased to 1.3, and a shock is apparent in the sharp pressure rise between $x/c = 0.06$ and 0.1. At $M_c = 0.5$ –0.6, the hot film data²² indicate that once transition has moved forward to the shock position, it tends to accompany the shock during any additional motion. There does not, however, appear to be an immediate shock-induced separation. The shock remains well-defined through $\alpha = 12.6^\circ$ (Fig. 17c), with a maximum local Mach number of approximately 1.5. The measured pressure ratio across the shock is now 2.2, in approximate agreement with the normal shock relations. At $\alpha = 12.8^\circ$ (Fig. 17d) the peak suction is reduced, and the shock becomes less distinct. This is the time when the pitching moment starts to drop (Fig. 8), although the lift continues to increase. By $\alpha = 13^\circ$ (Fig. 17e), the leading edge pressure distribution appears roughly triangular, with no clear shock. The forward 10% of chord remains supersonic. At $\alpha = 13.6^\circ$ (Fig. 17f) and 14.4° (Fig. 17g) the suction peak continues to drop, while the pressure distribution between 10 and 60% of chord fattens. At $\alpha = 16^\circ$ (Fig. 17h) the supersonic region has vanished, and there is a constant pressure plateau over the forward 40% of chord. At this time the lift has begun to drop (Fig. 8), and the moment has attained its most negative value.

The sequence of events during separation is clearly identified in the pressure time histories. Figure 18 shows ensemble averaged pressures during the period $0.36 \leq \tau \leq 0.56$, which covers the expansion of the supersonic region and the initiation of separation. The earliest events of interest are the bumps of increased pressure that occur at $x/c = 0.06$ and $\tau \approx 0.4$, and at $x/c = 0.1$ and $\tau \approx 0.44$. They coincide with the aft motion of the shock past each location. The initial indication of separation in the ensemble average is a drop in pressure observed downstream of the shock, at $x/c = 0.1$ and 0.149. It occurs at $\tau = 0.46$ ($\alpha \approx 12^\circ$). The individual cycle time histories (Fig. 19) show an oscillation at these locations which begins somewhat earlier, at $\tau \approx 0.45$ ($\alpha \approx 11.6^\circ$). This oscillation becomes quite strong by $\tau \approx$

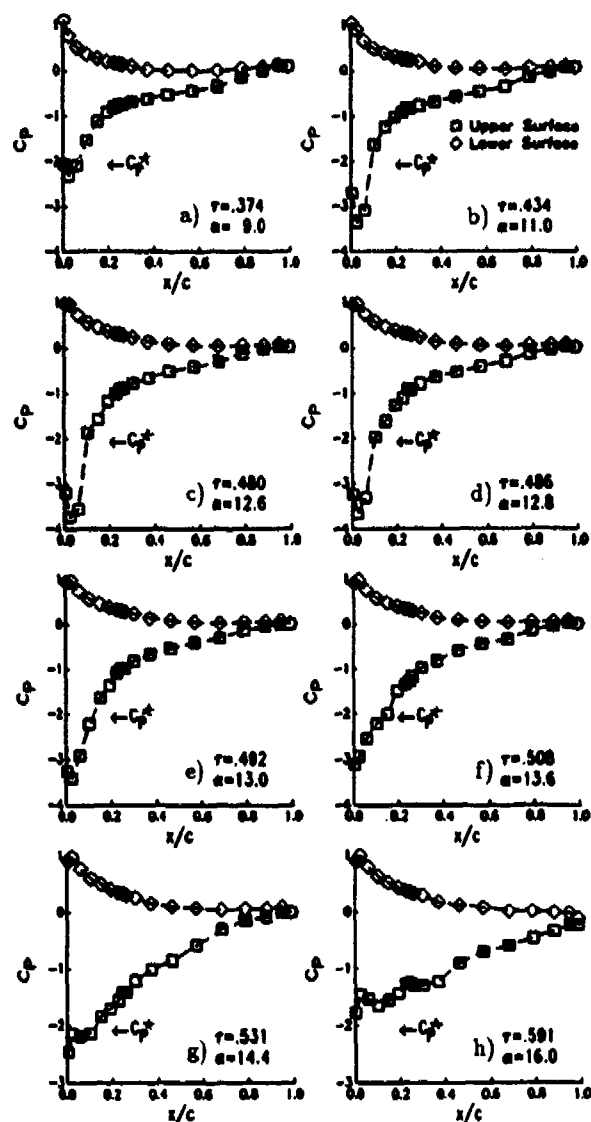


Fig. 17. Chordwise pressure distributions at $z/c = 0.59$, during an $A = 0.01$ ramp at $M_c = 0.5$ and $\Lambda = 30^\circ$.

0.47 ($\alpha = 12.2^\circ$). These signs of separation begin approximately $\Delta\tau = 0.04$ ($\Delta\alpha = 1.5^\circ$) before any comparable signs appear in the chordwise pressure distributions (Fig. 17).

Compared to the results for $M_c = 0.4$ (Fig. 16), the initial instability at M_c occurs earlier (by approximately $\Delta\alpha = 2^\circ$), and further aft (at $x/c = 0.1$ –0.14 instead of $x/c = 0.06$). These changes can be ascribed to a stronger shock which is located further aft. Well forward of the shock, at $x/c = 0.005$ and 0.026, the individual cycle time histories at $M_c = 0.5$ (Fig. 19) are extremely smooth during these initial stages of separation, with no indications of instability. There is a small oscillation just upstream of the shock at $x/c = 0.06$, but it does not seem to grow in magnitude until after suction has been lost at $\tau = 0.48$. The loss of leading edge suction in the ensemble averaged time histories (Fig. 18) occurs as a gradual progression, which moves forward from $x/c = 0.1$ at $\tau = 0.45$, to $x/c = 0.06$ at $\tau = 0.48$, and finally

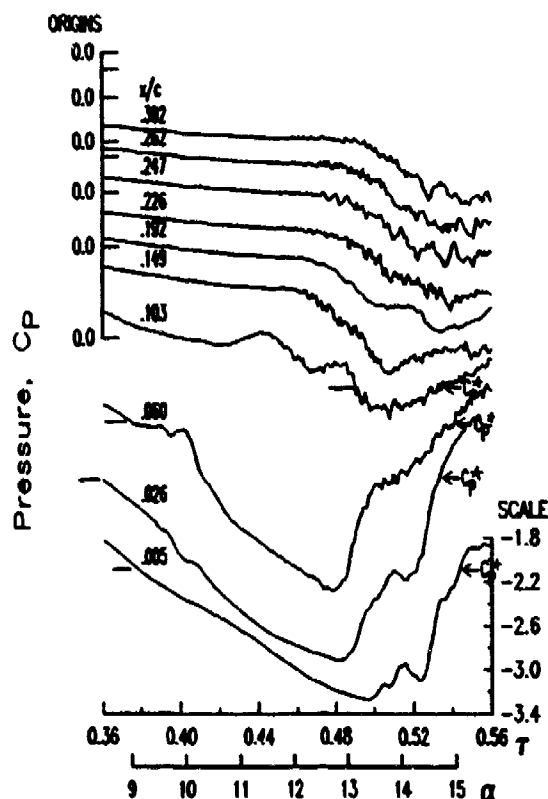


Fig. 18. Pressure time histories at $z/c = 0.59$, during an $A = 0.01$ ramp at $M_c = 0.5$ and $\Lambda = 30^\circ$.

to $x/c = 0.005$ at $\tau = 0.50$. The entire process requires approximately $\Delta\alpha = 2^\circ$.

The contour plot for this condition (Fig. 20) shows that separation also moves aft as a region of negative pressure (stall vorticity), in a manner resembling that observed at lower Mach number. In fact, the only significant changes from the isobars at $M_c = 0.4$ (Fig. 15) are a direct reflection of the stronger supersonic region (the shock is represented by the dense set of horizontal isobars between $\tau = 0.42$ and 0.48), and the earlier stall. (Note that the interval between isobars has been reduced from 0.2 to 0.1 to compensate for the reduced range in C_p .) The overall pattern is quite similar.

$M_c = 0.6$ RESULTS

In order to stay within structural load limits, the highest pitch rate at $M_c = 0.6$ was limited to $A = 0.005$.¹ Based upon trends observed at other conditions,^{6,21} the reduction in rate from $A = 0.01$ probably results in somewhat lower maximum lift and moment coefficients and in an earlier stall. However, it is likely that the mechanics of the

¹The peak lift on the model at this condition was 3440 lbs, and the peak pitching moment was 375 ft-lbs. These loads were applied during a ramp period of 0.05 sec.

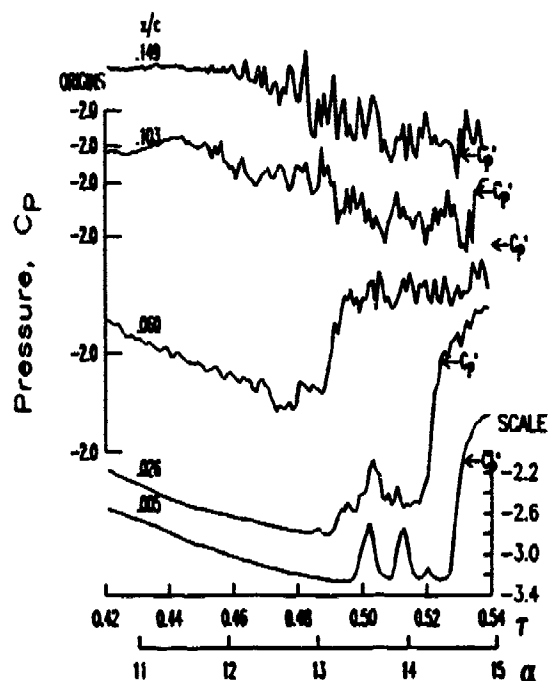


Fig. 19. Individual cycle pressure time histories at $z/c = 0.59$, during an $A = 0.01$ ramp at $M_c = 0.5$ and $\Lambda = 30^\circ$.

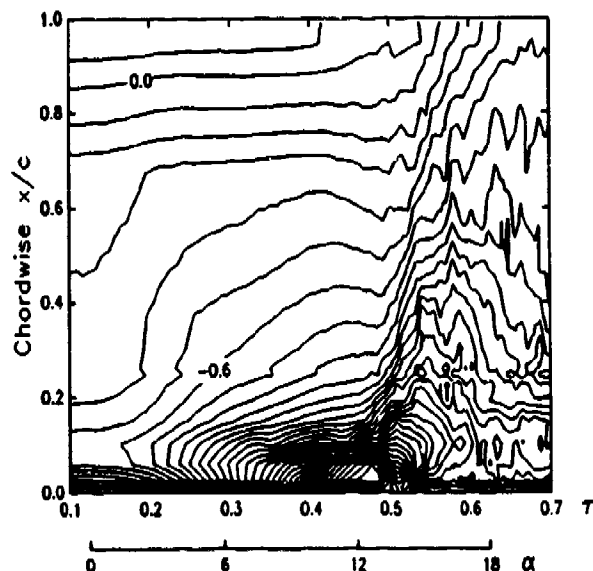


Fig. 20. Pressure contours at $z/c = 0.59$, during an $A = 0.01$ ramp at $M_c = 0.5$ and $\Lambda = 30^\circ$.

separation and stall process, which are of primary current interest, are not substantially altered.

As shown by the pressure distribution in Fig. 21a, at $M_c = 0.6$ a shock between $x/c = 0.1$ and 0.14 first becomes apparent at $\alpha = 5^\circ$. As α increases, the shock strengthens, reaching a local chordwise Mach number of 1.25 at $\alpha = 7^\circ$ (Fig. 21b). The shock moves aft past $x/c = 0.15$ at

$\alpha = 8^\circ$ (Fig. 21c), and continues to strengthen, reaching a peak local Mach number of 1.5 near $\alpha = 9^\circ$ (Fig. 21d). Indications of separation appear as the pressure distribution becomes distorted downstream of the shock at $\alpha = 10^\circ$ (Fig. 21e). The sharp shock disappears by $\alpha = 11^\circ$ (Fig. 21f), and the pressure distribution between $x/c = 0.2$ and 0.4 starts to fill in. The suction peak is then slowly reduced, and a pressure plateau expands to about $x/c \approx 0.2$, as shown in Fig. 21g at $\alpha = 12^\circ$. The plateau covers the entire forward 40% of chord by $\alpha = 12.8^\circ$ (Fig. 21h).

The ensemble averaged pressure time histories at $M_c = 0.6$ (Fig. 22) are qualitatively very similar to those at $M_c = 0.5$ (Fig. 18). The primary difference is that the shock is approximately 10% of chord further aft. The separation begins just downstream of the shock at $\alpha \approx 8^\circ$, and slowly expands both forward and aft. The drop in pressure first reaches $x/c = 0.3$ at $\alpha = 10^\circ$, and the suction collapse reaches $x/c = 0.005$ at $\alpha = 12^\circ$. The required intervals of $\Delta\alpha = 2$ and 4° for separation to propagate to $x/c = 0.3$ and

0.005, respectively, are 16 times greater than the equivalent intervals at $M_c = 0.2$ (0.12 and 0.24° , Fig. 4). In terms of the convection time scale, $\frac{U_c}{c}$, the interval is 32 times longer at $M_c = 0.6$.

The pressure contour plot at $M_c = 0.6$ shown in Fig. 23 shows the expected similarity to the $M_c = 0.5$ results in Fig. 19. The dense set of horizontal isobars corresponding to the shock illustrate the growth in the supersonic region from $\alpha = 4$ to 9° , and its rapid contraction by $\alpha = 12^\circ$. (The apparent jump in the chordwise (vertical) position of the shock at $r = 0.42$ is an artifact of the contouring package, which represents the shock as a linear fit between transducer locations.) It is perhaps significant that, even at $M_c = 0.6$, there is still a strong pattern of isobars that trace the motion of a negative pressure region from $r = 0.52$, $x/c = 0.2$ to $r = 0.62$, $x/c \approx 1.0$. Vorticity is still apparently being formed and propagated downstream at stall, although not in the form of the compact vortex present at $M_c = 0.2$ (Fig. 6a).

The final piece of information to be presented is the individual cycle time histories at $M_c = 0.6$. As shown in Fig. 24, the high frequency oscillations that signal the onset of instability first appear at $x/c = 0.22-25$ at $r \approx 0.47$ ($\alpha = 9^\circ$). (The transducer at $x/c = 0.192$ appears to have a poor high frequency response, and therefore is not able to detect these oscillations.) The oscillations (which may be more accurately described at this time as a region of aperiodic unsteadiness) expand in magnitude and chordwise extent as separation proceeds. As at $M_c = 0.5$, there are no oscillations prior to separation in the supersonic region, $x/c \leq 0.149$.

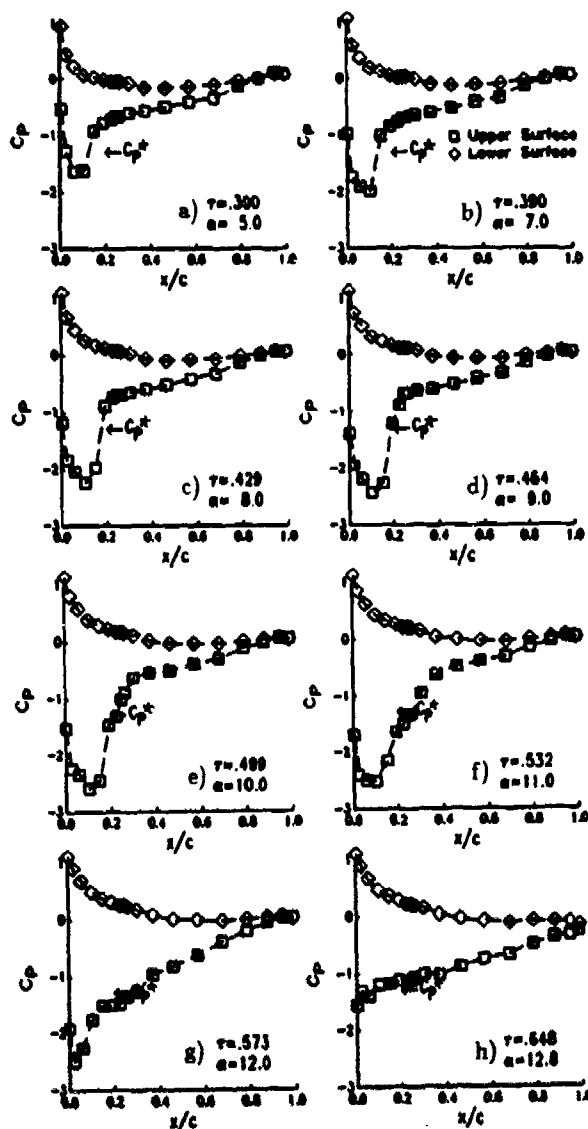


Fig. 21. Chordwise pressure distributions at $z/c = 0.59$, during an $A = 0.005$ ramp at $M_c = 0.6$ and $A = 30^\circ$.

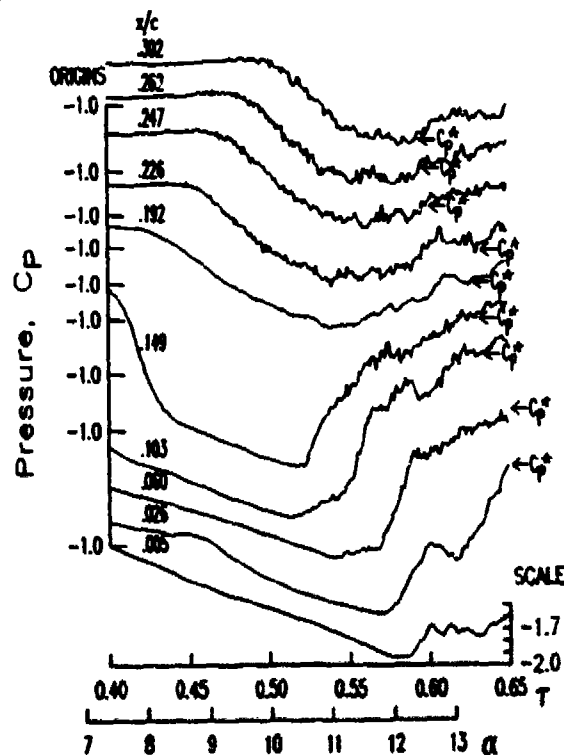


Fig. 22. Pressure time histories at $z/c = 0.59$, during an $A = 0.005$ ramp at $M_c = 0.6$ and $A = 30^\circ$.

SUMMARY AND CONCLUSIONS

Experimental information has been presented on the unsteady separation and dynamic stall process for pitching motions of a wing model at conditions representative of a full helicopter main rotor blade ($Re = 2-6 \times 10^6$, $A = 0.01$). The primary observations and interpretations that have been extracted from these results are as follows.

1. At low Mach number ($M_c = 0.2$), when the local velocities remain subsonic, separation begins near $x/c = 0.1$, and rapidly spreads (within an angle of attack increment of approximately 0.2°) to include loss of leading edge suction and formation of an intense and concentrated region of vorticity. This stall vortex then propagates downstream, increasing the lift and pitching moment.
2. Surface hot film measurements at $M_c = 0.2$ indicate that, by the onset of separation, the point of transition to turbulence has moved very close to the leading edge. There are no signs of a laminar separation bubble. Turbulent boundary layer separation near $x/c = 0.1$ appears to be the primary stall mechanism.
3. Time histories for individual cycles (realizations) of the motion show considerable variation over the small time scales that characterize separation at $M_c = 0.2$. Ensemble averages may therefore provide a misleading picture of the details of the phenomena.
4. At $M_c = 0.3$, a very small region of weakly supersonic velocities is formed near the leading edge. This region is the only visible difference from the results at $M_c = 0.2$. Thus the supersonic region is presumed to be the cause of a relatively high frequency oscillation observed near $x/c = 0.1$. The oscillation grows in amplitude until separation occurs, at an angle of attack 2° lower than at $M_c = 0.2$.
5. As Mach number increases to $M_c = 0.4, 0.5$, and 0.6 , the supersonic region appears at lower angle of attack, and is increased in strength and chordwise extent. The shock terminating this region also strengthens, reaching an upstream Mach number of 1.5 and a pressure ratio of 2.2 at $M_c = 0.5$. At low to moderate angles of attack (prior to separation), transition to turbulence occurs near the shock.
6. The high frequency pressure oscillations that precede separation also occur at lower angles of attack as Mach number increases. They originate shortly downstream of the shock, and appear to initiate a gradual separation. The separation requires up to 32 times longer (in terms of the convection time scale) at $M_c = 0.6$ than at $M_c = 0.2$ to expand from the point of initiation to cover the forward 30% of the chord.

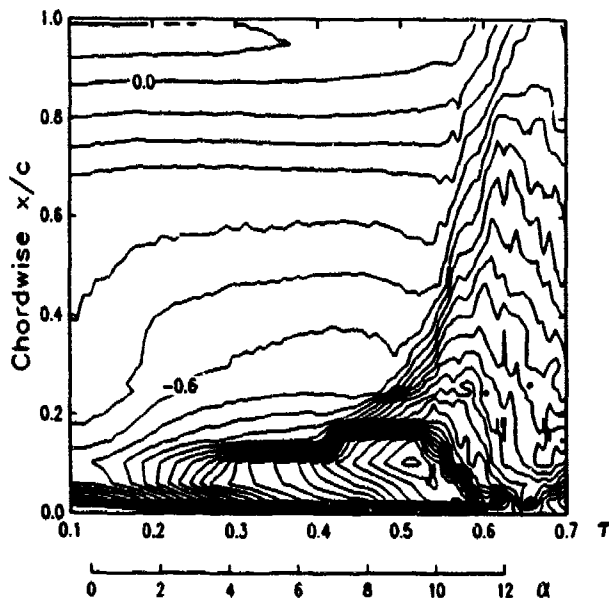


Fig. 23. Pressure contours at $z/c = 0.59$, during an $A = 0.005$ ramp at $M_c = 0.6$ and $A = 30^\circ$.

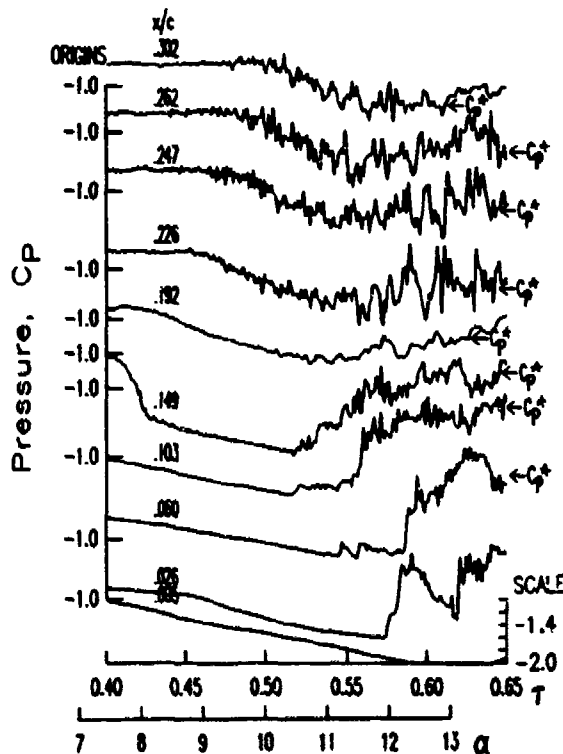


Fig. 24. Individual cycle pressure time histories at $z/c = 0.59$, during an $A = 0.005$ ramp at $M_c = 0.6$ and $A = 30^\circ$.

7. During this process, the sharp shock is replaced by a region of transition from supersonic to subsonic flow that is (on average) approximately linear with chordwise position. The aperiodic unsteadiness of this region is, however, very high. Eventually the flow becomes everywhere subsonic, and the pressure distribution takes the form of a conventional separation plateau.
8. The pressure signatures of the stall vortex become much less concentrated at $M_c \geq 0.4$, and disappear well before the trailing edge. At $M_c = 0.4$, a strong signature is visible only from $x/c \approx 0.05$ to 0.3 , while at $M_c = 0.6$, the signature vanishes by $x/c = 0.25$.

ACKNOWLEDGMENTS

The instrumented model, the wind tunnel test, and the analysis of the results were funded by the U.S. Army Research Office and the U.S. Air Force Office of Scientific Research, under Contract DAAL03-89-C-0013. Dr. Thomas Doligalski of ARO was the technical monitor. Capt. Hank Helin and Maj. Daniel Fant were the AFOSR representatives. The model support and drive system used in the experiment was supplied by the Sikorsky Aircraft Division of United Technologies. The author thanks Franklin Carta, Alfred Covino, John Ayer, and the staff of the UTRC LSWT for their assistance.

REFERENCES

1. Harper, P.W., and Flanigan, R.E., "The Effect of Rate of Change of Angle of Attack on the Maximum Lift of a Small Model," NACA TN 2061, 1949.
2. Liiva, J., and Davenport, F.J., "Dynamic Stall of Airfoil Sections for High-Speed Rotors," *Journal of the American Helicopter Society*, Vol. 13, pp. 49-55, Apr. 1968.
3. Dadone, L.U., "Two-Dimensional Wind Tunnel Test of an Oscillating Rotor Airfoil," NASA CR 2914, Dec. 1977.
4. St. Hilaire, A.O., Carta, F.O., Fink, M.R., and Jepson, W.D., "The Influence of Sweep on the Aerodynamic Loading of an Oscillating NACA 0012 Airfoil," NASA CR-3092, 1979.
5. McCroskey, W.J., McAlister, K.W., Carr, L.W., Pucci, S.L., Lambert, O., and Indergard, R.F., "Dynamic Stall on Advanced Airfoil Sections," *Journal of the American Helicopter Society*, Vol. 26, pp. 40-50, July 1981.
6. Lorber, P.F. and Carta, F.O., "Airfoil Dynamic Stall at Constant Pitch Rate and High Reynolds Number," *Journal of Aircraft*, Vol. 25, June 1988, pp. 548-556.
7. Fung, K.Y. and Carr, L.W., "Effects of Compressibility on Dynamic Stall," *AIAA Journal*, Vol. 29, February 1991, pp. 306-308.
8. Carr, L.W., Chandrasekhara, M.S., and Brock, N.J., "A Quantitative Study of Unsteady Compressible Flow on an Oscillating Airfoil," AIAA Paper 91-1683, 22nd Fluid Dynamics, Plasma Dynamics, and Structures Conference, Honolulu, HI, June 1991.
9. St. Hilaire, A.O. and Carta, F.O., "Analysis of Unswept and Swept Wing Chordwise Pressure Data from an Oscillating NACA 0012 Airfoil Experiment," NASA CR 3567, 1983.
10. Chandrasekhara, M.S. and Carr, L.W., "Flow Visualization Studies of the Mach Number Effects on the Dynamic Stall of an Oscillating Airfoil," *Journal of Aircraft*, Vol. 27, June 1990, pp. 516-522.
11. Carr, L.W., Chandrasekhara, M.S., Ahmed, S., and Brock, N.J., "A Study of Dynamic Stall Using Real Time Interferometry," AIAA Paper 91-0007, 29th Aerospace Sciences Meeting, Reno, NV, Jan. 1991.
12. Ericsson, L.E. and Reding, J.P., Fluid Mechanics of Dynamic Stall Part II. Prediction of Full Scale Characteristics, *Journal of Fluids and Structures*, Vol. 2, pp. 113-143, 1988.
13. Visbal, M.R., "Effect of Compressibility on Dynamic Stall of a Pitching Airfoil," AIAA Paper 88-0132, 26th Aerospace Sciences Meeting, Reno NV, Jan. 1988.
14. Ekaterinaris, J., "Compressible Studies of Dynamic Stall," AIAA Paper 89-0024, 27th Aerospace Sciences Meeting, Reno NV, Jan. 1989.
15. Patterson, M.T. and Lorber, P.F., "Computational and Experimental Studies of Compressible Dynamic Stall," *Journal of Fluids and Structures*, Vol. 4, 1990, pp. 259-285.
16. Currier, J. and Fung, K.Y., "An Analysis of the Onset of Dynamic Stall," AIAA Paper 91-0003, 29th Aerospace Sciences Meeting, Reno NV, Jan. 1991.
17. Visbal, M.R., "On Some Physical Aspects of Airfoil Dynamic Stall," ASME Symposium on Non-Steady Fluid Dynamics, Toronto, Canada, June 1990.
18. De Ruyck, J., Hazarika, B., and Hirsch, C., "Transition and Turbulence Structure in the Boundary Layers of an Oscillating Airfoil," Vrije Univ. Brussels Report STR-16, Dec. 1989.
19. Chandrasekhara, M.S. and Ahmed, S., "Laser Velocimetry Measurements of Oscillating Airfoil Dynamic Stall Flow Field," AIAA Paper 91-1799, 22nd Fluid Dynamics, Plasma Dynamics, and Lasers Conference, Honolulu HI, June 1991.
20. Leishman, J.G., "Dynamic Stall Experiments on the NACA 23012 Aerofoil," *Experiments in Fluids*, Vol. 9, pp. 49-58, 1990.

21. Lorber, P.F., Carta, F.O., and Covino, A.F. Jr., "Dynamic Stall Experiments on a Swept Three-Dimensional Wing In Compressible Flow," AIAA Paper 91-1795, 22nd Fluid Dynamics, Plasma Dynamics, and Lasers Conference, Honolulu HI, June 1991.
22. Lorber, P.F. and Carta, F.O., "Unsteady Transition Measurements on a Pitching Three-Dimensional Wing," Fifth Symposium on Numerical and Physical Aspects of Aerodynamic Flows, Long Beach, CA, Jan. 1992.
23. Lorber, P.F. and Carta, F.O., "Incipient Torsional Stall Flutter Experiments on a Swept Three-Dimensional Wing," AIAA Paper 91-0935, 32nd Structures, Structural Dynamics, and Materials Conference, Baltimore MD, April 1991.
24. Lorber, P.F. and Carta, F.O., "Unsteady Stall Penetration Experiments at High Reynolds Number", AFOSR TR-87-1202, April 1987.
25. Lorber, P.F., "Aerodynamic Results of a Pressure-Instrumented Model Rotor Test at the DNW", *Journal of the American Helicopter Society*, Vol. 36, pp. 66-76, Oct. 1991.

APPENDIX VIII

DYNAMIC STALL OF SINUSOIDALLY OSCILLATING THREE-DIMENSIONAL SWEPT AND UNSWEPT WINGS IN COMPRESSIBLE FLOW

Peter F. Lorber

United Technologies Research Center
East Hartford, CT

ABSTRACT

Measurements have been made of the unsteady aerodynamic response of a three dimensional wing to sinusoidal pitching oscillations. The model scale and test conditions were selected to simulate the Reynolds number, airfoil section, Mach number, reduced frequency, angular range, and sweep angles of a full scale helicopter main rotor blade. Surface pressure measurements at five spanwise locations are used to identify the physical processes and characterize the resulting airloads. Qualitative agreement is found with data for constant pitch rate ramps, implying that previous observations regarding the details of the stall process remain valid for sinusoidal motions. The effects of the primary test parameters on the airloads during large amplitude sinusoids are described. Study of a series of moderate amplitude motions at varied mean angle of attack suggest that it is not feasible to achieve significant unsteady lift enhancements and stall delays without generating a strong dynamic stall vortex and thus an undesirable unsteady pitching moment.

NOMENCLATURE

A	pitch rate, $\dot{\alpha}c/2U_c$
c	airfoil chord (17.3 in.)
C_D	section pressure drag coefficient, D/qc
C_L	section lift coefficient, L/qc
C_M	section $\frac{1}{4}$ chord moment coefficient, M/qc^2
C_P	pressure coefficient, $(P - P_\infty)/q$
C_P^*	pressure coefficient for locally sonic chordwise velocity
M_c	chordwise Mach number, $M_\infty \cos \Lambda$
M_∞	freestream Mach number
P_∞	freestream static pressure
q	dynamic pressure, $\frac{1}{2}\rho_\infty U_\infty^2$
$Q.S.$	quasi-steady force or moment coefficient
t	time

T	acquisition period
Re	Reynolds number, cU_c/ν
U_c	chordwise component of freestream velocity, $U_\infty \cos \Lambda$
U_∞	freestream velocity
x	distance along chord from leading edge
s	distance along span from tip leading edge
$\dot{\alpha}$	pitch rate, rad/sec
α	geometric angle of attack
	ramp: $\alpha = \alpha_{min}, \tau \leq 0.125$
	$\alpha = \alpha_{min} + 2(\tau - 0.125)(\alpha_{max} - \alpha_{min}),$
	$0.125 \leq \tau \leq 0.625$
	$\alpha = \alpha_{max}, \tau \geq 0.625$
	sine: $\alpha = \alpha_0 - \alpha_1 \cos 2\pi\tau$
α_{ss}	steady-state stall angle, $\alpha_{ss}(M_\infty, \Lambda, s)$
Λ	sweep-back angle
ν	kinematic viscosity
ρ_∞	freestream density
τ	nondimensional time, t/T
ω	circular frequency, $2\pi/T$

INTRODUCTION

The unsteady aerodynamics of a helicopter rotor blade have frequently been simulated by oscillating a model wing in a wind tunnel. Numerous experiments on two dimensional airfoils have been conducted to study large amplitude pitching motions that include dynamic stall.¹⁻⁹ These tests were conducted at Reynolds numbers up to those appropriate to full scale main rotor blades ($10^6 - 10^7$), and for a variety of Mach number ranges and airfoil sections. Many of the fundamental characteristics of the resulting airloads have been identified by either directly measuring the forces and moments on the model or by integrating surface pressure data. Another avenue has been to study the flow field around the model in order to gain insight into phenomena such as the development and propagation of the dynamic stall vortex.¹⁰⁻¹⁴

Experimental studies using three-dimensional geometries are more recent. Two basic geometries have received most attention: highly swept delta wings and

Presented at the AHS 48th Annual Forum, Washington, D.C., June 3-5, 1992. ©1992 by the American Helicopter Society, Inc. All rights reserved.

rectangular wings at low or zero sweep. The latter are more relevant to helicopter dynamic stall. An extensive series of experiments have been performed at the U.S.A.F. Academy and the University of Colorado on a rectangular 6 in. (15.6 cm) chord wing. Smoke wire flow visualization and surface pressure measurements were first used to examine constant pitch rate motions of the unswept wing.¹⁵⁻¹⁶ The inboard characteristics agreed well with 2D results, while interaction with the tip vortex was found to prolong the residence time of the stall vortex and increase the unsteady tip loads. Flow visualization and hot wire anemometry were used to examine sinusoidal oscillations of a similar model mounted at sweep angles of -30, 0, and +30°.¹⁷ The spanwise flow created by sweep strongly affected the unsteady vortex structure. Aft sweep reduced the influence of the tip vortex, while forward sweep greatly increased the region subject to strong 3D effects. Finally, sinusoidal oscillation of the pressure instrumented model¹⁸ also showed strong 3D effects near the tip. While these experiments have provided valuable insight, the geometry (NACA 0015 airfoil) and test conditions ($Re \approx 4 \times 10^4$ to 2×10^5 , $M < 0.1$, $k = 0.6-1.0$) are not representative of a helicopter blade.

The results contained in this paper are also for sinusoidal motion of a rectangular wing. This experiment, however, was designed to simulate (as closely as practical on a single, non-rotating wing) the conditions of a full-scale helicopter main rotor blade. This required attempting to match Reynolds number, Mach number, frequency, airfoil section, sweep angle, and angle of attack range. Effects such as rotational body forces, plunging motions, and unsteady variations in Mach number and sweep angle were not simulated.

Other results from this program have been described in a series of earlier papers. References 19 and 20 describe the experiment and survey the results for constant pitch rate (ramp) motions. They identify the dependence of the surface pressures and loads upon the test parameters (pitch rate, wing sweep, Mach number, spanwise position, and tip geometry). The unsteady separation process is examined in Ref. 21, including the changes introduced by increasing M_c from 0.2 to 0.6. Reference 22 describes how the laminar to turbulent boundary layer transition location responds to the unsteady pitching motion. Finally, small amplitude oscillations ($\alpha_1 \approx 0.5-2^\circ$) about mean angles near static stall were used to simulate the initial stages of stall flutter.²³

While many of the features identified in these papers are relevant to large amplitude sinusoidal motions (and will be summarized in a following section), there are sufficient differences between sinusoidal and ramp motions to warrant further investigation. For high reduced frequencies in particular, the addition of a peri-

odic wake structure and the lack of an initial steady-state, low α starting condition may alter the separation process and the resulting aerodynamic loads. The negative pitch rate portions of the sinusoids also provide a convenient way to examine reattachment.

DESCRIPTION OF EXPERIMENT

The model was a straight, rectangular, untwisted, semi-span wing of 17.3 in. (44 cm) chord and 48 in. (122 cm) span (Fig. 1). The aspect ratio of a full-span wing would be 5.6. The wing consisted of a steel spar and fiberglass airfoil panels, and had a Sikorsky SSC-A09 9% thickness cambered section.¹⁹ The wing was mounted at sweep angles of 0, 15, and 30° from the side wall of the 8 ft (2.4 m) octagonal test section of the UTRC Large Subsonic Wind Tunnel. Additional airfoil panels were added at non-zero sweep angles in order to keep the wing tip $\frac{1}{4}$ chord at the tunnel centerline. The tip was always perpendicular to the leading and trailing edges. All conditions reported in this paper used an approximate body-of-revolution tip cap. A hydraulic rotary drive oscillated the model in pitch about the line connecting the root and tip $\frac{1}{4}$ chord. Two pitching waveforms were used, sinusoids and constant rate ramps. For this model, the Mach and Reynolds numbers are approximately related by $Re = M_c \times 10^7$.

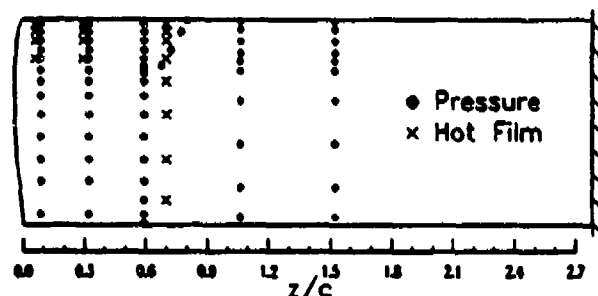


Fig. 1. Wing planform and instrumentation locations.

Unsteady surface pressure measurements were made by 112 miniature transducers distributed among five spanwise stations. The suction surface transducer locations are shown by the dots in Fig. 1. The chordwise arrays on the upper surface had 10, 14, or 18 transducers each. There were 18 transducers on the lower surface at $z/c = 0.59$, and 6 at each of the other stations. The transducers were installed to retain a smooth surface contour and achieve a flat frequency response to at least 4 kHz. The pressures were integrated along the chord at each spanwise station using Gaussian quadrature to determine the unsteady lift, pressure drag, and pitching moment coefficients. Sixteen flush-mounted surface hot film gages (identified by the x-marks in Fig. 1) were used to identify transition and separation locations.

The signals from both the pressure transducers and hot film gages were passed through 10 kHz low pass filters and digitised (to 15 bit accuracy) at a rate of 1024 samples per oscillation period (T). Ensemble-averaged time histories were computed using 20 periods. Both the individual cycle data and the ensemble averages were recorded on digital magnetic tape. Note that all conversions to coefficient used the chordwise velocity component, $U_c = U_\infty \cos \Lambda$. A more complete description of the experiment is provided in Refs. 20 and 22. The complete data set (295 steady and 607 unsteady conditions) will be made available in a technical report and a set of digital data tapes.

PREVIOUS RESULTS

Experimental results obtained with this model in steady state, for low amplitude sinusoids, and for ramps have been described in previous publications. The primary conclusions will now be summarised to provide a starting point for the material to be introduced in this paper.

In steady flow, aerodynamic load characteristics are as expected for a simple subsonic wing.²⁰ The effects of increasing Mach number include increasing the lift curve slope in attached flow, reducing the maximum load coefficients, and reducing the stall angle. For the unswept 3D wing, the tip vortex reduces the effective angle of attack, generating attached flow spanwise load distributions in approximate agreement with lifting line models. Prior to stall, the effects of sweep on the pressures and airloads on the inboard portion of the wing can be accounted for using the swept infinite wing normalisation ($q = q_\infty \cos^2 \Lambda$). Such simple correlations do not suffice close to the wing tip or after stall.

For small amplitude oscillations,²³ the primary concern is stability, as determined by the sign of the aerodynamic pitch damping. If the instantaneous angle of attack never exceeds the static stall angle, α_{ss} , the damping was found to be positive, and in general agreement with unsteady thin airfoil theory. Motions about mean angles (α_0) near α_{ss} typically have negative damping. The basic mechanism is an unsteady delay in stall beyond α_{ss} during the pitch-up portion of the cycle, a loss of leading edge suction at stall (leading to a negative or nose-down moment), and finally a delay in reattachment during pitch-down. The resulting hysteresis in C_M causes the negative damping. This mechanism was observed for the complete range of reduced frequencies ($0.1 \leq k \leq 0.6$), Mach numbers ($0.2 \leq M_c \leq 0.6$), and sweep angles ($\Lambda = 0, 15$, and 30°) tested. If α_0 is high enough so that the flow remains separated throughout the cycle, the damping was found to again become positive. Three-dimensionality and sweep alter the damping characteristics primarily

through their effects on α_{ss} . As α_0 is increased with the unswept wing, the inboard region stalls first, followed by the tip. Since negative damping occurs only for $\alpha_0 \approx \alpha_{ss}$, the unswept wing therefore is never simultaneously unstable. At $\Lambda = 30^\circ$, stall occurs over the entire span within $\Delta\alpha = 1^\circ$, allowing a simultaneous instability.

For large amplitude ramps at low Mach number ($M_c = 0.2$) and high Reynolds number ($Re = 2 \times 10^6$), the following separation and stall mechanism was observed at all sweep angles. At the initial steady state condition ($\alpha = 0$) pressure gradients are low, and the upper surface boundary layer remains laminar for $x/c \leq 0.3$.²² As α increases, the adverse pressure gradients downstream of the suction peak cause the transition point to move very close to the leading edge ($x/c \leq 0.026$), leading to an essentially turbulent boundary layer by $\alpha \approx 10$ – 12° . This boundary layer separates, starting near $x/c = 0.1$, and the separation very quickly (within $\Delta\alpha = 0.2^\circ$) expands, leading to loss of leading edge suction and formation of an intense and concentrated stall vortex.²¹ The vortex propagates downstream, increasing the lift, drag, and pitching moment.²⁰ The fundamental characteristics are quite similar to those identified on the 2D model,⁸ and in many earlier experiments.^{1–18}

At $M_c = 0.3$, a small region of slightly supersonic flow ($M \approx 1.1$) develops near the leading edge. The supersonic region is believed to be the source of a relatively high frequency oscillation²¹ that appears near $x/c = 0.1$ and then grows, leading to separation at an angle of attack 2° lower than at $M_c = 0.2$. At $M_c = 0.4, 0.5$, and 0.6 , the supersonic region forms earlier, becomes stronger (reaching $M \approx 1.5$), and extends further downstream (to $x/c = 0.2$ at $M_c = 0.6$). At low angles of attack ($\alpha \approx 7$ – 10°) transition to turbulence is initiated near the shock, and does not move as far forward as at low Mach number.²² As α increases, high frequency pressure oscillations appear at the shock, beginning a gradual separation. It takes up to 32 times longer than at $M_c = 0.2$ for the separation to expand to cover the forward 30% of chord, and the stall vorticity is much more diffuse.²¹ This observation agrees with the visualization results of Refs. 13–14. Unsteady effects on the aerodynamic loads are still present, including measureable stall delays and increases in the maximum lift, drag, and moment.²⁰

The effects of other parameters (Λ , A , and tip cap geometry) on the airloads during ramps have also been examined.²⁰ Sweep and tip geometry effects are most significant very close to the wing tip and after the beginning of stall. The rollup of the tip vortex over the upper surface of the unswept wing distorts the pressure distributions and interacts with the stall vortex to increase the unsteady increment to C_L^{max} by up to a

factor of 2. This effect, which was first described in Refs. 15-16, is magnified when the approximate body of revolution tip cap is replaced by a flat plate at $z = 0$. The flat plate appears to generate a stronger and more compact vortex. For the swept wing, the tip vortex effect are weaker, as also observed in Refs. 17-18. The tip stalls at nearly the same α as the inboard region, and the unsteady increments to the tip loads are reduced.²⁰ After stall, there are large differences with sweep angle, including strong periodic oscillations at $\Lambda = 15^\circ$ and strong spanwise gradients at $\Lambda = 30^\circ$.

BASIC CHARACTERISTICS

Results for two sinusoidal conditions, $\alpha = 10^\circ - 10^\circ \cos 2\pi\tau$ and $\alpha = 20^\circ - 10^\circ \cos 2\pi\tau$, both at $M_c = 0.3$ (340 fps), $\Lambda = 0$, and $k = 0.1$ (7.5 Hz), will be described first. Figure 2 shows unsteady lift coefficient loops for these conditions at each of the five spanwise stations. Increasing time is indicated by the arrows. The triangles show the steady-state lift curves. The inboard lift loops ($s/c > 1$) exhibit the classic features of dynamic stall.^{1-9,15-20} Stall is delayed well past α_{st} , C_L^{max} is increased, and there is substantial hysteresis caused by delayed reattachment during the pitch-down portion of the cycle. At $\alpha_0 = 10^\circ$, stall occurs (C_L collapses) when the instantaneous pitch rate goes to 0 at $\alpha = 20^\circ$, while at $\alpha_0 = 20^\circ$, a more gradual loss of lift occurs near $\alpha = 22^\circ$. Close to the tip ($s/c = 0.08$), both the steady and unsteady behavior differ from the inboard results. Although the slope of the steady lift curve decreases after $\alpha = 15^\circ$ (when the inboard portion of the wing stalls), the steady lift near the tip continues to increase up to $\alpha \approx 23^\circ$, and only falls slightly at higher α . The unsteady lift continues to increase until $\alpha \approx 28^\circ$, and displays less hysteresis than at the inboard stations.

Pitching moment loops for these conditions are shown in Fig. 3. The inboard stations show a sharp drop in both the steady and unsteady moments at stall, with a peak unsteady C_M of -0.34 at $s/c = 1.52$. As identified by earlier studies^{2,3,6,8,23}, the moment loops are composed of three subloops. Large subloops which have a counter-clockwise sense (with increasing time) occur below and above α_{st} , while a small clockwise subloop occurs near α_{st} . The greater area of the counter-clockwise subloops indicates that the aerodynamic damping for these large amplitude motions is positive, in contrast to small amplitude motions²³ that enclose α_{st} . The moment stall characteristics for $s/c \leq 0.59$ are less abrupt than for $s/c \geq 1$, and the trend from $s/c = 1.52$ to 0.30 is for reduced peak moments as s is reduced. This trend is reversed at $s/c = 0.08$. This station has the strongest peak moment, $C_M = -0.37$ at $\alpha_0 = 20^\circ$. Both the trend and its reversal seem to be caused by the tip vortex, since it not only lowers the ef-

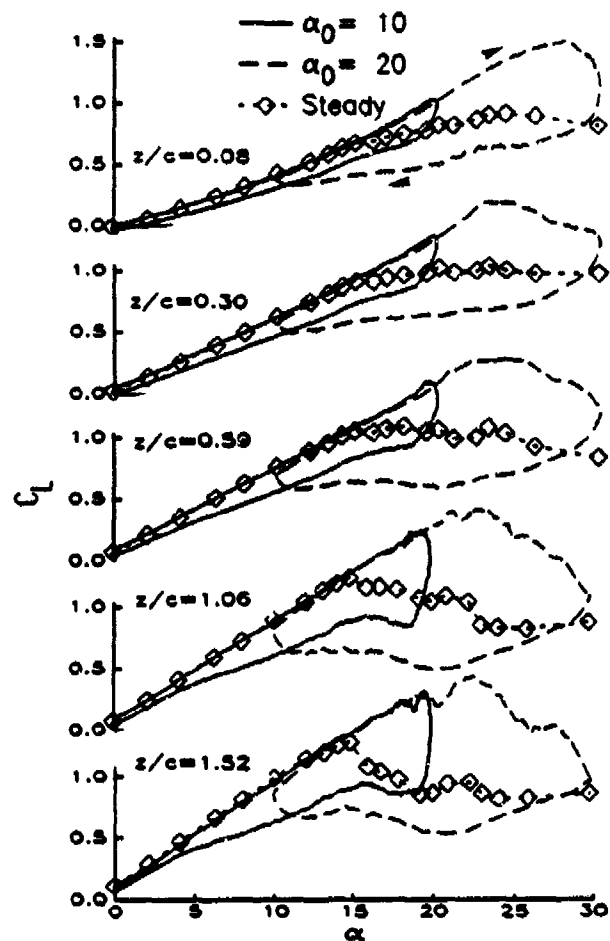


Fig. 2. Effect of mean angle and spanwise position on unsteady lift. ($\alpha = \alpha_0 - 10^\circ \cos 2\pi\tau$, $M_c = 0.3$, $\Lambda = 0$, and $k = 0.1$)

fective α , delaying and smoothing stall, but (very close to the tip) interacts with the stall vortex to strengthen the unsteady loads (as also observed in Refs. 15-16 and 20).

The blade pressure characteristics that are responsible for these loads will now be described. Figure 4 shows chordwise pressure distributions at $s/c = 0.59$ for the $\alpha = 20^\circ - 10^\circ \cos 2\pi\tau$ condition. The left column shows the pitch up portion of the cycle, and the right column shows the same α during pitch down. Each distribution is labeled both by α and by nondimensional time, τ . The results during pitch-up are very similar to those for a constant rate ramp.^{20,21} A strong suction peak develops during attached flow (Fig. 4a), generating a small supersonic bubble ($\alpha = 20^\circ$, Fig. 4b). Separation follows, and a stall vortex is formed (Fig. 4c). The vortex broadens and propagates aft (Fig. 4d), leading to massive separation (Fig. 4e). The separation persists during pitch-down (Figs. 4f, g, and h). Note the major differences between these distributions and those

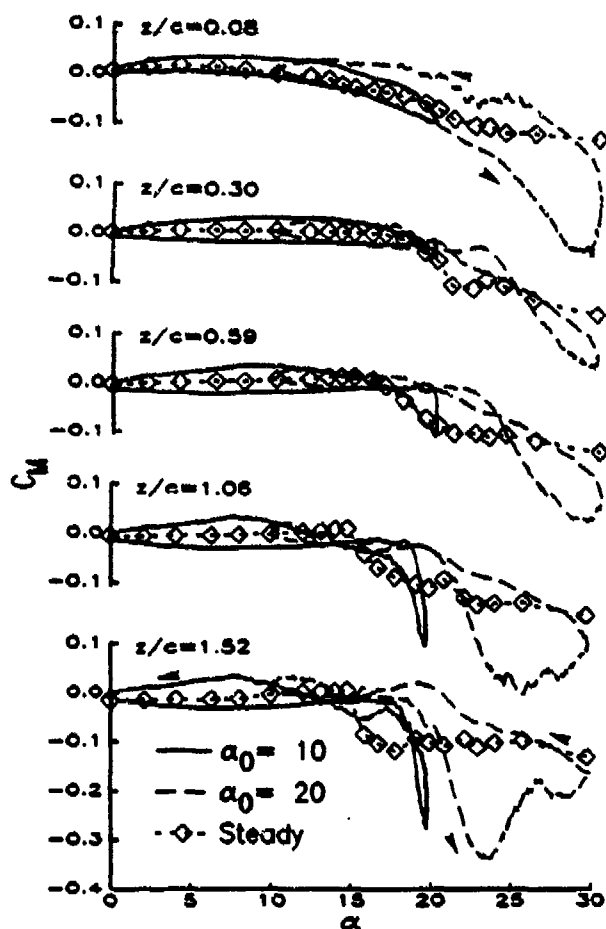


Fig. 3. Effect of mean angle and spanwise position on unsteady moment. ($\alpha = \alpha_0 - 10^\circ \cos 2\pi\tau$, $M_c = 0.3$, $\Lambda = 0$, and $k = 0.1$)

at the same α during pitch up (Figs. 4e, d, and c). The absence of the leading edge suction during pitch-down accounts for the lift and moment hysteresis. The flow begins to reattach by $\alpha = 22^\circ$ (Fig. 4h), with the formation of a small amount of leading edge suction. The suction peak grows, and reattachment slowly moves aft along the chord (Fig. 4i). By $\alpha = 15^\circ$ (Fig. 4j) the distribution has the appearance of attached flow, but both the leading edge suction and the overall fullness of the pressure distribution are less than during pitch-up (Fig. 4a). Similar sequences of pressure distributions occur at other spanwise locations away from the tip (not shown).

The behavior close to the tip is quite different, as shown in Fig. 5 by the chordwise pressure distributions at $z/c = 0.08$. At $\alpha = 15^\circ$ during pitch-up (Fig. 5a) there is already significantly higher load over the aft 30% of chord than at $z/c = 0.59$ (Fig. 4a). The aft load is caused by the rollup of the tip vortex over the upper surface of the tip, and is responsible for the smooth increases in negative C_M with α observed in Fig. 3.

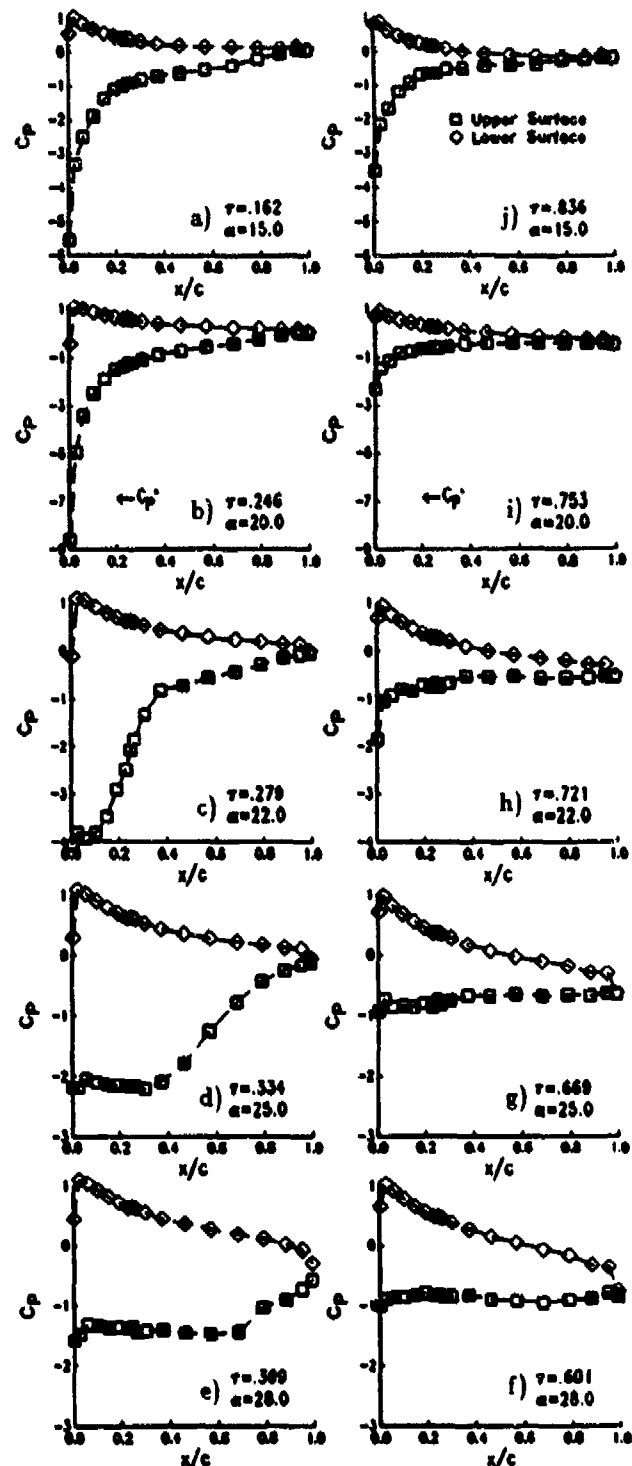


Fig. 4. Chordwise pressure distributions at $z/c = 0.59$ during pitch-up (left column) and pitch down (right column). ($\alpha = 20^\circ - 10^\circ \cos 2\pi\tau$, $M_c = 0.3$, $\Lambda = 0$, and $k = 0.1$)

Steady surface oil flow visualisations (not shown here) confirm the presence of the vortex. Both the leading edge suction peak and the vortex loading at the trailing edge increase as α is increased to 23° (Fig. 5b). For $\alpha >$

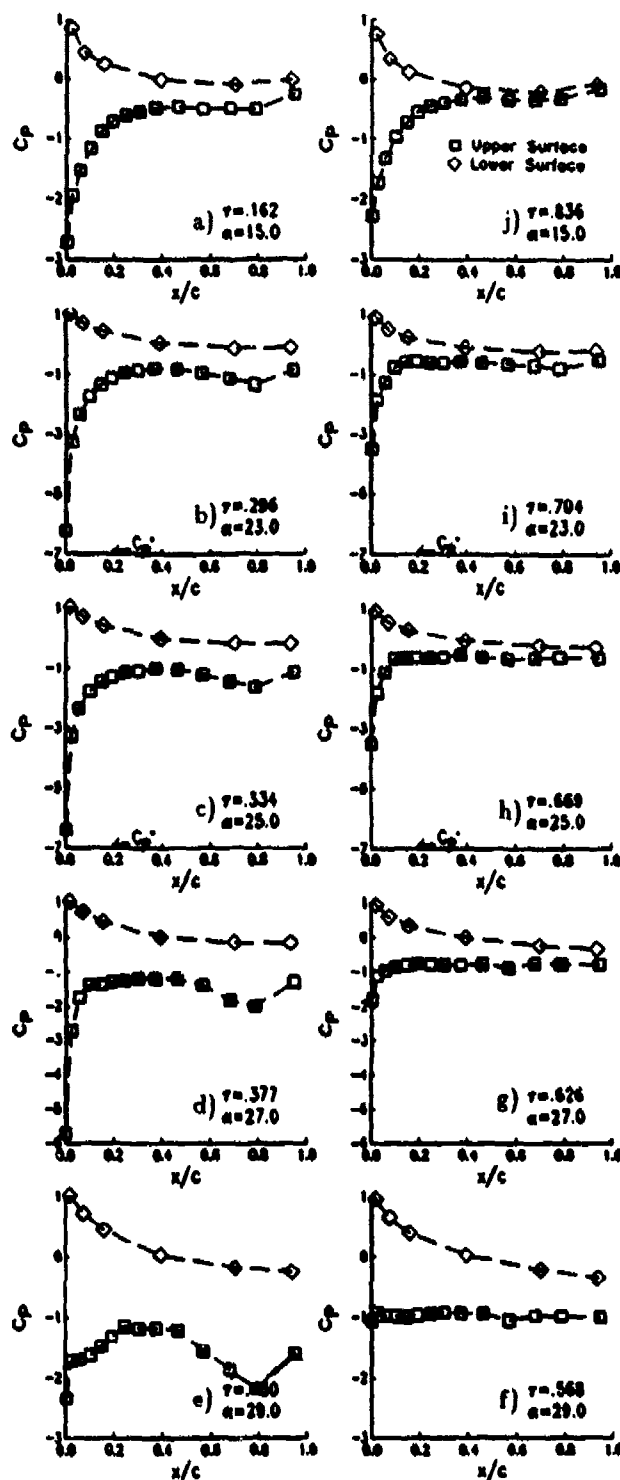


Fig. 5. Chordwise pressure distributions at $z/c = 0.08$. ($\alpha = 20^\circ - 10^\circ \cos 2\pi\tau$, $M_c = 0.3$, $\Lambda = 0$, and $k = 0.1$)

23° , the leading edge suction stops increasing, but the trailing edge suction does not (Figs. 5b-c), producing a more rapid increase in negative moment (Fig. 3). At $\alpha = 27^\circ$ (Fig. 5d) the flow begins to separate aft of the suction peak. The leading edge suction has almost vanished at $\alpha = 29^\circ$ (Fig. 5e), but substantial trailing edge

loading remains. There appears to be a brief period of complete upper surface separation during pitch-down (Fig. 5f), but the leading edge soon begins to reattach ($\alpha = 27^\circ$, Fig. 5g). The trailing edge suction is not as rapidly reestablished (Figs. 5h-i), perhaps because the inboard region of the blade is still stalled, and inboard lift is needed to generate the tip vortex. By $\alpha = 15^\circ$ (Fig. 5j), the flow appears essentially reattached, but the trailing edge loading is still less than during pitch-up (Fig. 5a).

Time histories of the ensemble-averaged upper surface pressures at the two stations for the $\alpha_0 = 10$ and 20° conditions are shown in Fig. 6. Fig. 6a is for $\alpha_0 = 20^\circ - 10^\circ \cos 2\pi\tau$, at $z/c = 0.08$. The bottom curve is for $x/c = 0.005$, with its C_p scale at the lower right. Origins for each curve are offset vertically, as indicated along the left axis. The horizontal axis shows both time (τ) and angle (α). The suction at $x/c = 0.005$ stops increasing near $\tau \approx 0.3$ ($\alpha = 23^\circ$, indicated by "A"), and a separation plateau is present from $\tau = 0.25$ to 0.62 . The separation is less obvious at the other stations. There is no clear trace of a stall vortex propagating back along the chord. The effect of the tip vortex appears strongest at $x/c = 0.788$, with a strong suction bump between $\tau = 0.36$ and 0.48 ("B"). At $z/c = 0.59$ (Fig. 6b) there is a strong negative pressure peak from the stall vortex that can be traced back from $x/c = 0.026$ to at least $x/c = 0.372$ ("C"). The leading edge separation plateau is also larger, extending from $\tau = 0.3$ to 0.7 .

For the lower mean angle condition ($\alpha_0 = 10^\circ$), the pressure time histories at $z/c = 0.08$ (Fig. 6c) show no separation plateau, but there are deviations from a smooth sinusoidal response between $\tau = 0.45$ and 0.70 ("D"). These reductions in suction are probably a reflection of the separation and loss of lift that are occurring on the inboard region of the wing. At $z/c = 0.59$ (Fig. 6d) the pressures at $x/c = 0.005$ indicate a rapid separation at $\tau = 0.43$ ($\alpha \approx 19^\circ$), and a gradual reattachment starting near $\tau = 0.5$ and completing by $\tau = 0.65$ ($\alpha \approx 16^\circ$). A strong stall vortex trace is also visible from $x/c = 0.06$ to 0.57 ("E").

The final results to be presented for these two conditions are the unsteady airload increments. As shown in Fig. 7, the steady-state results at each α (referred to as the quasi-steady or QS loads) have been subtracted from the C_L , C_M , and C_D loops (Figs. 2 and 3). Loops for $C_L - QS$ are shown in Fig. 7a for both the $\alpha_0 = 10^\circ$ and 20° conditions at $z/c = 1.52$ and 0.08 . At $z/c = 1.59$ $C_L - QS$ becomes strongly positive (up to $+1$) because of the delay in stall, and then negative (-0.2 to -0.35) during pitch down because of the delay in reattachment. The $C_L - QS$ loops at $z/c = 0.08$ are smoother, with reduced maximum positive increments. For $\alpha_0 = 10^\circ$ and $z/c = 0.08$, $C_L - QS$ is relatively

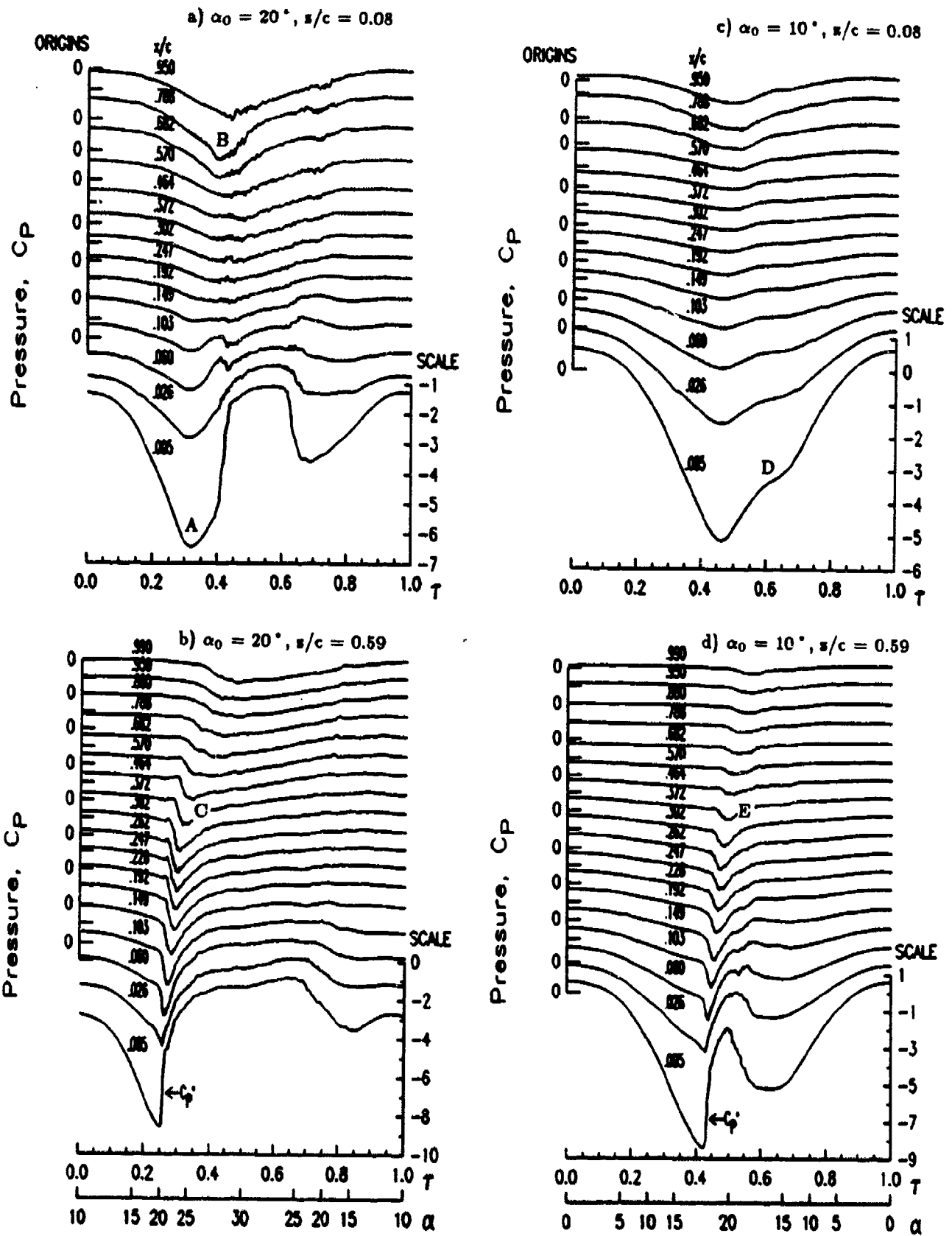


Fig. 6. Upper surface pressure time histories at two spanwise positions, for two mean angles. ($\alpha = \alpha_0 - 10^\circ \cos 2\pi r$, $M_c = 0.3$, $\Lambda = 0$, and $k = 0.1$.)

small (between +0.2 and -0.1) because the wing tip does not stall. The loops for $C_M - QS$ (Fig. 7b) are more complex. At $z/c = 1.52$ during pitch-up there is a small negative increment in attached flow, a positive increment caused by the stall delay, and finally a large negative increment (up to -0.2) generated by the stall vortex. During pitch-down the increment becomes positive as the flow reattaches from the leading edge aft (reestablishing leading edge suction before trailing edge loading). At $z/c = 0.08$, the $C_M - QS$ loop is simply connected, with an increasing negative increment during pitch up as the tip-vortex-induced suction near the trailing edge strengthens, and a generally positive increment during pitch-down as the leading edge suction becomes predominant. The pressure drag increments (Fig. 7c) remain quite small during attached flow, are negative during the unsteady delay in stall, and then become strongly positive (up to $C_D - QS = 0.3$ to 0.4) as the stall vortex propagates aft along the chord. $C_D - QS$ becomes negative during pitch-down, as the reattaching leading edge suction provides a thrust increment. (Note that C_D remains positive, and that skin friction drag is not included in these pressure integrations.)

SINUSOIDAL AND RAMP MOTIONS

The object of this section is to compare the unsteady aerodynamic load results for sinusoidal motion with results for ramp motion at similar conditions. The sinusoidal cases are the $k = 0.1$, $\alpha_1 = 10^\circ$ conditions described in the previous section. The ramp is from $\alpha = 0$ to 30° at a nondimensional rate of $A = 0.02$ ($550^\circ/\text{sec}$). The pitch-up portion of the ramp was described in Ref. 20. The complete motion consists of a several second delay at $\alpha = 0$, a constant rate pitch-up to 30° over a period of $0.5T$ (0.054 sec), holding at 30° for another $0.5T$, and then pitch-down to $\alpha = 0$ at the same rate. The primary differences between sinusoidal and ramp motions are the replacement of the steady-state initial condition with periodicity and of the constant rate with a rate of $A = k\alpha_1 \sin 2\pi\tau$. For this condition the maximum pitch rate is $k\alpha_1 = 0.0175$ at $\alpha = \alpha_0$.

Figure 8 shows the comparison of C_L and C_M loops at $z/c = 1.52$ and 0.08 . The solid line is the $A=0.02$ up-ramp, the dashed line is the down-ramp, the dotted line is the sinusoid at $\alpha_0 = 10^\circ$, the dot-dashed line is the sinusoid at $\alpha_0 = 20^\circ$, and the symbols are the steady data. The general conclusion is that there is good qualitative agreement, especially between the ramps and the $\alpha_0 = 20^\circ$ sinusoids. The lower α portion of the ramp data also agree with the $\alpha_0 = 10^\circ$ sinusoids until the sinusoid stalls near its maximum angle (20°). Some small differences are present, but the basic features of the unsteady stall process appear to be the

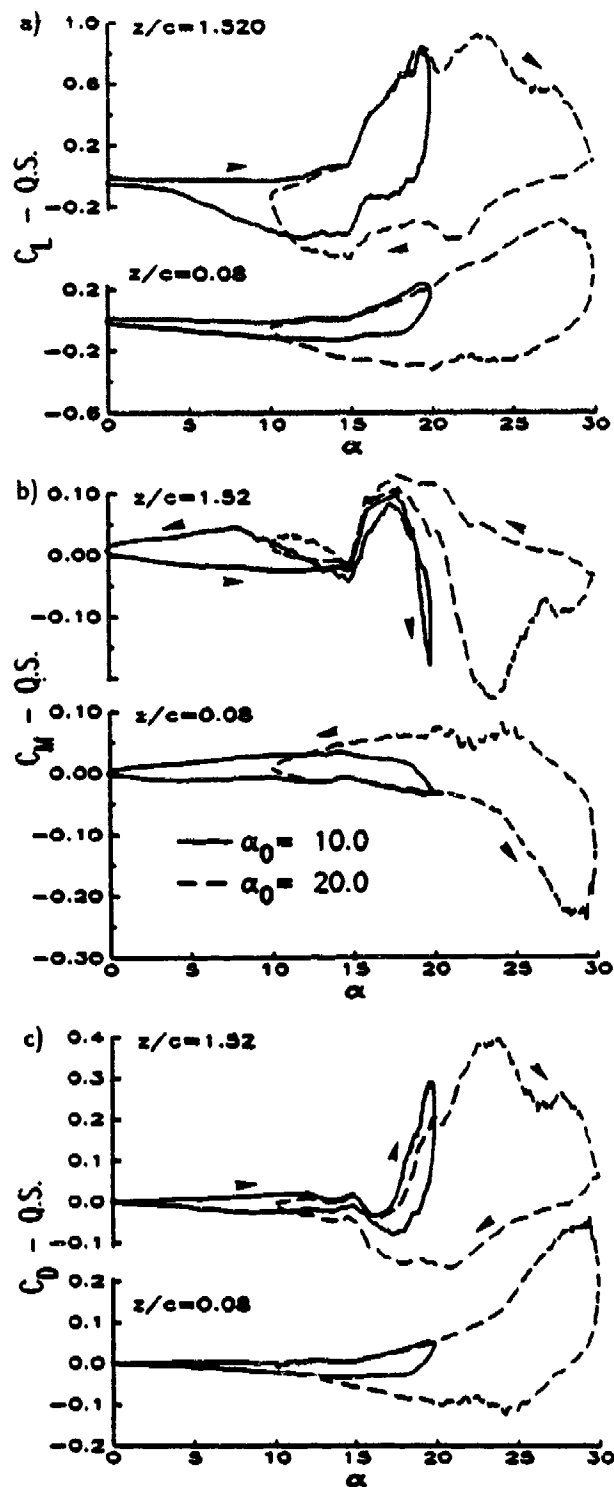


Fig. 7. Unsteady load increments at three spanwise positions and two mean angles. ($\alpha = \alpha_0 - 10^\circ \cos 2\pi\tau$, $M_c = 0.3$, $A = 0$, and $k = 0.1$)

same. Comparisons of airloads at other sweep angles ($\Lambda = 15$ and 30°), Mach numbers ($0.2 \leq M_c \leq 0.6$), and reduced frequencies ($0.05 \leq k \leq 0.15$) are not shown here, but there is a similar level of agreement.

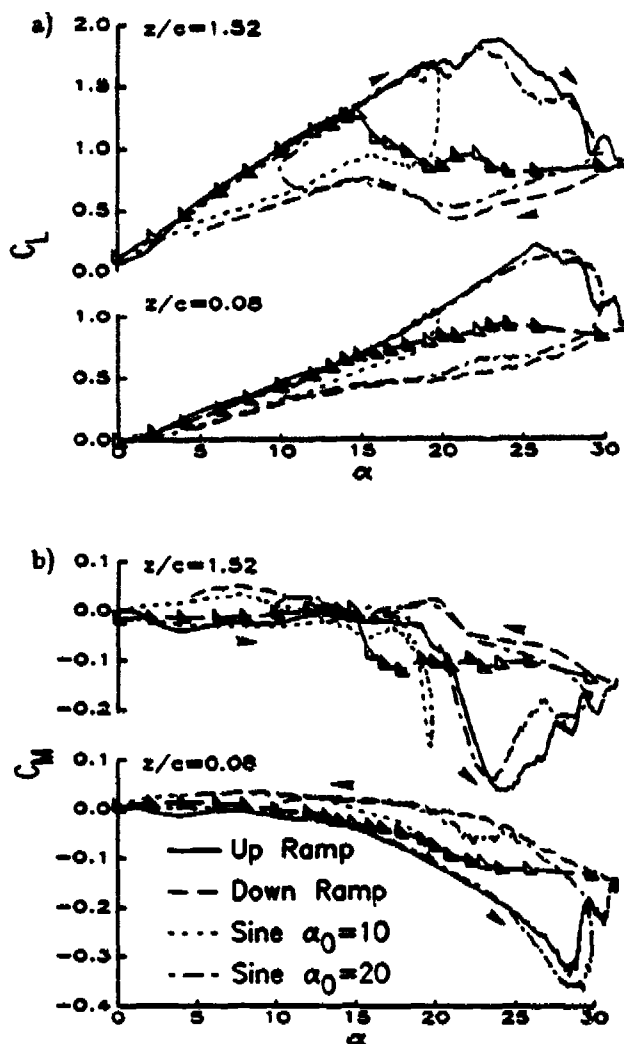


Fig. 8. Comparison of sinusoidal and ramp lift and moment. ($M_c = 0.3$, $\Lambda = 0$, and $k = 0.1$ or $\Lambda = 0.02$)

This is very encouraging, since it implies that the detailed information on the separation process obtained for ramps²⁰⁻²² should also apply to sinusoids. (This is also supported by the similarity between the sinusoidal pressure characteristics shown in Fig. 4-6 and similar results for ramps.²⁰)

MODERATE AMPLITUDE MOTIONS AND LIGHT STALL

In addition to the large amplitude ($\alpha_1 = 10^\circ$) motions described in the previous sections, moderate amplitude ($\alpha_1 = 6^\circ$) conditions were also tested for sequences of increasing mean angle. Lift and moment curves for the sequence $\alpha_0 = 10, 12, 14, 16$, and 18° at $M_c = 0.2$, $\Lambda = 0$, and $k = 0.1$, are shown in Fig. 9. The C_L curves (Fig. 9a) at $z/c = 1.52$ seem to fall within the same envelope. At $\alpha_0 = 10^\circ$, the flow remains

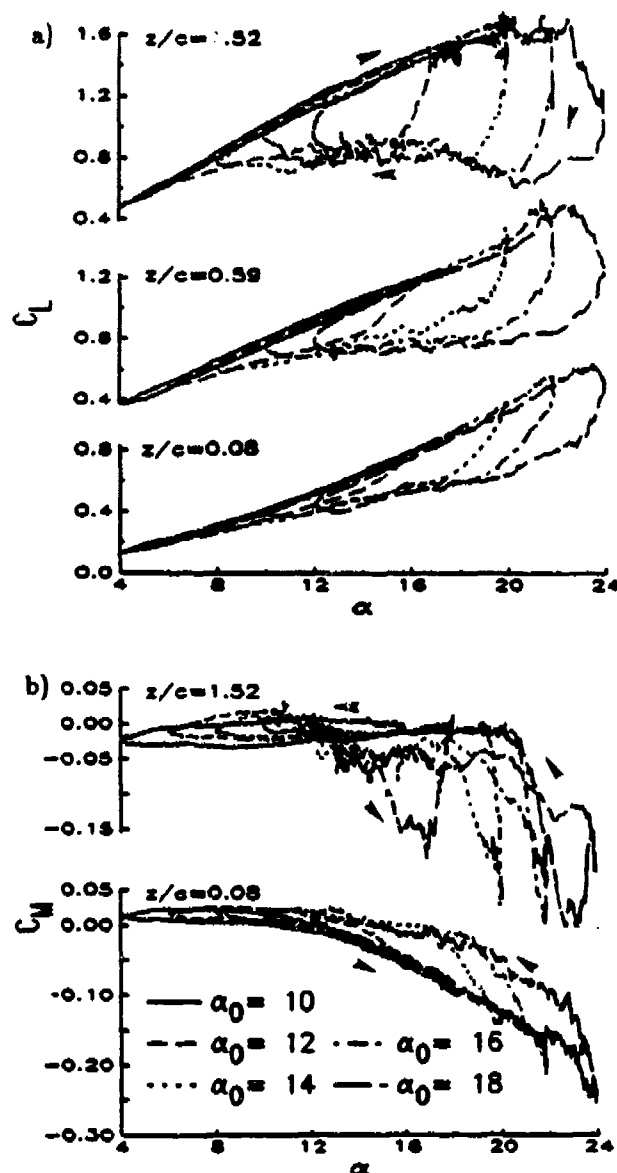


Fig. 9. Lift and moment loops for moderate amplitudes. ($\alpha = \alpha_0 - 6^\circ \cos 2\pi r$, $M_c = 0.2$, $\Lambda = 0$, and $k = 0.1$)

attached, and the loop is a narrow (and hard to see) ellipse. At higher α_0 , the lift follows the top of the envelope during pitch-up, but collapses when the pitch rate falls to zero. During pitch-down, the lift in separated flow follows the bottom of the envelope, and then recovers to the attached flow value when pitch-up resumes. Qualitatively similar behavior occurs at $z/c = 0.59$ and 0.08 . The hysteresis is reduced because proximity to the tip vortex has lowered the effective angle of attack and reduced penetration into stall. The C_M curves (Fig. 9b) at $z/c = 1.52$ and $z/c = 0.08$ also tend to fall within envelopes. At $z/c = 1.52$, however, there are also strong negative moment spikes for all values of α_0 greater than 10° , the only conditions which indi-

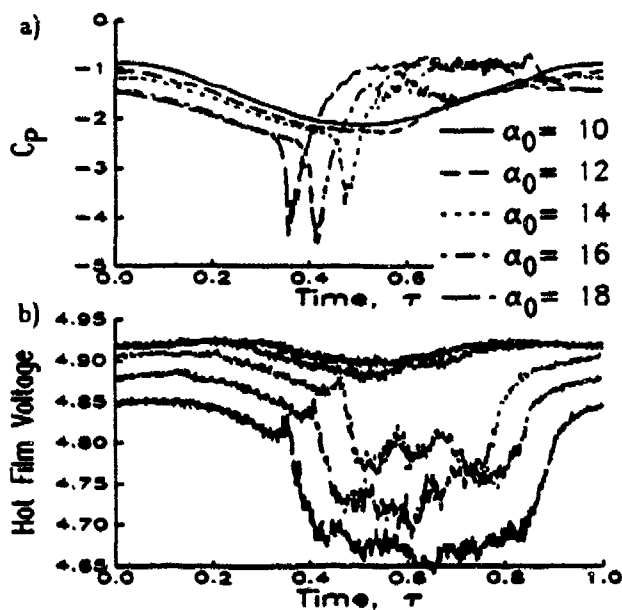


Fig. 10. Upper surface pressure and hot film time histories at moderate amplitudes. ($x/c=0.1$, $z/c=0.59$, $\alpha = \alpha_0 - 6^\circ \cos 2\pi\tau$, $M_c = 0.2$, $\Lambda = 0$, and $k=0.1$)

cate any substantial extension of the lift curve beyond the steady limits.

The pressure and hot film time histories shown in Fig. 10 illustrate the rapid growth in separation with α_0 . Fig. 10a shows pressure time histories at $z/c = 0.59$, $x/c = 0.1$ for the α_0 sequence described above. At $\alpha_0 = 10^\circ$ (the solid line), there is a smooth, sinusoidal response, with the minimum pressure occurring near $\tau = 0.5$, the time of maximum α . At $\alpha_0 = 12^\circ$ the response is somewhat distorted for $\tau > 0.6$, probably in response to separation occurring further inboard (Fig. 9a), but there are no major changes. This is confirmed by the hot film time histories shown in Fig. 10b. The output voltage (heat transfer) for $\alpha_0 = 10$ and 12° remains high throughout the cycle, indicating an attached turbulent boundary layer.²² In contrast, at $\alpha_0 = 14, 16$, and 18° the hot film voltages show a rapid reduction indicating separation. As α_0 increases, the drop occurs at progressively earlier values of τ . The separation is accompanied by a sharp negative pressure spike (Fig. 10a), indicating the formation of a dynamic stall vortex.^{8,20} The downstream propagation of this vortex is responsible for the negative moments shown in Fig. 9d. These results, together with similar results at other values of k , M_c , and Λ (not shown), suggest that the boundary between the onset of the benefits of forced unsteady motions (delays in stall and increases in C_L^{max}) and the development of the costs (unacceptably strong pitching moments) is extremely narrow. The boundary width is certainly less than the 2° spacing in α_0 studied here. No combinations of parameters that

generated significant additional lift or substantially delayed stall avoided the creation of a strong stall vortex and the subsequent moment and drag penalties.

FREQUENCY AND SWEEP EFFECTS

As shown in Fig. 11, the familiar effects of reduced frequency on the airloads are present during sinusoidal motions of this model. Lift (Fig. 11a) and moment (Fig. 11b) loops at $M_c = 0.3$ and $\Lambda = 0$ are compared

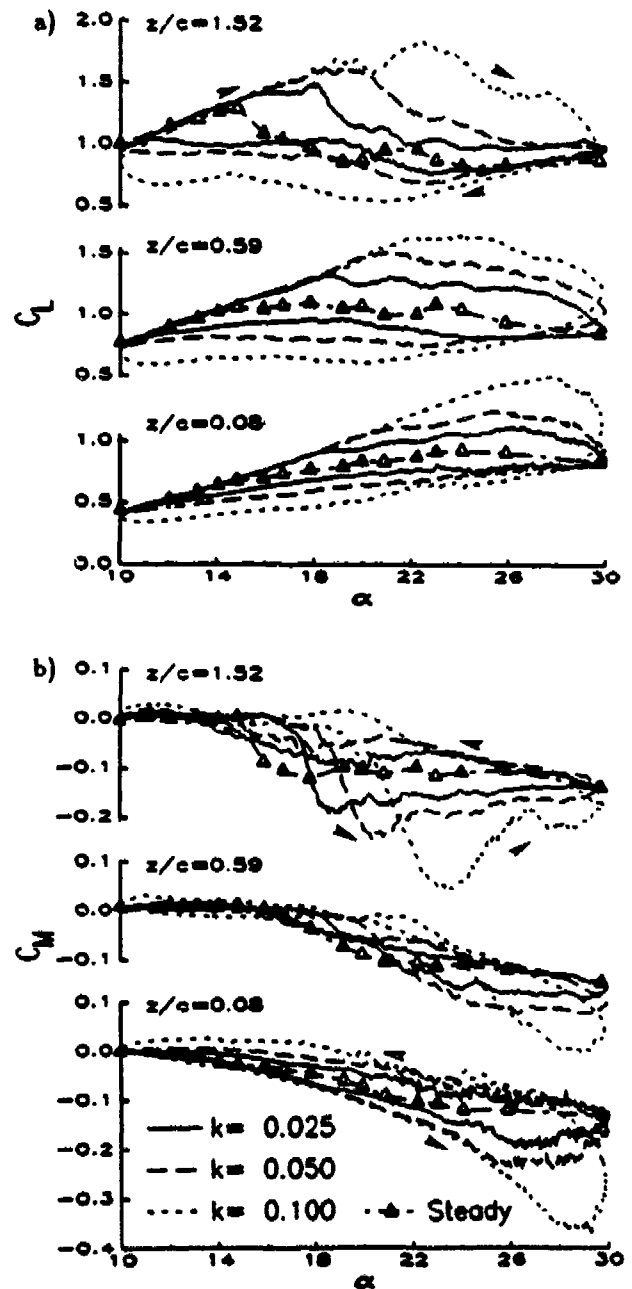


Fig. 11. Frequency effects on lift and moment. ($\alpha = 20^\circ - 10^\circ \cos 2\pi\tau$, $M_c = 0.3$, $\Lambda = 0$)

at $k = 0.025, 0.05$, and 0.10 . In general, increasing frequency increases maximum loads, delays stall, increases hysteresis, and delays reattachment. At $s/c = 1.52$ (far from the tip) the stall delays reach approximately 8° at $k = 0.1$, but stall is still very abrupt. At $s/c = 0.59$, the delays are about the same, but stall is more gradual. Instead of having a sharp negative peak followed by a reduction, the negative moments at this station continually become more negative until almost $\alpha = 30^\circ$. This tendency is even more pronounced at $s/c = 0.08$. Here the $k = 0.1$ condition appears to entirely avoid stall during the pitch-up, and the unsteady increments to lift and moment ($\Delta C_L^{max} = 0.60$, $\Delta C_M^{min} = -0.24$) are larger than at any other spanwise position. This is consistent with low speed, high frequency results at smaller scale,¹⁵⁻¹⁸ and with ramp data for the current model.²⁰

Sweep can also have a significant effect on the unsteady loads, especially near the tip. Figure 12 compares lift (Fig. 12a) and moment (Fig. 12b) loops at $\Lambda = 0, 15$, and 30° , for $M_c = 0.3$ and $k = 0.1$. Results are shown for $s/c = 1.06, 0.59$, and 0.08 . Steady data at $\Lambda = 0$ are also included. Both during pitch-up prior to stall and when the flow is massively separated during pitch-down, the inboard ($s/c = 1.06$ and 0.59) C_L and C_M results appear largely independent of sweep. There are, however, substantial differences during pitch-up after stall. At $s/c = 1.06$, the $\Lambda = 0$ and 30° lift loops (Fig. 12a) are very similar, while the $\Lambda = 15^\circ$ loops has a double peak indicating a temporal oscillation. At $s/c = 0.59$ and 0.08 , the hysteresis and unsteady load increments are reduced at $\Lambda = 15$ and 30° . Because the wing tip remains perpendicular to the leading edge, the tip vortex does not roll up over the swept wing. Ref. 17 also showed that the spanwise flows present with aft sweep weaken the tip vortex. The effects combine to suppress the interaction between the tip and stall vortices that enhances the unsteady tip loads at $\Lambda = 0$.

The temporal oscillations are investigated further in Fig. 13a, which shows upper surface pressure time histories at $s/c = 0.59$ for the $\Lambda = 15^\circ$ condition. Following the initial valley of low pressure associated with the dynamic stall vortex ("A"), there is a peak and a second valley ("B") that is probably associated with a second vortex. In contrast to the initial vortex, which is first visible near $x/c = 0.026$, the secondary vortex does not become apparent until $x/c \approx 0.3$. No secondary vortices are present at $\Lambda = 0$ (Fig. 6b) or at $\Lambda = 30^\circ$ (Fig. 13b). Similar oscillations also occurred during ramp motions²⁰ of this model at $\Lambda = 15^\circ$, and for the unswept 2D model.⁶ The oscillations in 2D had frequencies appropriate for von Karman vortex shedding from a bluff body of diameter $c \sin \alpha$. The frequencies for the 3D condition are similar, although there is

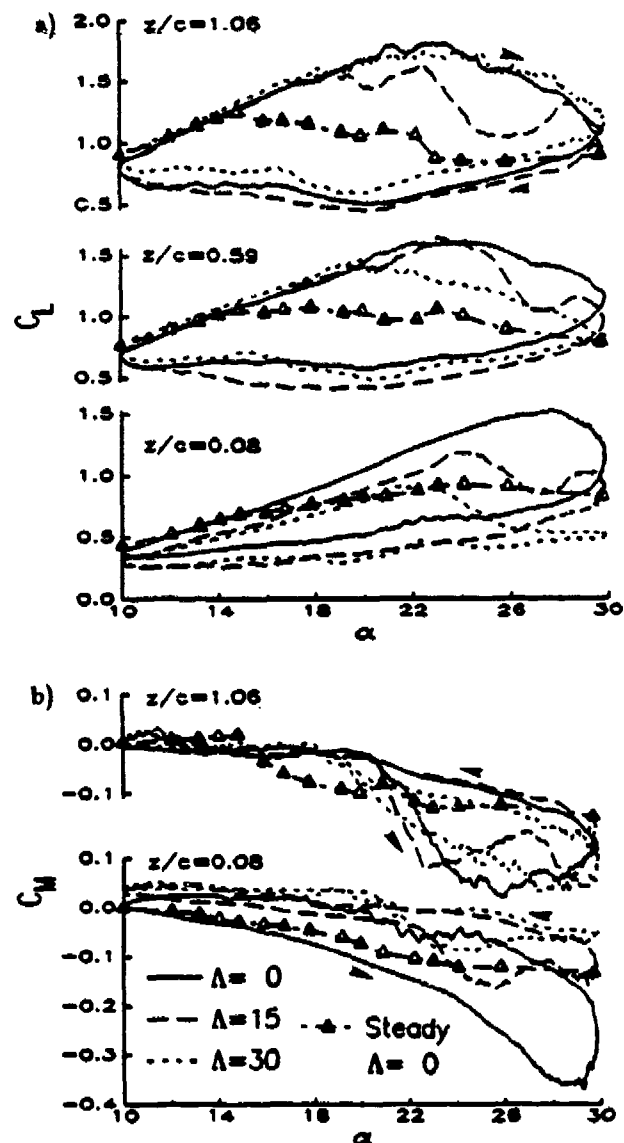


Fig. 12. Sweep effects on lift and moment. ($\alpha = 20^\circ - 10^\circ \cos 2\pi\tau$, $M_c = 0.3$, $k = 0.1$)

as yet no explanation why the oscillation is only strong at $\Lambda = 15^\circ$.

As was discussed in Ref. 20, sweep influences both the steady and unsteady response. The steady effects can be at least partially removed by subtracting out the quasi-steady response. Figure 14 shows $C_L - QS$ and $C_M - QS$ loops at $s/c = 1.06$ and 0.08 . Both the oscillations at $\Lambda = 15^\circ$ and the reduced unsteady tip loads at $\Lambda = 15$ and 30° are apparent.

MACH NUMBER EFFECTS ON AIRLOADS

Compressibility has been recognised as being of primary importance to dynamic stall.^{2,5,8,13-14,21-21} The effects of Mach number on the airloads on the 3D

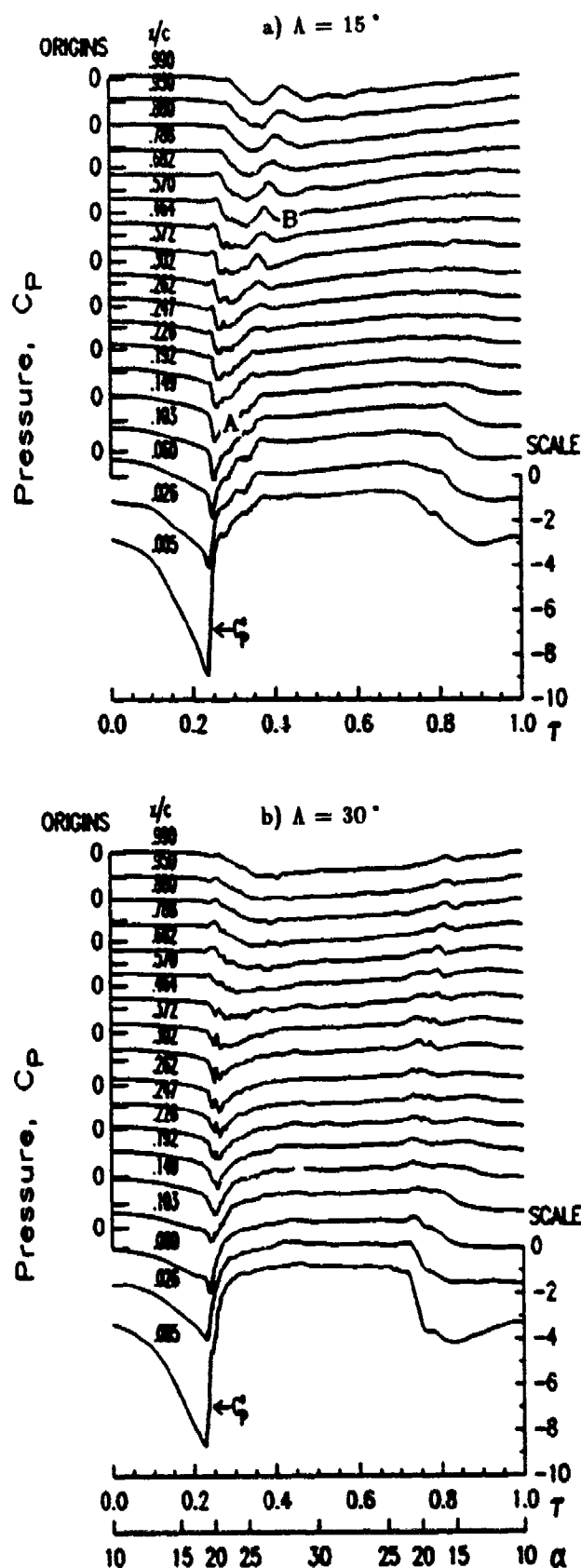


Fig. 13. Sweep effects on upper surface pressures. ($\alpha = 20^\circ - 10^\circ \cos 2\pi\tau$, $M_c = 0.3$, $k=0.1$, $x/c=0.59$)

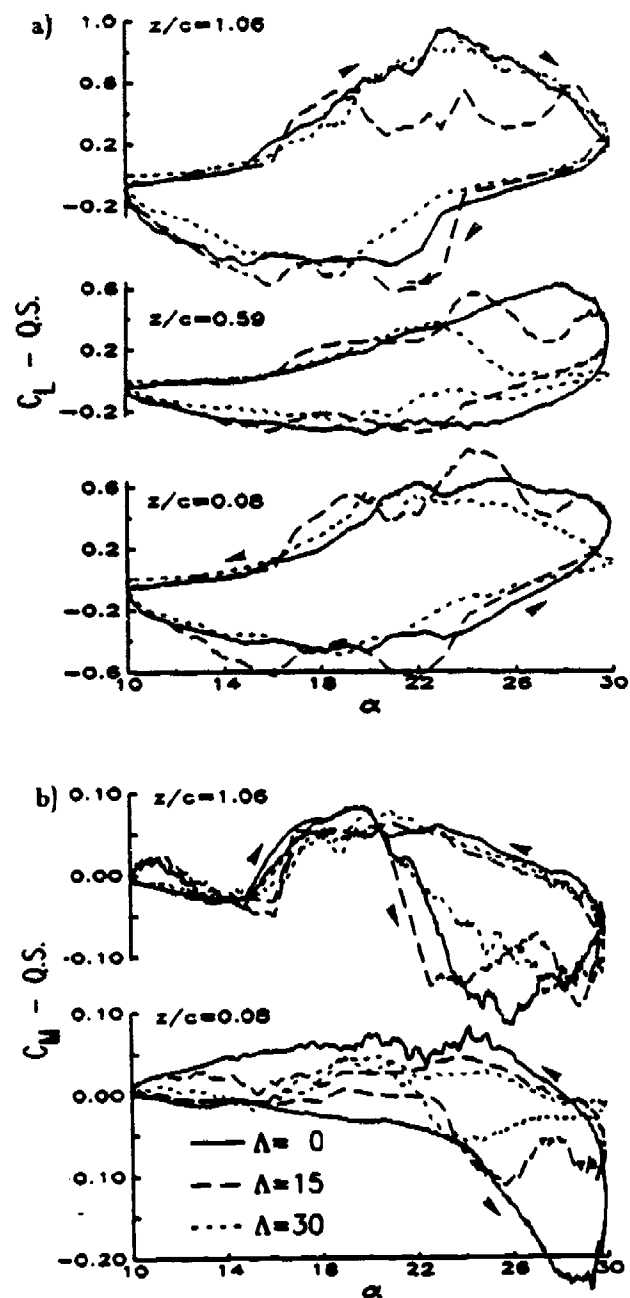


Fig. 14. Sweep effects on unsteady increments to lift and moment. ($\alpha = 20^\circ - 10^\circ \cos 2\pi\tau$, $M_c = 0.3$, $k = 0.1$)

model during sinusoidal motions are also substantial, particularly near stall and at higher M_c . For light stall and moderate Mach number conditions, the effects are less significant. Figure 15 shows lift loops at $M_c = 0.2$, 0.3 , and 0.4 , for the same sweep angle ($\Lambda = 0$), frequency ($k = 0.05$), and angular range ($\alpha = 10^\circ - 10^\circ \cos 2\pi\tau$). These relatively light stall loops are qualitatively similar. The major difference is a reduction in stall angle with Mach number. At $M_c = 0.2$, stall does not occur until the pitch rate approaches zero at $\alpha =$

20°. At $M_c = 0.3$ stall begins slightly earlier, near $\alpha = 18.5^\circ$, while at $M_c = 0.4$ the lift begins to drop near $\alpha = 16^\circ$. These reductions in the stall angle may be related to the formation of the leading edge supersonic region at $M_c = 0.3$, and the appearance of a shock at $M_c = 0.4$.²¹

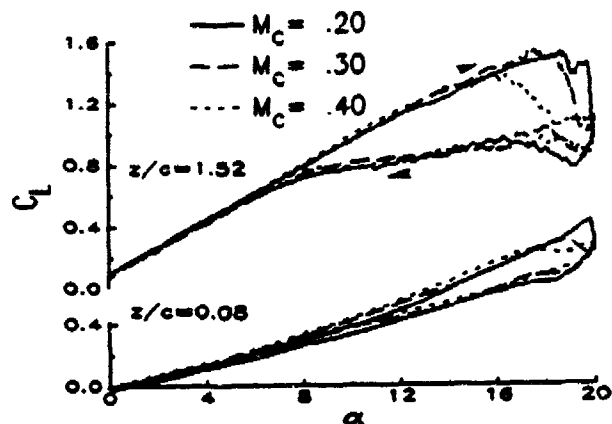


Fig. 15. Mach effects on lift for light stall and lower M_c . ($\alpha = 10^\circ - 10^\circ \cos 2\pi\tau$, $k = 0.05$, $\Lambda = 0$)

The differences are increased for deeper penetration into stall. Figure 16 shows lift and moment loops for the same three Mach numbers and reduced frequencies, but with $\alpha = 20^\circ - 20^\circ \cos 2\pi\tau$ used for the $M_c = 0.2$ and 0.3 conditions. (The $M_c = 0.4$ condition is still $\alpha_0 = 10^\circ$, since stall has occurred before $\alpha = 20^\circ$, and because higher values of α might exceed structural limits.) The primary difference is again a reduction in stall angle with Mach number, particularly at $z/c = 1.52$. The responses in both the attached and massively separated flow regimes differ only slightly with M_c . The amount of hysteresis is similar. As was observed for ramp motions,²¹ the major change occurs between $M_c = 0.3$ and 0.4 ; there is only a relatively small reduction in stall angle between $M_c = 0.2$ and 0.3 .

A comparison of lift and moment loops at the higher Mach numbers of $M_c = 0.4, 0.5$, and 0.6 is shown in Fig. 17. All of the results are at $k = 0.075$ and $\Lambda = 0$, and represent light to moderate stall penetration. As M_c increases, the peak C_L and C_M are reduced, stall occurs earlier, and the hysteresis is lessened. For the $M_c = 0.6$ condition, the tested α range creates only a light stall on the inboard portion of the wing at $\alpha \approx 9^\circ$. For $M_c = 0.4$ and 0.5 , the stall begins near $\alpha = 16$ and 12° , respectively, and the moment loops at $z/c = 1.52$ show strong negative moments and 'figure-eight' shapes indicating formation and propagation of dynamic stall vorticity. At $z/c = 0.08$, C_M becomes steadily more negative as α increases, indicating development of a wing tip vortex as at lower M_c (Fig. 3).

Loops of the unsteady load increments, $C_L - QS$ and $C_M - QS$, at $z/c = 1.52$ and 0.08 for the $M_c =$

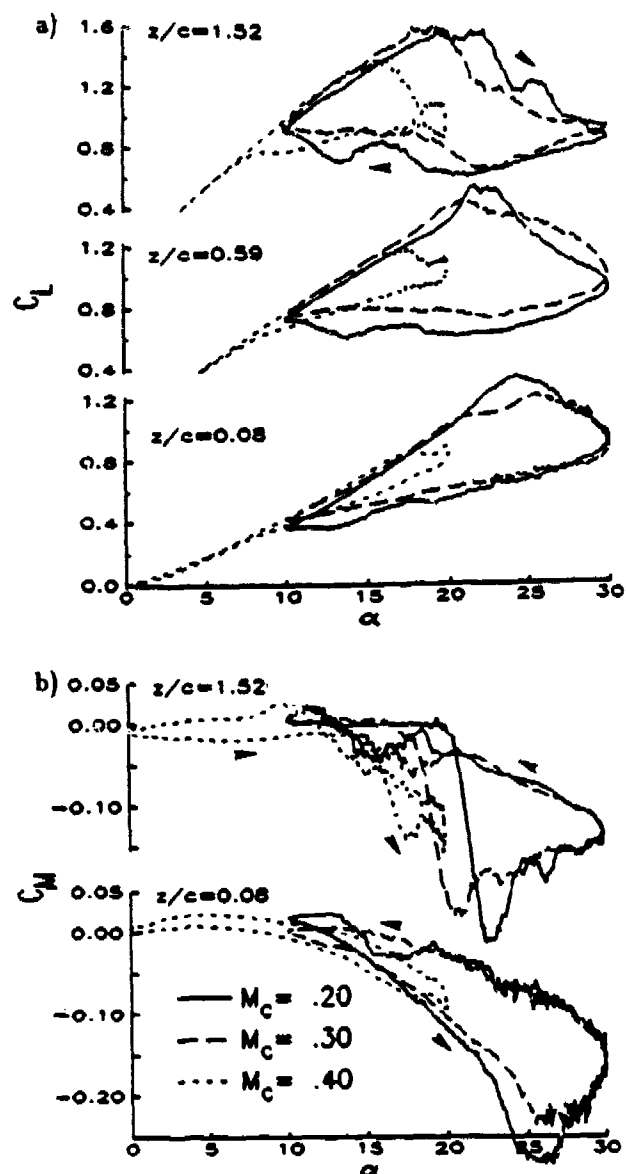


Fig. 16. Mach effects on lift and moment for deep stall and lower M_c . ($\alpha = 20^\circ - 10^\circ \cos 2\pi\tau$, $k = 0.05$, $\Lambda = 0$)

$0.4, 0.5$, and 0.6 conditions are shown in Fig. 18. The decrease in the magnitude of the unsteady increments with increasing M_c is clear. It is also clear that unsteady effects are still present at $M_c = 0.6$. There is particularly strong hysteresis in $C_L - QS$ and $C_M - QS$ at $z/c = 1.52$ in the attached flow region ($\alpha \leq 7^\circ$).

Figure 19 summarizes the unsteady lift effects by plotting the increase in the maximum lift coefficient, ΔC_L^{max} , and the delay in reaching maximum lift, $\Delta\alpha(C_L^{max})$, versus spanwise position for several of the highest frequency conditions at each M_c . The largest increase ($\Delta C_L^{max} = 1.0-1.2$), and the longest delay ($\Delta\alpha = 10-12^\circ$) occur for the highest frequency, lowest M_c condition. This condition also exhibits the largest in-

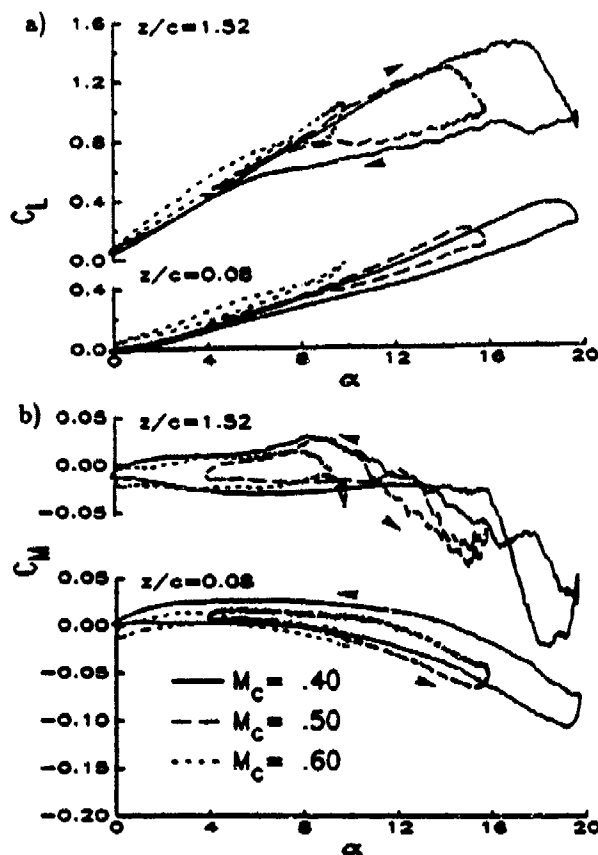


Fig. 17. Mach effects on lift and moment at higher M_c . ($k = 0.075$, $\Lambda = 0$)

crease in unsteady tip load above unsteady inboard loads. At $M_c = 0.3$ there is much less variation with spanwise position, and at higher M_c the unsteady increments are actually lower at the tip than inboard. The cause of the coupling between the effects of compressibility and three-dimensionality is not yet known.

SUMMARY AND CONCLUSIONS

This investigation of the unsteady aerodynamic response of a three dimensional wing to sinusoidal oscillations at conditions representing a full scale helicopter main rotor blade has produced the following observations:

1. The basic high amplitude dynamic stall characteristics on the inboard portion of the 3D wing at low Mach number ($M_c \leq 0.3$) are similar to earlier results, including those on the 2D version of this model. During pitch-up, there is a substantial stall delay, large unsteady increments to the airloads, and the formation of a strong leading edge vortex.

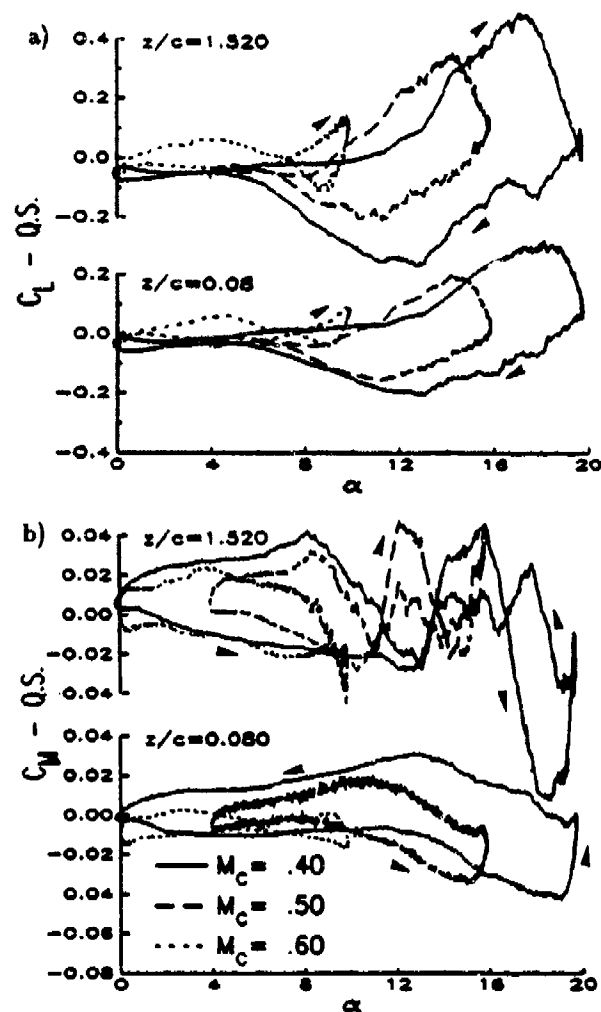


Fig. 18. Mach effects on unsteady increment to lift and moment. ($k = 0.075$, $\Lambda = 0$)

During pitch-down, flow reattachment begins near the leading edge and moves aft.

2. Near the tip of the unswept wing, the tip vortex alters these characteristics. The vortex not only lowers the effective angle of attack over a relatively large span, but also rolls up over the upper surface, increasing the trailing edge loading and generating a strong but smoothly increasing negative moment. Interaction between the tip and stall vortices increases the relative unsteady loads near the tip. During pitch down, the trailing edge load is reestablished later than the leading edge suction, causing considerable hysteresis.
3. Sinusoidal and ramp motions at equivalent maximum pitch rates generate similar aerodynamic responses, both during pitch-up and pitch-down. The detailed information on the separation process obtained for ramps²⁰⁻²² should therefore also

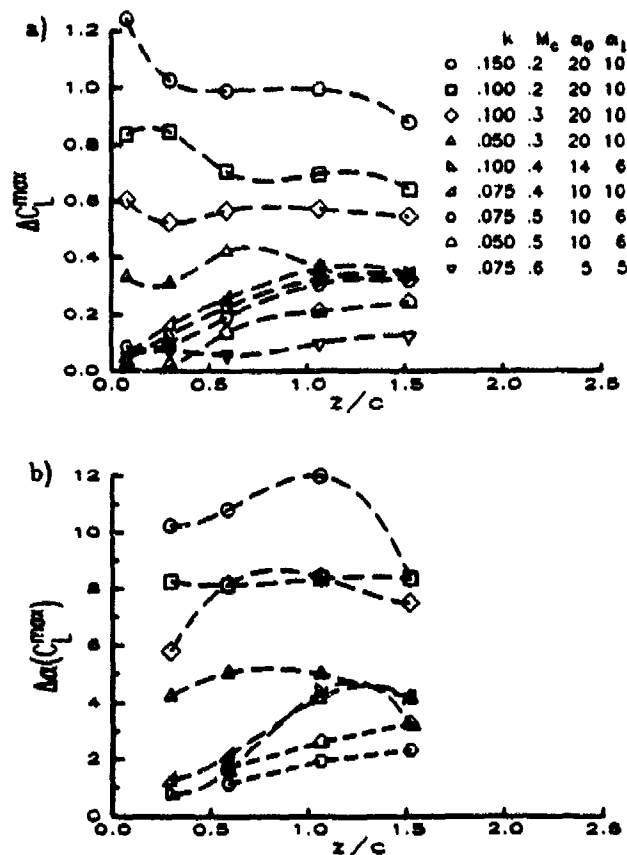


Fig. 19. Summary of unsteady lift increments and stall delays. ($\Lambda = 0$)

apply to sinusoids.

- A series of moderate amplitude ($\alpha_0 = 6^\circ$) conditions at increasing mean angle show an abrupt shift between conditions without stall and conditions with dynamic stall. No conditions were found that generated significant stall delays and C_L^{max} increments without creating a strong stall vortex and a large negative moment.
- Increased frequency delays stall, increases unsteady loads, and delays reattachment, as would be expected from 2D results.
- Prior to stall and away from the wing tip, sweep effects can be accounted for using the swept infinite wing normalisation. Tip loads and stall characteristics are very sweep-dependent. Increased sweep reduces the tip vortex effects, and hastens stall near the tip. Unsteady post-stall oscillations occur at $\Lambda = 15^\circ$ but not at either $\Lambda = 0$ or 30° .
- Mach number effects are relatively small for $M_\infty = 0.2$ and 0.3 , and in light stall. Stall occurs slightly earlier at $M_\infty = 0.3$, and is preceded by formation of a small leading edge supersonic zone.
- Results at $M_\infty = 0.4, 0.5$, and 0.6 show increasingly early stall and reduced unsteady effects. However, measurable unsteady stall delays, increases in loads, and hysteresis persist to the highest studied Mach numbers.

ACKNOWLEDGMENTS

The instrumented model, the wind tunnel test, and the analysis of the results were funded by the U.S. Army Research Office and the U.S. Air Force Office of Scientific Research, under Contract DAAL03-89-C-0013. Dr. Thomas Doligalski of ARO was the technical monitor. Capt. Hank Helin and Maj. Daniel Fant were the AFOSR representatives. The model support and drive system used in the experiment was supplied by the Sikorsky Aircraft Division of United Technologies. The author thanks Franklin Carta, Alfred Covino, John Ayer, and the staff of the UTRC LSWT for their assistance.

REFERENCES

- Ham, N.D., and Garelick, M.S., "Dynamic Stall Considerations in Helicopter Rotors," *Journal of the American Helicopter Society*, Vol. 13, pp. 49-55, April 1968.
- Liiva, J., and Davenport, F.J., "Dynamic Stall of Airfoil Sections for High-Speed Rotors," *Journal of the American Helicopter Society*, Vol. 14, pp. 26-33, Apr. 1969.
- Carta, F.O., and Niebanck, C.F., "Prediction of Rotor Instability at High Forward Flight Speeds, Volume III. Stall Flutter," U.S. Army Aviation Material Labs, Ft. Eustus, VA, USAAVLABS TR 68-18c, Feb. 1969.
- Dadone, L.U., "Two-Dimensional Wind Tunnel Test of an Oscillating Rotor Airfoil," NASA CR 2914, Dec. 1977.
- McCroskey, W.J., McAlister, K.W., and Carr, L.W., "Dynamic Stall Experiments on Oscillating Airfoils," *AIAA Journal*, Vol. 14, pp. 57-63, Jan. 1976.
- McCroskey, W.J., McAlister, K.W., Carr, L.W., Pucci, S.L., Lambert, O., and Indergard, R.F., "Dynamic Stall on Advanced Airfoil Sections," *Journal of the American Helicopter Society*, Vol. 26, pp. 40-50, July 1981.
- St. Hilaire, A.O., Carta, F.O., Fink, M.R., and Jepson, W.D., "The Influence of Sweep on the Aerodynamic Loading of an Oscillating NACA 0012 Airfoil," NASA CR-3092, 1979.

8. Lorber, P.F. and Carta, F.O., "Airfoil Dynamic Stall at Constant Pitch Rate and High Reynolds Number," *Journal of Aircraft*, Vol. 25, June 1988, pp. 548-556.
9. Leishman, J.G., "Dynamic Stall Experiments on the NACA 23012 Aerofoil", *Experiments in Fluids*, Vol. 9, pp. 49-58, 1990.
10. McAlister, K.W., and Carr, L.W., "Water Tunnel Visualisation of Dynamic Stall," *Journal of Fluids Engineering*, Vol. 101, pp. 376-380, Sept. 1978.
11. Robinson, M.C., and Luttges, M.W., "Unsteady Separated Flow: Forced and Common Vorticity About Oscillating Airfoils," Workshop on Unsteady Separated Flow, U.S.A.F. Academy, M. Francis and M. Luttges, eds., 1984, pp. 117-126.
12. Walker, J.M., and Chou, D.C., "Forced Unsteady Vortex Flows Driven by Pitching Airfoils," AIAA Paper 87-1331, 19th Fluid Dynamics, Plasma Dynamics, and Lasers Conference, Honolulu HI, June 1987.
13. Chandrasekhara, M.S. and Carr, L.W., "Flow Visualisation Studies of the Mach Number Effects on the Dynamic Stall of an Oscillating Airfoil," *Journal of Aircraft*, Vol. 27, June 1990, pp. 516-522.
14. Carr, L.W., Chandrasekhara, M.S., and Brock, N.J., "A Quantitative Study of Unsteady Compressible Flow on an Oscillating Airfoil," AIAA Paper 91-1683, 22nd Fluid Dynamics, Plasma Dynamics, and Structures Conference, Honolulu, HI, June 1991.
15. Robinson, M.C. and Wissler, J.B., "Pitch Rate and Reynolds Number Effects on a Pitching Rectangular Wing," AIAA Paper 88-2577, 6th Applied Aerodynamics Conference, Williamsburg VA, June 1988.
16. Walker, J.M and Robinson, M.C., "Dynamic Stall Development Dependence on Wing Planform," 4th Symposium on Numerical and Physical Aspects of Aerodynamic Flows, Long Beach CA, Jan. 1989.
17. Ashworth, J., Huyer, S., and Luttges, M., "Comparisons of Unsteady Flow Fields about Straight and Swept Wings using Flow Visualisation and Hotwire Anemometry," AIAA 87-1334, 19th Fluid Dynamics, Plasma Dynamics, and Lasers Conference, Honolulu HI, June 1987.
18. Ashworth J., Orisler, W., and Luttges, M., "Vortex Flows Created by Sinusoidal Oscillation of Three-Dimensional Wings," AIAA 89-2227, 7th Applied Aerodynamics Conference, Seattle WA, July 1989.
19. Lorber, P.F. and Carta, F.O., "Unsteady Stall Penetration Experiments at High Reynolds Number", AFOSR TR-87-1202, April 1987.
20. Lorber, P.F., Carta, F.O., and Covino, A.F. Jr., "Dynamic Stall Experiments on a Swept Three-Dimensional Wing In Compressible Flow," AIAA Paper 91-1795, 22nd Fluid Dynamics, Plasma Dynamics, and Lasers Conference, Honolulu HI, June 1991.
21. Lorber, P.F., "Compressibility Effects on the Dynamic Stall of a Three-Dimensional Wing," AIAA 92-0191, 30th Aerospace Sciences Meeting, Reno NV, Jan. 1992.
22. Lorber, P.F. and Carta, F.O., "Unsteady Transition Measurements on a Pitching Three-Dimensional Wing," 5th Symposium on Numerical and Physical Aspects of Aerodynamic Flows, Long Beach, CA, Jan. 1992.
23. Lorber, P.F. and Carta, F.O., "Incipient Torsional Stall Flutter Experiments on a Swept Three-Dimensional Wing," AIAA Paper 91-0935, 32nd Structures, Structural Dynamics, and Materials Conference, Baltimore MD, April 1991.

APPENDIX IX

TIP VORTEX, STALL VORTEX, AND SEPARATION OBSERVATIONS ON PITCHING THREE-DIMENSIONAL WINGS

Peter F. Lorber
United Technologies Research Center
East Hartford, CT

Abstract for the AIAA 24th Fluid Dynamics Conference
July 1993, Orlando, FL

Experimental results on the separated flow characteristics and the unsteady separation process for a pitching three-dimensional wing are described. New results are presented in several areas. The measured surface pressures and airloads are used to infer tip vortex characteristics and effects, and to identify leading edge dynamic stall vortex propagation patterns. Leading and trailing separation phenomena are investigated using the experimental measurements on the surface, and a useful correlation is found with Stratford's turbulent boundary layer separation criterion.

As shown in Fig.1, the experiment was conducted using a rectangular semi-span wing model that could be mounted at sweep angles of 0, 15, and 30°. The model scale and test conditions were selected to simulate conditions on a full scale helicopter main rotor blade (Mach numbers between 0.2 and 0.6, Reynolds numbers of 2-6 million, 9% thickness airfoil section, nondimensional pitch rates, $A = \dot{\alpha}c/2U$, of 0.001-0.025, and angles of attack, α , of 0-30°). Extensive surface instrumentation (112 pressure transducers identified by the dots in Fig. 1 plus 16 hot film gages) was used to identify the physical processes and quantify the effects of the test parameters.

Previous results from this program have been described in a series of papers. References 1 and 2 describe the experiment and survey the results for constant pitch rate (ramp) motions for two- and three-dimensional geometries, respectively. They identify the dependence of the surface pressures and loads upon the test parameters (pitch rate, wing sweep, Mach number, spanwise position, and tip geometry). The unsteady separation process is examined in Ref. 3, including the changes introduced by increasing M from 0.2 to 0.6. Reference 4 describes how the laminar to turbulent boundary layer transition location responds to the unsteady pitching motion. The response to large amplitude sinusoidal oscillations is covered in Ref. 5, while Ref. 6 describes results for small amplitude oscillations about mean angles near static stall, a simulation of the initial stages of stall flutter.

The wing tip vortex has been shown previously (Refs. 2,5,7) to strongly influence the aerodynamic loads on this model before, during, and after stall. The delays of stall and enhancements of the unsteady lift and pitching moment near the tip are particularly strong at low Mach number and for the unswept geometry. This paper will use measured pressure distributions at the spanwise station 8% of chord from the tip to examine tip vortex effects. Figure 2 shows an example for a test case with strong tip vortex effects, the unswept wing at $M_c = 0.2$ and $A = 0.02$. The three curves along the top show the growth of the distortion of the upper surface trailing edge pressures

at $\alpha = 10, 18$, and 26° . A quantitative estimate of the direct effects of the tip vortex was obtained by subtracting from the measured ΔC_P (lower surface - upper surface) the ΔC_P calculated by applying the $\Delta C_P \propto \alpha \sqrt{\frac{c-x}{x}}$ dependence of thin airfoil theory. This difference is computed from $x/c = 0.4$ to the trailing edge. The second row of plots in Fig. 2 show the measured ΔC_P distributions (squares) and the thin airfoil curves (solid lines). The agreement in shape shown at $\alpha = 10^\circ$ is also typical of attached flow conditions at all other spanwise positions ($z/c \geq 0.3$). The large increment to ΔC_P visible at $\alpha = 18$ and 26° can be integrated to estimate the increments to the lift and moment directly induced by the tip vortex.

This computation is performed at each instant during an unsteady ramp motion, producing normal force and moment curves such as those shown in Fig. 3. The solid lines are the measured loads, and the dashed lines are the computed tip vortex increments. The upper plots are close to the tip ($z/c = 0.08$), and show that virtually all of the negative (nose-down) C_M and up to 25% of the C_N is generated by the tip vortex distortion. The lower pair of plots in Fig. 3 are further from the tip, at $z/c = 0.3$. There is almost no contribution from tip vortex distortion prior to stall ($\alpha \leq 26^\circ$). After stall the pressure distributions are distorted by the leading edge vortex and massive separation; non-zero values of the dotted curves after stall are therefore not caused by the tip vortex. For the cases examined at $M_c = 0.2$ and 0.3 , tip vortex roll-up loads contribute 20-30% to the peak C_N and 60-70% to the peak C_M . The paper will quantify effects such as pitch rate and waveform (constant rate ramp vs sinusoid) on the tip vortex loads.

It will be further shown that tip vortex effects are very small for swept geometries, and, as Mach number is increased, the contribution of the tip vortex loads on even the unswept wing drops to C_N drops to 10% at $M=0.5$ (shown as the bottom plot in Fig. 3) and 3% at $M_c = 0.6$. The most likely explanation is the lower stall angle at higher M_c . The roll-up loads do not become significant (at any Mach number) until angles of attack above about 10° , and are strongest above 20° (Fig. 3). At higher M_c , the shock-induced stall (discussed in Ref. 3) occurs at a relatively low angle of attack, before a strong tip vortex is able to form. This appears to be the reason why the significant enhancements of the unsteady tip loads observed at low speed (Ref. 7) were not present at higher Mach number (Ref. 2).

A second application of the surface pressure results is to investigate the propagation of the dynamic stall vortex. The approach is to use the pressure vs. time results at each transducer to identify the time of minimum pressure, which is assumed to correspond to the passage of the vortex past that location on the wing. Figure 4 shows an example of the pressure time histories for the ten transducers at a single spanwise station. The minimum pressure locations are marked by circles in both the overall view of the entire $0-30^\circ$ ramp (left plot) and the close-up of the time of stall vortex propagation (right plot). This technique has been used on this model in earlier papers to estimate vortex propagation speeds for two-dimensional conditions (Ref. 1) and for individual spanwise locations on the unswept three-dimensional wing (Ref. 2). The information will be used in this paper to generate views of the stall vortex position on the wing planform at specific times. Figure 5 shows such views at sweep angles of $0, 15$, and 30° , for a chordwise Mach number of 0.3 and a pitch rate of $A=0.01$. Vortex positions are shown at time intervals of $t/T = 0.025$, or approximately $\Delta\alpha = 1.5^\circ$. For the unswept wing (top view), the vortex is first apparent inboard at $t/T = 0.40$ ($\alpha = 16.5^\circ$). At $z/c = 1.52$, the vortex propagates steadily aft, reaching the trailing edge at $\alpha = 21^\circ$. This corresponds to a speed of 25% of the freestream velocity. Closer to the tip, the vortex appears later (corresponding to the delay in stall caused by the reduction in effective angle of attack induced by the tip vortex, Refs. 1, 5-7), and propagates more slowly, as shown by

the reduced spacing between the vortex position curves. The initial propagation speed at $z/c = 0.08$ is reduced to 9% of U_c . This result is consistent with initial results for this experiment (Ref. 2), and with lower speed flow visualization data from other experiments (Refs. 7-8).

Vortex propagation patterns are quite different for swept geometries, as shown in the lower two views of Fig. 5. While the stall vortex still first appears on the inboard portion of the leading edge, the subsequent development appears quite different. The inboard propagation speed is reduced by sweep, in agreement with the swept tunnel-spanning wing results of Ref. 9. Closer to the tip, vortex propagation speeds are increased, both relative to the unswept case and relative to the inboard values. This behavior is not yet fully understood, but it is probably related to differences in tip vortex strengths (weaker with sweep) and roll-up locations (over the surface at $\Lambda = 0$ and outboard of the tip at $\Lambda = 15-30^\circ$).

The effect of pitch rate on the vortex propagation patterns is illustrated in Figs. 6 and 7, which are for the same Mach number ($M_c = 0.3$), motion, and pitch range as Fig. 5, but at pitch rates of $A = 0.005$ and 0.02 , respectively. The qualitative characteristics and the effect of sweep are similar. The absence of an identifiable stall vortex within 0.5 chord lengths of the tip at $A = 0.005$ and $A = 0$ (the upper view in Fig. 6) is the primary difference. Two effects combine to weaken the stall vortex here: the low pitch rate and the effective angle of attack reductions induced by the tip vortex. As expected, because vortex propagation speeds are tied to the chordwise velocity, the vortex remains over the wing for a wider range of angle at higher pitch rate ($\Delta\alpha = 3-5^\circ$ at $A = 0.005$ and $9-12^\circ$ at $A = 0.02$).

Vortex propagation patterns for sinusoidal motion are shown in Fig. 8, for the condition $\alpha = 20^\circ - 10^\circ \cos \omega t$, at $M_c = 0.3$ and $k = 0.1$. The basic characteristics are again similar to the $A = 0.01$ ramp results (Fig. 5), which are at approximately the same maximum pitch rate. The final comparison of vortex patterns is shown in Figures 9 and 10, which illustrate the effect of Mach number using $M_c = 0.2$ and 0.4 ramps at a constant nondimensional pitch rate of $A = 0.01$. The $M_c = 0.2$ results (Fig. 9) have the same appearance as the $M_c = 0.3$ results shown in Fig. 5, with the exception of an early initial appearance of the stall vortex, at $\alpha \simeq 20-21^\circ$ instead of $17-18^\circ$. This results from the early separation apparently induced by the appearance of locally supersonic flow near the leading edge (Ref. 3). At $M_c = 0.4$ (Fig. 10), patterns at 0 sweep are the same as at lower Mach number, as are the patterns over the forward portion of the wing at $\Lambda = 15$ and 30° . No distinct pressure signature of the stall vortex could be identified over the aft portion of the wing, especially at $\Lambda = 30^\circ$. The apparent early disappearance or dissipation of the stall vortex at higher Mach number was discussed in Refs. 2-3.

Two other issues related to the separated flow characteristics of this experiment will also be addressed. First, the measured pressure time histories in the presence of the stall vortex (such as Fig. 4) will be compared to the surface pressure signatures computed from the unsteady potential flow of a line vortex over a surface. This comparison generates estimates of the vortex strength, height above the surface, and propagation speed. While there is qualitative agreement with observations and expectations for these characteristics, the quantitative results show a vortex that is too strong, too high above the surface, and moving too rapidly. The paper will explore what can be learned from these differences, beyond the obvious fact that the dynamic stall vortex is not a concentrated line moving two-dimensionally in a potential flow. The second issue concerns vortex shedding following the primary stall vortex. The two-dimensional version of this experiment exhibited strong periodic vortex shedding after stall, at frequencies of 50-60 Hz, similar to those

expected for vortices shed from a bluff body of diameter equal to the vertical projection of the airfoil chord ($c \sin \alpha$). Strong post-stall oscillations were not observed for the three-dimensional wing, although weak oscillations were occasionally present inboard. At a sweep angle of 15° (but not at 0 or 30°) there were one to two rapid pressure changes that followed the primary stall vortex, possibly reflecting additional shed vortices. A more quantitative description of this as yet unexplained behavior will be provided in the paper.

The separation process inferred from the surface measurements on this model has been described in Refs. 3 and 4. At high Reynolds number and angle of attack, the suction surface boundary layer is turbulent downstream of the suction peak. At lower Mach number ($M_c \leq 0.3$), unsteady separation begins in the forward 5–10% of chord, and rapidly expands to eliminate the leading edge suction peak and form a strong stall vortex. Trailing edge separation, while often important in steady flows, does not seem to play a major part in this unsteady process. At higher Mach numbers, a local region of supersonic flow forms near the leading edge. An early but more gradual separation then occurs near the strong adverse pressure gradient (a well-defined shock for $M_c \geq 0.4$) terminating the supersonic region.

This paper will add to this interpretation by examining the surface pressure gradients and applying the turbulent boundary layer separation criterion of Stratford (Ref. 10) to the measured pressure distributions to identify likely separation locations at various steady and unsteady test conditions. Stratford's criterion is based on an approximate solution to the boundary layer equations in a steady adverse pressure gradient. The basic relation for predicting the separation location is:

$$C_P \left(x \frac{dC_P}{dx} \right)^{\frac{1}{2}} = 0.39 (10^{-6} R)^{\frac{1}{16}}, \quad (1)$$

with C_P , x , and R based upon the starting conditions for the adverse pressure gradient region. (A somewhat more complex relation is actually used here, to account for initial regions of laminar flow and favorable pressure gradient, and for variations in Reynolds number.) It is recognized that there are several valid objections to the application of this approximate steady flow, two-dimensional, constant gradient analysis to this unsteady problem. However its relative simplicity and need for no information other than the pressure and gradient make it worthwhile to see if any useful information can be obtained.

Figure 11 shows results for a sample case: the $z/c = 0.59$ results for a ramp at $A = 0.01$ and $M_c = 0.3$. The rows represent results at four angles of attack during the motion: $\alpha = 10, 14, 16$, and 18° . The left column is the pressure distribution (C_P based on the freestream velocity), the center is the pressure gradient (based on surface distance, s), and the right is the ratio of the left to right hand sides of Equation 1 (Stratford's ratios greater than one imply separation). At $\alpha = 10^\circ$ (top row) there is a moderate adverse pressure gradient over the forward 20% of chord, followed by a region of uniform gradient (in terms of dC_P/ds), with a slight increase near 80% of chord. (The region of favorable pressure gradient is very small for this airfoil at moderate to high angles of attack, extending only from the stagnation point near $x/c = .02$ on the lower surface to the suction peak near $x/c = 0.005$ on the upper surface.) The plot of the Stratford ratio for this case (in the upper right corner) shows two peaks, one near 15% of chord, and the other at 80–85%. The aft peak is much stronger, reaching 120% of the separation value. No convincing evidence has yet been seen of this predicted trailing edge separation in the surface measurements of this experiment. As angle of attack is increased, the suction peak pressures (left column) and the peak adverse gradients (center column) increase rapidly. Because the Stratford ratio depends on the

velocity at the suction peak, it increases more gradually, as shown by the third peak forming at the station closest to the leading edge. This peak first exceeds 1.0 at $\alpha \simeq 20^\circ$, approximately 1° before the first signs of separation are observed in the unsteady pressures (Ref. 3). The Stratford ratio peak near 15% of chord stays at an approximately constant value of 0.85-0.90, while the peak near 85% weakens as α increases. The leading edge peak seems most clearly connected to the separation process observed in the experiment. The paper will examine pressure gradients and Stratford's ratios for other conditions. In particular, comparisons will be made between steady and unsteady cases, and between low Mach number ($M_c = 0.2$) and compressible cases.

ACKNOWLEDGEMENT

This work was supported by Army Research Office contract DAAL-89-C-0013, monitored by Dr. Thomas Doligalski.

REFERENCES

1. Lorber, P.F. and Carta, F.O., "Airfoil Dynamic Stall at Constant Pitch Rate and High Reynolds Number," *Journal of Aircraft*, Vol. 25, June 1988, pp. 548-556.
2. Lorber, P.F., Carta, F.O., and Covino, A.F. Jr., "Dynamic Stall Experiments on a Swept Three-Dimensional Wing In Compressible Flow," AIAA Paper 91-1795, 22nd Fluid Dynamics, Plasma Dynamics, and Lasers Conference, Honolulu HI, June 1991.
3. Lorber, P.F., "Compressibility Effects on the Dynamic Stall of a Three-Dimensional Wing," AIAA 92-0191, 30th Aerospace Sciences Meeting, Reno NV, Jan. 1992.
4. Lorber, P.F. and Carta, F.O., "Unsteady Transition Measurements on a Pitching Three-Dimensional Wing," 5th Symposium on Numerical and Physical Aspects of Aerodynamic Flows, Long Beach CA, Jan. 1992.
5. Lorber, P.F., "Dynamic Stall of Sinusoidally Oscillating Three-Dimensional Swept and Unswept Wings in Compressible Flow," American Helicopter Society 48th Annual Forum, Washington DC, June 1992.
6. Lorber, P.F. and Carta, F.O., "Incipient Torsional Stall Flutter Experiments on a Swept Three-Dimensional Wing," AIAA Paper 91-0935, 32nd Structures, Structural Dynamics, and Materials Conference, Baltimore MD, April 1991.
7. Robinson, M.C. and Wissler, J.B., "Unsteady Surface Pressure Measurements on a Pitching Rectangular Wing," AIAA 88-0328, 26th Aerospace Sciences Meeting, Reno NV, Jan. 1988.
8. Ashworth, J. and Luttgies, M., "Comparisons in Three-Dimensionality in the Unsteady Flows Elicited by Straight and Swept Wings," AIAA 86-2280-CP, Atmospheric Flight Mechanics Conference, Williamsburg VA, Aug. 1986.
9. Freymuth, P., "Vortex Topology for Rectangular Wings in Pictures, Sketches, and Conjectures," AIAA 91-1824, 22nd Fluid Dynamics, Plasma Dynamics, and Lasers Conference, Honolulu HI, June 1991.
10. St. Hilaire, A.O. Carta, F.O., "Analysis of Unswept and Swept Wing Chordwise Pressure Data From an Oscillating NACA 0012 Airfoil Experiment," NASA CR-3567, 1983.
11. Stratford, B.S., "The Prediction of Separation of the Turbulent Boundary Layer," *J. Fluid Mechanics*, Vol. 5, Pt. 1, Jan. 1959, pp. 1-16.

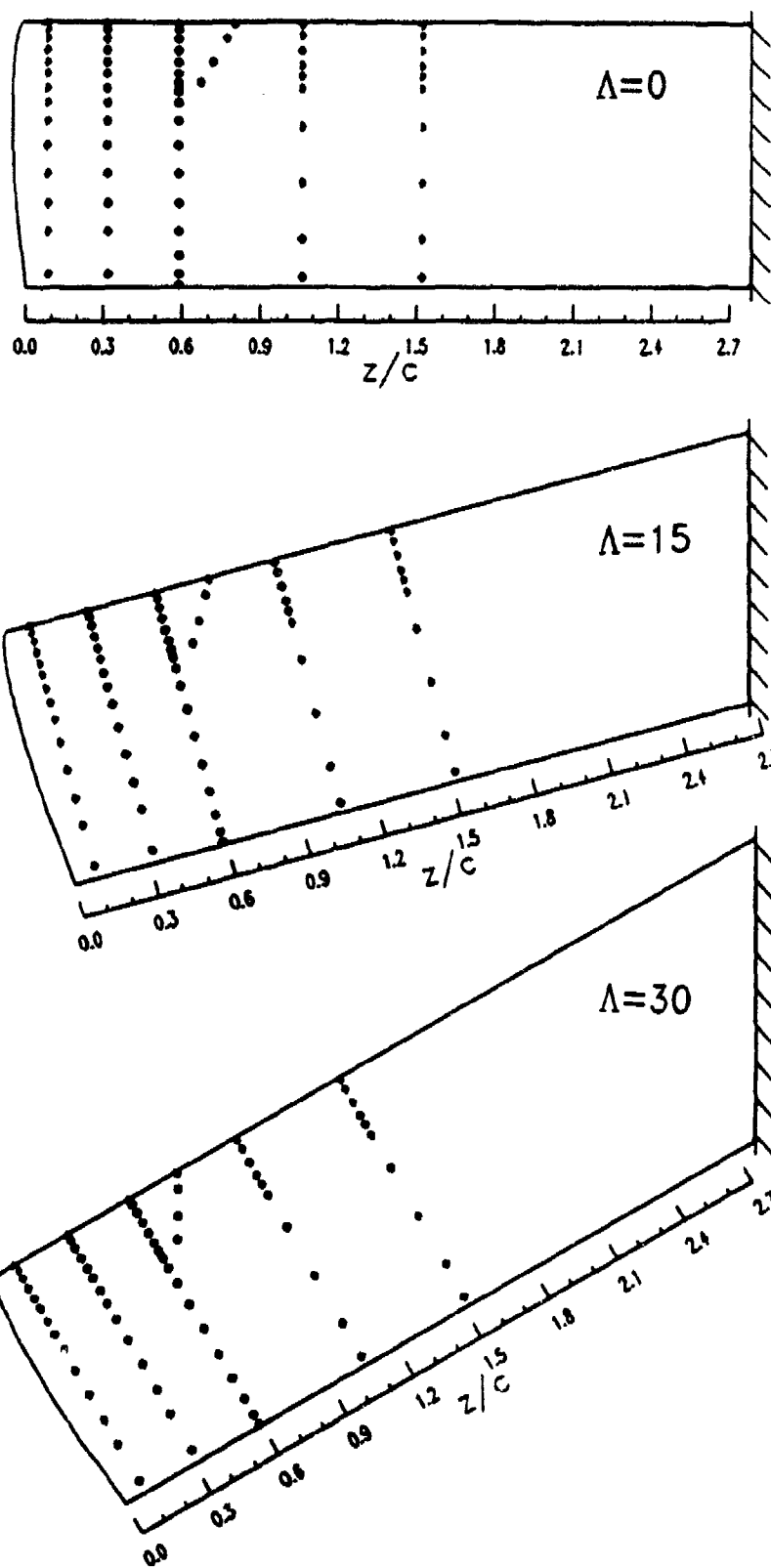


Figure 1. Planforms and upper surface pressure transducer locations

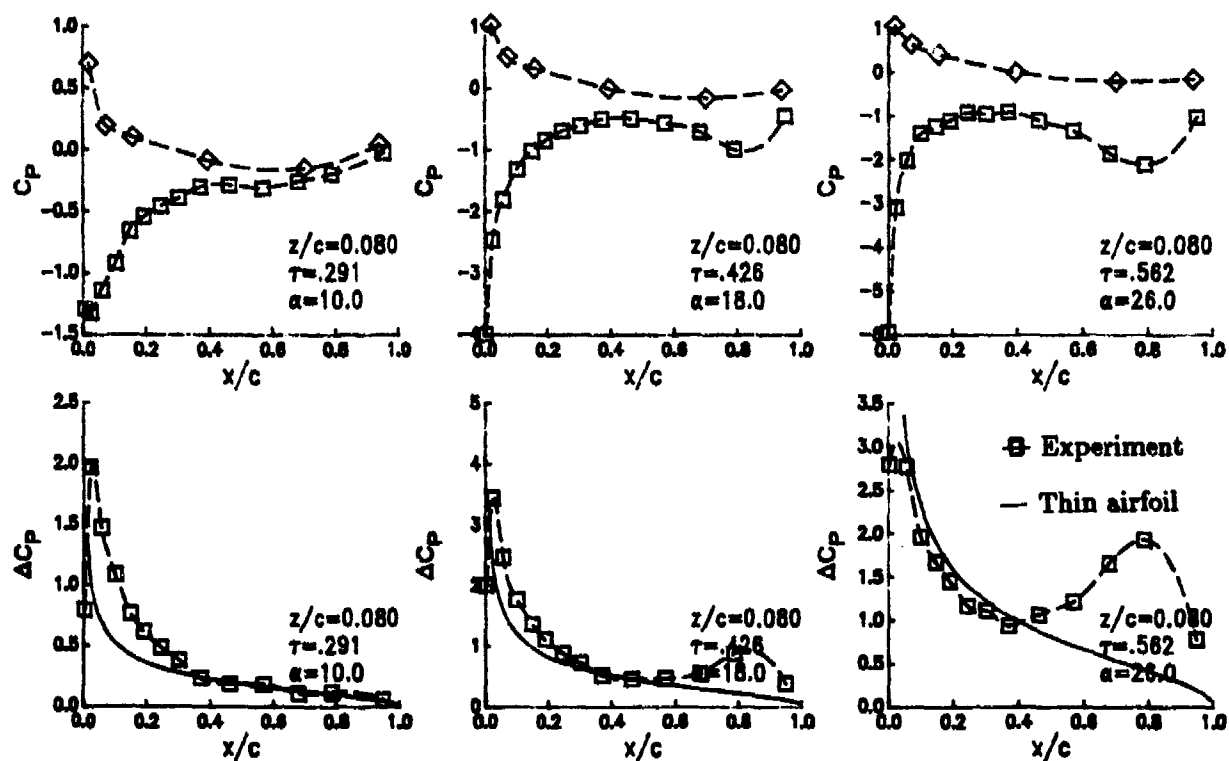


Figure 2. Pressure distributions showing the influence of the tip vortex.

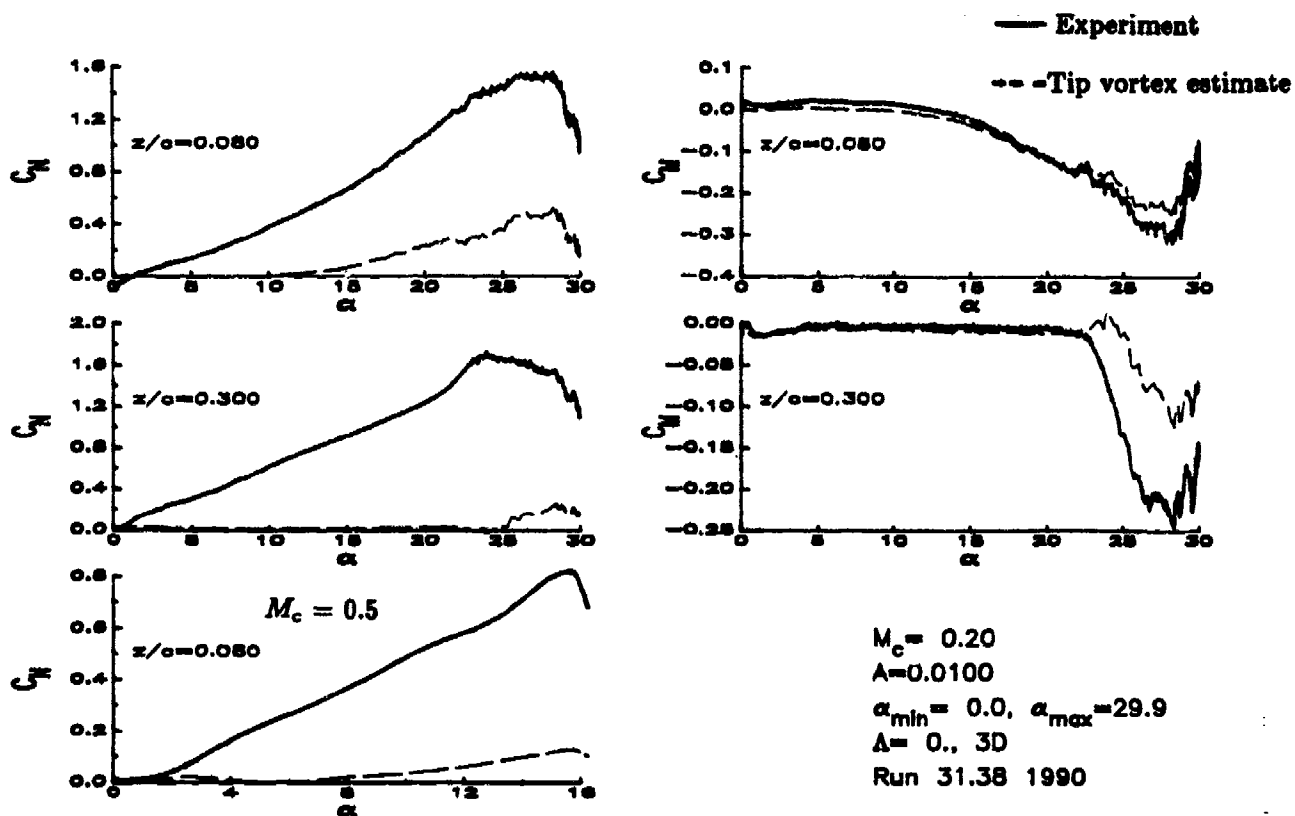


Figure 3. Comparison of normal force and moment with tip vortex load increments.

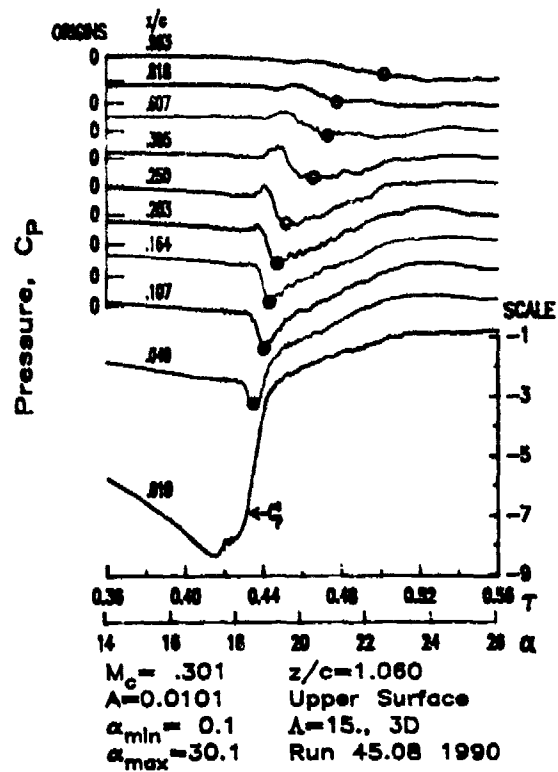
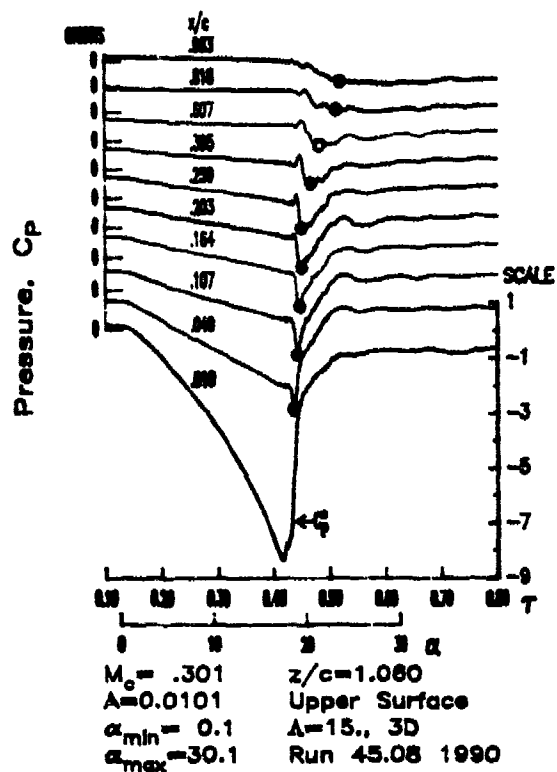


Figure 4. Pressure time histories, showing stall vortex position estimates.

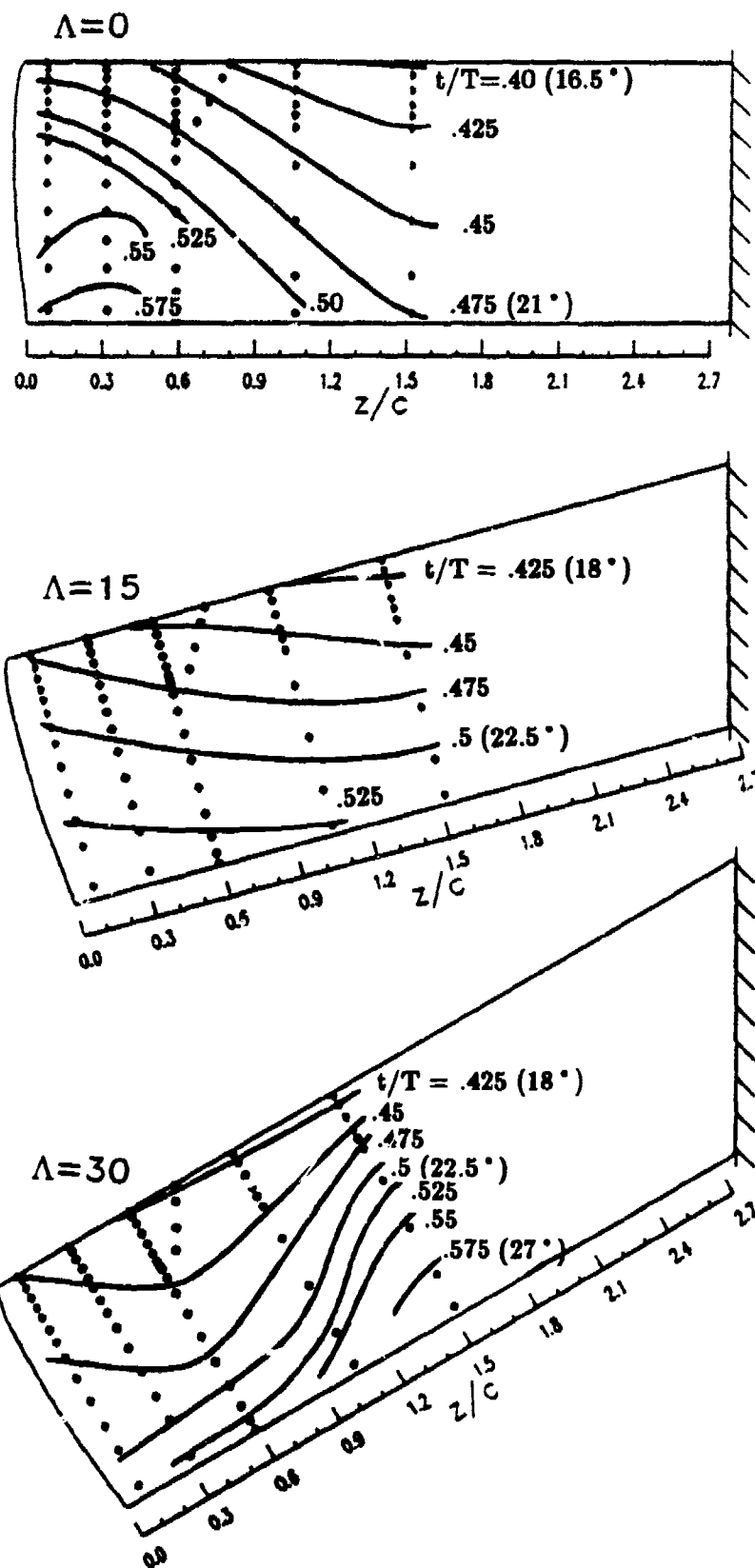


Figure 5. Stall vortex propagation patterns at $M = 0.3$ and $A = 0.01$.

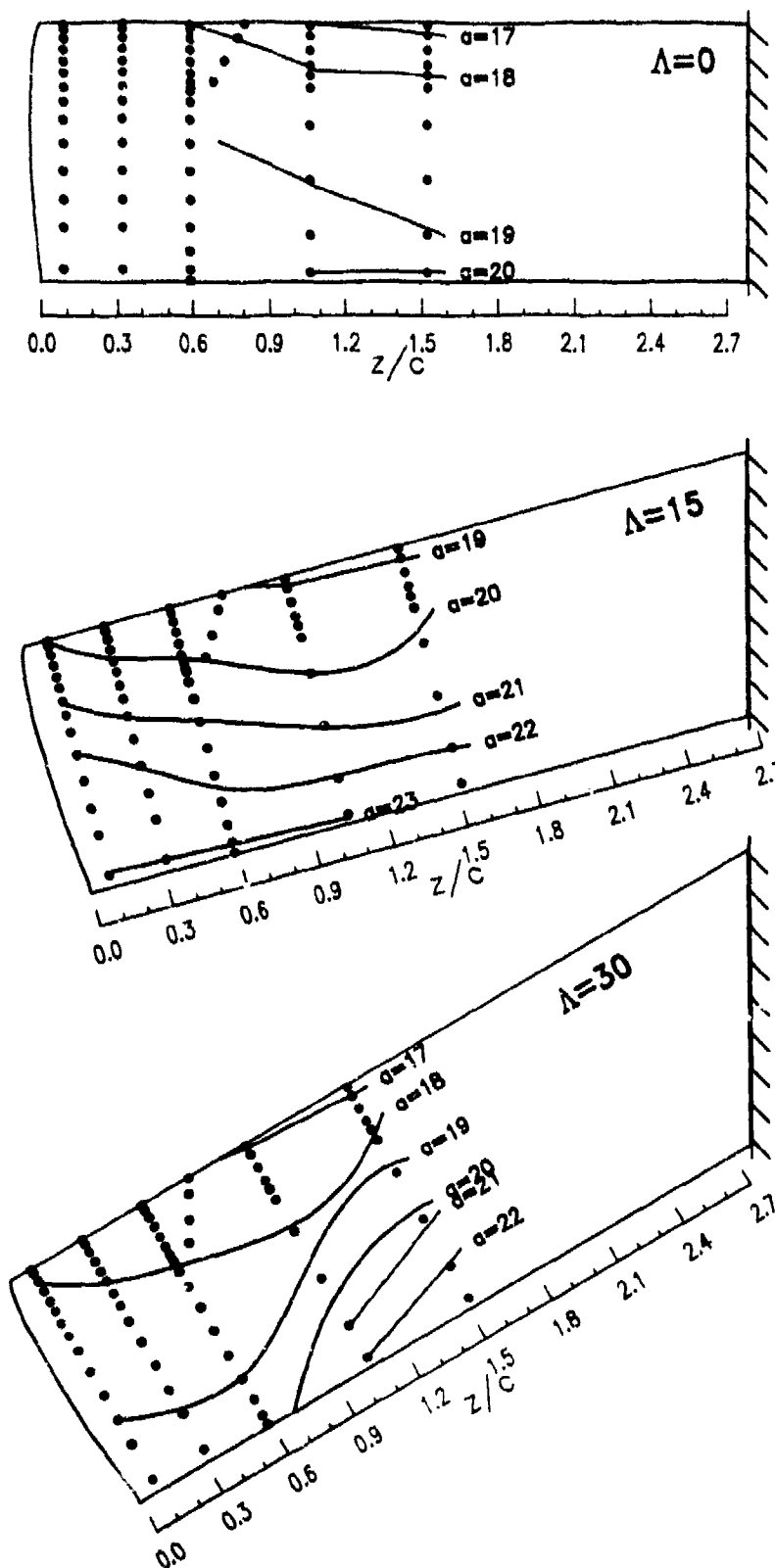


Figure 6. Stall vortex propagation patterns at $M_c = 0.3$ and $A = 0.005$.

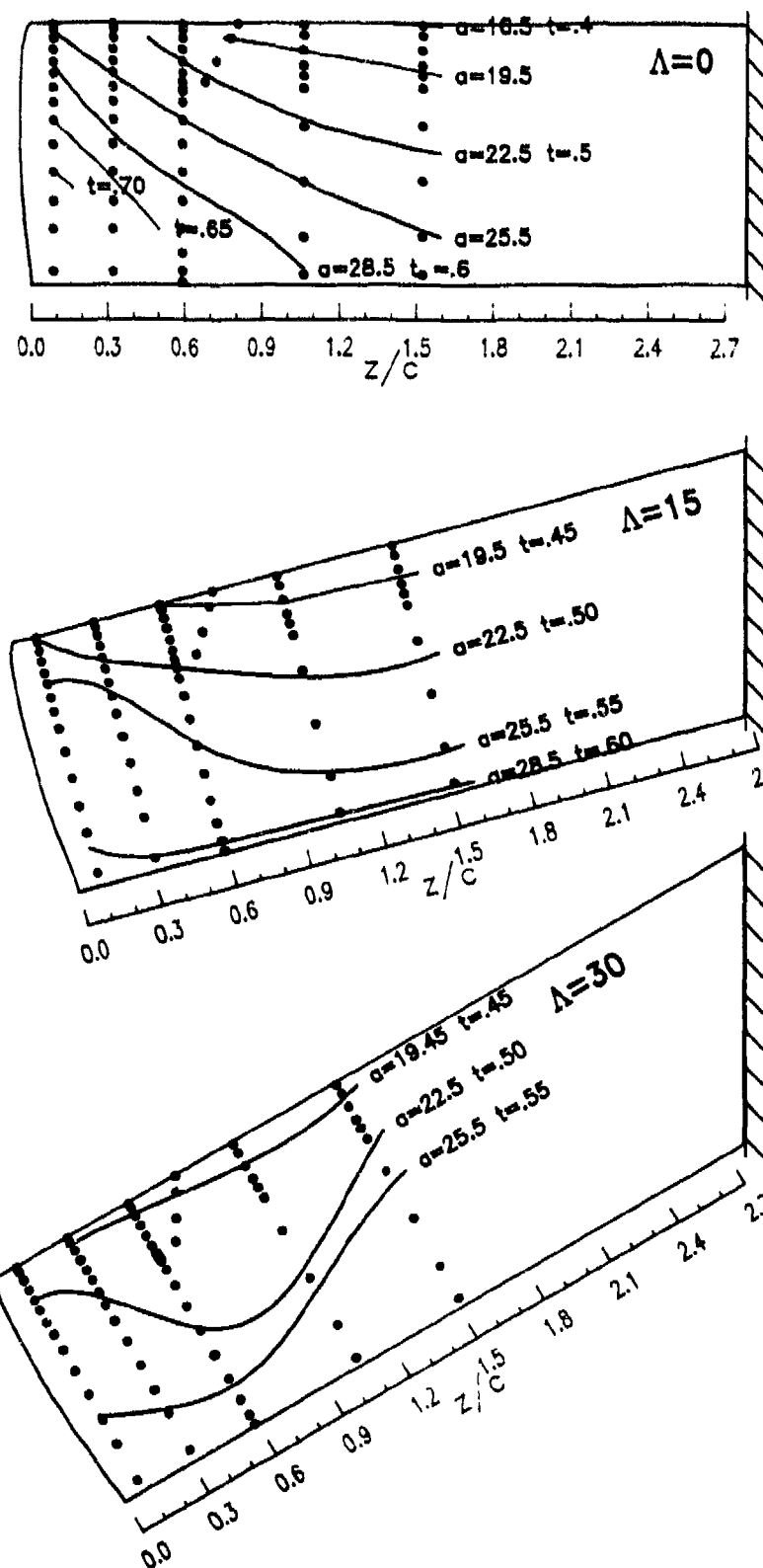


Figure 7. Stall vortex propagation patterns at $M_c = 0.3$ and $A = 0.02$.

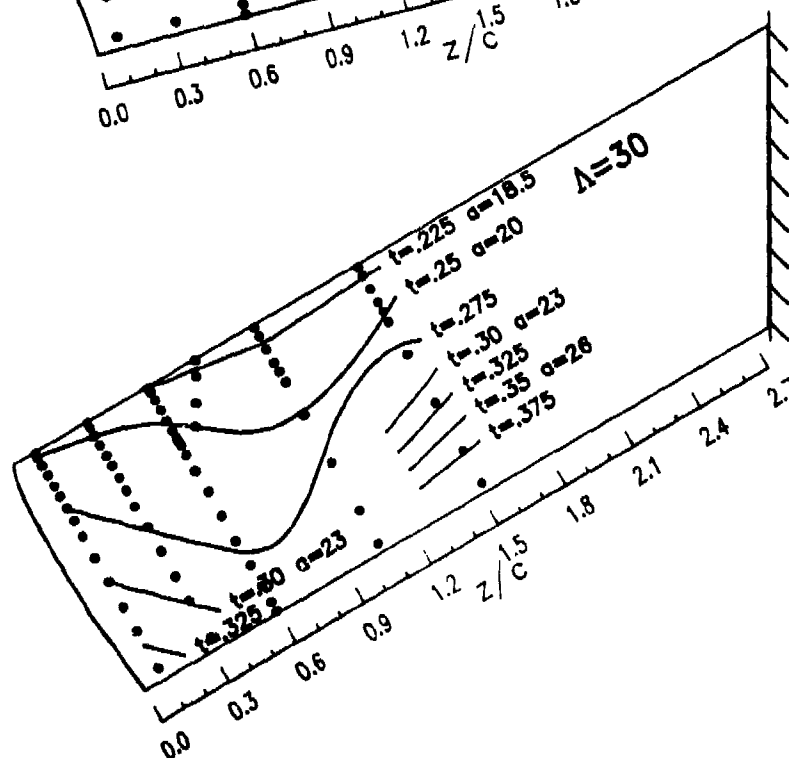
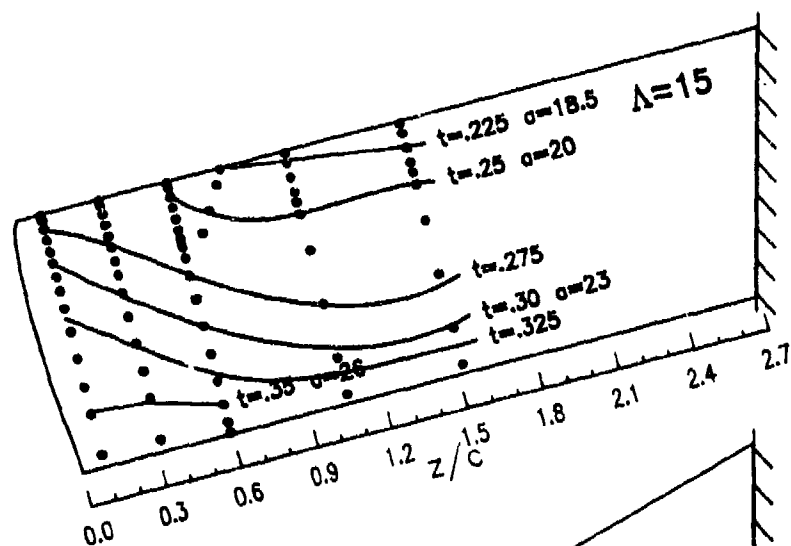
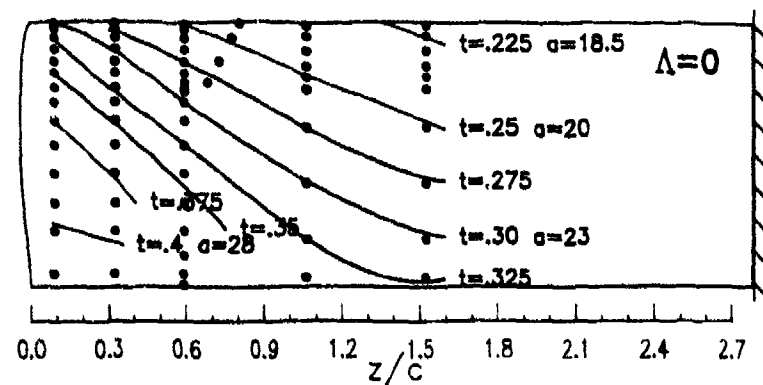


Figure 8. Stall vortex propagation patterns for sinusoidal motion at $M_c = 0.3$, $k = 0.1$, and $\alpha = 20^\circ - 10^\circ \cos \omega t$.

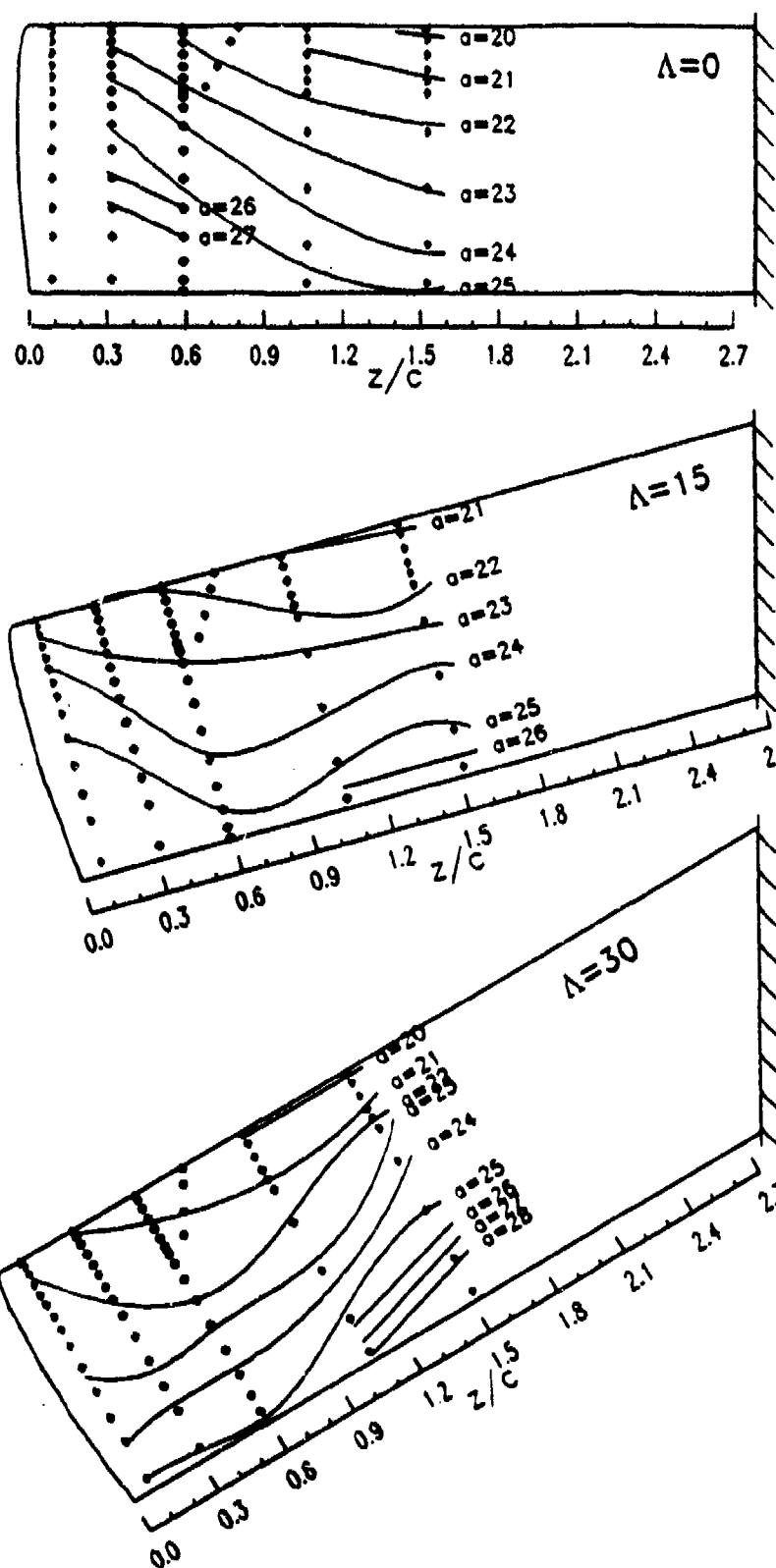


Figure 9. Stall vortex propagation patterns at $M_c = 0.2$ and $A = 0.01$.

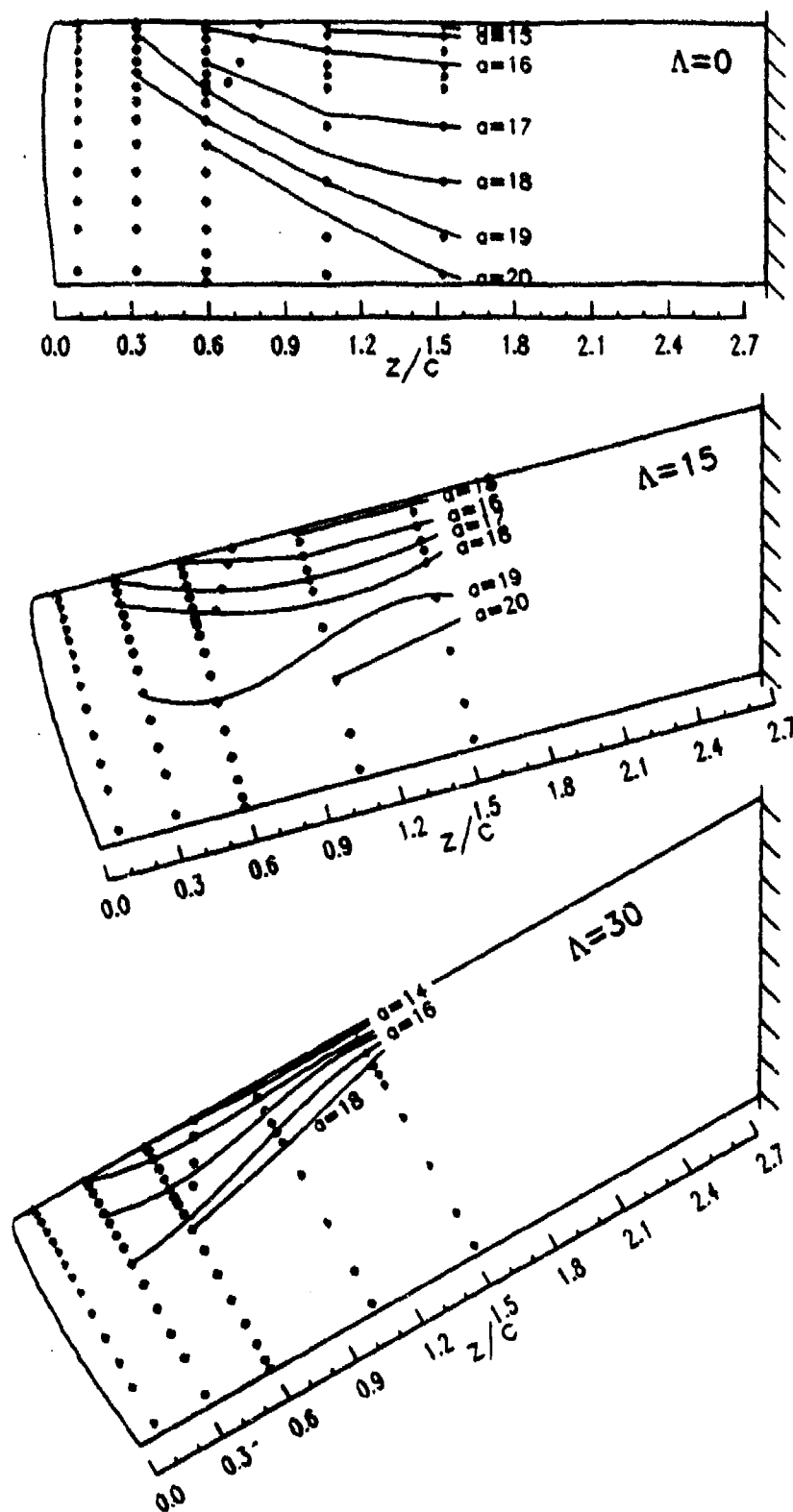


Figure 10. Stall vortex propagation patterns at $M_c = 0.4$ and $A = 0.01$.

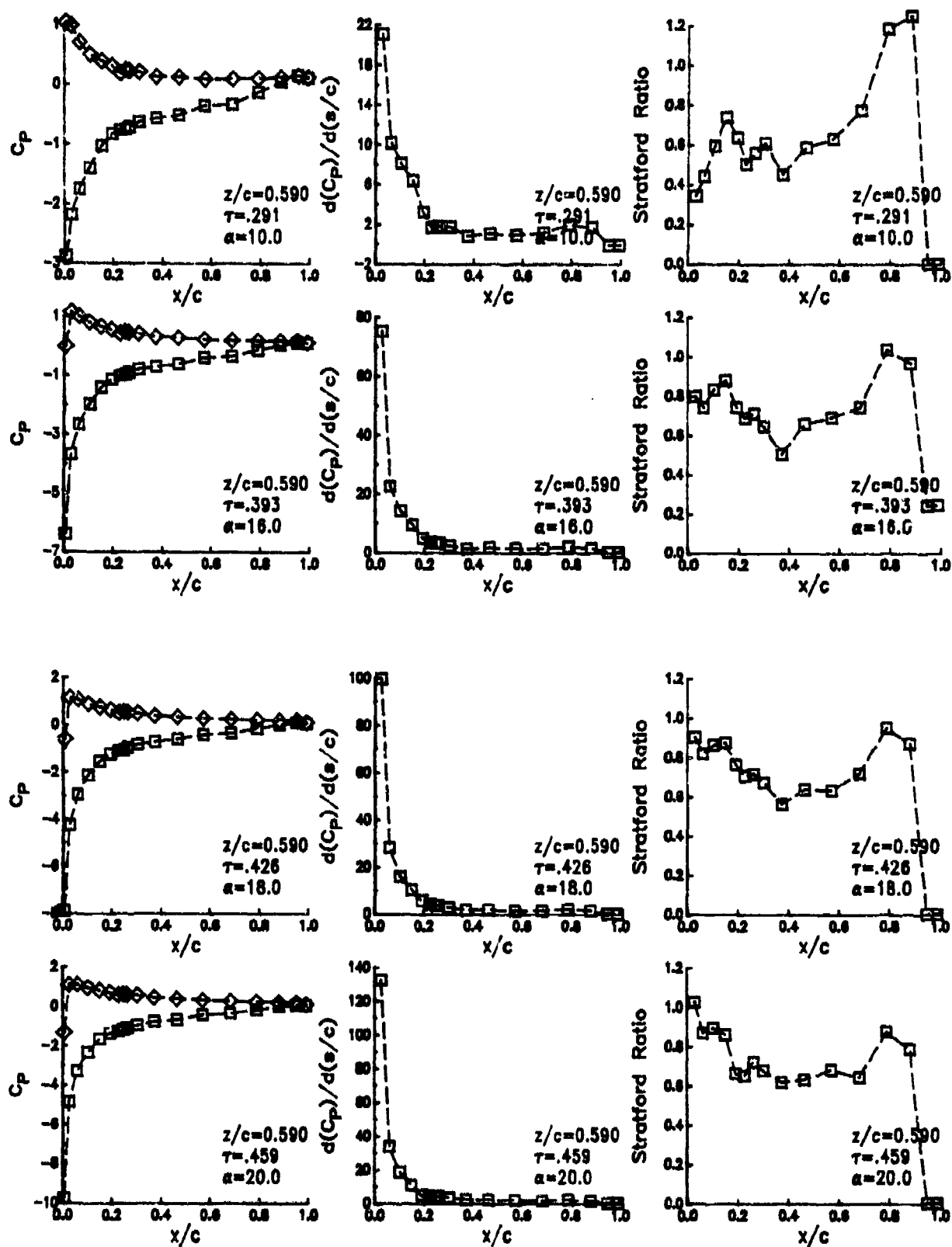


Figure 11. Surface pressure, local gradient, and Stratford ratio examples.

APPENDIX X AN EMPIRICAL MODEL FOR AERODYNAMIC DAMPING

Experimental measurements of the aerodynamic damping coefficient for small amplitude pitch oscillations (Ref. 1, also Appendix IV) exhibit complex dependencies on numerous parameters. Six independent variables are present: Mach number, reduced frequency, mean angle of attack, pitching amplitude, sweep angle, and spanwise location. Damping coefficients measured for each of the 260 test conditions are provided in Table X-1 of this Appendix. Because the regions of negative damping occur over a very narrow range of mean angle of attack, which is different for each set of test conditions, the tabulated data does not by itself provide sufficient resolution to determine all of the dependencies. However, many fundamental trends have been identified (Ref. 1), such as the qualitative effects of changes in frequency, Mach number, or pitching amplitude. In order to apply these results, a method of estimating the damping coefficient, $\Xi = -\int C_d d\alpha / \pi \alpha_1^2$, at arbitrary combinations of the variables is needed. The object of this Appendix is to describe an empirical procedure to provide this estimate. The procedure is primarily designed to provide a reasonable approximation to the experimental damping characteristics; it does not precisely match all or most of the specific measurements. A listing of the FORTRAN code for this procedure, function EDAMP, is included in Table X-2 of this Appendix.

The data clearly indicate that the occurrence of negative damping is very closely linked to the steady stall characteristics of the wing section. The first prerequisite for determining the damping is therefore to find the steady stall angle (α_{ss}) at the given Mach number, sweep angle, and spanwise position.

$$\alpha_{ss} = \alpha_{ss}(M, \Lambda, z, \text{airfoil}, \dots)$$

For current purposes, α_{ss} is defined as the angle corresponding to the onset of a rapid drop in the pitching moment. This stall angle is assumed to be an input to the empirical damping procedure. In the current model all effects of sweep, airfoil section, and spanwise position are assumed to be included in the determination of the steady stall angle. There are no direct effects of these parameters in the damping function. The direct inputs (in addition to α_{ss}) to function EDAMP are therefore the Mach number (M), the reduced frequency (k), the mean angle of attack (α_0), and the angular amplitude (α_1).

The single most significant quantity for determining the aerodynamic damping is the difference between the mean angle of attack (α_0) and the steady stall angle (α_{ss}). For fully attached flow ($\alpha_0 \ll \alpha_{ss}$), the damping is positive. There is a region of negative damping when α_0 is near α_{ss} , with a width proportional to the pitching amplitude (α_1). In fully separated flow ($\alpha_0 \gg \alpha_{ss}$) the damping is again positive. The magnitude of the positive and negative damping, and the location and width of the peak are influenced by parameters such as Mach number, frequency, and pitching amplitude. The empirical procedure uses a series of expressions to qualitatively model the observed dependencies.

The first parameter to be determined is the mean angle of attack for the negative damping peak, α_{us} . A delay beyond α_{ss} is postulated, proportional to

the square of the frequency:

$$\alpha_{us} = \alpha_{ss} + 0.2 k^2 \alpha_{ss}$$

This delay is similar, but not identical, to the frequency dependent delay in dynamic stall. The damping is the sum of two terms, the positive (background) value plus the negative peak.

$$\Xi(\alpha_0, \alpha_1, \alpha_{ss}, k, M) = \Xi_p + \Xi_n$$

For attached flow ($\alpha_0 < \alpha_{us}$) the positive term (Ξ_p) is $\pi k/2$, the result of incompressible thin airfoil theory (see Ref. 1). If the Mach number is high enough to produce supersonic flow over part of the section, the chordwise pressure distribution becomes qualitatively altered, increasing the positive damping. This effect is modelled by adding a coefficient to the positive damping term:

$$\Xi_p = A_a \pi k^2,$$

$$A_a = 1, \quad M < M_{sonic}, \quad \alpha_0 < \alpha_{us}$$

$$A_a = 1 + 30 k (M - M_{sonic})^2, \quad M \geq M_{sonic}, \quad \alpha_0 < \alpha_{us}$$

For the airfoils such as the NACA 0012, SC1095, and SSC-A09, M_{sonic} is approximately 0.3.

In separated flow, the positive term is increased by a constant, following a transitional region. The transitional region is represented a cosine function between 0 at $\alpha_0 = \alpha_{us}$ and the full value at $\alpha_0 = \alpha_{us} + \alpha_1$.

$$A_a = 1 + A_{a,fs} * .5(1 - \cos\left(\pi \frac{\alpha_0 - \alpha_{us}}{\alpha_1}\right)), \quad \alpha_{us} \leq \alpha_0 \leq \alpha_{us} + \alpha_1$$

$$A_a = 1 + A_{a,fs}, \quad \alpha_0 > \alpha_{us} + \alpha_1$$

In the model, $A_{a,fs}$ is set to 0.5. This number is somewhat arbitrary, since there is considerable scatter in the fully stalled damping results.

The negative peak is assumed to have a Gaussian distribution as a function of mean angle, with the magnitude proportional to terms dependent on the reduced frequency, Mach number, and pitching amplitude. Note that the amplitude of the exponential function drops by 87% at $\alpha_0 = \alpha_{us} \pm \alpha_1$.

$$\Xi_n = A_p \exp\left(-2 \left(\frac{\alpha_0 - \alpha_{us}}{\alpha_1}\right)^2\right)$$

$$A_p = A_{p,k} * A_{p,M} * A_{p,\alpha_1}$$

The frequency term ($A_{p,k}$) increases linearly from 0 at $k=0$, reflecting increased hysteresis in the separation and reattachment process. The sum of the positive and negative terms is held constant (at 3.0) above $k = 0.6$, since no data were obtained to justify any other value.

$$A_{p,k} = 6.6 k, \quad 0 \leq k \leq 0.6$$

$$A_{p,k} = 3.0 + \pi k/2, \quad k > 0.6$$

The Mach number term ($A_{p,M}$) is constant below $M = 0.4$, and drops linearly to 50% of its original value at $M = 0.6$. This term is included because compressibility has been found to reduce the hysteresis associated with unsteady separation. Above $M = 0.6$ the term is constant, since no data were obtained.

$$A_{p,M} = 1.0, \quad M \leq 0.4$$

$$A_{p,M} = 2.0 - 2.5 M, \quad 0.4 < M < 0.6$$

$$A_{p,M} = 0.5, \quad M \geq 0.6$$

The amplitude term (A_{p,α_1}) starts at zero when $\alpha_1 = 0$, and builds as a cosine function to a value of 1 at $\alpha_1 = 1^\circ$. This represents the need for finite amplitude to initiate the hysteresis necessary for negative damping. At higher amplitude the negative damping is also reduced, since the conditions for maximum hysteresis (attached flow during the increasing pitch half of the cycle and separated flow during the decreasing pitch half) cannot be maintained at high amplitude. This is represented by an exponential square decay, reaching a value of 0.2 at $\alpha_1 = 6^\circ$.

$$A_{p,\alpha_1} = 0.5(1 - \cos(\pi\alpha_1)), \quad \alpha_1 \leq 1^\circ$$

$$A_{p,\alpha_1} = \exp(-0.25(\alpha_1 - 1)^2), \quad \alpha_1 > 1^\circ$$

The characteristics of the damping function are illustrated in the following figures. Figure 1 shows damping as a function of mean angle at several different frequencies. All cases are for an amplitude of 1° and a Mach number of 0.2. The steady stall angle for these conditions is 16.5° . The damping in both attached and fully separated flows increases with frequency, but is constant with mean angle. The negative damping peak is centered about α_{ss} at low frequency, but is increasingly delayed at higher frequency (by the α_{ss} term). The magnitude of the negative peak increases until $k = 0.6$, and is constant thereafter. The width of the peak is constant at $\pm 1^\circ$ (α_1).

Figure 2 shows the effect of amplitude at constant frequency and Mach number. At the lowest amplitude ($\alpha_1 = 0.25^\circ$) the peak is narrow and weak. Both the width and magnitude increase until $\alpha_1 = 1^\circ$. At higher amplitudes the magnitudes are slowly reduced. The damping is always positive at for $\alpha_1 > 6^\circ$.

Figure 3 shows the effect of Mach number at constant frequency and amplitude. The attached damping shows an increased value at $M = 0.6$, while the fully separated values are the same at all Mach numbers. The width of the negative peak is the same at all Mach numbers, while the magnitude is reduced at $M = 0.6$. The reduction in the mean angle at the peak is a result of the effect of Mach number on the steady stall angle.

Figure 4 emphasizes the effect of frequency by plotting damping vs. k at several different mean angles. Amplitude and Mach number are fixed. At $\alpha_0 = 12^\circ$ and 14° the damping follows the attached flow ($\pi k/2$) line. At $\alpha_0 = 16^\circ$ there is a slight reduction at low frequency, and at $\alpha_0 = 16.5^\circ$ (α_{ss}) there is negative damping for $k \leq 0.3$. At $\alpha_0 = 18^\circ$ there is strong negative damping between $k = 0.3$ and 0.7 (a result of the increase in α_{ss} above α_{ss}). At $\alpha_0 = 20^\circ$ the flow is fully separated over this range of frequency, and there is a linear increase in positive damping at a slope greater than $\pi/2$.

Figure 5 shows a plot of damping vs. amplitude at several mean angles, for fixed frequency and Mach number. At $\alpha_0 = 16$ and 16.5° the damping starts out positive, and becomes negative at amplitudes of $1-2^\circ$, reaches peak negative values between $\alpha_1 = 2$ and 3° , and returns to positive near $\alpha_1 = 6^\circ$. Similar behavior occurs at $\alpha_1 = 18^\circ$, except that the initial positive damping is higher because the steady flow is separated. For mean angles outside of this range, the damping remains positive.

References

- 1) Lorber, P.F. and Carta, F.O., "Incipient Torsional Stall Flutter Experiments on a Swept Three-Dimensional Wing," AIAA Paper 91-0935, 32nd Structures, Structural Dynamics, and Materials Conference, Baltimore MD, April 1991.

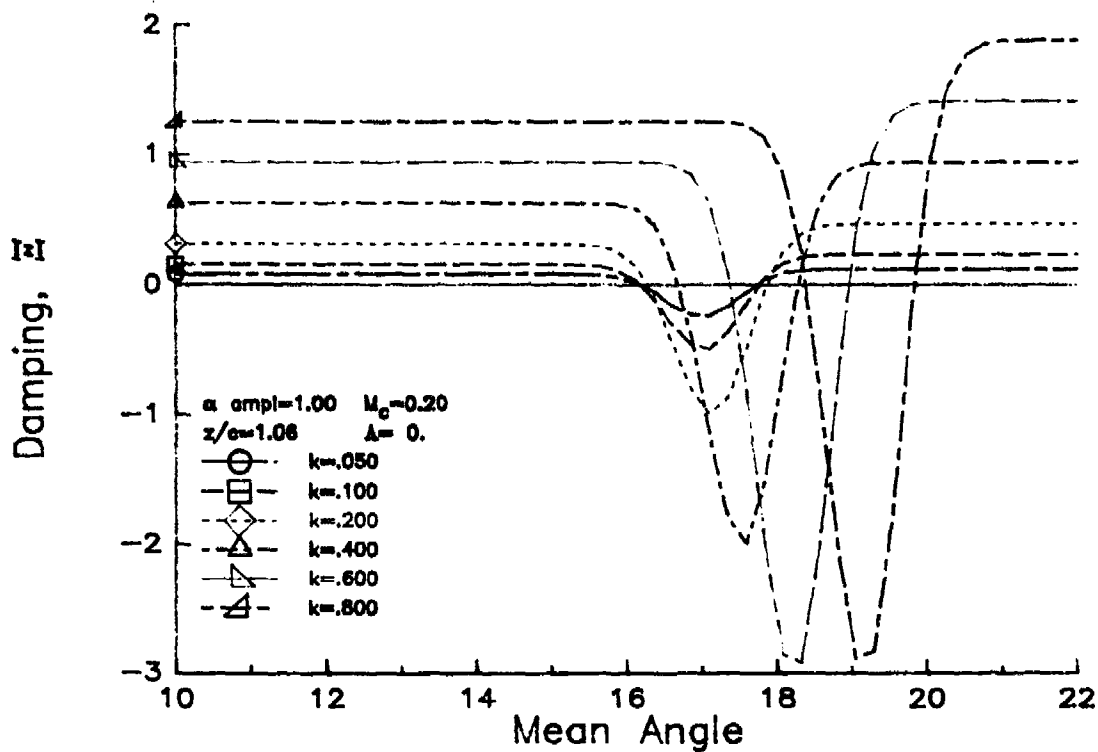


Figure 1. Frequency effect on empirical damping function.

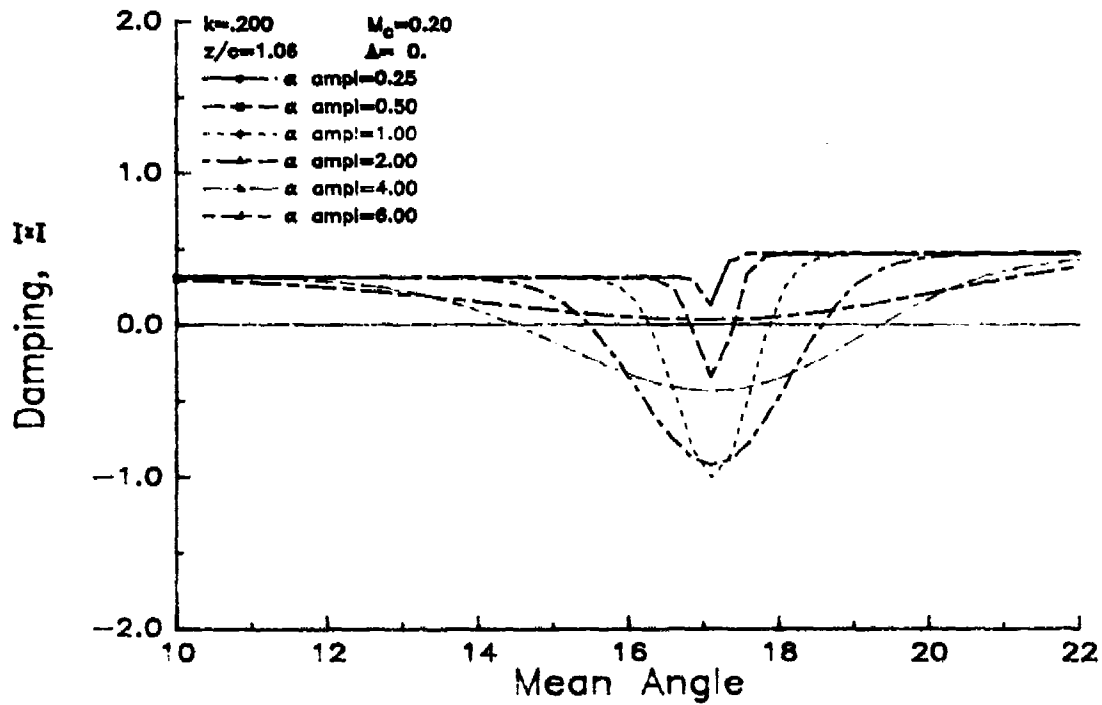


Figure 2. Amplitude effect on empirical damping function.

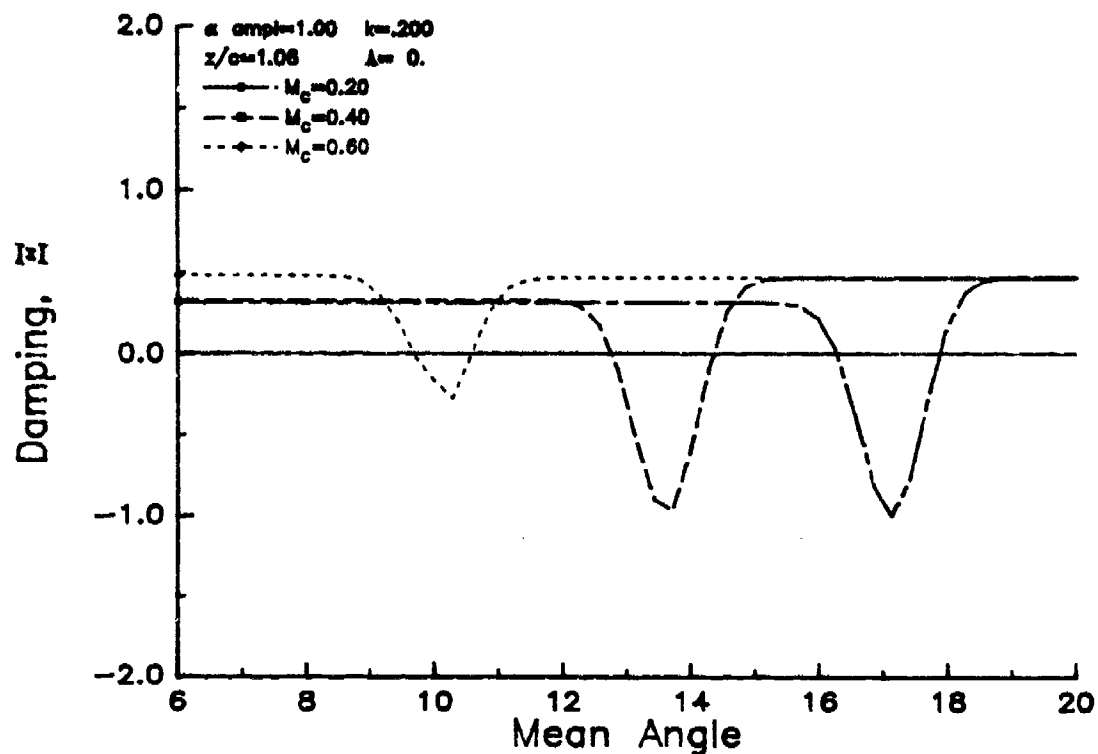


Figure 3. Mach number effect on empirical damping function.

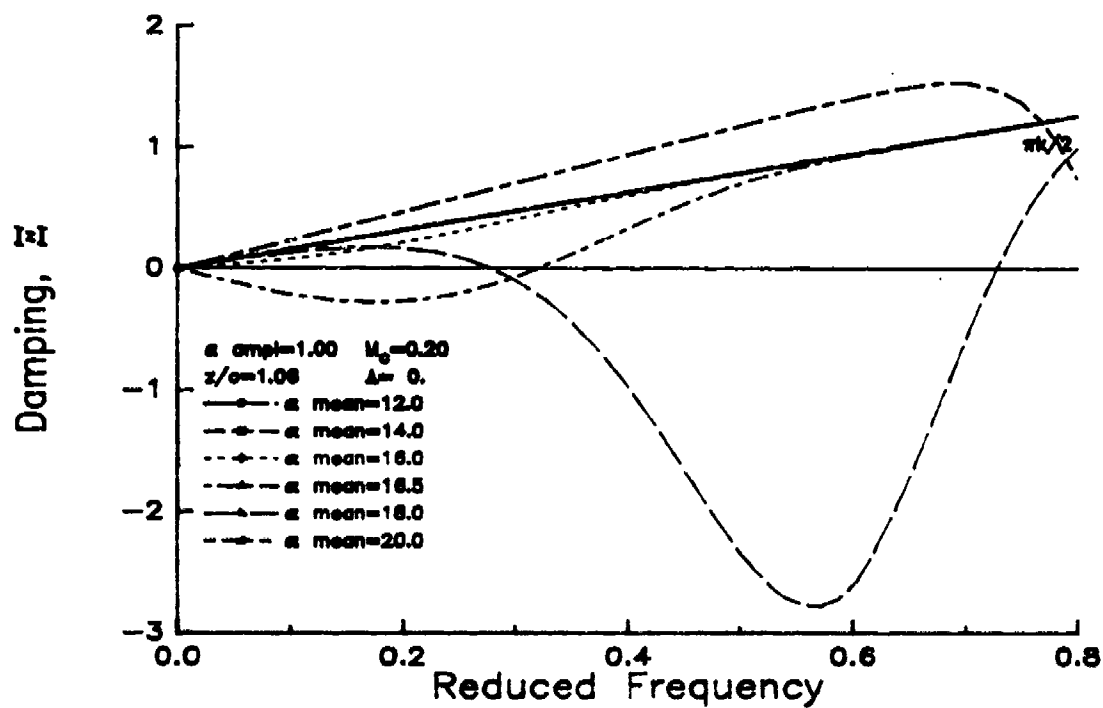


Figure 4. Frequency dependence at several mean angles.

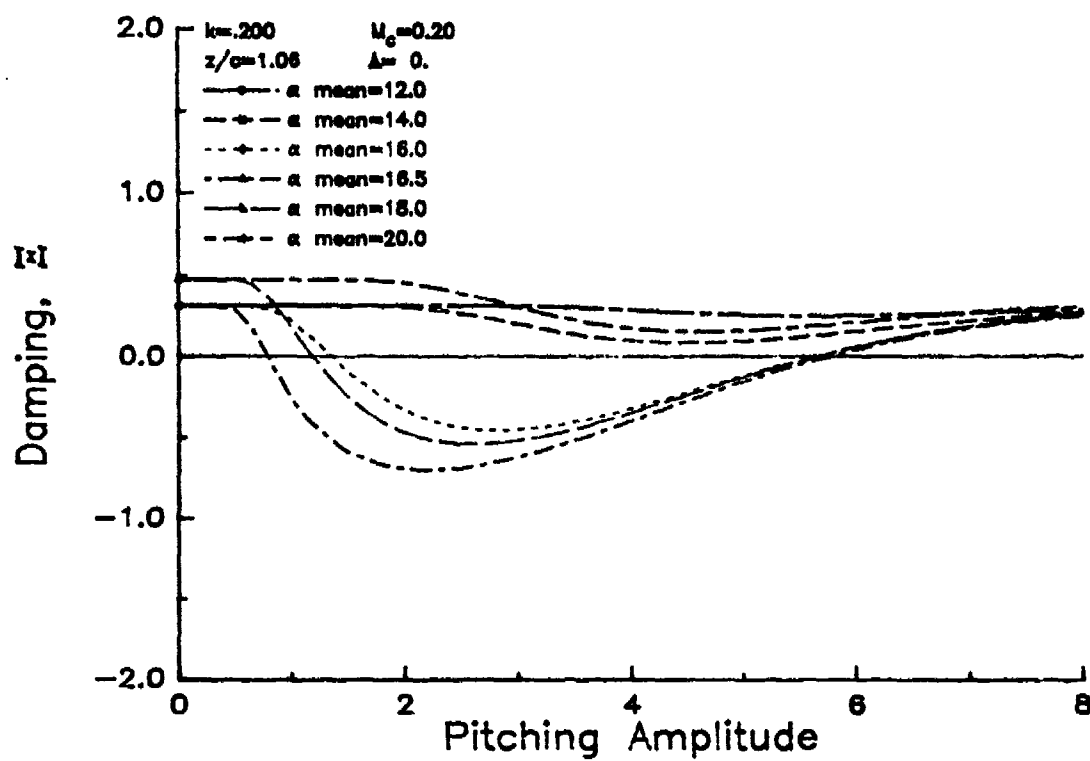


Figure 5. Amplitude dependence at several mean angles.

TABLE X-1
EXPERIMENTAL DAMPING COEFFICIENTS

Run	Λ	M_c	k	α_0	α_1	A_{max}	Damping Coefficient, Ξ @ $z/c=$				
							0.08	0.30	0.59	1.06	1.52
37.09	0.	.201	.200	10.0	1.00	0.0035	0.184	0.241	0.268	0.295	0.298
37.11	0.	.198	.205	12.1	1.01	0.0036	0.218	0.273	0.280	0.318	0.311
37.12	0.	.196	.205	14.0	1.00	0.0036	0.208	0.235	0.275	0.320	0.311
37.13	0.	.196	.205	15.0	1.00	0.0036	0.197	0.263	0.284	0.316	0.334
37.14	0.	.196	.205	16.0	1.00	0.0036	0.180	0.278	0.282	0.325	0.312
37.22	0.	.201	.199	16.6	1.00	0.0035	0.308	0.302	0.187	-0.295	0.617
37.16	0.	.201	.200	17.0	1.01	0.0035	0.243	0.293	0.294	0.031	0.680
37.17	0.	.196	.205	18.0	1.01	0.0036	0.303	0.305	0.247	0.162	1.343
37.18	0.	.201	.200	20.0	1.01	0.0035	0.377	0.133	0.640	0.669	1.133
37.19	0.	.200	.204	22.0	1.01	0.0036	0.190	-0.344	0.621	0.942	0.945
37.20	0.	.199	.204	24.0	1.01	0.0036	0.908	0.563	0.501	0.416	0.360
37.21	0.	.196	.204	26.0	1.00	0.0036	0.800	0.550	0.449	0.331	0.536
37.23	0.	.201	.200	12.0	1.98	0.0069	0.202	0.263	0.265	0.299	0.293
37.24	0.	.199	.200	14.0	1.98	0.0069	0.186	0.240	0.266	0.303	0.301
37.25	0.	.201	.200	16.0	1.98	0.0069	0.128	0.217	0.177	-0.224	-0.881
37.55	0.	.201	.198	16.6	1.95	0.0068	0.210	0.249	0.136	-0.570	-0.719
37.26	0.	.196	.204	18.0	1.96	0.0070	0.285	0.289	0.079	0.050	0.992
37.27	0.	.201	.200	20.0	1.95	0.0068	0.227	-0.261	0.253	0.991	1.138
37.29	0.	.201	.199	12.1	0.48	0.0017	0.210	0.268	0.279	0.307	0.314
37.30	0.	.201	.199	14.0	0.49	0.0017	0.188	0.241	0.283	0.311	0.326
37.31	0.	.198	.200	16.0	0.49	0.0017	0.183	0.296	0.286	0.316	0.324
37.32	0.	.196	.204	16.5	0.54	0.0019	0.284	0.381	0.094	0.232	0.015
37.33	0.	.201	.199	17.0	0.54	0.0019	0.273	0.266	0.290	-0.004	0.795
37.34	0.	.196	.204	18.0	0.54	0.0019	0.416	0.275	0.120	0.038	1.228
37.35	0.	.196	.204	20.0	0.48	0.0017	0.261	-0.420	0.831	1.109	0.951
37.56	0.	.196	.100	14.1	0.51	0.0009	0.093	0.123	0.147	0.168	0.179
37.57	0.	.201	.098	16.5	0.52	0.0009	0.133	0.118	0.141	0.196	0.219
37.58	0.	.201	.097	18.0	0.49	0.0008	0.169	0.126	0.080	0.241	0.536
38.03	0.	.196	.101	14.0	1.03	0.0018	0.079	0.129	0.133	0.157	0.165
38.04	0.	.201	.098	16.6	0.99	0.0017	0.145	0.087	0.089	0.196	0.138
38.05	0.	.196	.101	18.0	1.02	0.0018	0.180	0.136	-0.015	0.174	0.620
38.06	0.	.196	.101	14.0	1.99	0.0035	0.099	0.131	0.139	0.155	0.164
38.07	0.	.200	.098	16.6	1.97	0.0034	0.238	0.099	-0.116	-0.749	-1.110
38.09	0.	.201	.300	14.1	0.49	0.0025	0.301	0.409	0.417	0.479	0.472
38.10	0.	.201	.300	16.5	0.47	0.0025	0.286	0.403	0.410	0.060	0.361
38.11	0.	.196	.307	18.0	0.45	0.0024	0.328	0.438	0.229	0.094	1.570
38.32	0.	.196	.298	14.0	0.98	0.0051	0.362	0.439	0.448	0.496	0.481
38.33	0.	.201	.291	16.6	1.04	0.0053	0.319	0.388	0.361	-0.499	0.530
38.34	0.	.199	.298	18.0	1.07	0.0056	0.370	0.386	0.343	0.053	1.310
38.15	0.	.196	.307	14.0	1.98	0.0106	0.327	0.408	0.422	0.466	0.467
38.16	0.	.201	.300	16.6	1.97	0.0103	0.206	0.330	0.170	-0.407	-0.324
38.17	0.	.201	.300	18.0	1.95	0.0102	0.294	0.327	0.251	-0.316	0.799
38.19	0.	.201	.390	14.0	0.47	0.0032	0.504	0.589	0.583	0.644	0.694
38.20	0.	.200	.400	16.5	0.45	0.0031	0.441	0.695	0.635	0.026	0.580
38.21	0.	.201	.390	18.1	0.49	0.0033	0.351	0.471	0.359	0.189	1.617
38.29	0.	.196	.409	14.0	1.03	0.0073	0.622	0.679	0.702	0.758	0.653

EXPERIMENTAL DAMPING COEFFICIENTS

Run	A	M _c	k	α_0	α_1	A _{max}	Damping Coefficient, Σ @z/cm				
							0.08	0.30	0.59	1.06	1.52
38.30	0.	.203	.399	16.6	1.03	0.0072	0.298	0.605	0.386	-0.062	0.047
38.31	0.	.196	.409	18.0	1.00	0.0071	0.197	0.704	0.565	0.118	0.937
38.25	0.	.201	.390	14.1	1.99	0.0135	0.569	0.625	0.646	0.707	0.674
38.26	0.	.210	.365	16.5	1.99	0.0127	0.430	0.487	0.338	-0.290	-0.606
38.27	0.	.196	.400	18.1	1.98	0.0138	0.254	0.243	0.111	-0.774	-1.132
38.35	0.	.196	.600	14.0	0.47	0.0049	0.947	1.227	1.254	1.361	1.447
38.36	0.	.196	.600	16.5	0.51	0.0053	0.779	1.001	0.916	0.001	-2.977
38.37	0.	.201	.585	18.0	0.51	0.0052	0.698	1.016	0.777	-0.543	-5.805
38.38	0.	.197	.585	14.0	1.00	0.0102	0.983	1.191	1.190	1.247	1.294
38.39	0.	.201	.599	16.6	1.00	0.0104	0.754	1.118	1.006	0.459	-1.382
38.40	0.	.196	.599	18.1	1.02	0.0107	0.764	1.155	0.919	0.213	-3.089
38.42	0.	.402	.101	10.1	1.02	0.0018	0.080	0.140	0.153	0.196	0.189
38.43	0.	.403	.101	11.1	1.01	0.0018	0.080	0.151	0.168	0.219	0.245
38.44	0.	.399	.101	12.1	1.01	0.0018	0.137	0.174	0.206	0.225	0.209
38.45	0.	.399	.102	13.0	1.00	0.0018	0.197	0.190	0.221	0.030	-0.176
38.46	0.	.402	.101	14.0	0.97	0.0017	0.298	0.218	0.102	-0.289	-0.968
38.47	0.	.398	.101	15.0	0.96	0.0017	0.299	0.218	0.033	0.177	0.367
38.48	0.	.398	.101	16.0	1.00	0.0018	0.326	0.183	-0.083	0.251	0.642
38.49	0.	.399	.101	17.0	1.00	0.0018	0.363	0.006	-0.057	0.366	0.327
38.50	0.	.402	.100	18.0	1.01	0.0018	0.387	-0.182	-0.192	0.352	0.482
38.55	0.	.402	.100	12.1	0.47	0.0008	0.193	0.207	0.238	0.300	0.354
38.56	0.	.400	.100	14.1	0.51	0.0009	0.318	0.211	0.172	0.056	-0.311
38.57	0.	.401	.101	16.0	0.48	0.0008	0.490	0.341	0.137	0.622	0.769
38.58	0.	.400	.100	18.0	0.41	0.0007	0.354	-0.444	-0.223	0.155	0.498
38.51	0.	.399	.102	12.0	2.02	0.0036	0.152	0.171	0.190	0.133	0.090
38.52	0.	.402	.101	14.0	2.01	0.0035	0.275	0.198	0.126	0.012	-0.554
38.53	0.	.404	.100	16.0	1.98	0.0035	0.332	0.138	-0.008	0.214	0.392
39.06	0.	.399	.250	12.1	0.46	0.0020	0.569	0.548	0.612	0.539	0.612
39.07	0.	.401	.250	14.0	0.43	0.0019	0.637	0.481	0.214	-0.862	-0.783
39.08	0.	.399	.248	16.0	0.42	0.0018	0.872	0.467	-0.337	0.116	1.534
39.09	0.	.405	.246	12.1	1.00	0.0043	0.393	0.498	0.529	0.442	0.436
39.10	0.	.402	.246	14.0	0.98	0.0042	0.574	0.478	0.138	-0.739	-0.746
39.11	0.	.404	.246	16.0	0.99	0.0043	0.643	0.318	-0.51	-0.086	0.627
39.12	0.	.402	.248	12.1	1.98	0.0085	0.429	0.512	0.164	0.231	0.195
39.13	0.	.402	.248	14.0	1.97	0.0085	0.559	0.488	0.152	-0.184	-0.331
39.14	0.	.404	.246	16.0	1.96	0.0084	0.681	0.350	0.146	0.020	0.212
39.17	0.	.604	.100	6.1	1.01	0.0018	0.105	0.225	0.260	0.277	0.302
39.18	0.	.604	.100	7.1	0.98	0.0017	0.117	0.235	0.270	0.324	0.328
39.19	0.	.603	.100	8.0	0.96	0.0017	0.161	0.247	0.280	0.309	0.286
39.20	0.	.601	.100	9.0	0.95	0.0016	0.159	0.241	0.300	0.236	0.248
39.21	0.	.604	.100	10.1	0.91	0.0016	0.198	0.255	0.239	0.154	-0.240
39.22	0.	.605	.100	6.0	0.40	0.0007	0.154	0.228	0.246	0.267	0.317
39.23	0.	.605	.100	8.0	0.44	0.0008	0.144	0.214	0.255	0.322	0.235
39.24	0.	.601	.100	10.0	0.37	0.0007	0.039	0.141	0.174	-0.113	-0.997
39.25	0.	.605	.100	6.1	2.03	0.0035	0.197	0.287	0.242	0.275	0.290
39.26	0.	.600	.101	8.1	2.02	0.0035	0.169	0.259	0.257	0.275	0.266

EXPERIMENTAL DAMPING COEFFICIENTS

Run	Λ	M_c	k	α_0	α_1	A_{max}	Damping Coefficient, Ξ @ $z/c=$				
							0.08	0.30	0.59	1.06	1.52
39.27	0.	.603	.201	6.1	0.49	0.0017	0.502	0.747	0.816	0.963	1.064
39.28	0.	.604	.201	8.0	0.42	0.0015	0.432	0.672	0.779	0.873	0.708
39.29	0.	.603	.201	10.0	0.47	0.0017	0.451	0.406	0.506	0.431	-0.512
39.30	0.	.605	.200	6.1	0.97	0.0034	0.464	0.721	0.746	0.864	0.940
39.31	0.	.603	.201	8.0	0.97	0.0034	0.428	0.678	0.764	0.778	0.663
39.32	0.	.602	.201	10.1	0.96	0.0034	0.525	0.521	0.549	0.240	-0.123
31.43	0.	.196	.100	8.1	6.01	0.0105	0.079	0.122	0.136	0.154	0.150
31.44	0.	.197	.100	10.0	6.01	0.0105	0.072	0.128	0.138	0.155	0.154
31.45	0.	.196	.100	12.0	6.00	0.0105	0.091	0.138	0.120	-0.057	-0.110
31.46	0.	.201	.099	14.0	5.97	0.0103	0.171	0.076	-0.099	-0.202	-0.153
31.47	0.	.196	.101	16.0	5.96	0.0105	0.219	-0.143	-0.240	-0.134	-0.129
31.48	0.	.201	.099	18.0	5.95	0.0103	0.292	-0.203	-0.306	-0.192	-0.038
31.49	0.	.196	.101	20.1	5.95	0.0105	0.449	-0.238	-0.256	0.025	0.210
31.50	0.	.201	.096	22.0	5.96	0.0100	0.623	0.231	0.347	0.527	0.608
31.51	0.	.201	.099	24.0	5.97	0.0103	0.742	0.427	0.638	0.492	0.578
39.03	0.	.402	.101	6.0	6.03	0.0106	0.083	0.134	0.149	0.167	0.169
39.04	0.	.397	.101	12.0	6.04	0.0106	0.167	0.140	0.076	0.055	0.128
39.05	0.	.405	.099	14.0	6.04	0.0105	0.215	0.101	0.056	0.146	0.111
35.21	0.	.601	.025	4.1	4.00	0.0017	0.021	0.044	0.055	0.061	0.060
35.22	0.	.603	.025	5.0	4.95	0.0021	0.026	0.045	0.052	0.058	0.059
35.23	0.	.602	.025	6.1	6.02	0.0026	0.028	0.042	0.051	0.049	0.045
35.26	0.	.602	.050	4.1	4.00	0.0035	0.056	0.097	0.110	0.128	0.128
35.27	0.	.602	.050	5.0	4.96	0.0044	0.059	0.097	0.112	0.120	0.122
35.28	0.	.605	.075	4.0	3.89	0.0051	0.088	0.146	0.178	0.183	0.202
35.29	0.	.598	.076	5.0	4.83	0.0064	0.068	0.141	0.178	0.199	0.195
43.20	15.	.199	.200	10.1	0.99	0.0035	0.165	0.244	0.263	0.296	0.305
43.21	15.	.199	.200	12.1	0.98	0.0034	0.186	0.245	0.268	0.307	0.335
43.22	15.	.199	.200	14.0	0.99	0.0035	0.192	0.248	0.276	0.311	0.304
43.23	15.	.199	.200	15.1	0.98	0.0034	0.204	0.259	0.289	0.329	0.350
43.24	15.	.199	.200	16.1	0.99	0.0034	0.235	0.263	0.278	0.311	0.332
43.25	15.	.199	.200	17.1	0.99	0.0035	0.228	0.260	0.287	0.217	0.260
43.26	15.	.199	.200	18.0	0.97	0.0034	0.094	-0.538	-0.585	-0.302	0.242
43.27	15.	.199	.200	19.1	0.97	0.0034	-0.277	-0.904	-0.712	-0.036	0.480
43.28	15.	.201	.200	20.1	0.98	0.0034	-0.153	-0.317	0.036	0.162	0.571
43.29	15.	.196	.200	22.1	0.98	0.0034	0.734	0.706	0.645	0.970	0.777
43.30	15.	.199	.200	24.0	0.97	0.0034	0.485	0.463	0.397	0.586	0.698
43.09	15.	.399	.075	10.0	0.98	0.0013	0.061	0.108	0.116	0.137	0.139
43.10	15.	.400	.076	11.0	0.98	0.0013	0.064	0.107	0.141	0.162	0.156
43.11	15.	.403	.075	12.0	0.99	0.0013	0.107	0.145	0.198	0.213	0.193
43.12	15.	.405	.075	13.0	0.98	0.0013	0.154	0.157	0.165	0.124	0.122
43.13	15.	.400	.075	14.0	0.95	0.0012	0.196	0.021	-0.122	-0.223	-0.241
43.14	15.	.400	.075	15.0	0.94	0.0012	0.024	-0.211	-0.245	-0.263	-0.573
43.15	15.	.402	.075	16.0	0.94	0.0012	0.036	-0.032	0.071	0.117	-0.072
43.16	15.	.400	.075	17.0	0.94	0.0012	0.085	0.026	0.180	0.123	0.259
43.17	15.	.405	.074	18.0	0.95	0.0012	-0.106	-0.137	0.065	0.117	0.336
43.18	15.	.403	.074	19.0	0.95	0.0012	-0.226	-0.209	-0.016	0.264	0.402

EXPERIMENTAL DAMPING COEFFICIENTS

Run	Λ	M_c	k	α_0	α_1	A_{max}	Damping Coefficient, Ξ @ $z/c=$				
							0.08	0.30	0.59	1.06	1.52
48.20	30.	.199	.200	10.1	1.01	0.0035	0.137	0.240	0.277	0.295	0.295
48.21	30.	.199	.200	12.1	1.02	0.0035	0.143	0.232	0.275	0.301	0.325
48.22	30.	.199	.200	14.1	1.02	0.0036	0.146	0.245	0.283	0.308	0.281
48.23	30.	.199	.200	16.0	1.02	0.0036	0.162	0.243	0.283	0.266	0.282
48.24	30.	.197	.204	17.0	1.01	0.0036	0.158	0.171	0.173	0.136	0.246
48.34	30.	.195	.204	17.6	0.98	0.0035	-1.129	-2.077	-1.930	-0.367	0.095
48.25	30.	.199	.200	18.0	1.01	0.0035	-0.836	-0.943	-0.626	-1.336	-1.874
48.35	30.	.199	.200	18.6	0.96	0.0034	-0.401	-0.555	-0.343	-0.795	-1.682
48.26	30.	.198	.200	19.1	1.00	0.0035	-0.449	-0.369	-0.043	-0.514	-1.459
48.36	30.	.199	.200	19.6	0.96	0.0033	0.082	0.165	0.438	0.499	-0.319
48.27	30.	.199	.200	20.0	1.02	0.0035	0.173	0.301	0.314	0.071	-0.509
48.28	30.	.199	.200	21.0	1.02	0.0036	0.473	0.635	0.553	0.742	0.448
48.29	30.	.199	.200	22.1	1.02	0.0036	0.258	0.392	0.472	0.578	0.613
48.30	30.	.201	.200	24.0	0.99	0.0035	0.280	0.315	0.401	0.538	0.645
48.31	30.	.195	.204	26.0	1.00	0.0035	0.178	0.261	0.299	0.456	0.525
48.32	30.	.199	.200	28.0	1.00	0.0035	0.150	0.321	0.293	0.262	0.491
48.37	30.	.203	.147	8.0	6.04	0.0155	0.094	0.168	0.190	0.205	0.194
48.38	30.	.199	.150	10.1	6.05	0.0158	0.099	0.176	0.202	0.219	0.207
48.39	30.	.199	.150	12.1	6.04	0.0158	0.103	0.173	0.199	0.211	0.206
48.40	30.	.199	.150	14.1	6.03	0.0158	-0.221	-0.404	-0.424	-0.279	0.005
48.41	30.	.196	.150	16.1	6.02	0.0157	-0.339	-0.517	-0.564	-0.685	-0.570
48.42	30.	.199	.150	18.1	6.01	0.0157	-0.275	-0.449	-0.468	-0.576	-0.787
48.43	30.	.199	.150	20.0	6.00	0.0157	-0.129	-0.301	-0.281	-0.374	-0.735
48.44	30.	.202	.150	22.1	5.99	0.0157	0.073	0.050	0.172	0.168	-0.335
48.45	30.	.199	.150	24.0	5.99	0.0157	0.192	0.371	0.479	0.462	0.414
52.11	30.	.199	.201	12.0	2.02	0.0071	0.138	0.238	0.268	0.305	0.265
52.12	30.	.199	.201	14.0	2.02	0.0071	0.147	0.238	0.265	0.290	0.291
52.13	30.	.202	.197	16.0	2.02	0.0070	0.093	0.049	0.116	0.246	0.287
52.19	30.	.199	.201	16.5	2.02	0.0071	-0.224	-0.575	-0.428	0.146	0.238
52.14	30.	.199	.201	17.0	2.02	0.0071	-0.720	-1.282	-1.542	-1.407	-0.945
52.15	30.	.199	.201	18.0	2.01	0.0071	-0.357	-0.456	-0.395	-0.692	-1.112
52.16	30.	.199	.201	19.0	2.00	0.0070	-0.301	-0.171	0.010	-0.266	-1.058
52.17	30.	.199	.201	20.0	2.01	0.0070	0.026	0.199	0.456	0.322	-0.207
52.18	30.	.203	.197	22.0	1.99	0.0069	0.236	0.362	0.468	0.620	0.589
52.20	30.	.202	.201	12.0	0.52	0.0018	0.156	0.244	0.271	0.305	0.280
52.21	30.	.200	.201	14.0	0.53	0.0019	0.152	0.224	0.248	0.305	0.305
52.22	30.	.199	.201	16.0	0.56	0.0020	0.159	0.179	0.196	0.225	0.237
52.23	30.	.195	.205	17.0	0.63	0.0023	-0.038	-0.311	-0.187	0.139	0.177
52.24	30.	.199	.201	17.5	0.55	0.0019	-0.122	0.455	0.605	-0.230	-0.691
52.25	30.	.201	.201	18.0	0.45	0.0016	0.184	0.955	1.112	-0.398	-0.247
52.26	30.	.199	.201	18.5	0.49	0.0017	0.091	0.930	0.622	-0.036	-0.391
52.27	30.	.199	.201	19.0	0.52	0.0018	0.057	0.365	0.628	0.019	-0.394
52.28	30.	.196	.205	20.0	0.50	0.0018	0.197	0.313	0.547	0.540	0.294
52.30	30.	.203	.100	16.0	0.49	0.0009	0.097	0.123	0.127	0.134	0.168
52.31	30.	.206	.099	18.0	0.43	0.0007	-0.008	0.296	0.347	-0.552	-0.864
52.32	30.	.199	.102	20.0	0.42	0.0008	0.335	0.382	0.649	0.942	0.554

EXPERIMENTAL DAMPING COEFFICIENTS

Run	Λ	M_c	k	α_0	α_1	A_{max}	Damping Coefficient, Ξ @ $z/c=$				
							0.08	0.30	0.59	1.06	1.52
52.33	30.	.199	.102	16.0	1.03	0.0018	0.089	0.113	0.120	0.123	0.157
52.34	30.	.199	.102	18.0	1.01	0.0018	-0.088	0.097	0.152	-0.299	-0.434
52.35	30.	.198	.102	20.1	1.01	0.0018	0.307	0.549	0.755	0.931	0.655
52.36	30.	.197	.102	16.0	2.03	0.0036	0.001	-0.104	-0.036	0.120	0.148
52.37	30.	.199	.102	18.0	2.02	0.0036	-0.163	-0.075	0.082	-0.226	-0.572
52.38	30.	.199	.102	20.0	2.02	0.0036	0.219	0.444	0.692	0.751	0.461
52.39	30.	.203	.299	16.1	0.48	0.0025	0.248	0.366	0.378	0.411	0.423
52.40	30.	.199	.304	18.0	0.47	0.0025	0.195	0.522	0.621	0.440	-0.062
52.41	30.	.199	.304	20.0	0.46	0.0024	0.246	0.312	0.401	0.394	0.017
52.43	30.	.199	.302	16.1	1.05	0.0055	0.234	0.320	0.342	0.305	0.380
52.44	30.	.199	.302	18.0	1.07	0.0056	-0.434	-0.711	-0.678	-0.867	-1.088
52.45	30.	.199	.302	20.1	1.06	0.0056	0.100	0.166	0.089	0.177	-0.448
52.46	30.	.195	.307	16.0	1.97	0.0106	0.244	0.356	0.388	0.424	0.435
52.47	30.	.199	.302	18.1	1.97	0.0104	-0.607	-1.143	-1.405	-1.659	-0.834
52.48	30.	.202	.296	20.0	1.97	0.0102	0.039	0.121	0.169	-0.474	-1.166
52.49	30.	.201	.301	17.1	1.00	0.0052	0.195	0.232	0.229	0.245	0.363
52.50	30.	.203	.296	19.1	0.99	0.0051	-0.271	-0.569	-0.283	-0.646	-1.150
52.51	30.	.201	.296	18.5	0.98	0.0051	-0.410	-0.516	-0.532	-0.847	-1.143
52.52	30.	.199	.301	17.5	0.97	0.0051	-0.275	-0.727	-0.621	-0.050	0.280
52.53	30.	.199	.400	16.1	0.49	0.0034	0.355	0.510	0.547	0.474	0.559
52.54	30.	.199	.502	16.1	0.47	0.0041	0.447	0.679	0.724	0.678	0.834
52.55	30.	.199	.502	18.0	0.47	0.0041	0.751	1.184	0.370	0.271	0.585
52.56	30.	.201	.502	20.0	0.46	0.0040	-0.636	-0.722	-0.063	0.010	-0.162
52.57	30.	.203	.493	16.0	1.01	0.0087	0.473	0.690	0.727	0.710	0.827
52.58	30.	.199	.502	17.0	1.02	0.0089	0.459	0.743	0.700	0.704	0.839
52.59	30.	.199	.502	18.1	1.11	0.0097	-0.693	-0.992	-0.921	-0.681	-0.696
52.60	30.	.203	.492	19.0	0.93	0.0080	0.003	0.135	0.041	-0.333	-0.771
52.61	30.	.195	.511	20.1	0.88	0.0079	0.367	0.642	0.526	0.656	-0.014
52.62	30.	.199	.501	16.1	1.91	0.0167	0.548	0.766	0.773	0.800	0.871
52.63	30.	.199	.502	18.0	1.96	0.0172	-0.064	-0.222	-0.360	-0.548	0.283
52.64	30.	.199	.502	20.0	1.96	0.0171	-0.583	-0.506	-0.538	-1.068	-1.457
52.66	30.	.199	.600	16.1	0.48	0.0051	0.832	1.151	1.148	1.169	1.355
52.67	30.	.206	.579	18.1	0.46	0.0047	-1.699	-1.095	-1.148	-0.641	-0.183
52.68	30.	.199	.600	20.0	0.48	0.0051	0.669	0.860	0.516	-0.117	-0.427
52.69	30.	.203	.589	19.0	0.51	0.0052	-0.230	-0.361	-0.103	-0.692	-1.213
52.70	30.	.197	.600	17.0	0.40	0.0042	1.129	1.670	1.626	1.456	1.571
52.71	30.	.201	.600	16.0	1.05	0.0110	0.923	1.261	1.241	1.307	1.433
52.72	30.	.199	.600	17.1	1.08	0.0113	0.946	1.345	1.241	1.192	1.356
52.73	30.	.199	.600	18.1	1.08	0.0114	-0.632	-1.172	-1.365	-0.222	-0.034
52.74	30.	.200	.589	19.0	1.01	0.0104	-0.482	-0.401	-0.734	-0.918	-0.384
52.75	30.	.203	.588	20.1	1.01	0.0103	-0.025	0.482	0.136	-0.534	-0.719
52.76	30.	.199	.599	21.0	1.00	0.0104	0.225	0.810	0.915	-0.068	-0.521
52.77	30.	.199	.599	22.0	1.00	0.0105	0.799	1.571	1.395	0.613	0.024
52.78	30.	.199	.599	23.0	1.02	0.0106	1.055	1.651	1.598	0.867	0.261
50.30	30.	.403	.099	10.1	1.01	0.0018	0.075	0.151	0.177	0.202	0.153
50.31	30.	.402	.100	11.1	1.03	0.0018	0.084	0.175	0.239	0.222	0.180

EXPERIMENTAL DAMPING COEFFICIENTS

Run	Λ	M_c	k	α_0	α_1	A_{max}	Damping Coefficient, Ξ @ $z/c=$				
							0.08	0.30	0.59	1.06	1.52
50.32	30.	.400	.100	12.1	1.02	0.0018	0.097	0.184	0.227	0.210	0.188
50.33	30.	.402	.099	13.1	1.02	0.0018	0.050	0.067	0.023	0.103	0.122
50.34	30.	.396	.101	14.1	1.00	0.0018	-0.033	-0.052	-0.109	-0.103	-0.061
50.35	30.	.402	.099	15.2	0.98	0.0017	-0.101	-0.113	-0.076	-0.261	-0.272
50.36	30.	.402	.100	16.1	0.95	0.0017	-0.160	-0.122	-0.062	-0.094	-0.051
50.37	30.	.402	.099	17.1	0.94	0.0016	-0.107	-0.033	0.198	0.450	0.103
50.38	30.	.402	.099	18.1	0.96	0.0017	-0.151	-0.026	0.335	0.384	-0.364
50.39	30.	.404	.099	19.2	0.95	0.0016	-0.005	0.092	0.321	0.416	-0.160
50.40	30.	.402	.100	20.1	0.95	0.0017	0.126	0.184	0.459	0.528	0.253
51.48	30.	.402	.099	12.0	0.49	0.0008	0.096	0.187	0.206	0.212	0.117
51.42	30.	.400	.100	13.0	0.48	0.0008	-0.003	-0.048	-0.029	0.071	0.209
51.43	30.	.400	.100	14.0	0.49	0.0009	0.000	0.031	0.050	-0.088	-0.321
51.44	30.	.403	.099	15.0	0.48	0.0008	-0.098	-0.213	-0.324	-0.881	-1.618
51.45	30.	.402	.099	15.9	0.52	0.0009	-0.210	-0.210	-0.026	0.153	-0.431
51.46	30.	.396	.100	17.0	0.57	0.0010	-0.098	-0.112	-0.005	0.207	0.181
51.47	30.	.400	.100	18.0	0.54	0.0009	0.152	0.188	0.418	0.330	0.279
51.49	30.	.400	.100	13.0	2.01	0.0035	0.028	0.045	0.058	0.024	-0.058
51.50	30.	.401	.100	15.0	1.96	0.0034	-0.178	-0.248	-0.178	-0.266	-0.617
51.51	30.	.400	.100	17.0	1.95	0.0034	-0.165	-0.145	-0.015	0.184	-0.535
52.02	30.	.401	.250	13.0	0.54	0.0024	-0.176	-0.348	-0.401	0.041	0.388
52.03	30.	.400	.249	15.1	0.49	0.0021	0.068	0.176	-0.171	-2.129	-2.208
52.04	30.	.399	.251	17.0	0.49	0.0021	-0.733	-0.610	-0.621	-0.250	-0.991
52.05	30.	.401	.249	13.1	1.03	0.0045	-0.039	-0.099	-0.114	0.066	0.271
52.06	30.	.402	.250	15.0	0.87	0.0038	-0.156	-0.228	-0.550	-1.536	-1.314
52.07	30.	.402	.249	17.0	0.94	0.0041	-0.541	-0.505	-0.659	-1.008	-1.327
52.09	30.	.408	.246	13.0	1.99	0.0085	0.057	0.056	-0.022	-0.173	-0.175
52.10	30.	.401	.251	15.1	1.97	0.0086	-0.365	-0.389	-0.462	-0.852	-0.704
54.08	30.	.600	.101	6.0	0.50	0.0009	0.141	0.256	0.284	0.337	0.368
54.09	30.	.600	.101	8.1	0.48	0.0009	0.114	0.250	0.267	0.255	0.279
54.10	30.	.598	.101	9.1	0.49	0.0009	-0.221	-0.307	-0.310	-0.114	0.217
54.11	30.	.600	.101	10.1	0.49	0.0009	0.012	0.010	-0.055	-0.318	-0.110
54.12	30.	.598	.101	11.1	0.46	0.0008	0.010	0.151	0.282	-0.235	-1.448
54.14	30.	.596	.101	12.1	0.49	0.0009	0.073	0.164	0.416	0.261	-0.525
54.15	30.	.601	.100	13.0	0.51	0.0009	0.182	0.289	0.420	-0.012	-0.646
54.17	30.	.603	.100	6.1	0.94	0.0016	0.149	0.280	0.323	0.377	0.367
54.18	30.	.604	.100	7.1	0.97	0.0017	0.113	0.252	0.266	0.327	0.311
54.19	30.	.602	.100	8.1	0.97	0.0017	0.073	0.206	0.242	0.255	0.291
54.20	30.	.599	.100	9.1	0.98	0.0017	0.018	-0.021	-0.012	-0.023	0.209
54.21	30.	.600	.100	10.1	0.91	0.0016	0.008	-0.054	-0.095	-0.319	-0.173
54.22	30.	.598	.101	11.1	0.93	0.0016	-0.065	-0.087	-0.165	-0.380	-0.069
54.23	30.	.599	.101	12.1	0.94	0.0016	-0.146	-0.007	-0.089	0.059	-0.392
54.27	30.	.599	.101	13.1	0.98	0.0017	0.040	-0.048	0.109	0.134	-0.303
54.24	30.	.600	.100	6.1	2.00	0.0035	0.125	0.255	0.274	0.312	0.287
54.25	30.	.602	.100	8.1	1.98	0.0035	0.066	0.156	0.186	0.175	0.219
54.26	30.	.600	.100	10.0	2.00	0.0035	-0.016	0.001	-0.011	-0.163	-0.063
54.29	30.	.601	.200	6.0	0.40	0.0014	0.571	1.149	0.998	1.223	1.200

EXPERIMENTAL DAMPING COEFFICIENTS

Run	A	M _c	k	α_0	α_1	A _{max}	Damping Coefficient, Ξ @z/c=				
							0.08	0.30	0.59	1.06	1.52
54.30	30.	.598	.201	8.0	0.47	0.0016	0.406	0.841	0.789	0.977	0.906
54.31	30.	.600	.200	10.0	0.27	0.0010	-0.173	-0.012	-0.563	-1.464	-0.090
54.32	30.	.600	.200	11.0	0.37	0.0013	-0.178	0.045	-0.195	-1.755	-2.628
54.33	30.	.600	.200	12.0	0.54	0.0019	-0.197	0.032	-0.096	-0.799	-1.727
54.34	30.	.598	.200	13.0	0.43	0.0015	-0.253	-0.283	-0.346	-0.133	-0.995
54.35	30.	.604	.199	6.0	0.96	0.0033	0.506	0.966	0.974	1.121	1.058
54.36	30.	.602	.199	7.0	0.94	0.0033	0.485	0.899	0.938	1.125	1.030
54.37	30.	.600	.200	8.1	0.90	0.0031	0.257	0.411	0.449	0.587	0.948
54.38	30.	.600	.200	9.0	0.90	0.0031	0.081	0.125	0.024	-0.108	0.445
54.39	30.	.600	.200	10.0	0.86	0.0030	-0.124	-0.124	-0.391	-0.974	-0.557
54.40	30.	.600	.200	11.0	0.85	0.0030	-0.081	0.084	0.101	-0.190	-1.120
54.41	30.	.600	.199	12.0	0.81	0.0028	-0.054	0.113	0.184	0.035	-1.440
47.45	30.	.202	.099	8.0	6.06	0.0104	0.061	0.110	0.126	0.136	0.127
47.46	30.	.198	.100	10.1	6.06	0.0106	0.064	0.115	0.134	0.144	0.140
47.47	30.	.198	.100	12.0	6.06	0.0106	0.067	0.116	0.136	0.142	0.140
47.48	30.	.196	.102	14.0	6.05	0.0108	-0.135	-0.261	-0.291	-0.241	-0.043
47.49	30.	.198	.100	16.0	6.04	0.0106	-0.210	-0.330	-0.340	-0.462	-0.511
47.50	30.	.198	.100	18.0	6.02	0.0106	-0.160	-0.281	-0.247	-0.313	-0.577
47.51	30.	.198	.102	19.9	6.01	0.0107	-0.086	-0.200	-0.104	-0.182	-0.531
47.52	30.	.198	.100	22.0	6.01	0.0105	0.058	0.111	0.238	0.234	-0.073
47.53	30.	.202	.098	24.0	6.01	0.0103	0.168	0.291	0.383	0.432	0.426
47.36	30.	.198	.050	8.0	6.00	0.0052	0.029	0.055	0.064	0.069	0.065

TABLE X-2
FORTRAN CODE FOR EMPIRICAL DAMPING MODEL

```

FUNCTION EDAMP(M,K,ALO,AL1,ALSS,IFLAG)
*
*   EMPIRICAL DAMPING COEFFICIENT FORMULA
*
*   M = CHORDWISE MACH NUMBER
*   K = REDUCED FREQUENCY (OM C/2U)
*   ALO= MEAN ANGLE (DEG)
*   AL1= AMPLITUDE (DEG)
*   IFLAG=2 TO PRINT DEBUG
*****
*
      REAL  M
      :      ,K
      :      ,M SONIC /0.3/ ;1ST APPEARANCE OF M LOCAL >1
      :      ,ALO
      :      ,AL1
      :      ,ALSS      ;LOCAL STEADY STALL ANGLE
*
      DATA PI /3.1415926535/
*
      IF(IFLAG.EQ.2) WRITE(6,5) M,K,ALO,AL1,ALSS
5      FORMAT(' IN: M=',F6.2,' K=',F6.2,' ALO=',F6.1,' AL1=',
1         F6.1,' ALSS=',F6.1)
*
      CHECK FOR <0 AMPLITUDE, 0 FREQUENCY, OR NEGATIVE MACH
      IF(AL1.LT.0. .OR. K.LE.0. .OR. M.LT.0.) THEN
          EDAMP = 0
          RETURN
          ENDIF
*
*   DELAY IN NEGATIVE PEAK PROPORTIONAL TO STEADY STALL ANGLE, K**2
      DAL = ALSS * 0.2 * K**2
      ALUS= ALSS + DAL
*
*   POSITIVE DAMPING CONTRIBUTION IS AA * PI * K / 2: (AA=1 IN ATTACHED)
      IF(ALO .GT. ALUS) THEN
*       IN FULLY STALLED FLOW, COEF (AA) IS INCREASED BY AAFS
          AAFS = 0.5
          IF(ALO .LE.ALUS+AL1 .AND. AL1.GT.0.) THEN
*              USE COSINE FUNCTION TO SMOOTHLY GO FROM ATTACHED VALUE (AA= 1)
*              AT ALO = ALUS TO AA = AAFS AT ALO = ALUS + AL1:
              AA = 1.0 + AAFS * 0.5 * (1.-COS( (ALO-ALUS)/AL1 * PI))
          ELSE
*              USE CONSTANT ABOVE ALDUS + AL1
              AA = 1.0 + AAFS
          ENDIF
      ELSE
*
          IN ATTACHED FLOW, FULLY SUBSONIC, USE AA = 1
          IF(M.LT.M SONIC) THEN
              AA = 1.0
          
```

```

ELSE
*   INCREASE ATTACHED POSITIVE DAMPING OVER PI K/2 AT HIGH MACH
    AA = 1.0 + 30.0*K * (M-M_SONIC)**2
    ENDIF
ENDIF

*
*
* FREQUENCY DEPENDENCE OF NEGATIVE PEAK:
IF(K.LE.0.6) THEN
*   INCREASES LINEARLY WITH K (NOTE POS TERM INCREASES PI K /2)
*   PEAK WILL BE -APK + PI K /2, (-3 AT K = .6)
    APK = 6.6 * K
ELSE
*   SUM OF NEG AND POS IS CONSTANT (-3) FOR K > 0.6
    APK = 3.0 + (PI/2. * K)
    ENDIF

*
* MACH EFFECT ON NEGATIVE PEAK:
IF(M.LE.0.4) THEN
*   CONSTANT BELOW M = 0.4
    APM = 1.0
ELSE IF(M.LE.0.6) THEN
*   DROPS LINEARLY BETWEEN 0.4 AND 0.6
    APM = 2.0 - 2.5*M
ELSE
*   SMALLER CONSTANT FOR M>0.6
    APM = 0.5
    ENDIF

*
*
* AMPLITUDE EFFECT:
IF(AL1.LE.1.0) THEN
*   COSINE FUNCTION BETWEEN 0 AT AL1=0 AND 1 AT 1DEG
    APA1 = 0.5*(1.0 - COS(PI*AL1/1.0))
ELSE
*   EXPONENTIAL SQUARE DECAY TO 0.2 AT 6 DEG
    APA1 = EXP(-((AL1-1.0)/4.0)**2)
    ENDIF

*
* NEGATIVE COEFFICIENT IS THE PRODUCT OF THREE TERMS
AP = 1.0 * APK * APM * APA1

*
* EXPONENT FOR GAUSSIAN NEGATIVE PEAK IN AMPLITUDE:
*   CENTERED ABOUT MEAN ANGLE = STALL ANGLE + DELAY
*   WIDTH PROPORTIONAL TO AMPLITUDE (E**-2 AT ALO+AL1)
IF(AL1.NE.0.) THEN
    AE = -2.0*((ALO-ALUS)/AL1)**2
ELSE
    AE = -100
    ENDIF
IF(AE.LT.-100.) AE = -100. ;BOUND NEGATIVE EXPONENT

```

```

*      DAMPING IS SUM OF POSITIVE AND NEGATIVE PEAK TERMS
      EDAMP = AA* PI*K/2. - AP*EXP(AE)
*
      IF(IFLAG.EQ.2) WRITE(6,10) EDAMP,AA,APK,APA1,DAL,AE
10     FORMAT(' DAMP=',F6.2,' AA=',F6.3,' APK=',F6.3,' APA1=',
1       F6.3,' DAL=',F5.2,' AE=',F8.3)
*
      RETURN
      END

```